B^0 Meson decays to $\rho^0 K^{*0}$, $f_0 K^{*0}$, and $\rho^- K^{*+}$, Including Higher K^* Resonances

A dissertation presented

by

Corry Louise Lee-Boehm

to

The Department of Physics

in partial fulfillment of the requirements

for the degree of

Doctor of Philosophy

in the subject of

Physics

Harvard University

Cambridge, Massachusetts

May 2011

Thesis advisor   Author

Prof. Masahiro Morii   **Corry Louise Lee-Boehm**

B^0 Meson decays to $\rho^0 K^{*0}$, $f_0 K^{*0}$, and $\rho^- K^{*+}$, Including Higher K^* Resonances

Abstract

The *BABAR* detector at the PEP-II asymmetric-energy e^+e^- collider at the SLAC National Accelerator Laboratory collected a sample of $(471.0 \pm 2.8) \times 10^6$ $B\overline{B}$ pairs during its operation from 1999–2008. The study of the branching fractions and angular distributions of B meson decays to hadronic final states without a charm quark probes the dynamics of both the weak and strong interactions, and plays an important role both in understanding CP violation in the quark sector and in searching for evidence for physics beyond the standard model. We present branching fraction measurements for the decays $B^0 \to \rho^0 K^{*0}$, $B^0 \to f_0 K^{*0}$, and $B^0 \to \rho^- K^{*+}$, where K^* is a $(K\pi)_0^*$ or $K^*(892)$; we also measure $B^0 \to f_0 K_2^*(1430)^0$. For the $K^*(892)$ channels, we report longitudinal polarizations (for ρ final states) and direct CP-violation asymmetries. We observe $\rho^0 K^*(892)^0$, $\rho^0 (K\pi)_0^{*0}$, $f_0 K^*(892)^0$, and $\rho^- K^*(892)^+$ with greater than 5σ significance, including systematics; $f_0 K^*(892)^0$, $\rho^- K^*(892)^+$, and $\rho^0 (K\pi)_0^{*0}$ are observed here for the first time. We present first evidence for $f_0 (K\pi)_0^{*0}$ with 3.0σ and $f_0 K_2^*(1430)^0$ with 4.4σ significance. We place an upper limit on $\rho^- (K\pi)_0^{*+}$. We find results consistent with no direct CP violation.

Contents

List of Figures

List of Tables

Acknowledgments

Many people deserve thanks for their support, instruction, and encouragement on the road to my Ph.D. First, I'd like to thank Masahiro Morii: without your faith, patience, and willingness to keep me as a grad student despite everything that got in the way of my research, I would not have made it this far. Bill Ford and Jim Smith first sparked my interest in particle physics and taught me much of what I know about research; thank you for continuing to support and encourage me all through grad school. Ale Gaz gave invaluable help on many practical matters for this analysis—I don't know what I would have done without such prompt, helpful, and encouraging emails. My *BABAR* review committee, Fergus, Matt, and Wolfgang, thanks for reading my giant BAD and providing helpful feedback on the analysis and publication. And a big thank you to my other *BABAR* collegues, especially Jim Hirschauer, Lei Zhang, Kris Chaisang, Tom Latham, Eugenia Puccio, Steve Robertson, . . . and everyone else who has answered my emails, built analysis tools, studied detector performance, and generally made *BABAR* a great experiment to work on.

I had the great fortune to be surrounded by wonderful friends during my time in Boston. Thank you Amy, Courtney, Josh, Liz, Elizabeth, Matt, and Jess for keeping me sane and happy. Special thanks to Rachel for being the best roommate ever, making it cool to walk around with banana peels, and giving me a home away from home in Boulder. Thanks to Veritas and Sergeant for love I could always count on to make me sneeze.

And to Josh. You are amazing. Thank you for letting me bounce my crazy collider physics issues off of you, thank you for holding me when I'm freaking out about bad backgrounds and looming deadlines, and thank you for taking care of life when it became too much for me to juggle. You made these last few years awesome. I look forward to tackling all of life's adventures with you at my side.

Chapter 1

Introduction

Experimental studies of charmless hadronic B decays provide a strong test of theoretical calculations and serve as a laboratory in which to search for potential new physics effects. New physics effects can arise from new particles and couplings in the loop diagrams through which many of these decays proceed. Identifying new physics effects requires a solid theoretical description of Standard Model (SM) processes, which is complicated by the interplay of long- and short-distance QCD effects. Many theoretical predictions have been made by Perturbative QCD (pQCD), QCD Factorization (QCDF), Soft Colinear Effective Theory (SCET), and Naïve Factorization (NF), though often with large uncertainties [1]. For an overview of the theoretical predictions and methods, see Sec. 3.1.

In this thesis, we describe the Maximum Likelihood (ML) fit analyses of B decays to quasi-two-body final states involving scalar (S), vector (V), and tensor (T) mesons. Specifically, we measure the following processes:

$$B^0 \to \rho^0 (K\pi)_0^{*0} \quad B^0 \to f_0 (K\pi)_0^{*0} \quad B^0 \to \rho^- (K\pi)_0^{*+}$$

$$B^0 \to \rho^0 K^*(892)^0 \quad B^0 \to f_0 K^*(892)^0 \quad B^0 \to \rho^- K^*(892)^+ \qquad (1.1)$$

$$B^0 \to f_0 K_2^*(1430)^0$$

The notation ρ and f_0 is used to refer to the $\rho(770)$ [2] and $f_0(980)$ [3]. Throughout this thesis we will use K^* to refer to any of the scalar $(K\pi)_0^*$, vector $K^*(892)$, or tensor $K_2^*(1430)$ resonances [2]. The notation $(K\pi)_0^*$ refers to the scalar $K\pi$, which we describe with a LASS model [4, 5], combining the $(K\pi)_0^*$ resonance together with an effective-range non-resonant component. We will discuss these mesons in more detail in Sec. 2.2. Charge-conjugate modes are implied throughout this thesis.

We reconstruct the ρ, f_0, and K^* candidates as:

$$
\begin{aligned}
\rho^0 &\rightarrow \pi^+\pi^- \\
f_0 &\rightarrow \pi^+\pi^- \\
\rho^- &\rightarrow \pi^0\pi^-
\end{aligned}
\qquad\qquad
\begin{aligned}
K^{*0} &\rightarrow K^+\pi^- \\
K^{*+} &\rightarrow K^+\pi^0
\end{aligned}
\tag{1.2}
$$

The dominant Feynman diagrams for these decays are shown in Fig. 1.1. The gluonic penguin graphs with a c or t quark in the loop are expected to dominate, as the tree is doubly CKM suppressed [6, 7].

In all cases, we report branching fractions for the decay processes. The branching fraction for $B^0 \rightarrow \rho^0 K^*(892)^0$, a $B \rightarrow VV$ final state, is defined as

$$
\mathcal{B}(B^0 \rightarrow \rho^0 K^{*0}) = \frac{\Gamma(B^0 \rightarrow \rho^0 K^*(892)^0)}{\Gamma(B^0 \rightarrow \text{all})} \;,
\tag{1.3}
$$

where Γ is the decay rate.

Because the branching fraction $\mathcal{B}(f_0 \rightarrow \pi^+\pi^-)$ is poorly measured, we report our measurements of channels involving an f_0 as $\mathcal{B}(B^0 \rightarrow f_0 K^{*0}) \times \mathcal{B}(f_0 \rightarrow \pi\pi)$, where we assume the isospin ratio $\Gamma(f_0 \rightarrow \pi^+\pi^-)/\Gamma(f_0 \rightarrow \pi\pi) = 2/3$ holds. For $(K\pi)_0^*$ decays, we report the branching fraction times $\mathcal{B}((K\pi)_0^* \rightarrow K\pi)$, as this is poorly measured at present. The Particle Data Group lists $\mathcal{B}((K\pi)_0^* \rightarrow K\pi) = (93 \pm 10)\%$, with no other decays of the $(K\pi)_0^*$ observed [2].

For the final states involving the vector $K^*(892)$, we also measure the CP-violating asymmetry

$$
\mathcal{A}_{ch} \equiv \frac{\Gamma^- - \Gamma^+}{\Gamma^- + \Gamma^+} \;,
$$
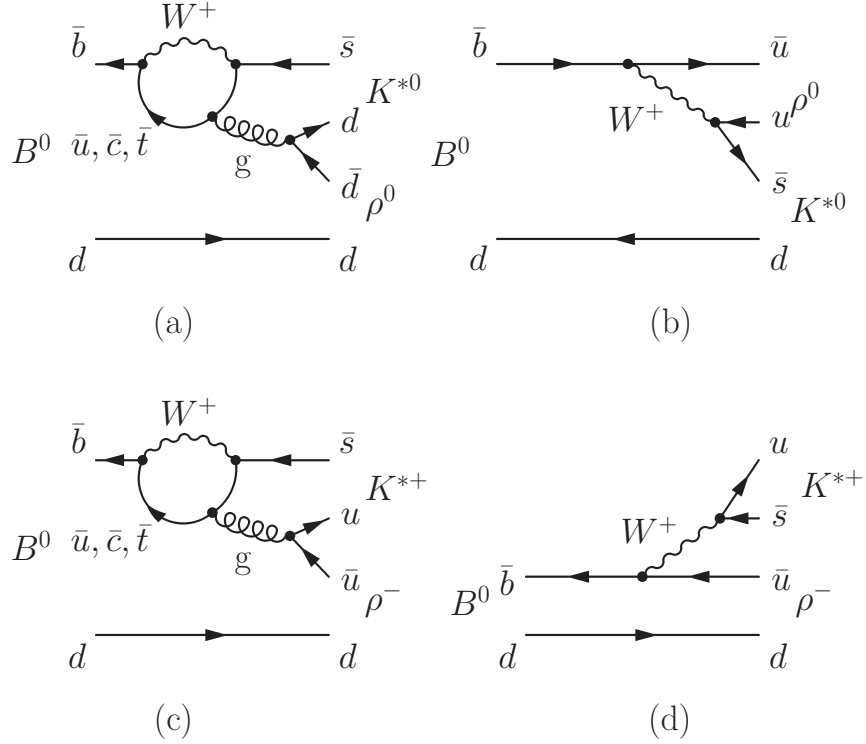
Figure 1.1: Feynman diagrams for (a–b) $B^0 \to \rho^0 K^{*0}$ and (c–d) $B^0 \to \rho^- K^{*+}$. Gluonic penguin diagrams (a, c) dominate over tree (b, d) contributions.

where the superscript on the decay width Γ refers to the charge of the kaon from the K^* decay. This quantity measures CP violation in decay (see Sec. 2.7), and $\mathcal{A}_{ch}$ is otherwise known as a direct CP-violating asymmetry. These asymmetries are of particular interest as they provide an alternative method for measuring the CKM angle γ (see Sec. 2.11.3) [8].

The decays $B^0 \to \rho^0 K^*(892)^0$ and $B^0 \to \rho^- K^*(892)^+$ are of the form $B \to VV$; these decays have three polarization states, which are, in principle, accessible experimentally. In practice, a full angular analysis requires a large number of signal events. In the analyses described in this thesis, we integrate over the azimuthal angle (the angle between the two vector meson decay planes), assuming uniform acceptance over this angle. We define the helicity angles θ_{K^*} and θ_ρ and the azimuthal angle ϕ as shown in Fig. 1.2.
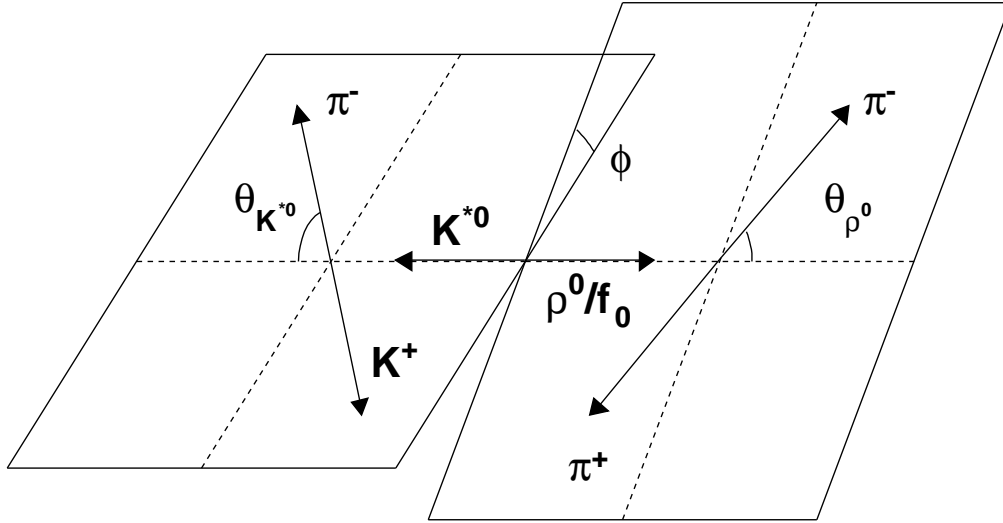
Figure 1.2: Definition of the helicity angles for $B^0 \to \rho^0 K^{*0}$.

The helicity angles are defined in the rest frame of the vector meson; θ_{K^*} is the angle between the charged kaon and the B meson in the K^* rest frame; θ_ρ is the angle between the positively charged (or only charged) pion and the B meson in the ρ rest frame. In the analysis of the $K^*(892)$ channels, we make use of the helicity observables, defined for $\alpha = \rho, K^*$ as $\mathcal{H}_\alpha = \cos(\theta_\alpha)$.

The longitudinal polarization fraction (f_L) can be extracted from the differential decay rate, parameterized as a function of θ_{K^*} and θ_ρ,

$$\frac{1}{\Gamma} \frac{d^2\Gamma}{d\cos\theta_{K^{*0}} d\cos\theta_{\rho^{+,0}}} \propto \frac{1}{4}(1 - f_L)\sin^2\theta_{K^*}\sin^2\theta_\rho + f_L\cos^2\theta_{K^*}\cos^2\theta_\rho . \tag{1.4}$$

QCD Factorization [9, 10] predicts a hierarchy pattern for the ρK^* polarization fractions,

$$f_L(K^{*+}\rho^0) > f_L(K^{*+}\rho^-) > f_L(K^{*0}\rho^+) > f_L(K^{*0}\rho^0) , \tag{1.5}$$

which would be interesting to test experimentally.

The $B \to \rho K^*(892)$ decays are of additional interest, as combined with flavor $SU(3)$, they can be used to improve the determination of the CKM angle α obtained from measuring $B^0 \to \rho^+\rho^-$ [11]; see Sec. 2.11.2.

The decays involving the scalar $(K\pi)^*_0$ and f_0 mesons are of special interest, as well, for the underlying structure of the scalar mesons is not well established theoretically. By comparing measured branching fractions of decays involving scalar mesons with theoretical predictions, we can test whether four-quark or two-quark models of scalar mesons better fit the data.

Predictions have been made for many of the decays described in this thesis. By comparing those predictions with theory, we can help refine theoretical models, improving our theoretical description of SM processes. In this way, should discrepancies be observed between theory and experiment, we can be confident that they are the result of new physics beyond the standard model, rather than coming from higher-order (Standard Model) corrections that have not been previously calculated.

The current state of theoretical predictions, as well as previous experimental measurements are given in Ch. 3. In Ch. 2 we lay down some of the theoretical framework for understanding B decays and CP violation. If the reader is already familiar with this material, s/he is encouraged to move directly to Sec. 2.11.2, where we discuss some applications of ρK^* measurements to constraining CKM matrix parameters. In Ch. 4 we describe the *BABAR* experiment. Ch. 6.1-9 detail the analysis of the B^0 decays measured in this thesis, with the results given in Ch. 8. We summarize our findings and discuss their relation to theoretical predictions in Ch. 10.

Chapter 2

Theoretical Overview

This chapter begins with a brief introduction to particle physics, introduces the reader to the mesons of interest for this thesis, and moves on to describe CP violation in greater depth. Understanding CP violation is one of the main goals of the B physics programs, and the $B \to \rho K^*$ decays measured here have some bearing on the issue. In this thesis, we follow the convention of $\hbar = c = 1$.

2.1 Overview of the Standard Model

Of the four fundamental forces, only three are relevant to the distance and energy scales of particle physics: the electromagnetic, strong, and weak forces. Over energies and distances we can experimentally probe, gravity is negligible by comparison. In the Standard Model of particle interactions (SM), we describe the interactions between particles as the exchange of gauge bosons (particles of integer spin). Different gauge bosons mediate the interactions, depending upon the force in question. The "force carrier" of electromagnetism is the familiar photon (γ). For the strong force, the gauge bosons are eight color gluons (g). The weak force is mediated by massive bosons, the W^+, W^-, and Z^0.

Table 2.1: Properties of gauge bosons in the Standard Model. For each boson the elementary charge, spin, mass, and interaction are given.

Boson	Charge	Spin	Mass (GeV)	Interaction
γ	0	1	0	Electromagnetic
$W^{\pm}$	± 1	1	80	Weak
Z^0	0	1	91	Weak
Gluon (8)	0	1	0	Strong
Higgs	0	0	Unknown	-

Table 2.2: Properties of fundamental fermions in the Standard Model. For each particle the elementary charge, mass, weak isospin and weak hypercharge for the left-handed components of each fermion are given. The right handed components are all $SU(2)$ singlets and thus have a weak isospin of zero. The fermions are separated into leptons (left) and quarks (right). Each family is separated into three generations. The associated anti-fermions have the equivalent quantum numbers as the fermion with the opposite sign.

Lepton	Q (e)	$(I_3)_L$	Y_L	Mass (MeV)	Quark	Q (e)	$(I_3)_L$	Y_L	Mass (MeV)
e	-1	$-\frac{1}{2}$	-1	0.511	u	$\frac{2}{3}$	$\frac{1}{2}$	$\frac{1}{3}$	3
ν_e	0	$\frac{1}{2}$	-1	0	d	$-\frac{1}{3}$	$-\frac{1}{2}$	$\frac{1}{3}$	7
μ	-1	$-\frac{1}{2}$	-1	105.7	c	$\frac{2}{3}$	$\frac{1}{2}$	$\frac{1}{3}$	1100
ν_μ	0	$\frac{1}{2}$	-1	0	s	$-\frac{1}{3}$	$-\frac{1}{2}$	$\frac{1}{3}$	60
τ	-1	$-\frac{1}{2}$	-1	1777	t	$\frac{2}{3}$	$\frac{1}{2}$	$\frac{1}{3}$	173,800
ν_τ	0	$\frac{1}{2}$	-1	0	b	$-\frac{1}{3}$	$-\frac{1}{2}$	$\frac{1}{3}$	5050

The strong interaction is described by the theory of Quantum Chromodynamics (QCD), based on the Lie algebra of $SU(3)_C$. The weak and electromagnetic forces are unified at the weak scale (where the scale is determined by the mass of the $W^{\pm}$ bosons, M_W) into the electroweak theory, described by $SU(2) \times U(1)$. Together, these three groups form the standard model, given by $SU(3)_C \times SU(2) \times U(1)$. The fundamental fermions (quarks and leptons) are specified as multiplets with certain transformation properties under these gauge groups [12]. The properties of the gauge bosons are given in Tab. 2.1, the fundamental fermions in Tab. 2.2 [13].

2.2 Mesons

Mesons are particles with integer spin, which are composed of a quark and an anti-quark. The two quarks do not have to be of the same flavor, and hence we will denote a meson generically as $q\overline{q}'$. For our upcoming discussions of CP violation we will focus on beauty mesons (B_d), so we discuss those first. We can represent the B_d-mesons as a system of two Isospin doublets $(I = 1/2)$. The top element of the doublet has $I_3 = +1/2$, the bottom element has $I_3 = -1/2$; we denote the quark content of the mesons in parentheses. Note that one can write similar isodoublets for the kaons, D-mesons, and B_s-meson systems.

$$B = +1 \quad \begin{bmatrix} B^+ \; (u\bar{b}) \\ B^0 \; (d\bar{b}) \end{bmatrix} \quad , \qquad B = -1 \quad \begin{bmatrix} \overline{B}^0 \; (\bar{d}b) \\ B^- \; (\bar{u}b) \end{bmatrix} \tag{2.1}$$

B-mesons are short-lived particles that rapidly decay into a variety of hadronic and/or leptonic final states. As the B_d mesons listed above are the lightest mesons containing a b quark, they decay by changing the flavor of the b quark; these decays are mediated by the weak interaction.

Mesons are intrinsically unstable, though for our purposes, we will regard the lowest lying meson states (the pseudoscalar pions and kaons) as stable, as they have comparatively long lifetimes, $\mathcal{O}(10^{-8})$ seconds. Compare this with the lifetime of the B^0 meson, 1.5×10^{-12} seconds. Mesons decaying strongly (such as the ρ and K^* to be discussed presently) decay even more rapidly.

Creating mesons out of the lowest-lying quarks $(q = u, d, s)$, one readily forms what is known as the pseudoscalar meson nonet, Fig. 2.1 (left). The mesons are stacked vertically in increasing strangeness (the s quark has strangeness $S = -1$, its antiquark has $S = +1$) and horizontally as a function of charge Q. The central mesons in the octet are linear combinations of $u\overline{u}$, $d\overline{d}$, and $s\overline{s}$.

The meson's spin J satisfies the relation

$$|l - s| < J < |l + s| \, , \tag{2.2}$$
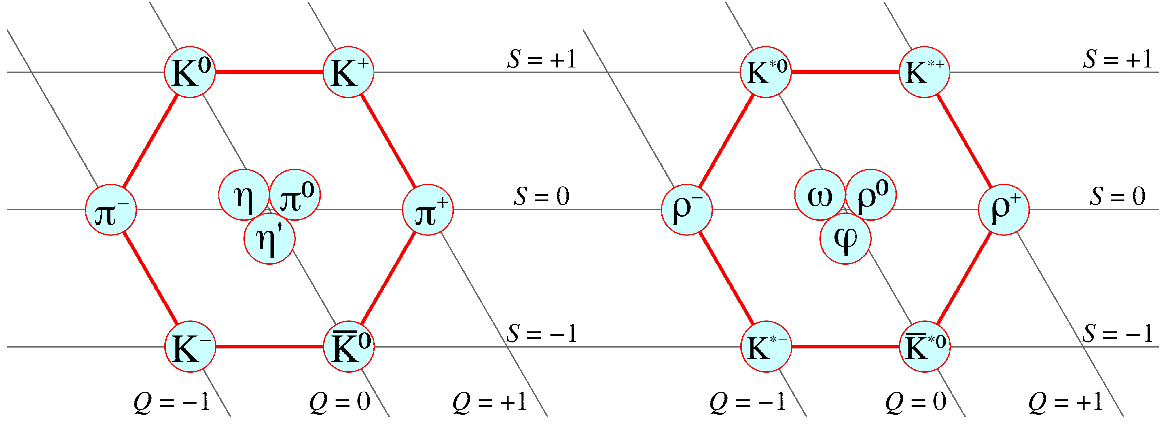
Figure 2.1: Pseudoscalar (left) and vector meson (right) nonets.

where l is the orbital angular momentum of the $q\overline{q}'$ state, and s is 0 (antiparallel quark spins) or 1 (parallel quark spins). The meson multiplets are delineated by their J^P value, where P is the parity eigenvalue (see Sec. 2.4 for a definition of parity). The pseudoscalars with $J^P = 0^-$ (Fig. 2.1 (left)) and the vectors with $J^P = 1^-$ (Fig. 2.1 (right)) are $l = 0$ states. The orbitally excited $l = 1$ states are the scalars ($J^P = 0^+$), axial vectors ($J^P = 1^+$), and tensors ($J^P = 2^+$) [2].

Although the makeup of the axial vector and tensor states is believed to be given by the quark model, the scalar states are not well understood. The light scalar mesons such as the $f_0(980)$ are believed by many to be four-quark states, which makes predicting branching fractions involving these states difficult. By measuring branching fractions involving these scalar mesons, we can test theoretical predictions that assume the scalars to be standard, two-quark mesons.

2.3 Flavor changing interactions

In the B-meson system, the massive b quark decays into a lighter, more stable quark. The only interaction that permits changes in quark flavor is the weak interaction. For example, a b quark can decay into a c quark by emitting a virtual W^-, which subsequently decays. One such diagram

describing this interaction can be seen in Figure 2.2.
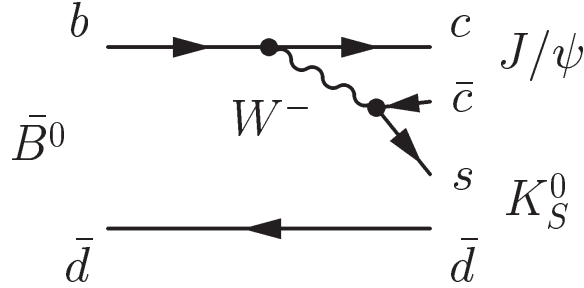
Figure 2.2: Tree diagram describing the decay $\overline{B}^0 \rightarrow J/\psi K_S^0$.

A b quark cannot, for instance, decay into an s quark by emitting a γ; only weak interactions can change quark flavor. Experimentally, only flavor changing charged currents (exchange of a $W^\pm$) have been observed. Although flavor changing neutral currents (exchange of a Z^0) are theoretically possible, their contribution is heavily suppressed in the Standard Model. It is, however, still possible for a b quark to decay into an s quark; this is a second-order weak interaction, and will be discussed further (and sample Feynman diagrams shown) in Sec. 2.11.1.

2.4   CP Violation

The non-conservation of charge conjugation and parity (CP, for short) has been a topic of great interest for physicists since the 1964 discovery that CP symmetry is violated in decays of neutral kaons [14, 15]. Like neutral kaons, the neutral B-meson was expected to exhibit CP violating asymmetries. Before the inception of the *BABAR* and Belle detectors at the PEP-II and KEKB asymmetric e^+e^- colliders, CP violation experiments in the B-meson system were difficult both due to a lack of statistics and due to the B-mesons being created at rest in the laboratory frame. With the large datasets collected by *BABAR* and Belle over roughly a decade of collisions, we have achieved a greater understanding of CP violation in the B-meson system.

In the analyses presented in this thesis, only CP violation in decay (see Sec. 2.7) is

measured. However, as measurements of ρK^* decays can be combined with other information to measure the CKM angles α and γ (see Sec. 2.10), we give a broader overview of CP violation and the Unitary Triangle.

2.4.1 Operator definitions

The charge conjugation (C) operation, amounts to a reversal of all the internal quantum numbers, which describe a particle. Under the C operation, for example, a particle with electric charge $Q = +1$ would end up with a charge of $Q = -1$. Additionally, quantum numbers such as beauty (B) are reversed. As a result, a B^0 ($d\bar{b}$) would become a $\overline{B}^0$ ($b\bar{d}$); thus the C operation caused a change of beauty $|\Delta B| = 2$. In general, the C operation can be said to change a particle into its antiparticle. Charge conjugation is a discrete, unitary operation; eigenfunctions of C have eigenvalues of ± 1. We refer to these states as even $(+1)$ and odd (-1). For a C eigenstate $|\psi_C\rangle$, we can write the charge conjugation operation as

$$C|\psi_C\rangle = \pm|\psi_C\rangle \ . \tag{2.3}$$

The P in CP violation represents the parity operation. Simply speaking, the parity operation can be thought of as reflecting an object in a mirror (plus a rotation of 180 degrees). For a vector $\vec{r}$, this means that $\vec{r} \overset{P}{\longrightarrow} -\vec{r}$. As with charge conjugation, we can define states of definite parity. These P eigenstates will also have eigenvalues of ± 1, as shown in equation (2.4) for a parity eigenstate $|\psi_P\rangle$.

$$P|\psi_P\rangle = \pm|\psi_P\rangle \tag{2.4}$$

Another discrete operation, related to C and P is time reversal, T. Just as parity reversed the spatial direction of vectors, so time reversal reverses the "direction" of time. That is, $t \overset{T}{\longrightarrow} -t$. Unlike parity and charge conjugation, however, we cannot write an eigenvalue equation for the T

operator on a wavefunction $|\psi\rangle$. This is a direct consequence of the antiunitarity of the T operator, which is required to preserve normalizability ($\langle\psi|\psi\rangle = 1$).

2.4.2   Relations between C, P, and T

Until the mid-1900's, parity, charge conjugation, and time reversal were all believed to be good symmetries of nature. Experiment currently verifies that P is a good symmetry for the electromagnetic and strong interactions. In 1957, however, Wu and her collaborators [16] showed that parity is not conserved in weak interactions. Subsequent work also showed that although charge conjugation is a good symmetry for the electromagnetic and strong interactions, it is maximally broken in weak interactions. Taken together, however, CP seemed to be a good symmetry. In 1964, however, it was observed that CP symmetry is slightly violated in the decays of neutral kaons [14, 15].

Although CP is no longer considered a good symmetry of nature, taken together with time reversal, the symmetry does appear exact. That is to say, practically any Hamiltonian H commutes with the operation CPT: $[H,\ CPT] = 0$.

Invariance of the Hamiltonian under the CPT operation, and the presence of CP violation in weak decays, requires that T symmetry also be weakly broken. A theoretical explanation for this was proposed by Kobayashi and Maskawa [6]. If a non-vanishing phase is present in the Standard Model, then CP violation is theoretically possible within the framework of the SM.

To be more precise, we can describe the coupling of particles to fields (eg. a b quark to a W^-) by a complex number. Through redefinition of the phase associated with that complex number (where the coupling is given by $re^{i\phi}$, and ϕ is the phase), we can make the coupling real. Depending upon the Lagrangian, which describes the field of interest, it may be possible to completely eliminate all complex phases, or some phases may remain. If there are complex phases, which renormalization cannot eliminate, CP violation can arise.

2.5   The CP **Operation on Mesons**

As it will be useful to our future discussion of CP violation in the charged and neutral B-meson systems, we will briefly discuss the CP operation on mesons. As above, We will denote the meson generically as $M = q\overline{q}'$. The meson M is said to be a flavor eigenstate; that is, it contains a definite flavor (quark) content. Flavor eigenstates are often the most useful basis in which to represent particles when discussing production, which frequently is the result of strong (flavor conserving) interactions. Flavor eigenstates are also useful when investigating decays, as it is natural to draw Feynman diagrams describing particle decay in terms of individual quarks.

We can also write down the CP-conjugate flavor eigenstate to M, which we denote as $\overline{M} = \overline{q}q'$. In general, flavor eigenstates are not eigenstates of CP. We can write the CP operation as $CP\,M = e^{i\xi_M}\overline{M}$. The phase ξ_M is arbitrary, and a redefinition of it does not change the physics. For the B^0 mesons, for example, we would write,

$$CP\,|B^0\rangle = e^{i\xi_B}|\overline{B}^0\rangle\,, \qquad CP\,|\overline{B}^0\rangle = e^{-i\xi_B}|B^0\rangle\ . \tag{2.5}$$

In the case where we have a CP eigenstate, M_{CP}, the CP operation simplifies and one is left with the original eigenstate times the eigenvalue ($\eta_{CP} = \pm 1$) of CP,

$$CP\,M_{CP} = e^{i\xi_{M_{CP}}}\overline{M}_{CP} = \eta_{CP}M_{CP}\ . \tag{2.6}$$

When the flavor eigenstate is not automatically a CP eigenstate (as is the case, for example, with neutral, flavor non-trivial mesons such as the B^0), it is possible to construct CP eigenstates as linear combinations of flavor eigenstates. For neutral mesons M and $\overline{M}$ as described above, the CP eigenstates are given by:

$$M_{\pm CP} = \left(M \pm \overline{M}\right)/\sqrt{2}\ . \tag{2.7}$$

Before the discovery of CP violation in the neutral kaon system, it was believed that the linear combinations given in equation (2.7) for the K^0 and $\overline{K}^0$ were not only the CP eigenstates,

but also eigenstates of mass and lifetime. Understanding that this is not the case leads us to write a slightly different equation for the mass/lifetime eigenstates of neutral, flavor non-trivial mesons. This will be discussed in more detail for the B-meson in Section 2.8.1, as the background to CP violation in mixing.

2.6   Types of CP Violation in the B Meson System

With an understanding of some of the physics background necessary for a discussion of CP violation, we summarize the three types of CP violation possible in the B-meson system.

1. *CP violation in decay* may occur in both charged and neutral B-meson decays. This violation manifests itself as an amplitude difference between a B-meson decay and the CP conjugate process. This is also referred to as "direct CP violation".

2. *CP violation in mixing* may occur when two neutral mass eigenstates cannot be CP eigenstates. This is also known as "indirect CP violation".

3. *CP violation in the interference between decays with and without mixing* may occur when both the B^0 and the $\overline{B}^0$ can decay into the same (CP eigenstate) final state.

We will begin our discussion with CP violation in decay, as this is the most conceptually-simple type of CP violation in the B-meson system.

2.7 CP Violation in Decay

CP violation in decay occurs when the rates for CP conjugate processes are not the same. As a result, this type of CP violation can occur in both neutral and charged systems. In order for such a rate difference to arise, a decay must have contributions from at least two Feynman diagrams. Not only must there be at least two diagrams, but there must also be phase differences between the

diagrams. There are two types of phase differences which much be present in order to have CP violation in decay: the so-called "strong" and "weak" phases.

Complex coupling constants can result in phases, which differ in sign between a process and its CP conjugate process; that is, the Lagrangian that contributes to the decay amplitude is complex. In the Standard Model, these phases arise only in the CKM matrix (discussed in Section 2.10), which describes weak interactions, hence they are called "weak phases". Depending upon the Feynman diagrams that contribute to the decay, there can be several different couplings and thus different weak phases present in a decay.

Another type of phase occurs even when the Lagrangian is real. This type of phase does not change sign between a process and its CP conjugate process; as a result, this does not lead to CP violation. These phases arise from intermediate states in the decay process; this rescattering is due mainly to strong interactions and the phases are are thus termed "strong phases".

For both strong and weak phases, it is important to note that the absolute phase carries no physical meaning because it is possible to perform a global phase rotation to change that value. As a result, we wish to look at differences between phases (eg. the difference between the strong phase of one contributing diagram and that of another), as these are physically meaningful quantities. With this in mind, we will write the amplitudes of a decay process and its CP conjugate with three parameters describing each diagram: A_i is the magnitude of the diagram's contribution to the overall amplitude of the decay, $e^{i\phi_i}$ describes the weak phase, and $e^{i\delta_i}$ describes the contribution of the strong phase in that diagram. Using this notation, we give the amplitude for a B-meson to decay into the final state f, with contributions from each diagram i, in equation (2.8). Equation (2.9) gives the amplitude for the CP conjugate process [17, 18].

$$A_f = \langle f|H|B\rangle = \sum_i A_i e^{i(\delta_i + \phi_i)} \tag{2.8}$$

$$\overline{A_{\overline{f}}} = \langle \overline{f}|H|\overline{B}\rangle = e^{i(\xi_f - \xi_B)} \sum_i A_i e^{i(\delta_i - \phi_i)} \tag{2.9}$$

Recall that we defined the overall phases ξ in equation (2.5).

If we look at the difference in rates between the two processes (recall that decay rates are proportional to the amplitude squared of the process) given in equations (2.8) and (2.9), we find (for $i \neq j$),

$$|A|^2 - |\overline{A}|^2 = -2 \sum_{i,j} A_i A_j \sin(\phi_i - \phi_j) \sin(\delta_i - \delta_j) \ . \tag{2.10}$$

Writing the rate difference in this way makes it clear that the two rates will be identical if the contributing Feynman diagrams have either the same relative strong or weak phases. We also note that if the theory were such that CP was conserved, then the weak phases for all possible diagrams would be equal.

Experimentally, it is very straightforward to measure CP asymmetries in charged decays. We define the asymmetry, A_{ch}, to be

$$A_{ch} = \frac{\Gamma(B^+ \to f) - \Gamma(B^- \to \overline{f})}{\Gamma(B^+ \to f) + \Gamma(B^- \to \overline{f})} = \frac{1 - |\overline{A}/A|^2}{1 + |\overline{A}/A|^2} \ . \tag{2.11}$$

where the ratio clearly must satisfy $|\overline{A}/A| \neq 1$ if CP violation is to be present. This is true in neutral decays, as well, though one must choose a final state that definitely tags whether the decay was from a B^0 or $\overline{B}^0$. For instance, in $B^0 \to \rho^0 K^{*0}$, the sign of the charged kaon from the decay $K^{*0} \to K^+ \pi^-$ tags whether one had a K^{*0} or a $\overline{K^{*0}}$, and thus whether the original parent particle was a B^0 or $\overline{B}^0$. As mentioned in Ch. 1, for the decays studied in this thesis, we measure

$$\mathcal{A}_{ch} \equiv \frac{\Gamma^- - \Gamma^+}{\Gamma^- + \Gamma^+} \ , \tag{2.12}$$

where the superscript on the decay width Γ refers to the charge of the kaon from the K^* decay.

The general statement of CP *violation in decay* is

$$\left| \frac{\overline{A}_{\overline{f}}}{A_f} \right| = \left| \frac{\sum_i A_i e^{i(\delta_i - \phi_i)}}{\sum_i A_i e^{i(\delta_i + \phi_i)}} \right| \neq 1 \ . \tag{2.13}$$

2.8 CP **Violation in Mixing**

The second and third types of CP violation can occur only in systems of self-conjugate pairs of mesons (the neutral K, D, B_d, and B_s systems). In this section, we investigate the second type of CP violation, CP violation in mixing. From the discussion of the CP operation on mesons in Section 2.5, we know that if CP is not a good symmetry of nature, then eigenstates of CP are not necessarily eigenstates of mass and lifetime. CP violation in mixing arises when we are unable to write mass/lifetime eigenstates as eigenstates of CP. In order to better understand when this occurs, we will discuss mass eigenstates and the mixing of flavor eigenstates for the neutral B-meson system.

2.8.1 **Mixing in the neutral B-meson system**

In order to understand the decay of our B-meson, we would like to consider the time evolution of a state, which has the general form

$$a(t)|B^0\rangle + b(t)|\overline{B}^0\rangle + c_1(t)|n_1\rangle + c_2(t)|n_2\rangle + c_3(t)|n_3\rangle + \ldots \quad , \tag{2.14}$$

where B^0 and $\overline{B}^0$ are our initial states ($a(0) \neq 0$, $b(0) \neq 0$) and n_1, n_2, $\ldots$ are states into which the B^0 or $\overline{B}^0$ can decay (these states do not initially exist, $c_i(0) = 0$). What we would like to calculate, in order to understand mixing in the B^0–$\overline{B}^0$ system, is the time evolution of the B^0 and $\overline{B}^0$; we are not interested in the myriad possible final states. We thus use the Wigner-Weisskopf approximation, which allows us to describe a beam of oscillating and decaying neutral mesons in its rest frame as a two-component wave function. This approximation treats the weak-interaction Hamiltonian as a perturbation to the strong and electromagnetic Hamiltonian. The B^0 and $\overline{B}^0$ are eigenstates of the strong and electromagnetic interactions with a common mass m_B and opposite flavor content. Because the strong and electromagnetic interactions are flavor-conserving, these interactions do not cause oscillations between the B^0 and $\overline{B}^0$ states; only when the weak interaction is considered do

we have mixing.

The Wigner-Weisskopf approximation can be used to describe mixing in any neutral meson system. We, however, will not explore this approximation in its general case but rather will focus on the B_d system; the interested reader can find a more general discussion in texts such as [19]. In our case we have

$$|\psi(t)\rangle = \psi_1(t)|B^0\rangle + \psi_2(t)|\overline{B}^0\rangle \ . \tag{2.15}$$

The time-evolution of this wavefunction is given by a Schrödinger-like equation

$$i\frac{d}{dt}\begin{pmatrix} a \\ b \end{pmatrix} = H\begin{pmatrix} a \\ b \end{pmatrix} \equiv \left(\mathbf{M} - \frac{i}{2}\mathbf{\Gamma}\right)\begin{pmatrix} a \\ b \end{pmatrix} \ . \tag{2.16}$$

The matrix H, however, is not Hermitian; if it were, the mesons would simply oscillate forever and never decay. The matrices $\mathbf{M}$ and $\mathbf{\Gamma}$, on the other hand, are Hermitian. We can write the "Hamiltonian" more explicitly as,

$$H = \begin{pmatrix} M - \frac{i}{2}\Gamma & M_{12} - \frac{i}{2}\Gamma_{12} \\ M_{12}^* - \frac{i}{2}\Gamma_{12}^* & M - \frac{i}{2}\Gamma \end{pmatrix} = \begin{pmatrix} M & M_{12} \\ M_{12}^* & M \end{pmatrix} - \frac{i}{2}\begin{pmatrix} \Gamma & \Gamma_{12} \\ \Gamma_{12}^* & \Gamma \end{pmatrix} \ , \tag{2.17}$$

where we have made the Hermiticity of $\mathbf{M}$ and $\mathbf{\Gamma}$ explicit. As we have chosen to look specifically at the B_d system, we can simplify equation (2.17) by using the fact that $\Gamma_{12} \ll M_{12}$. This allows us to re-write the Hamiltonian as

$$H = \begin{pmatrix} M - \frac{i}{2}\Gamma & M_{12} \\ M_{12}^* & M - \frac{i}{2}\Gamma \end{pmatrix} \ . \tag{2.18}$$

Determining the eigenvalues of our simplified Hamiltonian is straightforward. Doing the calculation, we find

$$\mu_\pm = M - \frac{i}{2}\Gamma \pm |M_{12}| \ . \tag{2.19}$$

The two eigenvalues give us two states of definite mass (if we hadn't simplified the Hamiltonian, these would also have different lifetimes). For the B_d system, we define the two eigenstates corresponding to these eigenvalues, labeling them $B_H = B_{Heavy}$ and $B_L = B_{Light}$. The eigenvalue for the B_L is $\mu_- = \mu_L = M - \frac{i}{2}\Gamma - |M_{12}|$; for the B_H we take the plus sign in equation (2.19). It is traditional to write

$$|B_H\rangle \;\; = \;\; p|B^0\rangle - q|\overline{B}^0\rangle \tag{2.20}$$

$$|B_L\rangle \;\; = \;\; p|B^0\rangle + q|\overline{B}^0\rangle \;, \tag{2.21}$$

with the requirement that $|p|^2 + |q|^2 = 1$. The eigenstates of the Hamiltonian are clearly distinct from the flavor eigenstates (B^0 and $\overline{B}^0$).

As B-meson production commonly occurs through (flavor conserving) strong interactions, we may start out knowing the flavor composition of our B-meson. For example, the (strong) decay of the $\Upsilon(4S)$ (a $b\overline{b}$ bound state) results in a B^0 and a $\overline{B}^0$ about half the time (the other 50% of the decays result in a B^+ and a B^-). Thus we know that at time $t = 0$ we have one B^0 and one $\overline{B}^0$. If we pick out the B^0 produced by the reaction, however, and "watch it" as it travels along, we will see that it does not remain a B^0, because the B^0 is a flavor eigenstate and particles propagate through space as mass eigenstates. Thus this initial B^0 seems to "mix" with a $\overline{B}^0$ as it travels along.

2.8.2   Relationships between mass and CP eigenstates

Equations (2.20) and (2.21) suggest that if the ratio $|q/p| = 1$, the two states ($|B_H\rangle$ and $|B_L\rangle$) are orthogonal. If this is true, these equations simplify to

$$B^0_{\pm CP} = \left(B^0 \pm \overline{B}^0\right)/\sqrt{2} \;, \tag{2.22}$$

where $B^0_{\pm CP}$ in the above equation is clearly recognizable as the two eigenstates of CP, as discussed in Section 2.5. From this, it is clear that the requirement $|q/p| = 1$ leads to CP conservation

in B^0–$\overline{B}^0$ mixing. We, however, are interested in CP non-conservation, and thus wish to investigate the situation when $|q/p| \neq 1$. Using equations (2.16), (2.19) and (2.21), we can solve for the ratio q/p.

$$\left(\mathbf{M} - \frac{i}{2}\mathbf{\Gamma} \right) \begin{pmatrix} p \\ q \end{pmatrix} = \begin{pmatrix} M - \frac{i}{2}\Gamma & M_{12} \\ M_{12}^* & M - \frac{i}{2}\Gamma \end{pmatrix} \begin{pmatrix} p \\ q \end{pmatrix} \tag{2.23}$$

$$= \left[M - \frac{i}{2}\Gamma - |M_{12}| \right] \begin{pmatrix} p \\ q \end{pmatrix} \tag{2.24}$$

Where the first equality just presents the Schrödinger equation explicitly for $|B_L\rangle$ and we use the $|B_L\rangle$ eigenvalue in the second equality. From here, we find that

$$\left(M - \frac{i}{2}\Gamma - |M_{12}| \right) p = \left(M - \frac{i}{2}\Gamma \right) p + (M_{12})\, q \ , \tag{2.25}$$

$$-|M_{12}|p = M_{12}q \ . \tag{2.26}$$

The ratio of p/q is clearly just

$$\frac{q}{p} = -\frac{|M_{12}|}{M_{12}} \ . \tag{2.27}$$

It can also be useful to consider the square of this ratio. When we write it this way, we can see that when the relative phase between M_{12} and M_{12}^* vanishes, $|p/q|^2 = 1$. The relative phase vanishes when $|B_H\rangle$ and $|B_L\rangle$ are CP eigenstates. We have established the condition for CP *violation in mixing* (in the B_d system) to be:

$$\left| \frac{q}{p} \right|^2 = \left| \frac{M_{12}^*}{M_{12}} \right| \neq 1 \ . \tag{2.28}$$

2.9 CP **Violation in the Interference between Decays with and without Mixing**

The third type of CP violation can arise when neutral B-mesons (or kaons, etc.) decay into final states, which are CP eigenstates (f_{CP}). These final states can be produced from either

B^0 or $\overline{B}^0$ decays. To better understand how such CP violation comes about, we will first look at the time evolution of a B-meson that at time $t = 0$ is known to be in a particular flavor eigenstate. We next introduce the parameter $\lambda_{f_{CP}}$. We will find that when $\lambda \neq \pm 1$, CP violation, and if another condition is satisfied, CP violation in the interference between decays with and without mixing, occurs. To avoid repeatedly writing such a long name, this type of CP violation is often abbreviated as "CP violation in the interference between mixing and decay".

2.9.1 Time evolution of neutral B-mesons

As discussed in Section 2.8, flavor eigenstates of the neutral B-meson are not mass eigenstates. From equations (2.20) and (2.21) we can rewrite the relationship between the mass and flavor eigenstates as

$$|B^0\rangle \;=\; \frac{1}{2p}\left(|B_L\rangle + |B_H\rangle\right) \tag{2.29}$$

$$|\overline{B}^0\rangle \;=\; \frac{1}{2q}\left(|B_L\rangle - |B_H\rangle\right) \ . \tag{2.30}$$

In order to simplify future calculations, we will turn specifically to the B_d system so we can continue to use the simplifying assumption that $\Gamma_{12} \ll M_{12}$. Recall that the eigenvalues of the simplified Hamiltonian in equation (2.17) are

$$\mu_\pm = M - \frac{i}{2}\Gamma \pm |M_{12}| \ . \tag{2.31}$$

Using the above relations along with equations (2.20) and (2.21), we can describe the time evolution of a state that begins at $t = 0$ as a flavor eigenstate. Recall that if we have a B^0 at time $t = 0$, that B^0 will "mix" with a $\overline{B}^0$ according to the time-dependent Schrödinger equation. We designate a state that starts out as a B^0 at $t = 0$ as $|B^0_{phys}(t)\rangle$, where from [17, 20] we have

$$|B^0_{phys}(t)\rangle \;=\; \frac{1}{2p}\left[e^{-i\mu_- t}\left(p|B^0\rangle + q|\overline{B}^0\rangle\right) + e^{-i\mu_+ t}\left(p|B^0\rangle - q|\overline{B}^0\rangle\right)\right] \tag{2.32}$$

$$=\; e^{-i(M - i\Gamma/2)t}\left[\cos\left(\frac{\Delta m_B t}{2}\right)|B^0\rangle + i\left(\frac{q}{p}\right)\sin\left(\frac{\Delta m_B t}{2}\right)|\overline{B}^0\rangle\right] \ . \tag{2.33}$$

We can write a similar equation for a state that starts out as a $\overline{B}^0$,

$$|\overline{B}^0_{phys}(t)\rangle = e^{-i(M-i\Gamma/2)t} \left[\cos\left(\frac{\Delta m_B t}{2}\right)|\overline{B}^0\rangle + i\left(\frac{p}{q}\right)\sin\left(\frac{\Delta m_B t}{2}\right)|B^0\rangle\right] \quad . \quad (2.34)$$

Equations (2.33) and (2.34) make it explicit that in the time evolution of the B^0 and $\overline{B}^0$, mixing is a result of the mass difference between the two mass eigenstates. If we wanted to write out the time evolution equations for the neutral kaon system, on the other hand, the lifetime difference, $\Delta\Gamma$, would be very important (though the Δm term still drives the oscillation between K^0 and $\overline{K}^0$ states).

The nature of the time evolution of B-mesons is extremely important in B factory experiments (such as *BABAR* and Belle), where an $\Upsilon(4S)$ decays into a coherent $B\overline{B}$ pair. The time evolution of the two B-mesons is such that when one is in the B^0 flavor eigenstate, the other is a $\overline{B}^0$. This property allows B physicists to "tag" whether a decay (eg. into a CP eigenstate, such as $J/\psi K_S^0$) was the result of a $|B^0_{phys}(t)\rangle$ or $|\overline{B}^0_{phys}(t)\rangle$ decay by knowing whether the other B-meson decayed as a $\overline{B}^0$ or B^0. In this way, physicists can measure time-dependent asymmetries in B^0 versus $\overline{B}^0$ decay rates as discussed in Section 2.9.4. We now look specifically at B decays into CP eigenstates and how they lead to CP violation in the interference between mixing and decay.

2.9.2   Neutral B decays into CP eigenstates

If the final state of our B decay is a CP eigenstate then it satisfies the relation

$$CP|f_{CP}\rangle = \eta_{f_{CP}}|f_{CP}\rangle \quad . \tag{2.35}$$

We are now interested in the decay amplitudes for a B^0 and $\overline{B}^0$ decaying into the final state f_{CP}:

$$A_{f_{CP}} = \langle f_{CP}|H|B^0\rangle \tag{2.36}$$

$$\overline{A}_{f_{CP}} = \langle f_{CP}|H|\overline{B}^0\rangle \quad . \tag{2.37}$$

Using this and the definitions of p and q from Section 2.8.1, we define the quantity $\lambda_{f_{CP}}$ as

$$\lambda_{f_{CP}} \equiv \frac{q\overline{A}_{f_{CP}}}{pA_{f_{CP}}} = \eta_{f_{CP}} \frac{q\overline{A}_{\overline{f}_{CP}}}{pA_{f_{CP}}} \ , \tag{2.38}$$

where the second equality comes from the relation $\overline{A}_{f_{CP}} = \eta_{f_{CP}} \overline{A}_{\overline{f}_{CP}}$. This form is useful both in calculations of theoretical time-dependent asymmetries and in the physical interpretation of $\lambda_{f_{CP}}$.

From the discussion of CP violation in decay (Section 2.7), we know that when CP is conserved, the decay amplitudes will satisfy:

$$CP \text{ conserved} \quad \Longrightarrow \quad \left| \frac{\overline{A}_{\overline{f}_{CP}}}{A_{f_{CP}}} \right| = 1 \ . \tag{2.39}$$

Our discussion of CP violation in mixing (Section 2.8) led to the observation that if CP is conserved, the following equation is also satisfied:

$$CP \text{ conserved} \quad \Longrightarrow \quad \left| \frac{q}{p} \right| = 1 \ . \tag{2.40}$$

Additionally, when CP is conserved, the relative phase between (q/p) and $(\overline{A}_{\overline{f}_{CP}}/A_{f_{CP}})$ vanishes, leaving us with: $\lambda_{f_{CP}} = \pm 1$. Clearly, if CP violation in decay and/or in mixing is present, then $|\lambda_{f_{CP}}| \neq 1$. However, it is possible to have both $|\lambda_{f_{CP}}| = 1$ and the presence of CP violation. This is the condition for *CP violation in the interference between decays with and without mixing* and arises when:

$$|\lambda_{f_{CP}}| = 1 \ , \quad Im\left\{ \lambda_{f_{CP}} \right\} \neq 0 \ . \tag{2.41}$$

2.9.3   Simplification of $\lambda_{f_{CP}}$

As we are interested in the imaginary part of $\lambda_{f_{CP}}$ in order to understand CP violation in the interference between mixing and decay, we will spend a little time here putting $\lambda_{f_{CP}}$ in terms of physically meaningful quantities. We will then be able to further interpret these quantities in terms of angles of the Unitarity Triangle (described in Section 2.10) for specific decay chains.

The Hamiltonian for weak decays can be written as a sum of contributions from individual diagrams. In writing the Hamiltonian we note that H must be unitary and that weak phases change sign between a process and its CP conjugate process. Using the transformation of the Hamiltonian under CP ($CP\,H_j\,CP = H_j^\dagger$) we have

$$H = \sum e^{i\phi_j} H_j + \sum e^{-i\phi_j} H_j^\dagger \ , \tag{2.42}$$

where, for a given j, the first term comes from a particular process and the second term arises from the CP conjugate process. In the case where only a single diagram can contribute to the decay (that is, when all other diagrams are highly suppressed) we can say, for example, that the process $B^0 \to f_{CP}$ is governed by H_k. If this is so, then the only contribution to $\overline{B}^0 \to f_{CP}$ is from $H_k^\dagger$. Making use of this information, we can rewrite equations (2.36) and (2.37) as in [20]:

$$A_{f_{CP}} = \langle f_{CP}|H|B^0\rangle \ = \ \langle f_{CP}|e^{i\phi_k}H_k|B^0\rangle \tag{2.43}$$

$$\overline{A}_{f_{CP}} = \langle f_{CP}|H|\overline{B}^0\rangle \ = \ \langle f_{CP}|e^{-i\phi_k}H_k^\dagger|B^0\rangle \tag{2.44}$$

$$= \ \langle f_{CP}|e^{-i\phi_k}CP\,H_k\,CP|B^0\rangle \tag{2.45}$$

$$= \ e^{-2i\phi_k}\eta_{f_{CP}}\langle f_{CP}|e^{i\phi_k}H_k|B^0\rangle\langle B^0|CP|\overline{B}^0\rangle \tag{2.46}$$

$$= \ e^{-2i\phi_k}\eta_{f_{CP}}A_{f_{CP}}\langle B^0|CP|\overline{B}^0\rangle \ . \tag{2.47}$$

Now that we know how to write $\overline{A}_{f_{CP}}$ in terms of $A_{f_{CP}}$, we will perform some more manipulations on $\lambda_{f_{CP}}$, itself. From equation (2.38), we know how to write $\lambda_{f_{CP}}$ in terms of p, q, and decay amplitudes. Recalling the simplification for the B_d system that $\Gamma_{12} \ll M_{12}$ and using the expression for q/p from equation (2.27), we can write,

$$\lambda_{f_{CP}} \equiv \frac{q\overline{A}_{f_{CP}}}{pA_{f_{CP}}} = -\frac{|M_{12}|}{M_{12}}\frac{\overline{A}_{f_{CP}}}{A_{f_{CP}}} \ . \tag{2.48}$$

The simplifying assumption that the width difference of the neutral B-meson mass eigenstates is negligible allows us to re-write equation (2.48) in terms of the Hamiltonian from equation (2.18) as

$$\lambda_{f_{CP}} = -\frac{|\langle B^0|H|\overline{B}^0\rangle|}{\langle B^0|H|\overline{B}^0\rangle}\frac{\overline{A}_{f_{CP}}}{A_{f_{CP}}} \ . \tag{2.49}$$

Now making use of equation (2.47), we can further simplify this expression into

$$\lambda_{f_{CP}} = -\frac{|\langle B^0|H|\overline{B}^0\rangle|}{\langle B^0|H|\overline{B}^0\rangle}e^{-2i\phi_k}\eta_{f_{CP}}\langle B^0|CP|\overline{B}^0\rangle \ . \tag{2.50}$$

We will return to this expression after a brief discussion of the CKM matrix in Section 2.10.

2.9.4 Measuring CP violation in the interference between mixing and decay

CP violation in the interference between decays with and without mixing is arguably the most important type of CP violation for B physicists today. As such, we will briefly discuss how one measures this type of CP violation, before discussing the CKM matrix.

As mentioned in Section 2.9.1, knowing the time-evolution of B-mesons allows physicists to measure asymmetries in the rates of B^0 and $\overline{B}^0$ decays into a particular final state. This is the basic idea behind measurements of CP violation in the interference between mixing and decay. Specifically, one compares the rate for a B-meson to decay into the state f_{CP} when the B starts out at time $t = 0$ as a B^0 versus the rate when at $t = 0$ a $\overline{B}^0$ is present. We thus define the time-dependent asymmetry as

$$A_{f_{CP}} = \frac{\Gamma(B^0_{phys}(t) \to f_{CP}) - \Gamma(\overline{B}^0_{phys}(t) \to f_{CP})}{\Gamma(B^0_{phys}(t) \to f_{CP}) + \Gamma(\overline{B}^0_{phys}(t) \to f_{CP})} \ . \tag{2.51}$$

If we delve slightly deeper into how the experiments are actually performed, however, we see that rather than knowing what species (B^0 or $\overline{B}^0$) the B-meson was at $t = 0$, physicists reconstruct a variety of particles in the detector. In the *BABAR* and Belle experiments, a pair of B-mesons is created from the decay of the $\Upsilon(4S)$, which is created in an asymmetric collision such that the center of mass of the $\Upsilon(4S)$ is moving relativistically ($\beta\gamma \approx 0.5$) with respect to the laboratory frame. As mentioned in Section 2.9.1, the two B-mesons evolve coherently until one decays. The relativistic motion of the $\Upsilon(4S)$ in the lab allows physicists to measure the time between production of the B-mesons and their subsequent decay by measuring the distance the B-meson traveled before decaying.

Say we determine that one of the B-mesons produced from a certain $\Upsilon(4S)$ decayed into

the final state (f_{CP}), which we are interested in; we will call this B-meson B_{rec} (because this is the

decay we are interested in, the B-meson is fully reconstructed from the tracks and electro-magnetic

showers in the detector). From the tracks (charged particles) and showers (photons, electrons, etc.)

in the detector for each $\Upsilon(4S)$ decay, it is in many cases possible to determine the species of the

other B-meson that was produced at the same time as B_{rec}. We call this B_{tag}, as we "tag" whether

it is a B^0 or $\overline{B}^0$, but are not particularly interested in how it decayed. We can then define the decay

rate $f_+(f_-)$ when B_{tag} is a $B^0(\overline{B}^0)$ as (for example, [21])

$$f_\pm(\Delta t) = \frac{e^{-|\Delta t|/\tau}}{4\tau} \left[1 \pm S_{f_{CP}} \sin\left(\Delta m_B \Delta t\right) \mp C_{f_{CP}} \cos\left(\Delta m_B \Delta t\right)\right] \ , \qquad (2.52)$$

where $\Delta t = t_{rec} - t_{tag}$ is the difference between the proper decay times of B_{rec} and B_{tag} and τ is

the mean lifetime of the B^0. We define $S_{f_{CP}}$ and $C_{f_{CP}}$ using the parameter $\lambda_{f_{CP}}$, as

$$S_{f_{CP}} \equiv \frac{2Im\{\lambda_{f_{CP}}\}}{1 + |\lambda_{f_{CP}}|^2} \ , \qquad C_{f_{CP}} \equiv \frac{1 - |\lambda_{f_{CP}}|^2}{1 + |\lambda_{f_{CP}}|^2} \ . \qquad (2.53)$$

Making use of these definitions, we write the time-dependent CP asymmetry

$$\begin{aligned} A_{f_{CP}} &= \frac{f_+(\Delta t) - f_-(\Delta t)}{f_+(\Delta t) + f_-(\Delta t)} \qquad &(2.54) \\ &= S_{f_{CP}} \sin\left(\Delta m_B \Delta t\right) - C_{f_{CP}} \cos\left(\Delta m_B \Delta t\right) \ . \qquad &(2.55) \end{aligned}$$

When $|\lambda_{f_{CP}}| = 1$ (no CP violation in decay is present), the only CP violation is from

the interference between mixing and decay and the expression in equation (2.55) reduces to:

$$A_{f_{CP}} = -Im\{\lambda_{f_{CP}}\} \sin\left(\Delta m_B \Delta t\right) \ . \qquad (2.56)$$

For these decays where $|\lambda_{f_{CP}}| = 1$, one can experimentally fit the time-dependent asymmetry with

a sine function to extract the value of $Im\{\lambda_{f_{CP}}\}$. In reality, experimentalists commonly fit the data

to a function that can include both sine and cosine terms. If the contribution of the cosine term

is negligible ($C_{f_{CP}} \sim 0$) then experiment has verified that $|\lambda_{f_{CP}}| = 1$. When this is the case,

$Im\{\lambda_{f_{CP}}\}$ can be cleanly interpreted in terms of parameters in the electroweak Lagrangian.

2.10   The CKM Matrix and Unitarity Triangle

A flavor-neutral particle such as the $\Upsilon(4S)$ (a $b\bar{b}$ meson) can decay strongly into a final state containing b quarks (eg. $B^0\overline{B}^0$); the B-meson, however, must decay weakly in order to change the flavor of the b quark. The quark mixing matrix, which describes the strength of flavor changing charged currents (weak interactions), is known as the CKM matrix (after Cabibbo, Kobayashi, and Maskawa) [7, 6].

The CKM matrix "rotates" the d, s, and b flavor eigenstates (quarks of definite flavor) into eigenstates of the weak interaction: d', s', and b'. We describe this with three quark doublets, pairing a u-type quark (u, c, or t) with the appropriately "rotated" d-type quark (d', s', or b'). We write this rotation operation in matrix form as

$$
\begin{pmatrix} d' \\ s' \\ b' \end{pmatrix} = \begin{pmatrix} V_{ud} & V_{us} & V_{ub} \\ V_{cd} & V_{cs} & V_{cb} \\ V_{td} & V_{ts} & V_{tb} \end{pmatrix} \begin{pmatrix} d \\ s \\ b \end{pmatrix} , \tag{2.57}
$$

where the matrix elements specify the weak coupling between two quarks (one u-type and one d-type). For example, V_{cb} gives the relative strength of the $b \rightarrow c$ transition. The CKM matrix (V) is commonly expressed in terms of the Wolfenstein Parameterization [22] with four parameters: λ, A, ρ, and η. We expand about the parameter λ, defined as $\lambda = |V_{us}| \approx 0.22$; the quantities A, ρ, and η are all $\mathcal{O}(1)$. The parameter η represents the CP-violating weak phase.

$$
V = \begin{pmatrix} 1 - \frac{1}{2}\lambda^2 & \lambda & A\lambda^3(\rho - i\eta) \\ -\lambda & 1 - \frac{1}{2}\lambda^2 & A\lambda^2 \\ A\lambda^3(1 - \rho - i\eta) & -A\lambda^2 & 1 \end{pmatrix} + \mathcal{O}(\lambda^4) \tag{2.58}
$$

Requiring that the CKM matrix be unitary leads to a variety of relationships among the matrix elements, such as

$$
V_{ud}V_{ub}^* + V_{cd}V_{cb}^* + V_{td}V_{tb}^* = 0 . \tag{2.59}
$$

This relationship can be represented by a triangle in the complex plane and is commonly referred to as the "Unitarity Triangle", for it is the only such relationship (derived from unitarity of the CKM matrix) where the three sides of the triangle have similar length ($|V_{ud}V_{ub}^*| \approx |V_{cd}V_{cb}^*| \approx |V_{td}V_{tb}^*| \propto \lambda^3$). Having sides of similar length makes the angles in this triangle large enough to be experimentally measured. In Figure 2.3, the Unitarity Triangle has been drawn using a phase convention where $(V_{cd}V_{cb}^*)$ is real. Additionally, the sides of the triangle have all been rescaled by dividing by $|V_{cd}V_{cb}^*|$ and the points are those given by the Wolfenstein parameterization.

Figure 2.3: The Unitary Triangle in the SM.

The angles α, β, and γ of the Unitarity Triangle can be determined by measuring CP violation in the B system. Lengths of the sides are determined by measuring decay rates and mixing (for example, $V_{tb} \propto \Delta m_B$). We discuss one measurement of α in Sec. 2.11.2 and γ in Sec. 2.11.3, as they pertain to the ρK^* measurements presented in this thesis.

Over-constraining the Unitarity Triangle is one of the main goals of today's B physics programs. The hope was that by making complimentary measurements of the Unitary Triangle parameters, we would expose discrepancies requiring the addition of beyond-the-Standard-Model physics. Although there have been hints of such disagreements (at the $\sim 2\sigma$ level), the experimental resolution available from the full *BABAR* and Belle datasets appears to be insufficient to expose non-

Standard Model physics effects. The current world knowledge of the Unitary Triangle is shown graphically in Fig. 2.4 [23].
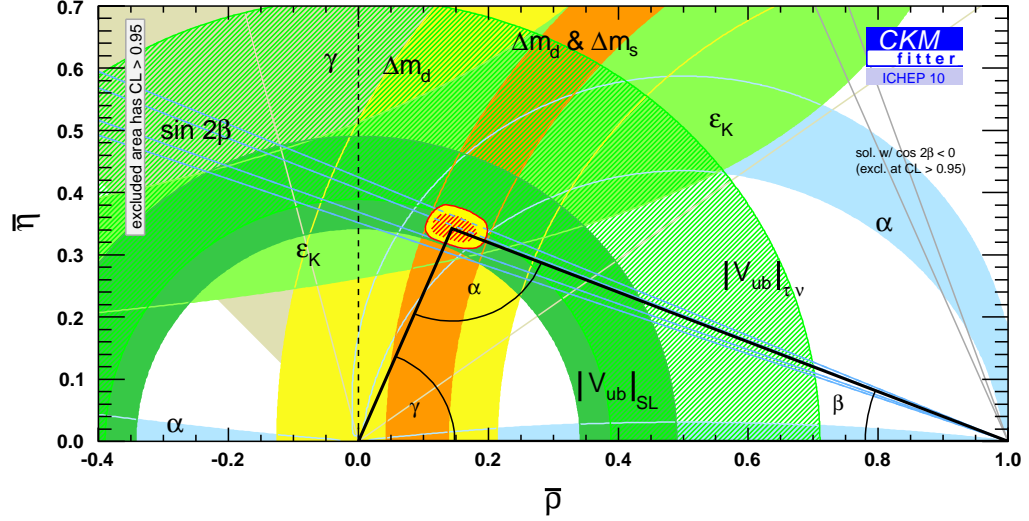
Figure 2.4: World average experimental constraints on the Unitary Triangle as of summer 2010.

2.11 Casting $\lambda_{f_{CP}}$ in Terms of CKM Parameters

We now return to our expression for $\lambda_{f_{CP}}$ from equation (2.50), which we give again below.

$$\lambda_{f_{CP}} = -\frac{|\langle B^0|H|\overline{B}^0\rangle|}{\langle B^0|H|\overline{B}^0\rangle} e^{-2i\phi_k} \eta_{f_{CP}} \langle B^0|CP|\overline{B}^0\rangle \ . \tag{2.60}$$

In the Standard Model, we determine the quantity $\langle B^0|H|\overline{B}^0\rangle$ from the box diagram shown in Figure 2.5 with a virtual t quark.

We can write the transitions corresponding to our matrix element, $\langle B^0|H|\overline{B}^0\rangle$, in terms of the relevant quarks as $b \to t \to d$ and $\overline{d} \to \overline{t} \to \overline{b}$. These transitions both introduce factors of $V_{tb}V_{td}^*$ so that the overall phase from the first term in equation (2.60) comes from $(V_{td}^*)^2 \propto e^{2i\beta}$ in the denominator. Thus we have introduced an overall phase of $e^{-2i\beta}$ into $\lambda_{f_{CP}}$. More
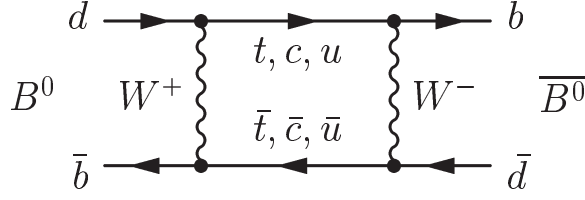
Figure 2.5: Box diagram describing B^0–$\overline{B}^0$ mixing in the SM.

complicated calculations are required in order to further simplify $\lambda_{f_{CP}}$, so we simply quote the

result and reference the interested reader to the literature (e.g. [17], [24]). In the end, recalling that

ϕ_k is the weak phase of the $B \to f_{CP}$ decay, $\lambda_{f_{CP}}$ simplifies into

$$\lambda_{f_{CP}} = \eta_{f_{CP}} e^{-2i\beta - 2i\phi_k} \ . \tag{2.61}$$

For certain decays, where we understand the weak phase ϕ_k, we further simplify this expression

into one containing only parameters of the Unitary Triangle, as discussed in Sec. 2.11.1–2.11.2.

2.11.1   Experimental measurements of $\sin(2\beta)$

As the B-meson is rather massive ($\approx 5.28 \, \text{GeV}/c^2$) there is a great deal of phase space

for its decay products. As a result, unlike the K^0, which decays into two pions about half the time

and three pions or a semi-leptonic channel the other half, the B-meson decays into a menagerie

of particles [2]. Looking only at hadronic decays for the moment, we would expect the B-meson

to decay primarily into charmed particles because the transition $b \to c$ is less suppressed in the

SM than the transition $b \to u$. Indeed this is experimentally verified with a number of charm

or charmonium decay channels that have branching fractions that are $\mathcal{O}(10^{-3})$, versus charmless

branching fractions, which are typically $\mathcal{O}(10^{-5})$ or less.

So the natural place to start looking for CP violation in the B-meson system is in charm

and charmonium decays, where statistics are reasonably good. If we wish to measure CP violation

in the interference between mixing and decay, we must be careful to choose final states that are

CP eigenstates. Some likely candidates include $J/\psi K_S^0$, $\psi(2S)K_S^0$, $\chi_{C1}K_S^0$, and $\eta_C K_S^0$, all of which have $\eta_{f_{CP}} = -1$, and $J/\psi K_L^0$, which has $\eta_{f_{CP}} = +1$. These decays have been used by both *BABAR* and Belle to measure the quantity $\sin(2\beta)$. Using equation (2.61), we can understand how measurements of time-dependent asymmetries in these modes give rise to a measurement of the angle β of the Unitarity Triangle.
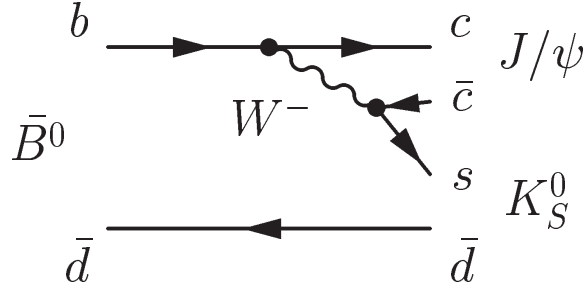
Figure 2.6: Tree diagram describing the decay $\overline{B}^0 \to J/\psi K_S^0$.

For illustration purposes, we will look at the decay $B \to J/\psi K_S^0$. This process is dominated by the "tree" diagram as shown in Figure 2.6. The quark transition for $\overline{B}^0 \to J/\psi K_S^0$ is $b \to c\overline{c}s$. If we look at the Wolfenstein parameterization of the CKM matrix, we see that the CP-violating phase η is introduced only in transitions from third generation (b, t) quarks to first generation (u, d) quarks. As the only quarks involved in the $\overline{B}^0 \to J/\psi K_S^0$ decay are from the second and third generations, ϕ_k for this decay is zero, and we find that $\lambda_{f_{CP}} = -e^{-2i\beta}$ (the negative sign is because $\eta_{f_{CP}} = -1$ for $J/\psi K_S^0$). Recall from equation (2.56) that physicists experimentally measure the quantity

$$A_{f_{CP}} = -Im\{\lambda_{f_{CP}}\}\sin(\Delta m_B \Delta t) \ . \tag{2.62}$$

(This is an oversimplification; the actual experiment is more difficult. For details, see the literature [21], [25].) Thus, knowing Δm_B for the B-meson system, fitting for a sinusoidal component allows us to determine $Im\{\lambda_{f_{CP}}\}$. For $J/\psi K_S^0$, this is just

$$Im\{\lambda_{f_{CP}}\} = \sin(2\beta); \qquad (B \to J/\psi K_S^0) \ . \tag{2.63}$$

The world average constraint on $\sin(2\beta)$ from charmonium decays is given by the blue diagonal constraint in Fig. 2.4.

Although charmonium modes provide for the easiest measurement of $\sin(2\beta)$ (because of relatively large branching fractions), it is possible to measure $\sin(2\beta)$ in other channels as well. Decays dominated by $b \to s$ penguin diagrams, such as Fig. 2.7 for $B^0 \to \eta' K_S^0$, also measure $\sin(2\beta)$ if the contamination from tree diagrams (with a $b \to u$ quark transition, and thus a different weak phase) are small. The validity of this assumption is measured by fitting for a cosine component as well as a sine component, as discussed in Sec. 2.9.4.
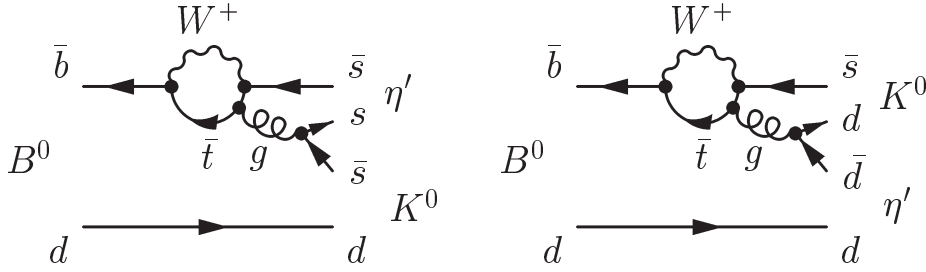
Figure 2.7: Penguin diagrams describing the decay $B^0 \to \eta' K_S^0$.

In Fig. 2.8, we show the world average measurements of $\sin(2\beta)$ from $b \to s$ penguin transitions, compared with the world average from the charmonium channels [26]. There is a hint of some systematic shift in the value of β from $b \to s$ penguin channels, but the significance is poor.

2.11.2   Experimental measurements of α using $\rho\rho$ and ρK^*

The Unitary Triangle angle β is the easiest to measure because we can make use of high-statistics charmonium modes. As we begin using charmless modes with smaller branching fractions to study Unitary Triangle parameters we run into difficulties when various (possibly higher-order) diagrams contribute to the same decay (recall that this can lead to CP violation in decay, for which case $|\lambda_{f_{CP}}| \neq 1$). In some channels, however, a particular diagram tends to dominate. This is the case with $B^0 \to \rho^+\rho^-$ and $\pi^+\pi^-$, where the tree diagram (shown on the left in Figure 2.9)

$$\sin(2\beta^{\mathrm{eff}}) \equiv \sin(2\phi_1^{\mathrm{eff}})$$ HFAG FPCP 2010 PRELIMINARY

b→ccs	World Average	0.67 ± 0.02
$\phi\, K^0$	Average	$0.56\,^{+0.16}_{-0.18}$
$\eta'\, K^0$	Average	0.59 ± 0.07
$K_S\, K_S\, K_S$	Average	0.74 ± 0.17
$\pi^0\, K^0$	Average	0.57 ± 0.17
$\rho^0\, K_S$	Average	$0.54\,^{+0.18}_{-0.21}$
$\omega\, K_S$	Average	0.45 ± 0.24
$f_0\, K_S$	Average	$0.62\,^{+0.11}_{-0.13}$
$f_2\, K_S$	Average	0.48 ± 0.53
$f_X\, K_S$	Average	0.20 ± 0.53
$\pi^0\,\pi^0\, K_S$	Average	-0.72 ± 0.71
$\phi\,\pi^0\, K_S$	Average	$0.97\,^{+0.03}_{-0.52}$
$\pi^+\,\pi^-\, K_S$ NR	Average	0.01 ± 0.33
$K^+\, K^-\, K^0$	Average	0.82 ± 0.07

-1.6 -1.4 -1.2 -1 -0.8 -0.6 -0.4 -0.2 0 0.2 0.4 0.6 0.8 1 1.2 1.4 1.6

$$C_f = -A_f$$ HFAG EndOfYear 2009 PRELIMINARY

$\phi\, K^0$	Average	-0.23 ± 0.15
$\eta'\, K^0$	Average	-0.05 ± 0.05
$K_S\, K_S\, K_S$	Average	-0.23 ± 0.13
$\pi^0\, K^0$	Average	0.01 ± 0.10
$\rho^0\, K_S$	Average	-0.06 ± 0.20
$\omega\, K_S$	Average	-0.32 ± 0.17
$f_0\, K_S$	Average	0.05 ± 0.12
$f_2\, K_S$	Average	$0.28\,^{+0.37}_{-0.41}$
$f_X\, K_S$	Average	$0.13\,^{+0.34}_{-0.36}$
$\pi^0\,\pi^0\, K_S$	Average	0.23 ± 0.54
$\phi\,\pi^0\, K_S$	Average	-0.20 ± 0.15
$\pi^+\,\pi^-\, K_S$ NR	Average	0.01 ± 0.26
$K^+\, K^-\, K^0$	Average	0.01 ± 0.07

-1.6 -1.4 -1.2 -1 -0.8 -0.6 -0.4 -0.2 0 0.2 0.4 0.6 0.8 1 1.2 1.4 1.6

Figure 2.8: Average values of $\sin(2\beta)$ (left) from $b \to s$ penguin channels compared to the world average value from charmonium channels (vertical gold band). The direct CP-violating parameter C for the equivalent channels is given on the right. The red dashed line indicates a value of S or $C = 0$.

dominates over the penguin contribution (right).

In the tree diagram, the decay can be described by the transition $\bar{b} \to \bar{u}u\bar{d}$; this introduces a coupling of V_{ub}^*, which has a phase of γ. If we assume that only the tree diagram contributes, then ϕ_k in equation (2.61) is given by γ. Assuming that $\alpha + \beta + \gamma = \pi$ for the Unitary Triangle, we can then write,

$$Im\{\lambda_{f_{CP}}\} = \sin(2\alpha); \qquad (B \to \pi^+\pi^-) \ . \tag{2.64}$$

Note that it has been experimentally demonstrated that the penguin contributions to $\pi^+\pi^-$ are larger than those in $\rho^+\rho^-$, as seen by the branching fractions [2],

$$\mathcal{B}(B^0 \to \pi^0\pi^0) = (1.62 \pm 0.31) \times 10^{-6} \tag{2.65}$$

$$\mathcal{B}(B^0 \to \rho^0\rho^0) = (7.3 \pm 2.8) \times 10^{-7} \ . \tag{2.66}$$
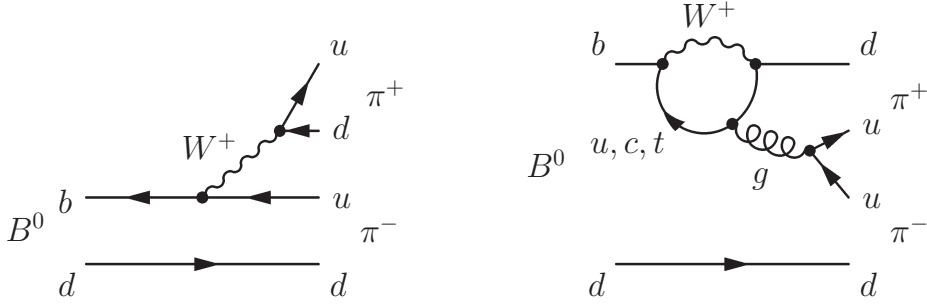
Figure 2.9: Tree diagram (right) and penguin diagram (left) for the decay $B^0 \to \pi^+\pi^-$

The larger "penguin pollution" in $\pi^+\pi^-$ makes the extraction of the CKM angle α theoretically complicated. The penguin pollution is a concern even for the $\rho^+\rho^-$ channels. The "standard" method for relating α_{eff} as measured in $B^0 \to \pi^+\pi^-$ or $\rho^+\rho^-$ to the CKM angle α involves isospin relations among the other $\pi\pi$ or $\rho\rho$ channels [27].

In Ref. [11], Beneke *et. al.* propose an alternate method for extracting α from $B^0 \to \rho^+\rho^-$, which uses information from $B \to \rho K^*$ decays in combination with flavor $SU(3)$. They relate the penguin amplitude in $\rho^+\rho^-$ to that of ρ^+K^{*0} and find that, even with the large uncertainties from $SU(3)$ breaking, they can compute α with smaller uncertainties than using the standard isospin analysis. Beneke *et. al.* note that an additional constraint could be obtained by using information on the longitudinally polarized $B^0 \to \rho^- K^{*+}$ decay. Prior to the work of this thesis, however, this was not feasible, as previous measurements [28] had provided only an upper limit on the decay rate.

2.11.3   Experimental measurement of γ using ρK^*

Most measurements of the Unitary Triangle angles require time-dependent measurements of CP violation in the interference between mixing and decay (see Sec. 2.9.4) which require large samples of signal events and are experimentally rather complex. In Ref. [8], Atwood and Soni propose a method for determining α and γ using only directly CP-violating parameters (see Sec. 2.7).

The direct CP-violating asymmetry $\mathcal{A}_{ch}$ can be measured in any decay which does not involve a CP eigenstate final state, and for which it is possible to determine the flavor of the parent B-meson. The decays described in this thesis, for instance, all involve a K^* in the final state, and we consider only its decays: $K^{*0} \rightarrow K^+\pi^-$ and $K^{*+} \rightarrow K^+\pi^0$; the sign of the kaon therefore tags the flavor of the B-meson, and we can write

$$\mathcal{A}_{ch} \equiv \frac{\Gamma^- - \Gamma^+}{\Gamma^- + \Gamma^+} \, ,$$

where the superscript on the decay width Γ refers to the charge of the kaon from the K^* decay.

The method of Atwood and Soni [8] requires input from one pure $b \rightarrow s$ penguin mode (a channel with no contribution from tree diagrams) such as $B^+ \rightarrow \rho^+ K^{*0}$ as well as from one channel with tree–penguin interference, such as $B^0 \rightarrow \rho^- K^{*+}$ or $B^+ \rightarrow \rho^0 K^{*+}$. The inclusion of information from multiple channels improves the measurement.

This method uses three approximations: $SU(3)$ is a good symmetry for penguin processes, the effects of electroweak penguins (with a Z^0 or γ from the loop instead of a gluon) are small, and the $q\overline{q}$ pair produced in the strong penguin (ie. the $u\overline{u}$ pair from the g in Fig. 2.9 (right)) does not form a single vector meson.

The improved measurements of ρK^* channels from this thesis will therefore allow for an improved measurement of γ through this method.

Chapter 3

Previous Results and Theoretical Predictions

All charge states of $B \rightarrow \rho/f_0 K^*(892)$ have previously been measured by *BABAR* on a dataset approximately half the total dataset [28]. The internal *BABAR* supporting documentation for these analyses can be found in BAD-1430 [29] for $\rho^- K^{*+}$, BAD-1211 [30] for $\rho^0 K^{*0}$ and $\rho^+ K^{*0}$, and BAD-1216 [31] for $\rho^0/f_0 K^{*+}$. *BABAR* has recently updated the measurement of $B^+ \rightarrow \rho^0/f_0 K^{*+}$ on the full dataset [32], and a full angular analysis is being performed on $B^+ \rightarrow \rho^+ K^{*0}$ (see BAD 1951 [33]). There are results from Belle on some of these modes [34, 35]. We summarize the current experimental landscape in Tab. 3.1.

3.1 Theoretical predictions using Heavy Quark Effective Theory

We have previously mentioned theoretical predictions for B-meson branching fractions, $\mathcal{A}_{ch}$, f_L, etc. without much discussion of how these predictions are made. In general, theoretical predictions of weak non-leptonic decays of a heavy meson are complicated by the interplay of short-distance (SD) and long-distance (LD) quantum chromodynamics (QCD) effects [1]. If we

Table 3.1: Summary of the current experimental measurements and recent theoretical predictions from QCDF. Branching fractions are in units of 10^{-6}. The upper limits (in parentheses if a central value is not significant) are at the 90% confidence level. [†]In [9, 36] it is pointed out than an error in [10] causes the f_L predictions for $\rho^0 K^{*0}$ ($\rho^0 K^{*-}$) to be under- (over-) estimated. The predicted $f_0 K^{*0}$ BF is multiplied by a factor of $1/2$, as Ref. [37] includes a factor of $\mathcal{B}(f_0 \to \pi^+ \pi^-) = 0.5$, whereas the previous *BABAR* result measured $\mathcal{B}(B \to f_0 K^*(892)) \times \mathcal{B}(f_0 \to \pi^+ \pi^-)$.

	BABAR[28, 32]	Belle[34, 35]	CY[9, 36]	BRY[10]
$B^0 \to \rho^0 K^{*0}$				
$\mathcal{B}$	$5.6 \pm 0.9 \pm 1.3$	$2.1^{+0.8+0.9}_{-0.7-0.5}$	$4.6^{+3.6}_{-3.5}$	$2.4^{+3.5}_{-2.0}$
f_L	$0.57 \pm 0.09 \pm 0.08$	—	$0.39^{+0.60}_{-0.31}$	[†]$0.22^{+0.53}_{-0.14}$
A_{CP}	$0.09 \pm 0.19 \pm 0.02$	—	—	$-0.15^{+0.17}_{-0.32}$
$B^0 \to \rho^- K^{*+}$				
$\mathcal{B}$	$5.4^{+3.8}_{-3.4} \pm 1.6 \ (12.0)$	—	$8.9^{+4.9}_{-5.6}$	$5.5^{+5.9}_{-3.3}$
f_L	$-0.18^{+0.52}_{-1.74}$	—	$0.53^{+0.45}_{-0.32}$	$0.61^{+0.38}_{-0.29}$
A_{CP}	—	—	—	$0.05^{+0.40}_{-0.17}$
$B^+ \to \rho^0 K^{*+}$				
$\mathcal{B}$	$4.6 \pm 1.0 \pm 0.4$	—	$5.5^{+1.4}_{-2.5}$	$4.5^{+3.4}_{-1.9}$
f_L	$0.78 \pm 0.12 \pm 0.03$	—	$0.67^{+0.31}_{-0.48}$	[†]$0.84^{+0.16}_{-0.25}$
A_{CP}	$0.31 \pm 0.13 \pm 0.03$	—	—	$0.16^{+0.23}_{-0.16}$
$B^+ \to \rho^+ K^{*0}$				
$\mathcal{B}$	$9.6 \pm 1.7 \pm 1.5$	$8.9 \pm 1.7 \pm 1.2$	$9.2^{+3.8}_{-5.5}$	$5.9^{+6.9}_{-3.7}$
f_L	$0.52 \pm 0.10 \pm 0.04$	$0.43 \pm 0.11^{+0.05}_{-0.02}$	$0.48^{+0.52}_{-0.40}$	$0.56^{+0.48}_{-0.30}$
A_{CP}	$-0.01 \pm 0.16 \pm 0.02$	—	—	$0.00^{+0.03}_{-0.02}$
	BABAR[28, 32]	Belle[34]	CCY[37]	
$B^0 \to f_0 K^{*0}$				
$\mathcal{B}$	$2.6 \pm 0.6 \pm 0.9 \ (4.3)$	< 2.2	$3.2^{+3.5}_{-1.3}$	
A_{CP}	$-0.17 \pm 0.28 \pm 0.02$	—	—	
$B^+ \to f_0 K^{*+}$				
$\mathcal{B}$	$4.2 \pm 0.6 \pm 0.3$	—	$3.7^{+3.6}_{-1.5}$	
A_{CP}	$-0.15 \pm 0.12 \pm 0.03$	—	—	

consider a hadronic decay $B \to M_1 M_2$, using the effective weak Hamiltonian, we can write the decay amplitude

$$A(B \to M_1 M_2) = \frac{G_F}{\sqrt{2}} \sum_i \lambda_i c_i(\mu) \langle M_1 M_2 | O_i | B \rangle (\mu) \tag{3.1}$$

where λ_i are the CKM [6, 7] matrix elements, O_i are the four-quark operators, and $c_i(\mu)$ are the Wilson coefficients that incorporate strong interaction effects above the scale μ. Evaluating the matrix elements of the four-quark operators $\langle M_1 M_2 | O_i | B \rangle$ is difficult. Heavy Quark Effective Theory (HQET) uses the factorization theorem, relying on the heaviness of the b quark, to disentangle SD QCD dynamics from non-perturbative hadronic effects. Power corrections of order Λ_{QCD}/m_b are suppressed in the heavy quark limit, though they remain the source of large theoretical uncertainties.

The most basic approach is given by Naïve factorization (NF), which approximates the matrix element $\langle M_1 M_2 | O_i | B \rangle$ as a product of a decay constant and a form factor: $\langle M_1 | J_{1\mu} | 0 \rangle \langle M_2 | J_2^\mu | B \rangle$, where J_μ is a bilinear current.. Naïve factorization, however, fails to accurately predict most hadronic branching fractions. Three popular theoretical approaches go beyond the straightforward vacuum-insertion assumption of NF: QCD factorization (QCDF), perturbative QCD (pQCD), and soft-collinear effective theory (SCET). Further discussion of these approaches is beyond the scope of this thesis. In the limits $m_b \to \infty$ and $\alpha_s \to \infty$, where m_b is the b quark mass and α_s is the strong coupling constant, QCDF and pQCD recover NF [1].

Recent results from QCD Factorization [9, 36, 10, 37] make predictions for many of the branching fractions and longitudinal polarizations of interest here. We include those predictions in Tab. 3.1. The $f_0 K^*$ predictions from [37] use $\mathcal{B}(f_0 \to \pi^+\pi^-) = 0.5$; we have factored this back out to compare to the experimental results, which measure $\mathcal{B}(B \to f_0 K^*) \times \mathcal{B}(f_0 \to \pi^+\pi^-)$. As it is difficult to make theoretical predictions when one assumes the scalar mesons are four-quark states (see Sec. 2.2), the predictions in [37] assume that the f_0 is a $q\bar{q}$ meson.

As mentioned in Ch. 1, QCD Factorization [9, 36, 10] predicts the following hierarchy

Table 3.2: Summary of recent theoretical predictions from QCDF and pQCD. Branching fractions are in units of 10^{-6}. The two scenarios reported in Ref. [38] represent two interpretations of the scalar mesons (see text). For simplicity, we have added the theory errors in quadrature.

Branching Fraction	QCDF [37]	pQCD SI [38]	pQCD SII [38]
$\mathcal{B}(B^0 \to \rho^0 K_0^*(1430)^0)$	37^{+27}_{-14}	$0.47^{+0.24}_{-0.21}$	$4.8^{+1.5}_{-1.0}$
$\mathcal{B}(B^0 \to \rho^- K_0^*(1430)^+)$	51^{+71}_{-27}	$3.3^{+1.1}_{-1.0}$	$10.5^{+4.4}_{-2.6}$
$\mathcal{B}(B^+ \to \rho^0 K_0^*(1430)^+)$	21^{+30}_{-12}	$3.4^{+1.2}_{-0.9}$	$8.4^{+4.6}_{-3.3}$
$\mathcal{B}(B^+ \to \rho^+ K_0^*(1430)^0)$	66^{+75}_{-33}	$3.2^{+1.1}_{-0.9}$	$12.1^{+4.8}_{-3.1}$

pattern for the ρK^* polarization fractions,

$$f_L(K^{*+}\rho^0) > f_L(K^{*+}\rho^-) > f_L(K^{*0}\rho^+) > f_L(K^{*0}\rho^0) \,. \tag{3.2}$$

The $(K\pi)_0^*$ and $K_2^*(1430)$ channels have not been previously studied experimentally. We have theoretical predictions from QCD factorization [37] and perturbative QCD [38], which we summarize in Tab. 3.2.

In Ref. [37], Cheng *et. al.* find that the rates for $B \to \rho K_0^*(1430)$ are larger than those for $\pi K_0^*(1430)$. As the later have been measured experimentally, this work will allow us to test this prediction. Cheng *et. al.* also point out that their predictions for $B \to a_0(980)K$ and $B^0 \to a_0^+(980)\pi^-$ rates will be too high compared to experimental limits if one assumes that the $a_0(980)$ is a conventional $q\bar{q}$ bound state. They thus conclude that the scenario in which the scalar mesons with masses above $1\,\mathrm{GeV}$ are the lowest lying $q\bar{q}$ scalar states, and the lighter scalar mesons are four-quark states is the preferable assumption.

Ref. [38] presents the results of two scenarios: SI, in which the $K_0^*(1430)$ is viewed as part of the first excited state scalar nonet; and SII, in which the $K_0^*(1430)$ and associated scalar nonet is considered to be the scalar $q\bar{q}$ ground state (in this case, the scalar nonet with masses below $1\,\mathrm{GeV}$ is considered to be exotic states, such as four-quark bound states). The authors conclude that the second scenario SII is preferable. These predictions use only leading-order diagrams. In Ref. [38],

the authors note that should the branching fraction of $\rho^0 K_0^*(1430)^0$ be larger than $\mathcal{O}(10^{-7})$, it would

indicate that this decay may be sensitive to next-to-leading-order corrections.

Chapter 4

Experimental Overview

The results described in this thesis are obtained from a sample of $(471.0 \pm 2.8) \times 10^6$ $B\overline{B}$ pairs collected with the *BABAR* detector at the PEP-II asymmetric-energy e^+e^- collider at the SLAC National Accelerator Laboratory. These data correspond to the full *BABAR* dataset collected from 1999–2008. In this chapter we give an overview of both PEP-II and *BABAR*.

4.1 PEP-II Collider at SLAC

PEP-II [39] is an e^+e^- collider fed by the 3.2km-long Stanford Linear Accelerator Center (SLAC) linac. A schematic of the collider is shown in Fig. 4.1, in which the linac is labeled "existing injector." PEP-II consists of two counter-circulating rings: the electron beam (shown in red in Fig. 4.1) has an energy of $9.0\,\mathrm{GeV}$, and is termed the "high energy ring"; the positron beam (blue), the "low energy ring," has an energy of $3.1\,\mathrm{GeV}$. The center-of-mass (CM) energy is $10.58\,\mathrm{GeV}$, the mass of the $\Upsilon(4S)$ resonance. The $\Upsilon(4S)$ decays to $B\overline{B}$ pairs $> 96\%$ of the time at 90% confidence level, with approximately equal rates of B^+B^- and $B^0\overline{B}^0$ [2]. At the $\Upsilon(4S)$ CM energy, the $B\overline{B}$ production cross section is approximately $\sigma(e^+e^- \to B\overline{B}) = 1.1\mathrm{nb}$.

With the asymmetric energy configuration, the $\Upsilon(4S)$ is produced with a Lorentz boost
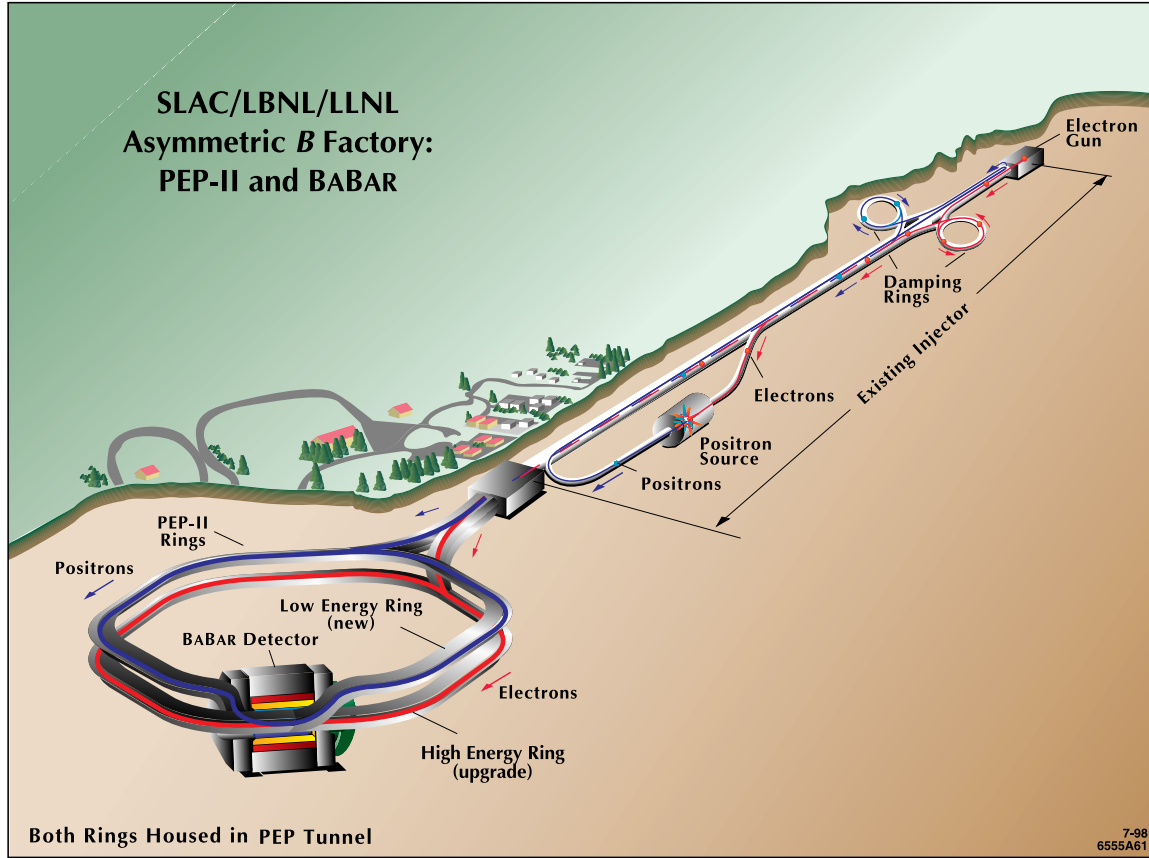
Figure 4.1: Schematic of the PEP-II collider and SLAC linac.

of $\beta\gamma = 0.56$. This boost makes it possible to reconstruct the B meson decay vertices, determine their relative time of decay, and thus perform the time-dependent analyses described in Sec. 2.9.4.

PEP-II was designed to operate at a luminosity of $3 \times 10^{33}\,\mathrm{cm}^{-2}\mathrm{s}^{-1}$. However, due to extraordinary efforts by our accelerator physics colleagues, PEP-II achieved a peak luminosity of $12.069 \times 10^{33}\,\mathrm{cm}^{-2}\mathrm{s}^{-1}$. Additional innovations such as trickle injection enabled allowed PEP-II to deliver excellent integrated luminosities. Trickle injection involved "trickling" additional electrons or positrons into the storage rings (during active collisions), in order to keep high currents in both beams despite losses from normal operations. The integrated luminosity delivered by PEP-II (blue) and recorded by *BABAR* (red) throughout the operation of the experiment is plotted in Fig. 4.2.

As of 2008/04/11 00:00

BaBar
Run 1-7

PEP II Delivered Luminosity: 553.48/fb
BaBar Recorded Luminosity: 531.43/fb
BaBar Recorded Y(4s): 432.89/fb
BaBar Recorded Y(3s): 30.23/fb
BaBar Recorded Y(2s): 14.45/fb
Off Peak Luminosity: 53.85/fb

Delivered Luminosity
Recorded Luminosity
Recorded Luminosity Y(4s)
Recorded Luminosity Y(3s)
Recorded Luminosity Y(2s)
Off Peak
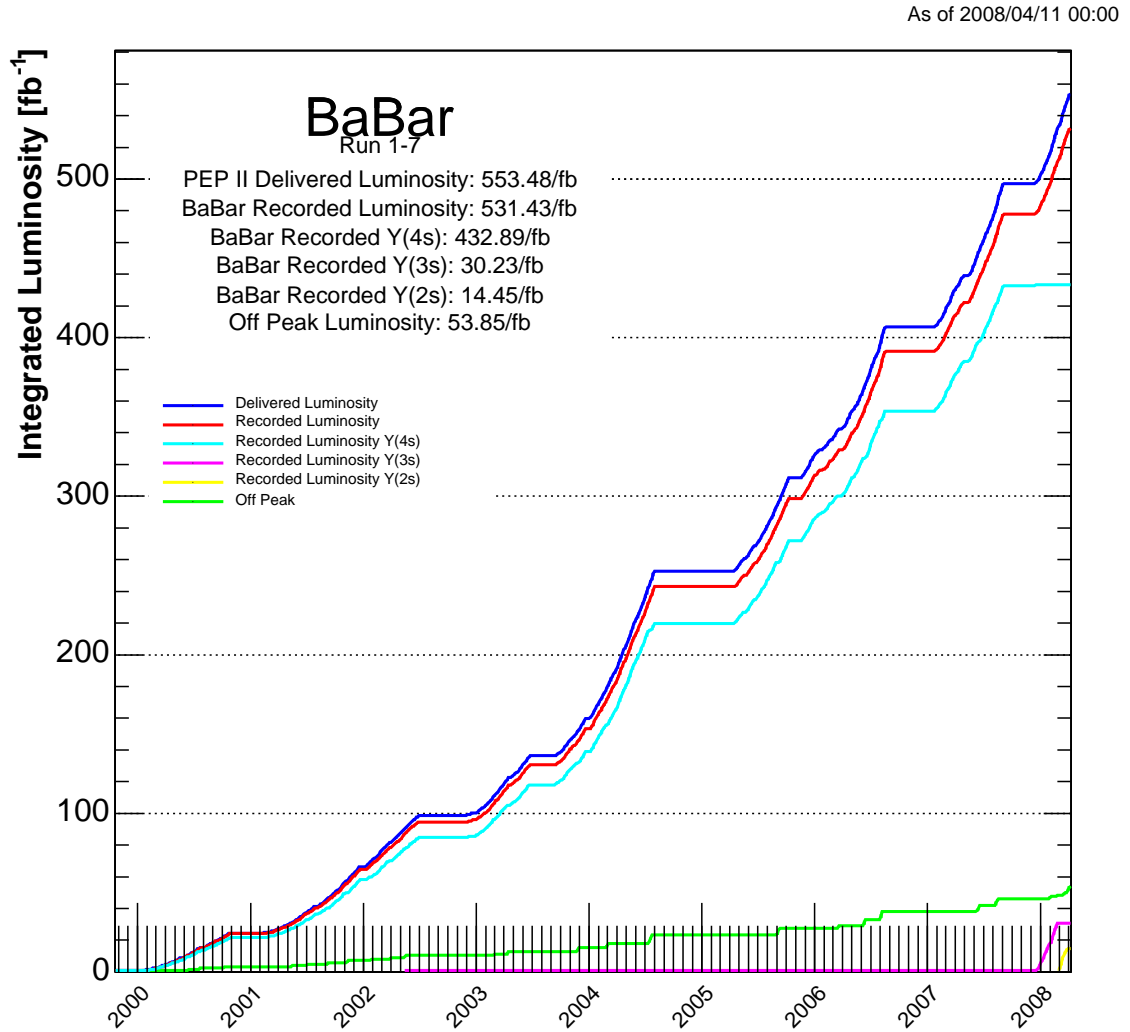
Figure 4.2: Integrated luminosity delivered by PEP-II and recorded by *BABAR*.

Additional collisions below the $\Upsilon(4S)$ resonance were delivered by PEP-II and recorded by *BABAR*. These "off-resonance" events are used to cross-check continuum $e^+e^- \rightarrow q\bar{q}$ ($q = u, d, s, c$) production, but are not essential for the work reported in this thesis.
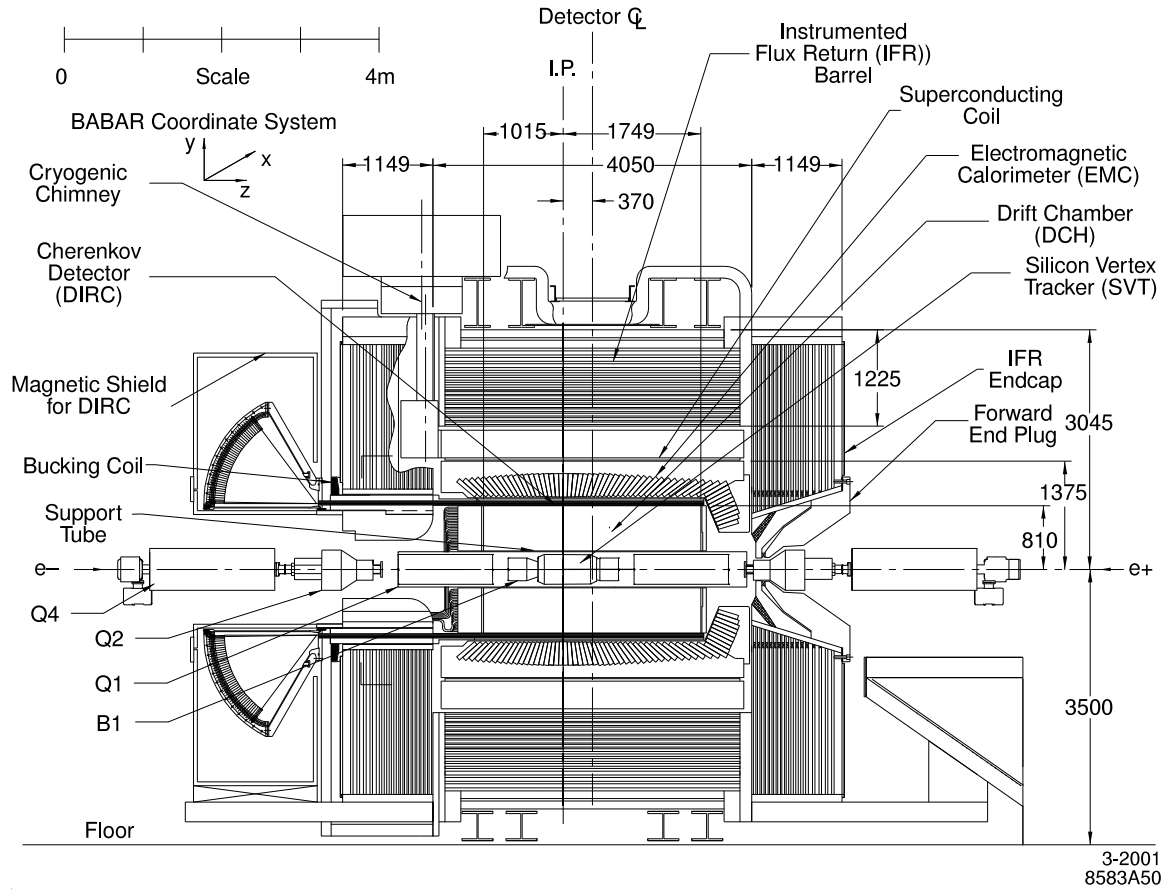
Figure 4.3: Longitudinal section of the *BABAR* detector.

4.2   The *BABAR* detector

The *BABAR* detector [39] is a multi-purpose, cylindrical detector designed and built by the large, international *BABAR* collaboration. Fig. 4.3 shows a longitudinal section of the *BABAR* detector; Fig. 4.4 shows an end view. In order to take advantage of the boosted CM provided by the asymmetric energy collisions, the entire *BABAR* detector is offset from the interaction point, with greater than 50% of the detector in the direction of the boost (toward the incoming low-energy ring), as can be seen in Fig.. 4.3.

The *BABAR* detector consists of cylindrical detector systems, with the particle vertexing
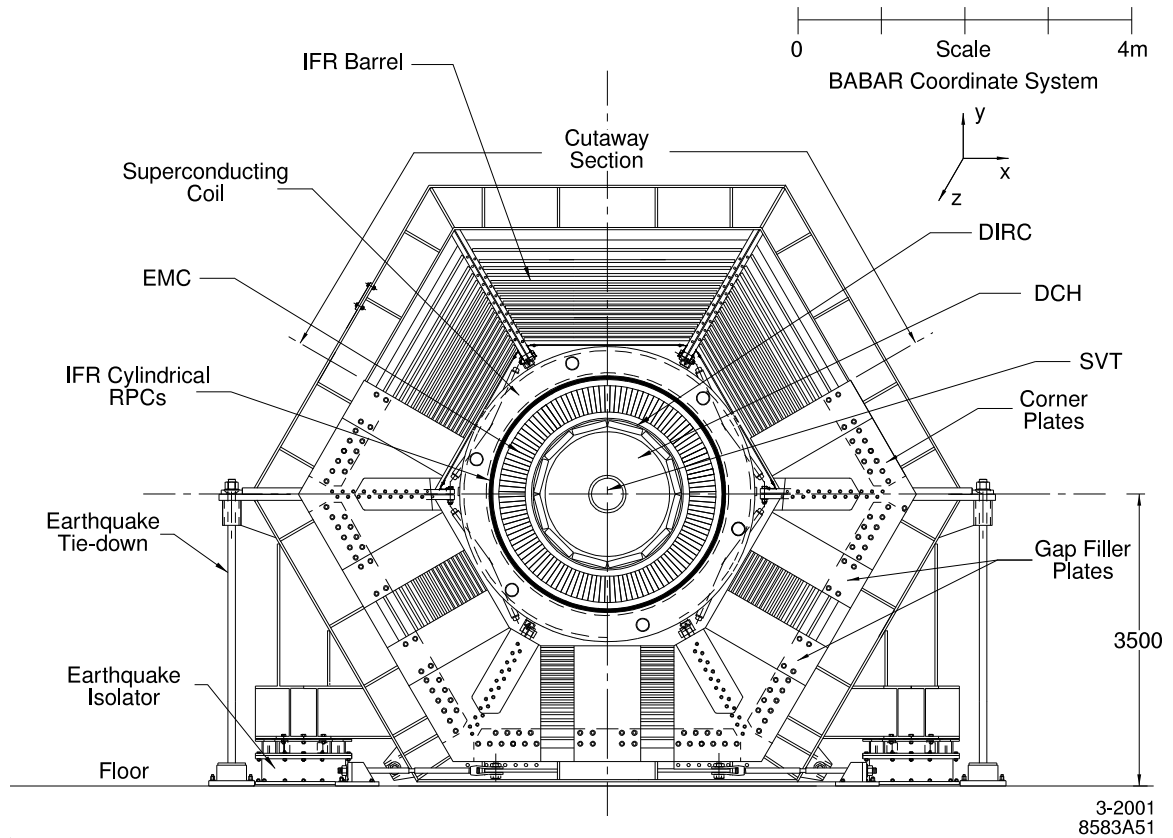
Figure 4.4: End view of the *BABAR* detector.

and tracking systems closest to the interaction point, in order to minimize the amount of material traversed by the particles before detection. The inner detector consists of a silicon vertex tracker (SVT), a drift chamber (DCH), a ring-imaging Cherenkov detector (DIRC), and a CsI(Tl) electromagnetic calorimeter (EMC). These are surrounded by a superconducting solenoid, designed to produce a 1.5T magnetic field in the central region. The steel flux return of the solenoid was initially instrumented with resistive plate chambers (RPCs) for muon and neutral hadron (K_L^0) identification. Early on in the operation of *BABAR*, the resistive plate chambers were found to be degrading. Many efforts were made to halt this degradation, with some success. In 2004, some of the RPCs were replaced with limited streamer tubes; the replacement of the barrel RPCs was completed in 2006.

The detector covers a polar angle from 350 mrad in the forward direction and 400 mrad in the backward direction, defined relative to the high energy beam. The experiment's z-axis coincides with the principle axis of the drift chamber, which is about 20 mrad offset from the beam axis in the horizontal plane. The positive y-axis points upwards, the x-axis points away from the center of the PEP-II storage rings.

Care was taken to minimize the amount of material traversed by high energy particles on their way to detector systems. The average momentum of a charged particle from a B meson decay is less than $1\,\mathrm{GeV}$; thus the precision of track parameters is sensitive to multiple Coulomb scattering. Similarly, any material traversed by low-energy photons impacts their energy resolution and detection efficiency in the calorimeter. The vertex detector and several PEP-II magnets are housed in a support tube, the central region of which is constructed of a carbon-fiber composite in order to minimize the number of radiation lengths traversed by particles.

In Tab. 4.1, we provide an overview of the detector subsystems, their angular acceptance, number of channels, number of layers, segmentation, and performance for $1\,\mathrm{GeV}$ particles (unless otherwise stated). The performance statistics are from Ref. [39], published in 2002, and have changed somewhat during detector operation. More detail on each subsystem can be found in the following sections.

4.2.1   Silicon vertex tracker

Charged particle tracking in *BABAR* is performed by two systems, the silicon vertex tracker (SVT) and the drift chamber (DCH).

The SVT is composed of five layers of double-sided silicon strip detectors, that are assembled into modules with electronic readouts at both ends, thus limiting the amount of inactive material within the acceptance volume. The strips on opposite sides of each sensor are oriented orthogonally to each other, with ϕ- and z-measuring strips. The SVT is shown in Fig. 4.5.
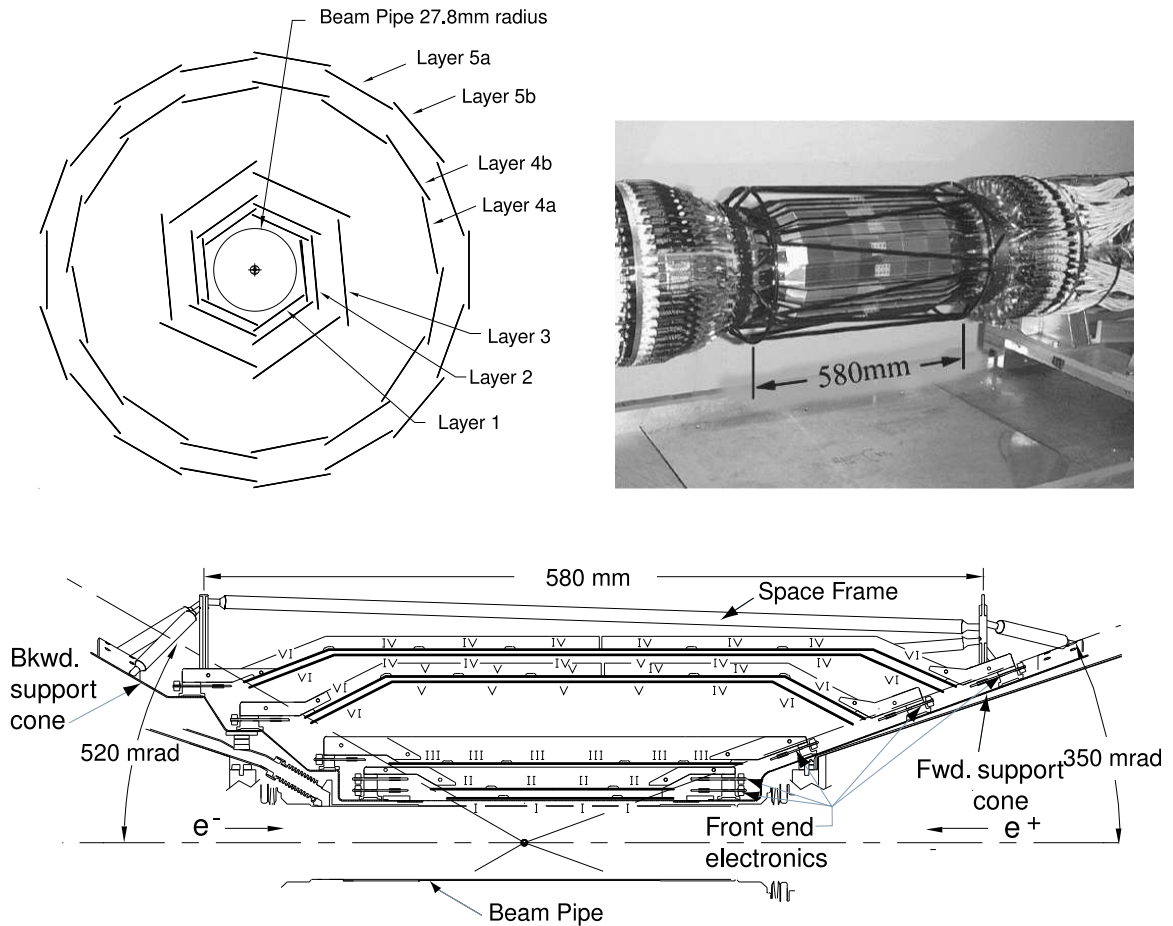
Figure 4.5: Schematic of the silicon vertex tracker silicon strip sensor modules, transverse (top left) and longitudinal (bottom) section. In the longitudinal section, the bottom half of the SVT is not shown. Photo of the fully assembled SVT (top right); the outer layer of sensors are visible, as is the black carbon-fiber space frame.

Table 4.1: Overview of the coverage, segmentation, and performance of the *BABAR* detector systems. The notation (C) and (F) refer to the central barrel and forward components of the system, respectively. The detector coverage in the laboratory frame is specified in terms of the polar angles θ_1 (forward) and θ_2 (backward). The number of readout channels is listed. Performance numbers are quoted for $1\,\text{GeV}$ particles, except where noted, and are based on the first year's data taking. The performances for the SVT and DCH are quoted for a combined Kalman fit [39]. The IFR is not included as its performance and specifications have changed dramatically over the course of the experiment.

System	θ_1	θ_2	Channels	Layers	Segmentation	Performance
SVT	20.1	-29.8	150K	5	$50 - 100\,\mu\text{m}\ r - \phi$	$\sigma_{d_0} = 55\,\mu\text{m}$
					$100 - 200\,\mu\text{m}\ z$	$\sigma_{z_0} = 65\,\mu\text{m}$
DCH	17.2	-27.4	7,104	40	$6 - 8\,\text{mm}$	$\sigma_\phi = 1\text{mrad}$
					drift distance	$\sigma_{\tan\lambda} = 0.001$
						$\sigma_{p_t}/p_t = 0.47\%$
						$\sigma(dE/dx) = 7.5\%$
DIRC	25.5	-38.6	10,752	1	$35 \times 17\,\text{mm}^2$	$\sigma_{\theta_C} = 2.5\text{mrad}$
					$(r\Delta\phi \times \Delta r)$	per track
					144 bars	
EMC(C)	27.1	-39.2	2×5760	1	$47 \times 47\,\text{mm}^2$	$\sigma_E/E = 3.0\%$
					5760 crystals	$\sigma_\phi = 3.9\text{mrad}$
EMC(F)	15.8	27.1	2×820	1	820 crystals	$\sigma_\theta = 3.9\text{mrad}$

The inner three layers primarily provide position and angle information, used to determine decay vertexes for particles of interest (ie. B^0-mesons). These layers are mounted as close to the water-cooled beryllium beam pipe as practical, in order to minimize the impact of multiple Coulomb scattering in the beam pipe on vertex determination. The innermost layer is 32mm from the center of the beam pipe (the beam pipe has a radius of 27.8mm).

The outer two layers are at larger radii, with the fourth layer at a radius of 91-127mm from the center of the beam pipe; the range of radii for the layer is due to the arch-like shape of the fourth and fifth layers (see Fig. 4.5 (bottom)), so designed as to increase the angular acceptance while limiting the amount of required silicon. The outer layers are designed to provide coordinate and angle measurements necessary to link SVT tracks with those reconstructed in the drift chamber.
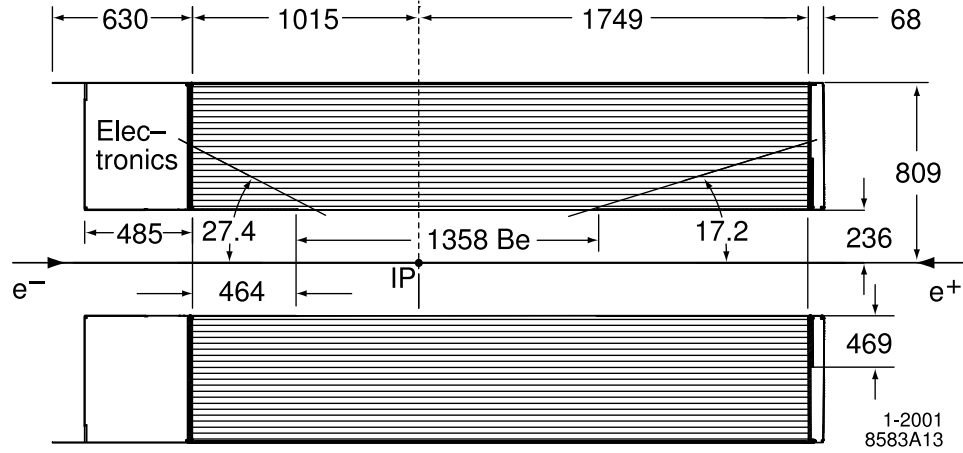
Figure 4.6: Drift chamber layout, longitudinal section. Dimensions are given in millimeters.

4.2.2 Drift chamber

The drift chamber is designed primarily to obtain momentum measurements for charged particles. Information from the DCH is also used in a charged particle trigger and to measure the ionization energy loss dE/dx. dE/dx measurements provide particle identification information, which is combined with information from the Cherenkov detector in the barrel region; in the extreme forward and backward regions, particle identification relies on the DCH. A schematic of the DCH is shown in Fig. 4.6.

The DCH has a relatively small radius (57cm instrumented, extending to a radius of 81cm from the interaction point), but is almost 3m long. It is composed of 40 layers of hexagonal cells. The DCH readout electronics are mounted on the backward endplate of the chamber, minimizing the amount of material in front of the calorimeter endcap.

In addition to its principle tasks, the DCH is also used to reconstruct decay and interaction vertices outside the SVT, such as K_S^0 decays. As a result, the DCH must be able to measure the longitudinal position of tracks with a resolution of about 1mm. This is achieved by placing 24 of the 40 layers at small angles to the z-axis. The layers are arranged in groups of four, creating ten

superlayers. Within a superlayer, the wires have the same angular orientation. Each superlayer is staggered by half a cell. This arrangement allows for track segment finding within a superlayer, even if one out of the four signals in that superlayer is missing. A schematic of the drift cell layout is shown in Fig. 4.7 (left) for the four innermost superlayers.

Each drift cell is hexagonal in shape, approximately 11.9mm by 19.0mm along the radial and azimuthal directions, respectively. The sense wires are $20\,\mu$m diameter gold-coated tungsten-rhenium, kept at a positive high voltage (around 1900V). The other wires that make up the drift cells are gold-coated aluminum, with the field wires kept at ground potential. The DCH is filled with a 80:20 helium:isobutane gas mixture at a constant overpressure of 4 mbar.

The specific energy loss, $\mathrm{d}E/\mathrm{d}x$, is derived from measuring the total charge deposited in each drift cell, as part of a feature extraction algorithm, and integrated over approximately $1.8\,\mu$s. The $\mathrm{d}E/\mathrm{d}x$ measurement as a function of track momenta is given in Fig. 4.7 (right).

4.2.3   Detector of internally reflected Cherenkov light

Particle identification (PID) is crucial to the B physics program at *BABAR*. The ability to distinguish charged kaons from pions is important in flavor tagging (and thus in the study of CP violation in the interference between mixing and decay; see Sec. 2.9.4) as well as for analyses such as the ones described in this thesis. In $B^0 \to \rho^0 K^{*0}$, for instance, the ability to distinguish the K^+ from a π^+ is the difference between $\rho^0 K^{*0}$ and $\rho^+\rho^-$, which have similar branching fractions but are governed by different physical processes.

The detector of internally reflected Cherenkov light (DIRC) is a novel system designed to provide a $\sim 4\sigma$ or greater separation between charged kaons and pions from the pion Cherenkov threshold of $700\,\mathrm{MeV}$ up to $4.2\,\mathrm{GeV}$. As mentioned above, PID below $700\,\mathrm{MeV}$ relies primarily on $\mathrm{d}E/\mathrm{d}x$ measurements in the DCH and SVT.

The DIRC is based on the principle that reflecting light from a flat surface maintains the
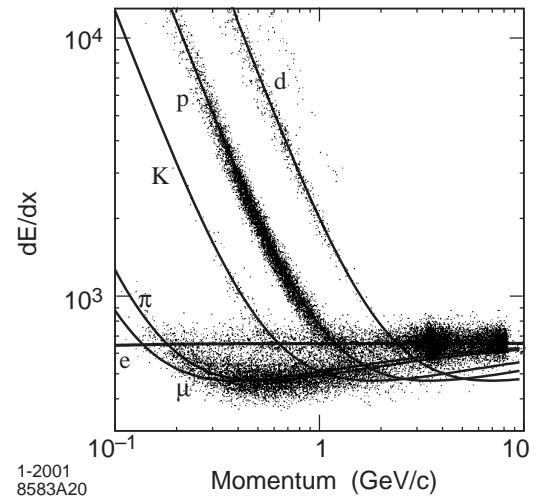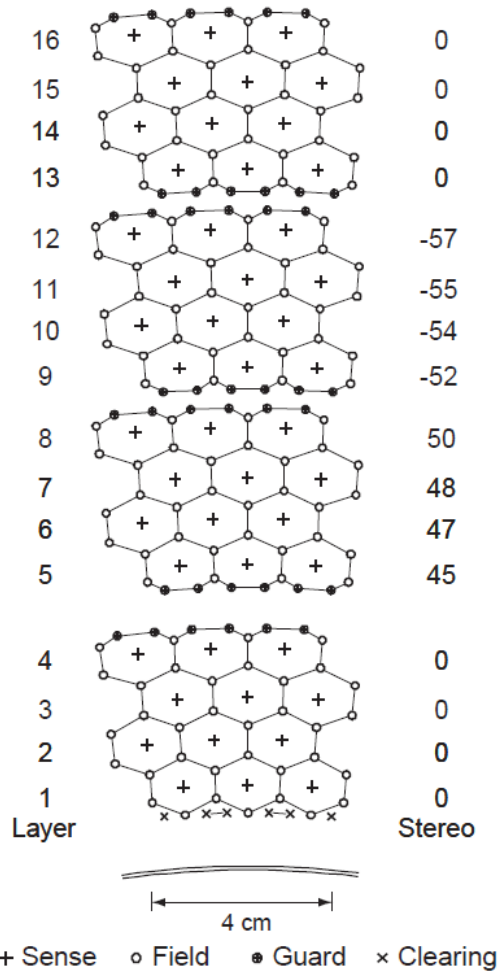
Figure 4.7: Schematic layout of drift cells for the four innermost DCH superlayers (left). Lines have been added between field wires to aid in visualization of the drift cells. The numbers on the right give the stereo angles (mrad) of the sense wires in each layer. The 1mm-thick beryllium inner wall of the DCH is shown at the bottom. DCH measurements of dE/dx as a function of track momenta (right); the lines represent Bethe-Bloch predictions for six particle species.

magnitudes and angles of the incoming photons. Fig. 4.8 (left) shows a schematic of one of the DIRC bars, which acts as both a radiator and light pipe for photons trapped in the radiator by total internal reflection. The photons are generated by Cherenkov radiation, which is caused by a charged particle traversing a medium at a speed greater than the speed of light in that medium. The photons are emitted at an angle from the particle's trajectory, the Cherenkov angle θ_C defined by

$$\cos \theta_C = \frac{1}{n\beta} \tag{4.1}$$

where n is the index of refraction of the medium (for the DIRC radiators, fused silica, $n = 1.473$) and $\beta = v/c$ is the speed of the particle in units of c. For particles with $\beta \simeq 1$, some photons will always lie within the limit for total internal reflection, and will be transported to either one or both ends of the bar, depending upon the particle incident angle.
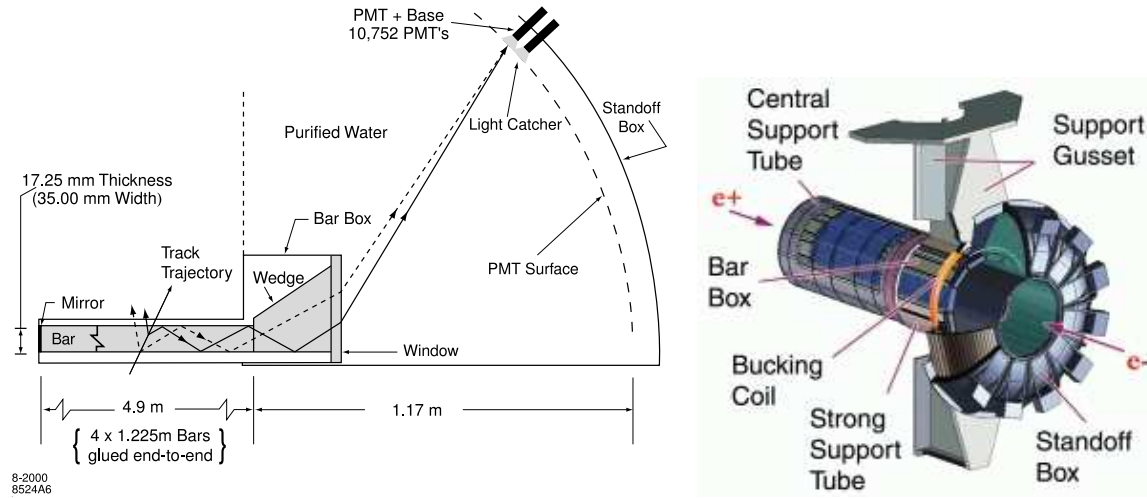
Figure 4.8: Right: Schematic of DIRC silica bar and instrumentation. Left: diagram of the mechanical support structure for the DIRC.

The DIRC bars are 17mm thick, 35mm wide, and 4.9m long, and made of fused synthetic silica. The bars are placed in 12 hermetically sealed aluminum-hexcel boxes; the 12 boxes are arranged in a dodecagonal barrel around the DCH. Within each box, 12 bars are optically isolated by $\sim 150\,\mu$m air gap between neighboring bars. At the forward end of each bar, a mirror is

affixed to each bar to reflect incident photons to the backward end. At the backward end, a fused silica wedge at the bar exit reflects photons at large angles to the bar axis, reducing the size of the detection surface and recovering photons that would otherwise be lost due to internal reflection at the silica/water interface. The photons leave the silica for a water-filled standoff box ($n \simeq 1.346$), which is instrumented with a densely packed array of photomultiplier tubes (PMTs). The PMTs are surrounded by reflecting light catcher cones, which capture photons which would otherwise miss the active area of the PMTs; the effective active surface area for light collection is about 90%. A schematic of the DIRC is shown in Fig. 4.9.
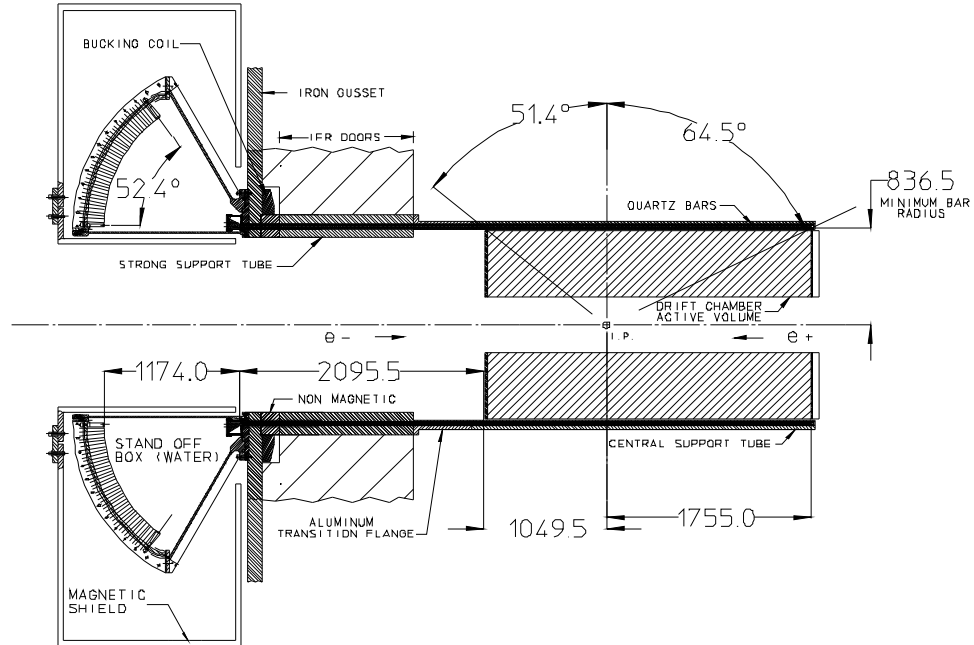
Figure 4.9: Layout of the DIRC, longitudinal section. Dimensions are given in millimeters.

The expected Cherenkov light pattern at the instrumented surface is essentially a conic section, where the cone's opening angle is the Cherenkov angle θ_C modified by refraction at the exit from the fused silica. The single photon resolution is about 10mrad.

Fig. 4.10 (left) shows an event display of the DIRC readout for an $e^+e^- \to \mu^+\mu^-$ event.
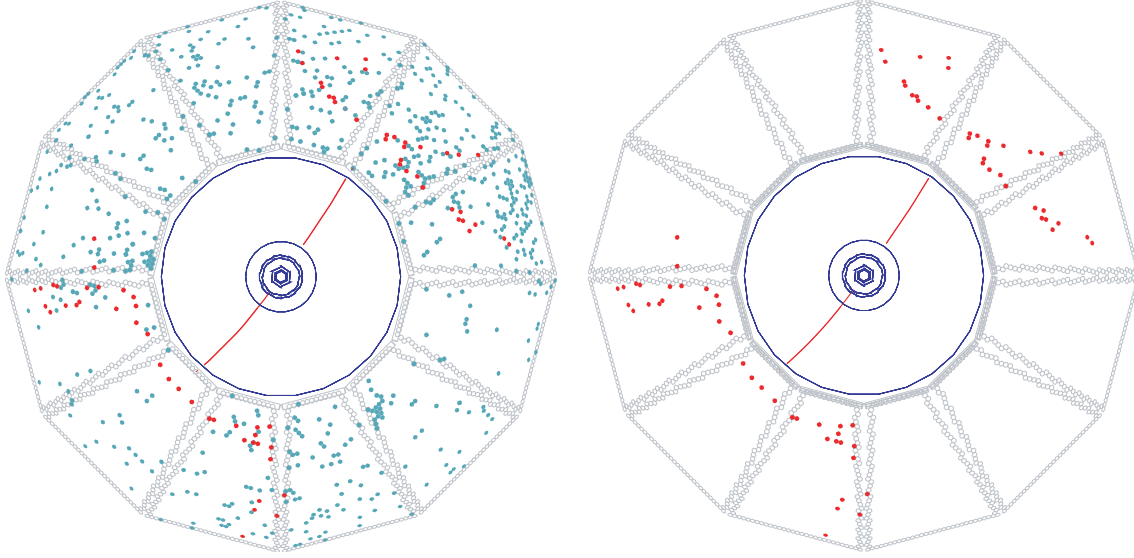
Figure 4.10: Display of an $e^+e^- \to \mu^+\mu^-$ event reconstructed in *BABAR* with two different time cuts. On the left, all DIRC PMTs with signals within the ±300 ns trigger window are shown. On the right, only those PMTs with signals within 8 ns of the expected Cherenkov photon arrival time are displayed.

On the left, we show all DIRC PMT signals within the ±300ns trigger window. Most of the background comes from low energy photons from the PEP-II machine hitting the standoff box. The time distribution of real Cherenkov photons from a single event is about 50ns wide. Given a track pointing at a particular DIRC bar and a candidate signal in a PMT within the optical phase space of that bar, the Cherenkov angle can be determined up to a 16-fold ambiguity. The goal of the reconstruction software is to associate the correct track with the candidate PMT signal, requiring that the photon have the correct transit time from its production in the bar to detection at the PMT, within the measurement error of 1.5ns. The reconstructed Cherenkov photons associated with the $\mu^+\mu^-$ tracks are shown in Fig. 4.10 (right).

In Fig. 4.11 we show measurements of θ_C as a function of track laboratory momentum. As can be seen, the DIRC provides clean $K - \pi$ separation at low momenta, and some separation at the highest momenta. The curves are theoretical predictions from Eq. (4.1).
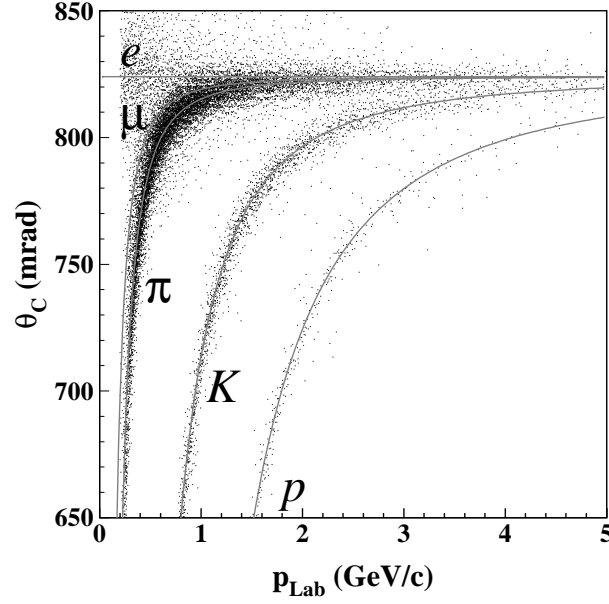
Figure 4.11: DIRC measurements of θ_C versus track momenta. The lines represent predictions from Eq. (4.1).

4.2.4 Electromagnetic calorimeter

The electromagnetic calorimeter (EMC) is designed to detect electromagnetic showers with high efficiency and excellent energy and angular resolution over the energy range from $20\,\mathrm{MeV}$ to $4\,\mathrm{GeV}$. This allows for the detection of low energy π^0's and η's from B decays, as well as higher energy photons from other processes. The EMC is built in two sections: the cylindrical barrel region and a conical forward endcap, which cover 90% of the solid angle in the center-of-mass system. The EMC is a total-absorption calorimeter composed of a finely segmented array of thallium-doped cesium iodide CsI(Tl) crystals, which are read out by silicon photodiodes. The photodiodes are matched to the spectrum of scintillation light in the crystals. The barrel consists of 5.760 crystals arranged in 48 distinct rings with 120 identical crystals in each ring. The endcap is composed of 820 crystals in eight rings. A schematic of the EMC is given in Fig. 4.12.

The crystals have a tapered trapezoidal cross section, as shown in Fig. 4.13. They range in
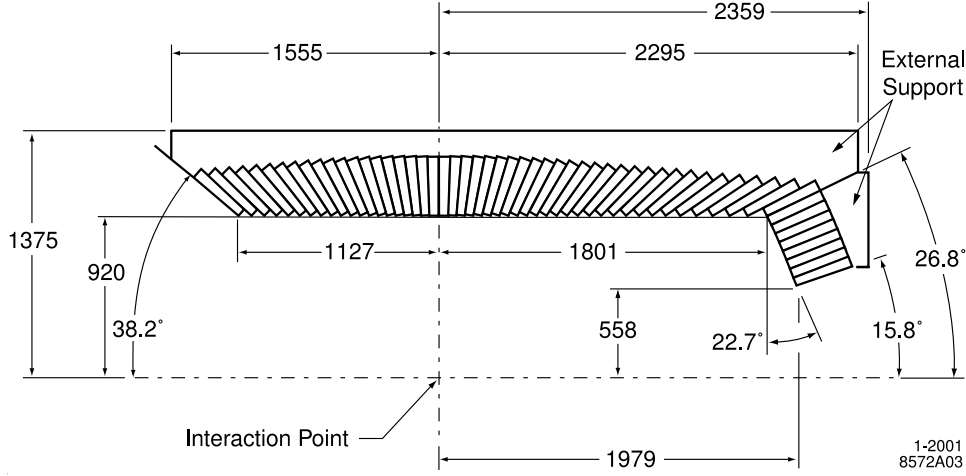
Figure 4.12:   Layout of the crystals of the EMC, longitudinal section. Dimensions are given in millimeters. The bottom half of the EMC is not shown.

length from $29.6\,\mathrm{cm}$ in the backward direction to $32.4\,\mathrm{cm}$ in the forward direction, with the length

increase designed to limit the amount of shower leakage from higher-energy particles.

At low energy, the resolution is measured with a radioactive source, which yields $\sigma_E/E =$

$(5.0 \pm 0.8)\%$ at $6.13\,\mathrm{MeV}$. At high energy, the resolution is derived from Bhabha scattering, where

the energy of the detected shower can be predicted from the polar angle of the $e^\pm$. This resolution

is determined to be $\sigma_E/E = (1.9 \pm 0.07)\%$ at $7.5\,\mathrm{GeV}$. A fit to the energy dependence yields

$$\frac{\sigma_E}{E} = \frac{(2.32 \pm 0.30)\%}{\sqrt[4]{E}} \oplus (1.85 \pm 0.12)\% \;, \tag{4.2}$$

where E is the incident energy in units of GeV.

4.2.5   Instrumented flux return

In order to detect muons and neutral hadrons (mostly K_L^0 and neutrons), the steel flux

return of the solenoid magnet is instrumented. The steel in the barrel and the two end doors is

segmented into layers, increasing in thickness from 2 cm on the inside to 10 cm at the outside. The
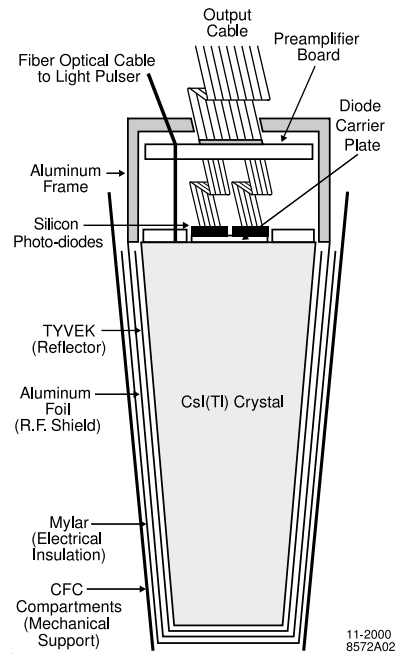
Figure 4.13: Schematic of EMC crystal and instrumentation (not to scale).

layout of the instrumented flux return (IFR) is shown in Fig. 4.14. Initially, the IFR used single gap resistive plate chambers (RPCs) in the spaces between the steel. RPCs detect streamers from particles ionizing an argon-freon-isobutane gas via capacitive readout strips on both sides of the gap.

Early in the operation of *BABAR*, the RPCs began losing efficiency. Numerous attempts were made to slow this premature aging, to varying degrees of success. It was determined that much of the problem was due to the linseed oil (used to coat the bakelite surfaces facing the gap) running and pooling. In 2002, efforts began on designing a replacement system. In 2004, limited streamer tubes (LSTs) were installed in the top and bottom sextants of the barrel IFR. In 2006, the remaining barrel RPCs were replaced by LSTs.

Of the 19 RPC layers in the barrel, only the innermost 18 were accessible for replacement; after replacing the inner 18 layers in each sextant, the 19th layer RPCs were deactivated. To com-

Barrel
342 RPC
Modules

3200

3200

FW

920

19 Layers

1940   1250

BW

18 Layers

4-2001
8583A3

432 RPC
Modules
End Doors
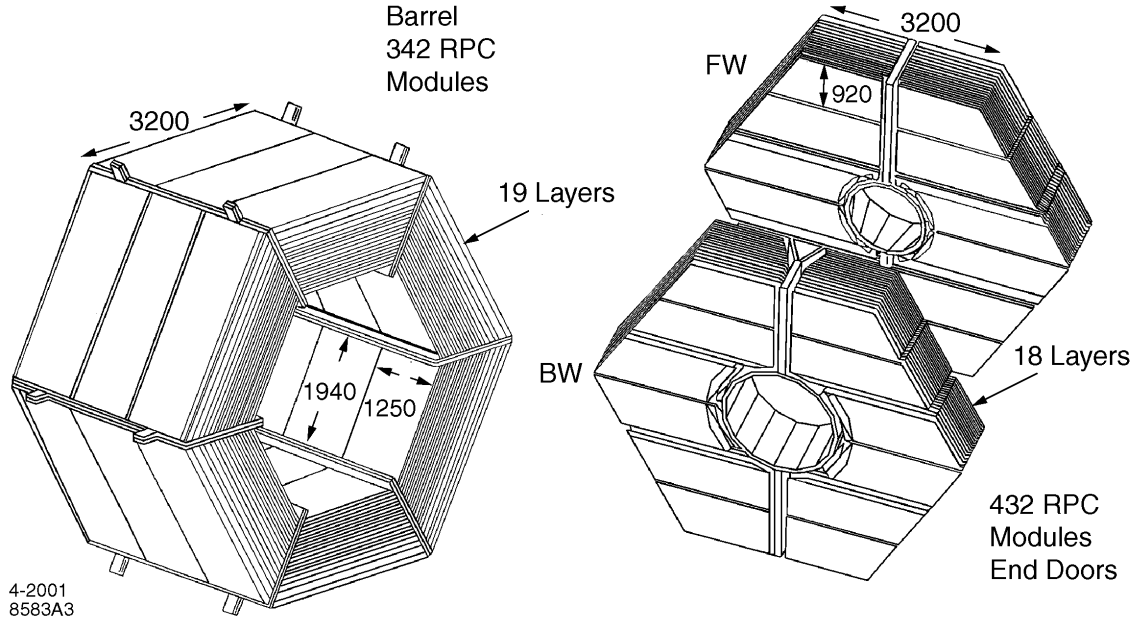
Figure 4.14:   Schematic of the IFR for the barrel section (left) and forward (FW) and backward (BW) end doors (right).

pensate for the loss of absorption, brass was installed in six layers to increase the total absorption length.

The LSTs [40] are 17 mm wide, 15 mm high PVC tubes, roughly 3.5 m long, with a gold-plated anode wire in the center, which is kept at high voltage. The walls of the tube are painted with a water-based graphite paint and maintained at ground potential. The tubes are filled with a (89:3:8) mixture of CO_2, Argon, and isobutane. When a charged particle passes through the tube, the gas is ionized and a streamer builds up; information on this streamer is read out from the anode wire. Simultaneously, a charge is induced on a plane mounted below the tube. The charge from the wire gives position information in ϕ, the induced charge is read out by strips segmented in z. The radial position of the tubes (their layer) gives information in r.
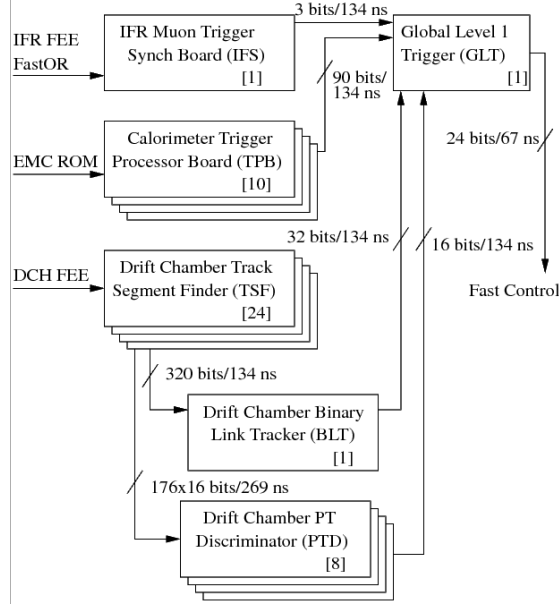
Figure 4.15: L1 trigger schematic. Indicated on the figure are the number of components (in square brackets) and the transmission rates between components in terms of total signal bits.

4.2.6 The *BABAR* trigger

At design luminosity ($3 \times 10^{33}\,\mathrm{cm}^{-2}\mathrm{s}^{-1}$), beam-induced background rates are around 20 kHz each for ≥ 1 track(s) in the drift chamber with $p_t > 120\,\mathrm{MeV}$ and at ≥ 1 EMC cluster with $E > 100\,\mathrm{MeV}$. The goal of the trigger system is to keep the total event rate under 120 Hz. The total trigger efficiency is required to exceed 99% for all $B\overline{B}$ events and to be at least 95% for continuum ($e^+e^- \to u\overline{u}, d\overline{d}, s\overline{s}, c\overline{c}$). To achieve this, *BABAR* uses two levels of trigger: Level 1 (L1) in hardware followed by Level 3 (L3) in software.

The L1 trigger uses information on charged tracks in the drift chamber, showers in the EMC, and tracks in the IFR. A schematic of the L1 trigger is shown in Fig. 4.15 for initial *BABAR* running.

As the luminosity of PEP-II has consistently exceeded design expectations, the L1 drift chamber trigger was upgraded to handle a higher data rate. The drift chamber track segment finder

(TSF) was updated to send additional high-resolution information to a new hardware module, the ZPD, created in a Harvard-led effort. The ZPD uses both the stereo and axial layers of the DCH (the original trigger system, the PTD, a "p_t discriminator," used only axial) and performs a fast χ^2 minimization to fit track segments to a helix and extract curvature ($1/p_T$) and z_0. Whereas the original PTD provided only p_T information, the addition of z_0 information allows us to reject tracks from the known background hot spots that are > 15 cm up- or down-stream of the interaction point.

The L3 trigger receives the output from the L1 trigger, performs event reconstruction and classification, and applies selection filters. L3 runs on an online computer farm, and refines and augments the selection methodology used in L1. Better DCH track reconstruction (and improved vertex resolution) as well as EMC cluster filters greatly reduce the amount of beam backgrounds and Bhabha events. As L3 operates in software, it is highly flexible and can be modified to suit the varying demands of luminosity and physics requirements.

4.3   Particle identification

The *BABAR* particle identification (PID) group developed several classifiers for performing charged particle ID. In the analyses described in this thesis, we make use of the pion KM [41] and the kaon BDT classifiers. All classifiers have several levels of tightness (where a tighter classifier has lower misidentification rates and a lower efficiencies); the choice of which level to use is based upon the requirements of the analysis. This analysis uses the `tight` criterion for the kaon BDT selector (see Fig. 4.16) and the `loose` criterion for the pion KM selector (Fig. 4.17).

The KM selectors use the Error Correcting Output Code (ECOC) technique [42], which combines multiple binary classifiers (in this case Bootstrap Aggregate Decision Trees), which are trained to consider different samples as signal vs. background. The selector uses seven classifiers, which consider between one and three of the following classes as signal: K, π, p, and/or e, as
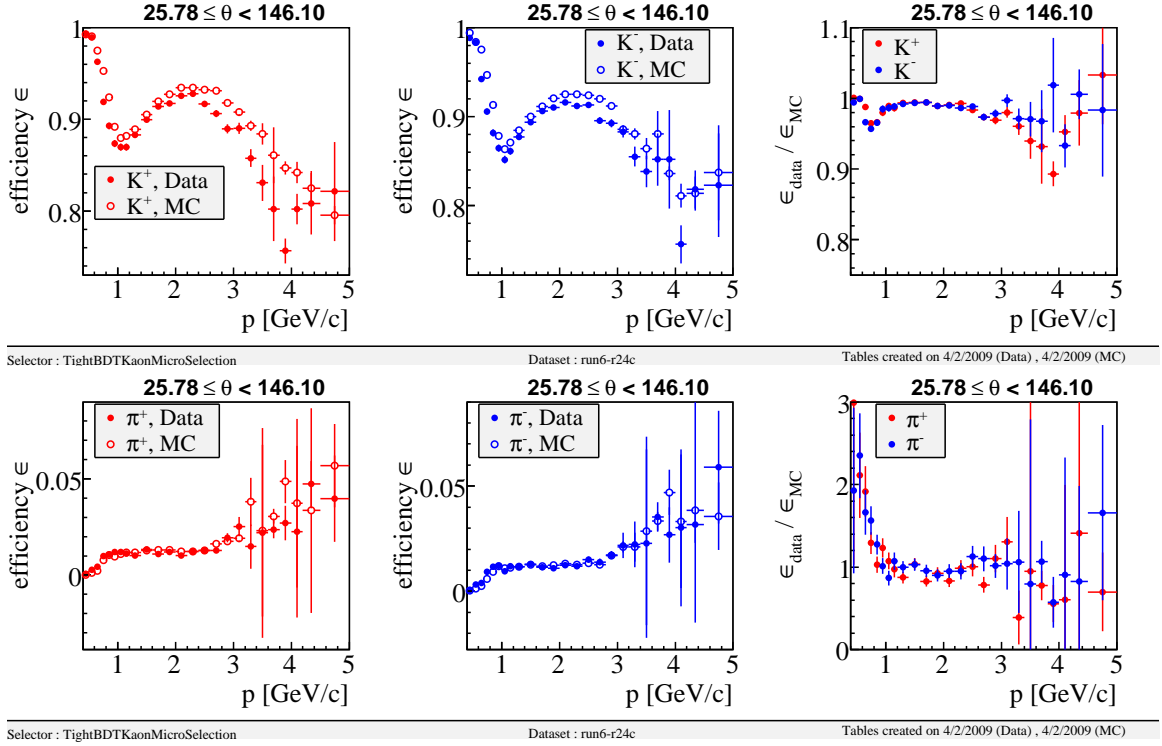
Figure 4.16: Tight kaon BDT selector kaon efficiency (top) and pion mis-ID rate (bottom) as a function of track momentum. Left to right: efficiency for $+$ tracks, $-$ tracks, and the ratio of data to MC efficiency.

shown in Tab. 4.2. Each classifier outputs a real number between -1 and 1 according to its own definition of signal and background. We then compare the sum of the squared distance (generalized Hamming distance) of the output values for each classifier with the rows of Tab. 4.2, to determine which particle species is most likely; we call this distance H_a where a is the particle type (K, π, p, or e).

To define which tracks end up in which PID list, the KM selector considers H_a for that particle type, as well as the ratio of Hamming distances for the other particle types. Ie. the pion selector is based on H_π, H_K/H_π, H_p/H_π, and H_e/H_π. We then define constants for each PID list and tightness level: the smaller the value of H_π, the more likely the track is to be a π; the smaller the ratio H_K/H_π, the more likely the track is to not be misidentified as a kaon.
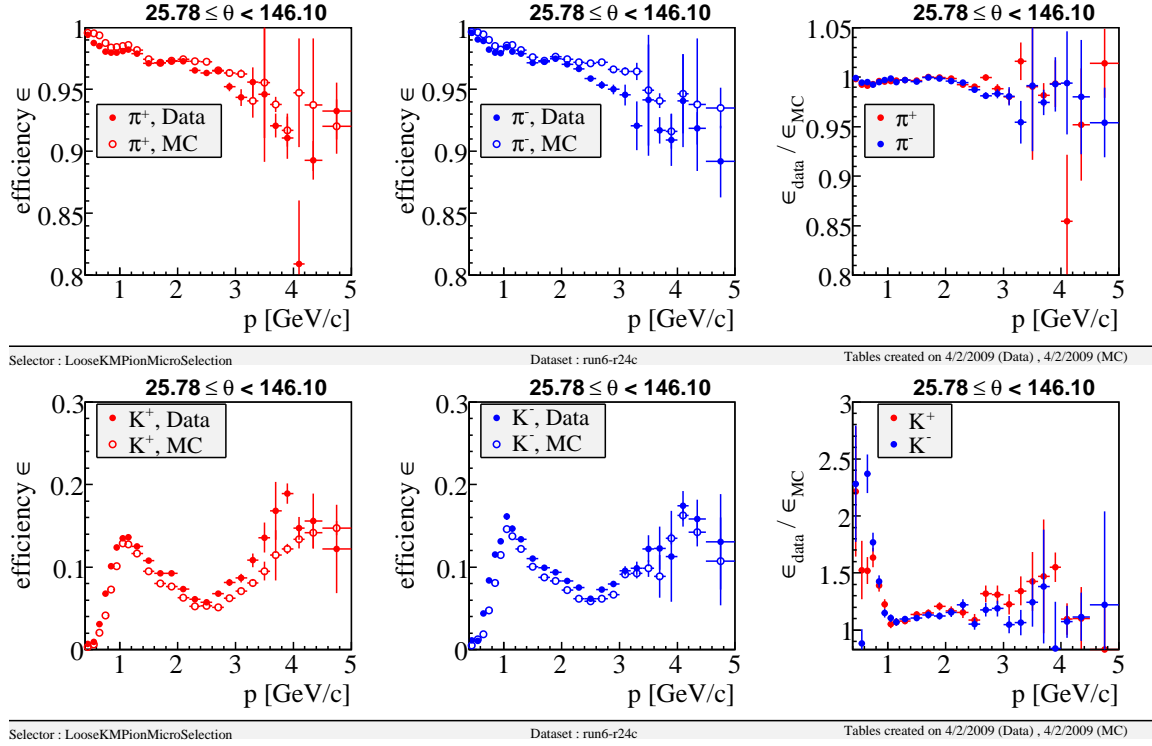
Figure 4.17: Loose pion KM selector pion efficiency (top) and kaon mis-ID rate (bottom) as a function of track momentum. Left to right: efficiency for + tracks, − tracks, and the ratio of data to MC efficiency.

Table 4.2: Exhaustive indicator matrix for the seven classifier outputs used in creating the KM PID selector. Each column indicates what training samples (K, π, p, e) are considered signal (1) or background (-1) for a given classifier ($t_0 \ldots t_6$).

Class	t_0	t_1	t_2	t_3	t_4	t_5	t_6
K	1	1	1	1	1	1	1
π	-1	1	-1	1	-1	1	-1
p	1	-1	-1	1	1	-1	-1
e	1	1	1	-1	-1	-1	-1

The kaon BDT selector is based on the same type of Bootstrap Aggregate Decision Tree classifiers, but considers only kaon and pion hypotheses. As a result, it has somewhat lower pion mis-ID rates for a given efficiency than the kaon KM selector. The trade-off is that the kaon BDT

selector is not designed to reject e or p. As the most problematic backgrounds in this analysis are from charmless B decays (ie. $B^0 \to \rho^+ \rho^-$, where one pion is misidentified as a kaon), the improved $K - \pi$ separation was chosen to be more important.

The kaon and pion samples come from $D^* \to D^0 \pi^+$ with $D^0 \to \pi^+ K^-$, with a number of preselection cuts applied [41]. The binary classifiers combine information from 36 variables, with output from all detector subsystems except the IFR.

Chapter 5

Analysis Overview

In the analyses described in this thesis, a B candidate is formed by combining two resonance candidates—one with a $\pi\pi$ final state and one with a $K\pi$ final state—to form a neutral B-meson candidate. The signal channels are: $B^0 \to \rho^0 K^{*0}$, $B^0 \to f_0 K^{*0}$, and $B^0 \to \rho^- K^{*+}$, where K^* is used generically to refer to the scalar $(K\pi)_0^*$, vector $K^*(892)$, or tensor $K_2^*(1430)$. The notation ρ refers to the $\rho(770)$ [2] and f_0 refers to the $f_0(980)$ [3]. The notation $(K\pi)_0^*$ refers to the scalar $K\pi$, which we describe with a LASS model [4, 5], combining the $(K\pi)_0^*$ resonance together with an effective-range non-resonant component.

We reconstruct the ρ, f_0, and K^* candidates as:

$$
\begin{aligned}
\rho^0 &\to \pi^+\pi^- \\
f_0 &\to \pi^+\pi^- \\
\rho^- &\to \pi^0\pi^-
\end{aligned}
\qquad
\begin{aligned}
K^{*0} &\to K^+\pi^- \\
K^{*+} &\to K^+\pi^0
\end{aligned}
\tag{5.1}
$$

We place loose selection criteria (cuts) on our ρ, f_0, K^*, B^0, etc. candidates, designed to maintain high signal efficiency and allow for large enough tails in the discriminating variables to parameterize backgrounds well (Ch. 6.2). We use large samples of simulated B-meson decays (Monte Carlo) to determine the dominant B decay backgrounds, which survive our preselection

64

(Ch. 7.2). Although the dominant backgrounds in this analysis come from $e^+e^- \to q\overline{q}$ events, $B\overline{B}$ backgrounds must be treated carefully, as they usually appear more signal-like in the discriminating variables.

Once we have determined our $B\overline{B}$ background categories, we create probability density functions (PDFs) of four to seven discriminating variables (depending upon the analysis) for the relevant event categories: signal, $B\overline{B}$ backgrounds, $q\overline{q}$ background. These PDFs are used in an extended, unbinned maximum likelihood (ML) fit to extract the signal yields, branching fractions (BFs), f_L, and $\mathcal{A}_{ch}$ values of interest (Ch. 7.1).

Before unblinding the dataset to determine signal yields, BFs, etc., we perform numerous validation studies to verify that the ML fitter is performing as expected and to verify that it can handle the desired number of degrees of freedom. We also use these studies to understand any biases in the yield extraction procedure (Ch. 7.4).

Although we initially considered an analysis strategy in which all K^* resonances would be fit simultaneously, the number of potential signal (or signal-like) final states, which were highly correlated, proved problematic. Instead, we consider two mass regions, the low mass region (LMR) for measuring the $K^*(892)$ branching fractions and the high mass region (HMR) for determining the $(K\pi)_0^*$ and (where appropriate) $K_2^*(1430)$ BFs. These regions are defined by:

$$\text{Low mass region} \quad : \quad 0.750 < m_{K\pi} < 1.000\,\text{GeV} \tag{5.2}$$

$$\text{High mass region} \quad : \quad 1.000 < m_{K\pi} < 1.550\,\text{GeV} \tag{5.3}$$

The HMR is fitted first, and the measured $(K\pi)_0^*$ BFs used in the LMR fit. Initial studies of the HMR indicated that there was no need for an non-resonant $\pi\pi$ component. In the $K\pi$ invariant mass spectrum, the LASS parameterization (see Ch. 6.2) includes a non-resonant S-wave $K\pi$; no additional non-resonant component is included.

The main portion of this thesis focuses on the $K^*(892)$ analysis, as this was the primary

signal of interest. In most ways, the analysis procedure for the HMR is similar to that in the LMR.

Additional details on the HMR fits are presented in App. B and C.

Chapter 6

Data Samples, Event Reconstruction and Selection

In this chapter, we discuss the *BABAR* data samples used in this analysis as well as the various *BABAR* software packages involved in the data analysis. We then go on to discuss the event reconstruction and selection criterea involved in preparing the data for the Maximum Likelihood fit to extract the signal yields of interest.

6.1 Data Samples

The analyses described in this thesis are based on *BABAR*'s Computing Model 2 (CM2) data reconstructed in analysis-51 (release 24.3.6) and analyzed in analysis-43 (release 22.3.4). We analyze the full run 1 to run 6 dataset of $\Upsilon(4S)$ on-resonance ($429\,\mathrm{fb}^{-1}$) and off-resonance ($44.8\,\mathrm{fb}^{-1}$) with the run 1 to 6 samples taken from the tagged dataset BFourBody-Run{1,2,3,4,5,6}-OnPeak-R24a3-v06. Tab. 6.1 gives the detailed luminosities and B counting in each run. We esti-

mate the number of $B\bar{B}$ pairs from the on-resonance data to be

$$N_{B\bar{B}} = (471.0 \pm 2.8) \times 10^6 .\qquad(6.1)$$

Table 6.2 lists the additional packages and their version numbers used in the analysis.

Table 6.1: Luminosities and B counting for on- and off-resonance datasets. Uncertainties combine statistical and systematic contributions.

	On-resonance				Off-resonance	
	Runs	Lumi (pb^{-1})	$N_{B\bar{B}}$		Runs	Lumi (pb^{-1})
Run 1	3303	20596	22555999	$\pm$ 137694	297	2622
Run 2	5193	62068	68430457	$\pm$ 412936	590	7030
Run 3	3678	32680	35763258	$\pm$ 216993	267	2496
Run 4	6663	100802	111421254	$\pm$ 670995	648	10228
Run 5	8057	133887	147620363	$\pm$ 888260	676	14546
Run 6	4115	79041	85194672	$\pm$ 513624	347	7887
Total	31009	429074	471000000	$\pm$ 2800000	2825	44809

Table 6.2: Packages and tags used for analysis-51 (release 24.3.6) and analysis-43 (release 22.3.4).

Package	a51 Tag	a43 Tag
BetaPid	V00-15-04	—
BtaTupleMaker	V00-03-29	—
ProdDecayFiles	HEAD	—
Q2BUser	HEAD	HEAD
RooFitCore	V02-00-09-03	V02-00-09-03
RooFitModels	V02-00-09	V02-00-09
RooRarFit	V00-01-72	V00-01-68
SimpleComposition	V00-04-27	—
workdir	V00-04-21	V00-04-21

Monte Carlo (MC) simulation [43, 44] is used to describe signal and $B\bar{B}$ backgrounds; the simulation is generated in *BABAR*'s Simulation Production release 10 (SP10). The signal MC samples are listed in Table 6.3. The signal and background MC samples are generated with conditions covering the full data period.

Table 6.3: Monte Carlo mode numbers and number of SP10 events generated (in thousands) for signal and non-resonant background MC samples. The signs for particles given in "Decay" should be taken as those which correspond to the given analysis. (ie. "$\pi\pi K\pi$" for $\rho^- K^{*+}_{K^+\pi^0}$ represents $\pi^+\pi^0 K^+\pi^0$.)

Decay	$(\rho^0/f_0)K^{*0}$		$\rho^- K^{*+}_{K^+\pi^0}$	
	Mode	# evts	Mode	# evts
$\rho K\pi$	7608	4269k	7610	4261k
$\rho K^*(892)$ long.	2359	429k	2499	429k
$\rho K^*(892)$ trans.	2360	429k	2500	429k
$\rho K_2^*(1430)$ long.	10012	373k	9908	423k
$\rho K_2^*(1430)$ trans.	10013	373k	9909	423k
$f_0 K^+\pi^-$	9988	4269k	—	—
$f_0 K^*(892)^0$	3359	429k	—	—
$f_0 K_2^*(1430)^0$	9906	423k	—	—
$\pi\pi K\pi$	10253	4272k	10256	4280k
$\pi\pi K^*(892)$	2495	427k	10254	427k
$\pi\pi K_2^*(1430)$	10252	427k	10255	428k

To determine the importance of various $B\overline{B}$ backgrounds, we use generic $B\overline{B}$ MC: SP-1237-BFourBody-Run{1,2,3,4,5,6}-R24a3-v03.tcl for $B^0\overline{B}^0$ and SP-1235-BFourBody-Run{1,2,3,4,5,6}-R24a3-v03.tcl for B^+B^-. These samples have a luminosity about three times that of data, and include all known B decays with their measured (or predicted) rate. Once the dominant $B\overline{B}$ background modes are identified, we use exclusive MC samples to better understand the backgrounds; see Sec. 7.2.

6.1.1 $(K\pi)_0^*$ signal MC

The $J^P = 0^+$ component of the $K\pi$ spectrum, which we denote $(K\pi)_0^*$, is poorly understood; we use the LASS parameterization [4, 5] which consists of the $K_0^*(1430)$ resonance together

with an effective-range non-resonant component. The amplitude is given by

$$
\begin{aligned}
\mathcal{A}(m_{K\pi}) &= \frac{m_{K\pi}}{q\cot\delta_B - iq} + e^{2i\delta_B}\frac{m_0\Gamma_0\frac{m_0}{q_0}}{(m_0^2 - m_{K\pi}^2) - im_0\Gamma_0\frac{q}{m_{K\pi}}\frac{m_0}{q_0}}\,, \\
\cot\delta_B &= \frac{1}{aq} + \frac{1}{2}rq\,,
\end{aligned}
\tag{6.2}
$$

where $m_{K\pi}$ is the $K\pi$ invariant mass, q is the momentum of the $K\pi$ system, and $q_0 = q(m_{K\pi})$. We use the following values for the scattering length and effective-range parameters: $a = 2.07 \pm 0.10\,(\mathrm{GeV})^{-1}$ and $r = 3.32 \pm 0.34\,(\mathrm{GeV})^{-1}$ [5]. For the resonance mass and width we use $m_0 = 1.412\,\mathrm{GeV}$ and $\Gamma_0 = 0.294\,\mathrm{GeV}$.

In order to create samples of $\rho^0(K\pi)_0^{*0}$, $f_0(K\pi)_0^{*0}$, and $\rho^-(K\pi)_0^{*+}$ events, we begin with MC generated according to three-body phase space. We perform reconstruction and most of the preselection cuts (see Ch. 6.2), with the exception of the resonance mass and helicity cuts and the D vetoes. We then reweight the $K\pi$ distribution to match the LASS parameterization using LAURA++, an analysis package written by several *BABAR* collaborators. Tab. 6.4 gives the LASS scattering length and effective-range parameters parameters used in this analysis.

Table 6.4: LASS parameters [45]

LASS Scattering Length	2.07 ± 0.10
LASS Effective Range	3.32 ± 0.34

For the $\rho(K\pi)_0^*$ channels, we perform a second reweighting procedure, after all selection cuts except for the one on ρ helicity have been applied. We reweight the flat $\pi\pi$ helicity distribution to the expected $\mathcal{H}^2$ shape by checking whether a $[0, 1]$ random number is less than $\mathcal{H}_\rho^2$ (where $\mathcal{H}_\rho$ is the flat distribution); if the event passes this test, it is retained. The efficiency of this procedure is about 34%. The overall MC efficiency in these channels is then given by

$$
\epsilon = \frac{N_{sel}}{N_{gen} \times \epsilon_{LAURA} \times \epsilon_{\mathcal{H}_\rho}}\,,
\tag{6.3}
$$

where N_{sel} is the number of events surviving preselection and reweighting, N_{gen} is the number of three-body phase space events generated, ϵ_{LAURA} and $\epsilon_{\mathcal{H}_\rho}$ are given by the ratio of events retained by the reweighting procedure divided by the number of events entering the reweighting.

6.2 Event Processing and Selection

A B candidate is formed by combining two resonance candidates—one with a $\pi\pi$ final state and one with a $K\pi$ final state—to form a neutral B-meson candidate. We reconstruct the ρ, f_0, and K^* candidates as:

$$
\begin{aligned}
\rho^0 &\rightarrow \pi^+\pi^- \\
f_0 &\rightarrow \pi^+\pi^- \\
\rho^- &\rightarrow \pi^0\pi^-
\end{aligned}
\qquad
\begin{aligned}
K^{*0} &\rightarrow K^+\pi^- \\
K^{*+} &\rightarrow K^+\pi^0
\end{aligned}
\qquad (6.4)
$$

A B-meson candidate is characterized kinematically by the energy-substituted mass m_{ES} and by the energy difference ΔE, defined in the $\Upsilon(4S)$ frame as

$$
\begin{aligned}
m_{ES} &= \sqrt{\tfrac{1}{4}s - \mathbf{p}_B^{*2}} \qquad \text{and} \\
\Delta E &= E_B^* - \tfrac{1}{2}\sqrt{s},
\end{aligned}
$$

where $q_B^* = (E_B^*, \mathbf{p}_B^*)$ are the four vectors of the B-candidate in the $\Upsilon(4S)$ frame, and s is the square of the invariant mass of the electron-positron system. The small correlation between these variables is accounted for in the correction of the fit bias (see Ch. 7.4). Signal events peak at 0 in ΔE and at the B mass [2] in m_{ES}, with a resolution in ΔE of 17-37 MeV and m_{ES} of about 2.5 MeV.

6.2.1 BFourBody Skim

We skim the data and $B\overline{B}$ generic MC samples with the BFourBody skim. BFourBody filters the AllEvents stream based on the BFGMultiHadron tag bit and applies the following selec-

tions:

- A B-candidate with four daughters is formed from the charged tracks in the GoodTracksVery-
  Loose list (h^+) and the neutrals list pi0DefaultMass (π^0);

- $|\Delta E| < 0.3\,\text{GeV}$; $|m_{ES} - \sqrt{s}/2| < 0.1\,\text{GeV}/c^2$;

- At least one charged track is required in addition to those from the signal B.

The BFourBody skim combines nine skim sub-categories identified by tag bits. For each (sub)decay analyzed in this document, we require an "OR" of two related tag bits, given in Tab. 6.5. Taking the OR of the "1" and "2" categories removes any cut on $\cos\theta_{\text{T}}$, the cosine of the angle between the thrust direction of the B and the rest of the event (ROE).

Table 6.5: Tag bits, for each decay mode, required from the BFourBody skim.

Decay	Tag Bit 1	Tag Bit 2	Description
$\rho^0 K^{*0}$	B4bodyhhhh1	B4bodyhhhh2	$B^0 \to h^+ h^- h^+ h^-$
$\rho^- K^{*+}_{K^+\pi^0}$	B4bodyhhpp1	B4bodyhhpp2	$B^0 \to h^+ h^- \pi^0 \pi^0$

6.2.2   Reconstruction

Once the data are skimmed, we reconstruct B candidates as follows. No mass constraints are applied to the ρ, f_0, or K^* candidates, but we use TreeFitter to vertex the B, and require the vertex probability be between $(-0.1, 1)$.

- The π^0 candidate is formed from two photons from the GoodPhotonLoose list;

- Two oppositely charged tracks from the GoodTracksVeryLoose list are combined to form a
  $\rho^0 \to \pi^+\pi^-$ or $f_0 \to \pi^+\pi^-$ candidate;

- A π^0 and a GoodTracksVeryLoose charged track are combined to form a $\rho^+ \to \pi^+\pi^0$ candidate;

- Two oppositely charged tracks (GoodTracksLoose for the kaon, GoodTracksVeryLoose for the pion) are combined to form a $K^{*0} \to K^+\pi^-$ candidate;

- A GoodTracksVeryLoose charged track is combined with a π^0 candidate to form a $K^{*+} \to K^+\pi^0$ candidate;

- B^0 candidates are formed from a ρ or f_0 candidate and a K^*.

After the candidate list is formed, we apply the following preliminary cuts before B candidates are considered for the ML fit.

- For preliminary event-shape selection, we use the "thrust angle" θ_T, defined as the angle between the thrust axis of the B candidate decay products and the thrust axis of the rest of the event. For signal events, the distribution of $|\cos\theta_\mathrm{T}|$ is flat, while it is strongly peaked at $+1$ for continuum background. We require $|\cos\theta_\mathrm{T}| < 0.7$.

- $N_\mathrm{tracks} \geq N_\mathrm{tracks\,in\,decay\,mode} + 1$ (In order to be able to define a thrust vector for the rest of the event),

- $|\Delta E| \leq 0.1\,\mathrm{GeV}$ in $\rho^0 K^{*0}$,

- $-0.17 < \Delta E \leq 0.1\,\mathrm{GeV}$ in $\rho^- K^{*+}$; this cut is asymmetric to account for the long low-side tail on ΔE resulting from poorly reconstructed π^0's,

- $5.26 \leq m_{ES} \leq 5.2893$ GeV,

- Tag08 tagging category Fisher discriminant in the range $[-4, 5]$ (see App. F),

- $470 < m_{\pi\pi} < 1070$ MeV (except for in the high $\pi^+\pi^-$ mass sideband study, used to understand the $B^0 \to f_2(1270)K^*(892)^0$ background, which requires $470 < m_{\pi\pi} < 1470$ MeV; see App. D),

- $750 < m_{K\pi} < 1000$ MeV for the low mass region (LMR),

- $1000 < m_{K\pi} < 1500$ MeV for the high mass region (HMR),

- Helicity cuts for the ρ and K^* are summarized in Tab. 6.6. Note that we use $|\cos(\theta_{\rho^0})|$ as our PDF variable for $\rho^0 K^{*0}$, as the helicity distribution of $\rho^0 \to \pi^+\pi^-$ is symmetric. For $\rho^- K^{*+}$, we use the signed $\cos(\theta_{\rho^-})$ distribution, as the acceptance for and background from soft π^0's is worse than that from soft π^-'s.

Table 6.6: Helicity cuts applied to the ρ and K^* mesons.

Mode	$\mathcal{H}(\rho)$	$\mathcal{H}(K^*)$
$\rho^0 K^{*0}$	$-0.9 < \mathcal{H}_{\rho^0} < 0.9$	$-0.85 < \mathcal{H}_{K^*} < 1.0$
$\rho^- K^{*+}_{K^+\pi^0}$	$-0.8 < \mathcal{H}_{\rho^+} < 0.9$	$-0.80 < \mathcal{H}_{K^*} < 1.0$

- We require the π^0 to satisfy:

  - $120 < m^{\pi^0}_{\gamma\gamma} < 150$ MeV/c^2,

  - $E_{\pi^0} > 250$ MeV,

  - $E_\gamma > 50$ MeV for the π^0 daughters,

- PID requirements are (see Sec. 4.3):

  - Charged pion candidates must satisfy the Loose criteria of the `pionKM` selector,

  - Charged kaon candidates must satisfy the Tight criteria of the `kaonBDT` selector,

  - The efficiency of the selectors in MC is corrected to match the response in real data (PID tweaking),

Table 6.7: Number of MC events generated (# evts gen), number selected (# evts out), total MC efficiency (ϵ), SXF rate, and number of combinations per event for signal MC samples. "ln" and "tr" designate longitudinal and transverse polarizations, respectively.

	$\rho^0 K^{*0}$ ln	$\rho^0 K^{*0}$ tr	$f_0 K^{*0}$	$\rho^- K^{*+}_{K^+\pi^0}$ ln	$\rho^- K^{*+}_{K^+\pi^0}$ tr
# evts gen	429000	429000	429000	429000	429000
# evts out	61506	107552	78501	21185	47963
ϵ (%)	14.34 ± 0.05	25.07 ± 0.06	18.30 ± 0.06	4.94 ± 0.03	11.18 ± 0.05
SXF (%)	7.30	1.86	4.13	21.9	12.9
# comb/evt	1.06	1.02	1.03	1.17	1.13

- To reduce $B \to D$ decay backgrounds, we construct possible D candidates from the tracks

  and π^0 candidates, and require that the invariant mass fall outside some range of the nominal

  D mass ($m_{D0} = 1.8645\,\text{GeV}$, $m_{D+} = 1.8693\,\text{GeV}$). The specific D vetoes are:

  - $\rho^0 K^{*0}$: $|m_{K^+\pi^-} - m_{D^0}| > 40\,\text{MeV}$, $|m_{K^+\pi^-\pi^-} - m_{D^-}| > 40\,\text{MeV}$

  - $\rho^- K^{*+}_{K^+\pi^0}$: $|m_{K^+\pi^-} - m_{D^0}| > 20\,\text{MeV}$, $|m_{K^+\pi^-\pi^0} - m_{D^0}| > 40\,\text{MeV}$ (the π^0 comes

    either from the ρ^- or K^{*+})

For events that contain more than one signal candidate, we select the candidate with the largest B vertex probability. Before this selection there are 1.02 candidates per event in $\rho^0 K^{*0}$ on-peak data and 1.16 candidates per event in $\rho^- K^{*+}$ on-peak data. See Tab. 6.7 for specific values in signal MC.

We define self-cross-feed (SXF) candidates as those in which one or more of the generated particles in the B decay tree does not match the corresponding reconstructed particle. SXF rates for each signal channel are given in Tab. 6.7. We include SXF events in the signal model.

Fig. 6.1 shows the effect of the D vetoes and helicity cuts on $B^0 \to D^-\pi^+$ with $D^- \to K^+\pi^-\pi^-$ in the $\rho^0 K^{*0}$ analysis. This is the dominant D background in this mode that has the same final state as signal. The other dominant D backgrounds typically lose a soft pion and thus

do not have signal-like features in m_{ES} or ΔE, making them similar to $q\overline{q}$ background. Some D

backgrounds are explicitly included in the maximum likelihood fits; see Sec 7.2.
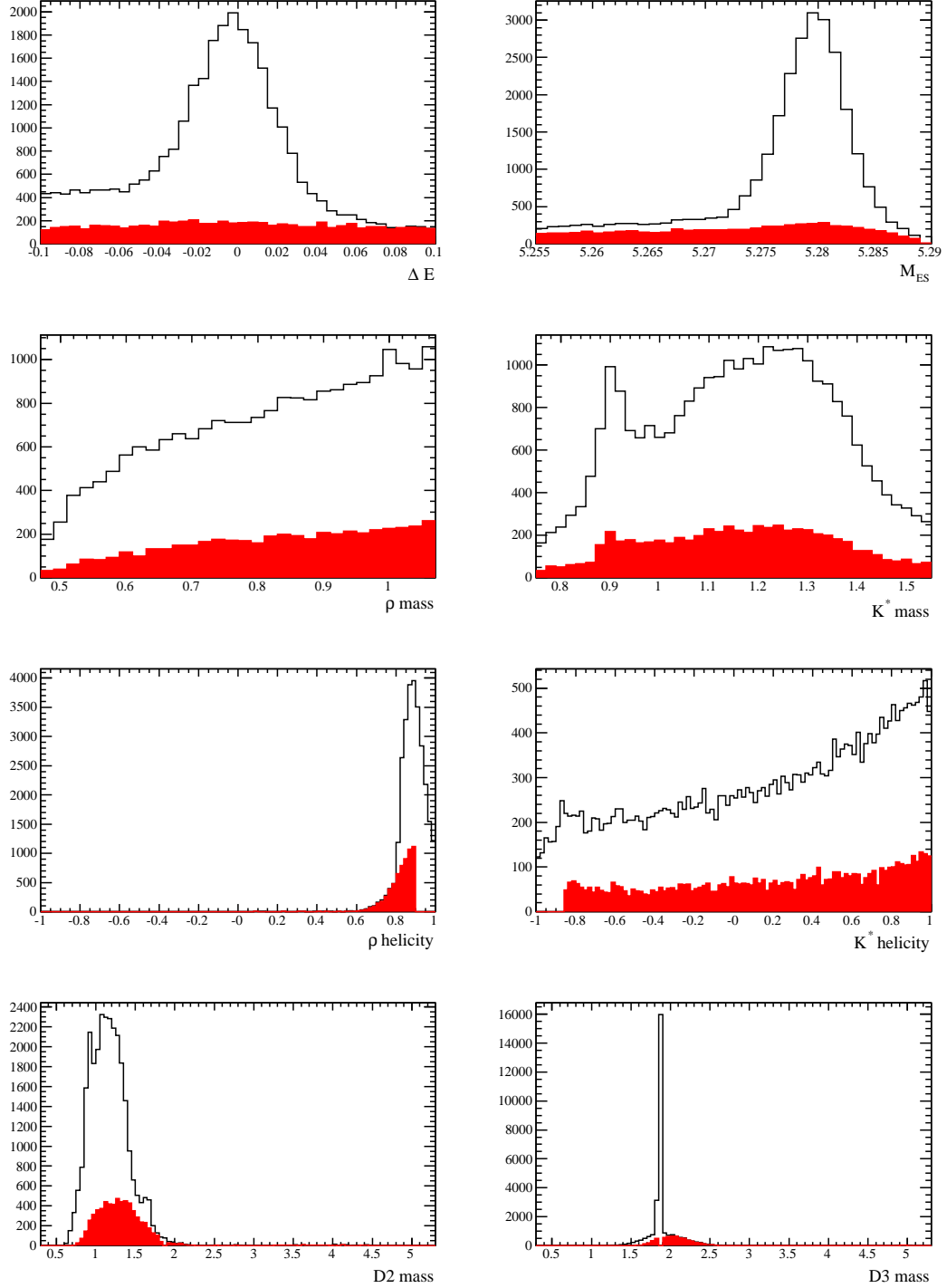
Figure 6.1: The red (solid) histograms show those $B^0 \to D^- \pi^+$, $D^- \to K^+ \pi^- \pi^-$, events surviving all $\rho^0 K^{*0}$ preselection cuts; black histograms do not include D vetoes or helicity cuts. From top to bottom, left to right: ΔE, m_{ES}, ρ mass, K^* mass, $\mathcal{H}_{\rho^0}$, $\mathcal{H}_{K^*}$, 2-body D^0 mass, 3-body D^+ mass. The MC efficiency for selecting this mode as a $\rho^0 K^{*0}$ candidate is 1.2% after all cuts.

Chapter 7

Maximum Likelihood Fit Definition and Validation

7.1   Maximum Likelihood Fit

We perform unbinned multivariate maximum likelihood (ML) analyses, using the `RooRarFit` fitting package [46]. The cuts on the quantities used as input to the ML fit are loose to allow for high efficiency and to provide sufficient sidebands to characterize the background well.

The probability density functions (PDFs) describe the shape of the discriminating variables (observables) for each category of signal and background, as defined in subsequent sections. Each PDF involves parameters that are determined by fitting various samples of data and Monte Carlo. These PDF parameters are fixed for the ML fit. The exceptions to this are the dominant $q\overline{q}$ background parameters, which are initially determined on on-peak sidebands far from the signal region. These parameters are allowed to float in the final ML fit, incorporating their uncertainties into the statistical uncertainty on the fit results.

78

7.1.1 Low mass region fit

In the low mass region, we obtain the yields, charge asymmetries $\mathcal{A}_{ch}$, and longitudinal polarization fractions f_L from extended maximum-likelihood fits to the seven observables: ΔE, m_{ES}, $\mathcal{F}$, the masses and helicities of the two resonance candidates $m_{\pi\pi}$, $m_{K\pi}$, and $\cos\theta_{\mathcal{H}_\rho}$, $\cos\theta_{\mathcal{H}_{K^*}}$. The fits distinguish among several categories: $q\bar{q}$ background, $B\overline{B}$ background (see Sec. 7.2), and signal; the categories are defined in Sec. 7.1.3. The signals $\rho^0 K^*(892)^0$ and $f_0 K^*(892)^0$ are fit simultaneously. For each event i and category j we define the probability density functions (PDFs) $\mathcal{P}_j$ as

$$\mathcal{P}_j^i = \mathcal{P}_j(m_{ES}{}^i)\mathcal{P}_j(\Delta E^i)\mathcal{P}_j(\mathcal{F}^i)\mathcal{P}_j(m_{\pi\pi}^i)\mathcal{P}_j(m_{K\pi}^i)\mathcal{P}_j(\cos\theta_{\mathcal{H}_\rho}^i)\mathcal{P}_j(\cos\theta_{\mathcal{H}_{K^*}}^i), \quad (7.1)$$

with the resulting likelihood $\mathcal{L}$:

$$\mathcal{L} = \frac{e^{-\sum_j Y_j}}{N!}\prod_{i=1}^{N}\sum_j Y_j \mathcal{P}_j^i, \quad (7.2)$$

where Y_j is the yield for category j and N is the number of events entering the fit. For the ρ^0/f_0 analyses, we use the absolute value of $\mathcal{H}_\rho$ in the fit, as the distribution is symmetric. We split the yields by the flavor of the decaying B meson in order to measure $\mathcal{A}_{ch}$. We find correlations among the observables to be occasionally as high as 30% in simulations of the $B\overline{B}$ backgrounds, whereas they are small in the data samples, which are dominated by $q\bar{q}$ background. In signal, correlations are typically less than 1% and occasionally as large as 14%. Correlations amongst observables are accounted for in the fit bias (see Sec. 7.4) and are tabulated for the $K^*(892)$ channels in App. A.

7.1.2 High mass region fit

In the high mass region, the ML fit uses only the observables: ΔE, m_{ES}, $\mathcal{F}$, $m_{\pi\pi}$, and $m_{K\pi}$. The charge asymmetry is not floated in these fits and, as no helicity information is included, we do not float f_L for the VT (vector–tensor) channels.

For $\rho^-(K\pi)_0^{*+}$, these five observables are combined in an extended ML fit, as above.

For the $\rho^0/f_0(K\pi)_0^{*0}$ and $f_0 K_2^*(1430)^0$ channels, we perform the fit in two steps. In the first step, we perform an ML fit using only ΔE, m_{ES}, $\mathcal{F}$, and $m_{K\pi}$. This first step allows us to extract "inclusive" $(K\pi)_0^{*0}$ and $K_2^*(1430)^0$ signals from the background $q\bar{q}$ and $B\bar{B}$ events, without any requirements on the $\pi^+\pi^-$ mass distribution. The PDF for the first step can be written as

$$\mathcal{P}_j^i = \mathcal{P}_j(m_{ES}{}^i)\mathcal{P}_j(\Delta E^i)\mathcal{P}_j(\mathcal{F}^i)\mathcal{P}_j(m_{K\pi}^i) \tag{7.3}$$

for event i and category j.

We apply the *sPlot* technique [47] to the results of this first fit, which allows us to calculate a weight value for each event in each category (signal, $B\bar{B}$ background, etc.) based upon the covariance matrix from the likelihood fit and the value of the PDF for that event. Specifically, the *sWeight* for event i of category n is given by

$$sWeight_n^i = \frac{\sum_{j=1}^{N_c} V_{nj}\mathcal{P}_j^i}{\sum_{k=1}^{N_c} Y_k\mathcal{P}_k^i} \tag{7.4}$$

where N_c is the number of categories in the fit, V_{nj} is the covariance matrix element for categories n and j, and Y_k is the yield of category k, as in Eq. (7.2).

One can think of the *sWeight* on a given event as indicating how much that event contributes to the total yield in that category; *sWeights* can be less than zero and even greater than one, but the sum of all *sWeights* for a given category reproduces the ML fit yield for that category.

The *sWeights* from this procedure are used to create two datasets: the *sWeighted* $(K\pi)_0^{*0}$ signal and the *sWeighted* $K_2^*(1430)^0$ signal sample. These weighted datasets allow us to accurately plot the $\pi^+\pi^-$ mass distribution for the two signal samples we are interested in; these *sPlots* are faithful representations of $m_{\pi\pi}$ for the $(K\pi)_0^{*0}$ and $K_2^*(1430)^0$ signal components, assuming no correlation between $m_{\pi\pi}$ and the observables used to generate the *sWeights*. As mentioned above, the correlations are generally small.

In the second step, we fit the *sWeighted* $(K\pi)_0^{*0}$ and $K_2^*(1430)^0$ $m_{\pi\pi}$ distributions to ρ^0 and f_0 hypotheses (a non-resonant $\pi^+\pi^-$ component was found to be unnecessary). This fit gives us the final signal yield for the $\rho^0(K\pi)_0^{*0}$, $f_0(K\pi)_0^{*0}$, and $f_0 K_2^*(1430)^0$ channels. This procedure also measures the $\rho^0 K_2^*(1430)^0$ yield, but as we do not include helicity information in the fit, we cannot measure f_L, and thus we consider that yield a background.

Due to the two-step nature of the $\rho^0/f_0(K\pi)_0^{*0}$ and $f_0 K_2^*(1430)^0$ fits, the statistical uncertainty has two components. The first is from the uncertainty on the $m_{\pi\pi}$ fit to extract the fraction of ρ^0/f_0 events in the *sWeighted* sample. The second is a fraction of the uncertainty on the "inclusive" $(K\pi)_0^{*0}$ or $K_2^*(1430)^0$ yield, the coefficient of which is given by the ratio of ρ^0 or f_0 events to the sum of the two.

7.1.3 ML Fit Categories

Both the LMR and HMR $\rho^0 K^{*0}$ analyses include the following fit components: $\rho^0 K^{*0}$, $f_0 K^{*0}$, seven $B\overline{B}$ backgrounds, and $q\overline{q}$ background. The yields of the B backgrounds are fixed in the final fit. The B backgrounds are described in Ch. 7.2.

For LMR $\rho^0 K^*(892)^0$, the $B\overline{B}$ background components are: $B^0 \to f_2(1270)K^*(892)^0$; $B^0 \to \rho^0(K\pi)_0^{*0}$; $B^0 \to f_0(K\pi)_0^{*0}$; $B^0 \to a_1^- K^+$ with $a_1^- \to \rho^0\pi^-$; a branching fraction-weighted combination of 13 other charmless B decay channels, which have a high probability of passing our selection; $B^0 \to D^-\pi^+$ with $D^- \to K^+\pi^-\pi^-$; and a combination of three $B \to \overline{D}^0 X$ channels with $\overline{D}^0 \to K^+\pi^-\pi^0$.

For the $(K\pi)_0^{*0}$ and $f_0 K_2^*(1430)^0$ signals, the background categories are the same, except that $K^*(892)^0$ events replace the $(K\pi)_0^{*0}$ background categories, and 28 B decay channels are included in the cocktail of charmless decays. As is described in Sec. 7.1.2, the first stage of this fit is insensitive to the exact nature of the $\pi^+\pi^-$ resonance; therefore $\rho^0 K^*(892)^0$, $f_0 K^*(892)^0$, and $f_2(1270)K^*(892)^0$ are included in the same $K^*(892)^0$ category.

The $\rho^- K^{*+}$ analyses includes the following fit components: $\rho^- K^{*+}$, four $B\overline{B}$ backgrounds, and $q\overline{q}$ background. For $\rho^- K^*(892)^+$, the four $B\overline{B}$ background categories are: $B^0 \rightarrow \rho^-(K\pi)_0^{*+}$, $B^0 \rightarrow a_1^- K^+$ with $a_1^- \rightarrow \rho^- \pi^0$, $B^0 \rightarrow \rho^+ \rho^-$, and $B^- \rightarrow \overline{D}^0 \rho^-$ with $\overline{D}^0 \rightarrow K^+ \pi^- \pi^0$. For $\rho^-(K\pi)_0^{*+}$, $\rho^- K^*(892)^+$ replaces the signal mode as a background, and the other categories remain the same.

In the HMR fits, the $K^*(892)$ yields are allowed to float. In the LMR, the $(K\pi)_0^*$ branching fractions are fixed to the values measured in the HMR. The $B^0 \rightarrow f_2(1270)K^*(892)^0$ background yield is determined using a high $m_{\pi^+ \pi^-}$ sideband, as described in Sec. D; this yield is fixed in the $\rho^0 K^*(892)^0$ fit. All other $B\overline{B}$ backgrounds are modeled from the simulation, with yields fixed to experimentally measured $\mathcal{B}$ values [2]. For a few channels entering the combination background of 13 charmless modes, no measurements exist; in those cases, theory predictions are combined with educated guesses and a 100% uncertainty is assigned to the branching fractions. Uncertainties on the $B\overline{B}$ branching fractions are accounted for in systematic uncertainties (see Sec. 9).

7.2 $B\overline{B}$ Backgrounds

The continuum $e^+ e^- \rightarrow q\overline{q}$ ($q = u, d, s, c$) background is the dominant background for the B-decay modes studied in this thesis. This background is mostly the result of random combinations of tracks and neutrals, and is very weakly peaked in all kinematic variables. This statement is also typically true for the smaller B to charm ($b \rightarrow c$) background, whose kinematic properties don't typically allow for significant peaking in any discriminating mass or energy variables. However, the wide mass ranges in this analysis allow for moderate contributions from charm background, and we are forced to include some B to charm backgrounds as separate components in the fit.

Although smaller, the background coming from other charmless B decays tends to peak in at least some of the discriminating variables. This background is generally composed of decay

modes with final states similar to that of the signal, typically with one additional (feed-down) or one fewer (feed-up) track or neutral in the final state, or with a mis-identified particle (ie. $B^0 \rightarrow \rho^+ \rho^-$ appearing as background to $B^0 \rightarrow \rho^- K^{*+}$ because the π^+ is mis-identified as a K^+). Due to the peaking nature of these backgrounds, careful consideration of their impact is necessary.

We have performed a variety of studies related to $B\overline{B}$ backgrounds using SP10 Monte Carlo. We have applied the full analysis selection to the generic $B^0 \overline{B}^0$ and $B^+ B^-$ MC, independently studying the $b \rightarrow c$ and charmless backgrounds. From these studies, we obtain a list of dominant background modes. We obtain exclusive MC samples ($\sim 200k - 1M$ events for charmless samples; up to $5M$ events for $b \rightarrow c$ backgrounds) for each of the significant $B\overline{B}$ background samples.

Modes with a large number of expected background events in the on-peak sample that also have distinctive, signal-like features (ie. $B^0 \rightarrow a_1^- K^+$ for $\rho^0 K^{*0}$) may be taken as separate background components. The remaining charmless backgrounds may be combined in a cocktail in appropriate proportions. Analogously, cocktails of $b \rightarrow c$ backgrounds with similar characteristics (ie. the D^0 cocktail in $\rho^0 K^{*0}$) may be formed.

The details of which background components are included and, in the case of cocktails, exactly what goes into each component, are given below for the individual modes. The tables in this section use a common labeling scheme. We show selection efficiency ("MC ϵ"), the measured or estimated branching fraction ("Est. $\mathcal{B}$"), appropriate product branching fraction for the resonance daughters ("$\prod \mathcal{B}_i$"), estimated background normalized to 471 million $B\overline{B}$ events ("#$B\overline{B}$ Bkg"), and the number of events included in the file we use to make PDFs ("# in file"). A * after the $\mathcal{B}$ indicates that it is estimated since no measurement exists.

The uncertainty in the number of events expected, in the case of the cocktail channels, is determined by adding in quadrature the uncertainty in the number of events in each mode within the cocktail (based on BF and MC ϵ uncertainty).

In the LMR, all $B\overline{B}$ yields are fixed in the final ML fit. In the HMR, the $K^*(892)$ yields are allowed to float. The HMR $B\overline{B}$ backgrounds are similar to the LMR, and the details are therefore relegated to the appendices, App. **B** and **C**.

7.2.1 $B\overline{B}$ **Background in** $\rho^0 K^*(892)^0$

Seven categories of $B\overline{B}$ background are included in the $\rho^0 K^*(892)^0$ analysis.

1. $B^0 \rightarrow \rho^0 (K\pi)_0^{*0}$

2. $B^0 \rightarrow f_0 (K\pi)_0^{*0}$

3. $B^0 \rightarrow f_2(1270) K^*(892)^0$

4. $B^0 \rightarrow a_1^- K^+$ with $a_1^- \rightarrow \rho^0 \pi^-$

5. $B^0 \rightarrow D^- \pi^+$ with $D^- \rightarrow K^+ \pi^- \pi^-$

6. D^0 cocktail with $D^0 \rightarrow K^- \pi^+ \pi^0$

7. Charmless cocktail

$\rho^0 (K\pi)_0^{*0}$ **and** $f_0 (K\pi)_0^{*0}$ **Background to** $\rho^0 K^*(892)^0$

The $(K\pi)_0^{*0}$ and non-resonant S-wave $K^+\pi^-$ are described by a LASS parameterization, and the amount of $\rho^0 (K\pi)_0^{*0}$ and $f_0 (K\pi)_0^{*0}$ in the nominal fit region is determined by a study of the high $K^+\pi^-$ mass region (HMR). The study is described in App. **B**. From this study, we expect the following event yields for run 1-6 in the nominal fit region:

$$N_{\rho^0 (K\pi)_0^{*0}} = 215 \pm 34 \,,$$

$$N_{f_0 (K\pi)_0^{*0}} = 19 \pm 6 \,.$$

$f_2(1270)K^*(892)^0$ **Background to** $\rho^0 K^*(892)^0$

The $f_2(1270)$ contributes significantly at high $\pi^+\pi^-$ mass. We determine the expected number of $f_2(1270)K^{*0}$ events by fitting a wider $\pi^+\pi^-$ mass range, and extrapolating down into the nominal fit region. The study is described in App. **D**. From this study, we expect the following event yield for run 1-6 in the nominal fit region:

$$N_{f_2(1270)K^{*0}} \;\; = \;\; 47 \pm 3 \,.$$

$a_1^-(\rho^0\pi^-)K^+$ **Background to** $\rho^0 K^*(892)^0$

This background is included as a separate component because its final state is identical to the signal final state (ie. it is "signal" in a Dalitz plot sense). Further details are given in Tab. 7.1. We expect the following number of events in the run 1-6 dataset:

$$N_{a_1^- K^+} = 15 \pm 3 \,.$$

Table 7.1: $a_1^-(\rho^0\pi^-)K^+$ background for $\rho^0 K^*(892)^0$.

Signal mode: $\rho^0 K^*(892)^0$ Bkg. channel	Mode #	MC ϵ (%)	Est. $\mathcal{B}$ (10^{-6})	$\prod \mathcal{B}_i$	#$B\overline{B}$ Bkg
$B^0 \to a_1^-(\rho^0\pi^-)K^+$	4871	0.38	16.3 ± 3.7	0.500	15

$D^-\pi^+$ **Background to** $\rho^0 K^*(892)^0$

$B^0 \to D^-\pi^+$ with $D^- \to K^+\pi^-\pi^-$ is included as a separate component because its final state is identical to the signal final state (ie. it is "signal" in a Dalitz plot sense). Despite the D vetoes, this background has a 0.18% MC efficiency and some peaking structure in m_{ES} and ΔE. Further details are given in Tab. 7.2. We expect the following number of events in the run 1-6

dataset:

$$N_{D^-\pi^+} = 209 \pm 10 \ .$$

Table 7.2: $B^0 \to D^-\pi^+$ with $D^- \to K^+\pi^-\pi^-$ background for $\rho^0 K^*(892)^0$.

Signal mode: $\rho^0 K^*(892)^0$ Bkg. channel	Mode #	MC ϵ (%)	Est. $\mathcal{B}$ (10^{-4})	$\prod \mathcal{B}_i$	#$B\overline{B}$ Bkg
$B^0 \to D^-\pi^+$ $(D^- \to K^+\pi^-\pi^-)$	2437	0.18	26.8 ± 1.3	0.093	209

Of the six dominant $b \to c$ backgrounds, $B^0 \to D^-\rho^+$ $(D^- \to K^+\pi^-\pi^-)$ is topologically quite similar to $B^0 \to D^-\pi^+$ $(D^- \to K^+\pi^-\pi^-)$. This channel has $\mathcal{B} = (76 \pm 13) \times 10^{-4}$ and $\prod \mathcal{B}_i = 0.093$. We perform embedded toy studies (see Ch. 7.4 for the general procedure) in which we embed the expected number of $D^-\rho^+$ background events and either increase the $D^-\pi^+$ yield proportionally, or keep it fixed at the expected number of events. In both of these studies, the biases on the signal yields are consistent with the nominal biases reported in Sec. 7.4. Due to low MC statistics in $D^-\rho^+$, we do not explicitly include $B^0 \to D^-\rho^+$ $(D^- \to K^+\pi^-\pi^-)$ events in the background models, but are confident they will not affect the signal biases.

D^0 **Cocktail Background to** $\rho^0 K^*(892)^0$

Of the five remaining dominant $b \to c$ backgrounds, three contain a D^0 meson with $D^0 \to K^-\pi^+\pi^0$, and are combined in a "D^0 cocktail", as shown in Tab 7.3. Due to rounding of values in the MC ntuples, applying the preselection requirements upon input to RooRarFit results in a lower number of events passing preselection than is listed in Tab 7.3; this scaling is taken account of in our expected number of events in the run 1-6 dataset, which is,

$$N_{D^0 \text{ Cocktail}} = 433 \pm 23 \ .$$

Table 7.3: D^0 cocktail background for $\rho^0 K^*(892)^0$.

Signal mode: $\rho^0 K^*(892)^0$ Bkg. channel	Mode #	MC ϵ (%)	Est. $\mathcal{B}$ (10^{-6})	$\prod \mathcal{B}_i$	#$B\overline{B}$ Bkg	# in file
$B^+ \to \overline{D}^0_{K^+\pi^-\pi^0}\pi^+$	2422	0.1	4750 ± 190	0.140	322.2	1568
$B^+ \to \overline{D}^0_{K^+\pi^-\pi^0}\rho^+$	2441	0.01	13400 ± 1800	0.140	123.2	599
$B^+ \to \overline{D}^{*0}\pi^+$	2423	0.04	5190 ± 260	0.087	79.8	388
$(\overline{D}^{*0} \to \overline{D}^0\pi^0, \overline{D}^0 \to K^+\pi^-\pi^0)$						
Total					525.2	2555

Of the six dominant $b \to c$ backgrounds, $B^0 \to D^{*-}\pi^+(D^{*-} \to \overline{D}^0\pi^-, \overline{D}^0 \to K^+\pi^-\pi^0)$ is topologically quite similar to the channels in the D^0 cocktail. This channel has: $\mathcal{B} = (27.6 \pm 1.3) \times 10^{-4}$, $\prod \mathcal{B}_i = 0.095$, and MC $\epsilon = 0.03\%$, leading to an expected number of events in the on-peak sample of $N_{D^{*-}\pi^+} = 38$. We perform embedded toy studies (see Ch. 7.4 for the general procedure) in which we embed the expected number of $D^{*-}\pi^+$ background events and either increase the D^0 cocktail yield proportionally, or keep it fixed at the expected number of events. In both studies, the biases on the signal yields are consistent with the nominal biases reported in Sec. 7.4. Due to low MC statistics in $D^{*-}\pi^+$, we do not explicitly include $B^0 \to D^{*-}\pi^+$ events in the background models, but are confident they will not affect the signal biases.

Charmless Cocktail Background to $\rho^0 K^*(892)^0$

The remaining dominant charmless $B\overline{B}$ background modes are combined into a cocktail, as shown in Tab 7.4. Due to rounding of values in the MC ntuples, applying the preselection requirements upon input to RooRarFit results in a lower number of events passing preselection than is listed in Tab 7.4; this scaling is taken account of in our expected number of events in the run 1-6 dataset, which is,

$$N_{\text{Chmls Cocktail}} = 76 \pm 22 \ .$$

Table 7.4: Charmless $B\overline{B}$ backgrounds for $\rho^0 K^{*0}$.

Signal mode: $\rho^0 K^{*0}$ Bkg. channel	Mode #	MC ϵ (%)	Est. $\mathcal{B}$ (10^{-6})	$\prod \mathcal{B}_i$	#$B\overline{B}$ Bkg	# in file
$B^+ \to a_1^0 K^+$	4874	0.2	20^*	1.000	19	812
$B^+ \to \eta'_{\rho\gamma} K^+$	6748	0.15	$71.1^{+2.6}_{-2.6}$	0.293	15.2	650
$B^+ \to K^+\pi^-\pi^+$ (Dalitz)	6846	0.03	$51.0^{+2.9}_{-2.9}$	1.000	8	342
$B^+ \to \rho^+ K^{*0}_{K^+\pi^-}(L, f_L = 0.48)$	2244	0.58	$4.4^{+1.0}_{-1.0}$	0.666	8	340
$B^0 \to K^{*0}_{K^+\pi^-}\mu^+\mu^-$	4777	2.18	$1.05^{+1.5}_{-1.3}$	0.666	7.2	307
$B^0 \to \overline{K}^{*0}_{K\pi}K^{*0}_{K\pi}(L, fL = 0.8)$	2398	2.39	$1.28^{+0.33}_{-0.31}$	0.444	6.4	273
$B^0 \to a_1^0 K^{*0}(L, f_L = 0.7)$	5329	0.18	7^*	0.667	4	171
$B^+ \to \rho^+ K^{*0}_{K^+\pi^-}(T, f_L = 0.48)$	2243	0.25	$4.8^{+1.1}_{-1.1}$	0.666	3.8	162
$B^+ \to f_0 K^{*+}_{K^+\pi^0}$	3357	0.51	$5.2^{+1.3}_{-1.3}$	0.222	2.8	118
$B^0 \to \overline{K}^{*0}_{K\pi}K^{*0}_{K\pi}(T, fL = 0.8)$	2399	4.97	$0.26^{+0.08}_{-0.08}$	0.444	2.7	115
$B^+ \to \rho^+\rho^0(L, f_L = 0.95)$	2390	0.02	$22.8^{+1.8}_{-1.9}$	1.000	2.4	103
$B^+ \to \rho^0 K^{*+}_{K^+\pi^0}(L, f_L = 0.78)$	2355	0.4	$3.6^{+1.0}_{-1.0}$	0.333	2.3	97
$B^0 \to a_1^-(\rho^0\pi^-)\pi^+$	2011	0.03	$31.7^{+3.7}_{-3.7}$	0.500	2	84
$B^0 \to \rho^0\rho^0(L, f_L = 0.75)$	2396	0.49	$0.55^{+0.22}_{-0.24}$	1.000	1.3	54
$B^+ \to a_1^0\pi^+$	4156	0.01	$20.4^{+5.8}_{-5.8}$	1.000	1.2	51
$B^0 \to \rho^0\rho^0(T, f_L = 0.75)$	2397	0.83	$0.18^{+0.07}_{-0.08}$	1.000	0.7	30
$B^+ \to \rho^0 K^{*+}_{K^+\pi^0}(T, f_L = 0.78)$	2356	0.3	$1.0^{+0.3}_{-0.3}$	0.333	0.5	20
Total					87.5	3729

7.2.2 $B\overline{B}$ Background in $\rho^- K^*(892)^+$

Four categories of $B\overline{B}$ background are included in the $\rho^- K^*(892)^+$ analysis.

1. $B^0 \to \rho^-(K\pi)_0^{*+}$

2. $B^0 \to a_1^- K^+$ with $a_1^- \to \rho^-\pi^0$

3. $B^0 \to \rho^+\rho^-$

4. $B^- \to \overline{D}^0(K^+\pi^-\pi^0)\rho^-$

$\rho^-(K\pi)_0^{*+}$ **Background to** $\rho^- K^*(892)^+$

The amount of $\rho^-(K\pi)_0^{*+}$ background in the nominal fit region is determined by a study of the high $K^+\pi^0$ mass region (HMR). More details are included in App. C. We expect the follow-

ing event yields in the nominal fit region:

$$N_{\rho^-(K\pi)_0^{*+}} = 60 \pm 23 .$$ (7.5)

$a_1^-(\rho^-\pi^0)K^+$ **Background to** $\rho^- K^*(892)^+$

This background is included as a separate component because its final state is identical to

the signal final state (ie. it is "signal" in a Dalitz plot sense). Further details are given in Tab. 7.5.

In run 1-6 data, we expect:

$$N_{B^0 \to a_1^- K^+} = 7 \pm 2 .$$

Table 7.5: $B^0 \to a_1^-(\rho^-\pi^0)K^+$ Background to $\rho^- K^*(892)^+$

Signal mode: $\rho^- K^*(892)^+$ Bkg. channel	Mode #	MC ϵ (%)	Est. $\mathcal{B}$ (10^{-4})	$\prod \mathcal{B}_i$	#$B\overline{B}$ Bkg
$B^0 \to a_1^-(\rho^-\pi^0)K^+$	4960	0.19	16.3 ± 3.7	0.5	7

$\rho^+\rho^-$ **Background to** $\rho^- K^*(892)^+$

The decay $B^0 \to \rho^+\rho^-$ is included as a separate component because it is essentially a

signal final state, except for mis-identifying a charged pion as a kaon. This results in a shifted mean

for ΔE, but very signal-like m_{ES} and ρ mass distributions. Further details are given in Tab. 7.6. In

run 1-6 data, we expect:

$$N_{\rho^+\rho^-} = 9 \pm 1 .$$

Table 7.6: $B^0 \to \rho^+\rho^-$ Background to $\rho^-K^*(892)^+$

Signal mode: $\rho^-K^*(892)^+$ Bkg. channel	Mode #	MC ϵ (%)	Est. $\mathcal{B}$ (10^{-4})	$\prod \mathcal{B}_i$	#$B\overline{B}$ Bkg
$B^0 \to \rho^+\rho^-(L, f_L = 0.978)$	2498	0.08	23.7 ± 3.1	1.0	9

$D^0\rho^-$ **Background to** $\rho^-K^*(892)^+$

The dominant $b \to c$ background for $\rho^-K^*(892)^+$ is $B^- \to D^0(K^+\pi^-\pi^0)\rho^-$. Efficiencies, etc. are given in Tab. 7.7. In run 1-6 data, we expect:

$$N_{D^0\,(K^+\,\pi^-\,\pi^0)\rho^-} = 129 \pm 17 .$$

Table 7.7: $B^- \to D^0(K^+\pi^-\pi^0)\rho^-$ background to $\rho^-K^*(892)^+$.

Signal mode: $\rho^-K^*(892)^+$ Bkg. channel	Mode #	MC ϵ (%)	Est. $\mathcal{B}$ (10^{-4})	$\prod \mathcal{B}_i$	#$B\overline{B}$ Bkg
$B^- \to D^0(K^+\pi^-\pi^0)\rho^-$	2441	0.015	134 ± 18	0.139	129

Of the remaining dominant charm background modes, mode 2191 ($B \to \overline{D}^0_{K^+\pi^-\pi^0}\pi^0$) is the next most important, with an expected 15 events in the run 1-6 data sample. Given this background is not especially signal-like, we do not expect a bias from neglecting this (or other, less important) $b \to c$ backgrounds.

Other Charmless Backgrounds to $\rho^-K^*(892)^+$

To ensure that we are not biasing the fit yield by neglecting charmless background modes, we create a cocktail of the remaining dominant modes (see Tab. 7.8) and generate 500 pure toy experiments (see Ch. 7.4 for details on this procedure) with all of the above fit components included. We then run an additional 500 pure toy experiments that are identical, except we also embed 26

events from the charmless cocktail. The difference in mean bias between these two studies is consistent with zero. We therefore conclude that $\rho^- K^*(892)^+$ does not require an additional charmless cocktail background component.

Table 7.8: Other charmless backgrounds to $\rho^- K^*(892)^+$.

Signal mode: $\rho^- K^*(892)^+$ Bkg. channel	Mode #	MC ϵ (%)	Est. $\mathcal{B}$ (10^{-4})	$\prod \mathcal{B}_i$	$\#B\overline{B}$ Bkg	# in file
$B^+ \to a_1^0 K^+$	4874	0.08	20*	1.000	7.7	350
$B^0 \to a_1^-(\rho^-\pi^0)K^{*+}_{K^+\pi^0}(L, f_L = 1)$	5323	0.47	20*	0.167	7.4	334
$B^+ \to \pi^0\pi^0 K^{*+}(892)_{K^+\pi^0}$ (N.R.)	10566	0.11	15*	0.667	5.1	230
$B^+ \to a_1^0 K^{*+}_{K^+\pi^0}(L, f_L = 1)$	5327	0.24	10*	0.333	3.7	168
$B^+ \to \rho^+\pi^- K^+$	2488	0.02	10*	1.000	1.2	53
$B^+ \to \rho^0 K^{*+}_{K^+\pi^0}(L, f_L = 0.78)$	2355	0.18	$3.6^{+1.0}_{-1.0}$	0.333	1	44
Total					26.1	1179

7.3 Probability Density Functions

For each component of the maximum likelihood fit (signals, $q\overline{q}$ background, $B\overline{B}$ backgrounds), a probability density function (PDF) must be determined. The PDFs are determined with fits to the distributions for each of the observables (m_{ES}, ΔE, $\mathcal{F}$, etc.) in well-identified samples of signal and background. The samples used to determine the PDF shapes are: Signal MC, data in sidebands chosen to avoid potential signal events, and exclusive MC from the $B\overline{B}$ background modes listed in Ch. 7.2.

Different samples are used for different PDFs, depending on the circumstances. For continuum background, we determine PDF shapes from sidebands of the on-resonance data. For all variables except m_{ES}, we used the sideband: $m_{ES} < 5.27\,\text{GeV}$. For fitting m_{ES}, we use data satisfying $|\Delta E| > 0.07\,\text{GeV}$ for $\rho^0 K^{*0}$ and $\Delta E < -0.12$ and $\Delta E > 0.08\,\text{GeV}$ for $\rho^- K^{*+}$.

PDFs appear in App. A.1 for $\rho^0 K^*(892)^0$, App. A.2 for $\rho^- K^*(892)^+$, App. B for $(K\pi)^{*0}_0$

Table 7.9: PDF parameterizations for $\rho^0 K^{*0}$. For the helicities, only the resolution function is listed (see Sec. 7.3.2). DG=Double Gaussian, G=Gaussian, BifG=Bifurcated Gaussian, CB=Crystal Ball, Exp=Exponential, PN=Polynomial of order N (Chebychev polynomials except in the case of the helicities), and dip=Gaussian with negative amplitude (see Sec. 7.3.2). A + indicates the PDF is a sum of the listed components, $\times$ indicates a product. For resonant masses, the PDF is often fit on one MC sample and used in several backgrounds; sometimes a polynomial is added to account for larger tails in the mass distribution. These are indicated by giving the name of the MC sample used to determine the PDF.

Decay	m_{ES}	ΔE	$\mathcal{F}$	$m(K^+\pi^-)$	$\mathcal{H}(K^+\pi^-)$	$m(\pi^+\pi^-)$	$\mathcal{H}(\pi^+\pi^-)$
$\rho^0 K^*(892)^0$	CB	DG	BifG	DG	P3	DG	P3$\times$dip
$f_0 K^*(892)^0$	CB	DG	BifG	DG	P1	DG	P2$\times$dip
$q\bar{q}$ continuum	ARGUS	P1	BifG+G	$\rho^0 K^{*0}$+P2	P3	$\rho^0 K^{*0} + f_0 K^{*0}$+P2	P2
$\rho^0(K\pi)_0^{*0}$	CB	DG	BifG	P1	P2	DG	P1
$f_0(K\pi)_0^{*0}$	CB	DG	BifG	P1	P2	DG	P1$\times$dip
$f_2(1270)K^*$	G+ARGUS	G+P1	BifG	DG	P2	G+P2	P4
$a_1^- K^+$	G+ARGUS	G+P1	BifG	P4	Exp+P2	$\rho^0 K^{*0}$+P3	P2
$D^- \pi^+$	G+ARGUS	G+P1	BifG	G+P1	P4	P2	G
D^0 Bkg	ARGUS	P1	BifG	G+P1	P6	P2	G
Chmls Bkg	G+ARGUS	P1	BifG	$\rho^0 K^{*0}$+P2	Exp+P2	G+$f_0 K^{*0}$+P2	P4

Table 7.10: PDF parameterizations for $\rho^- K^{*+}_{K^+\pi^0}$. Abbreviations are equivalent to Tab. 7.9.

Decay	m_{ES}	ΔE	$\mathcal{F}$	$m(K^+\pi^0)$	$\mathcal{H}(K^+\pi^0)$	$m(\pi^+\pi^0)$	$\mathcal{H}(\pi^+\pi^0)$
$\rho^- K^*(892)^+$	CB	DG	BifG	DG	P5	DG	P3$\times$dip
$q\bar{q}$ continuum	ARGUS	P1	BifG+G	$\rho^- K^{*+}$+P2	P4	$\rho^- K^{*+}$+P1	P2
$\rho^-(K\pi)_0^{*+}$	CB	DG	BifG	P1	P4	DG	P1
$a_1^- K^+$	G+ARGUS	P4	BifG	P1	Exp	G+P1	P2
$\rho^- \rho^+$	G+ARGUS	P4	BifG	G+P1	P3	$\rho^- K^{*+}$	P2
$D^0 \rho^-$	ARGUS	P2	BifG	P1	P5	P2	P6

and $f_0 K_2^*(1430)^0$, and App. C for $\rho^-(K\pi)_0^{*+}$. Tab. 7.9 lists the PDF shapes used for $\rho^0 K^*(892)^0$, Tab. 7.10 lists those for $\rho^- K^*(892)^+$. Similar parameterizations are used in the HMR fits. In all cases, the best candidate is chosen before the PDFs are determined.

In the analyses described in this thesis, we determine all PDF shapes from the samples described above. We then run the ML fit using these PDF shapes. In our final fits to on-peak data,

as well as in our validation studies (see Sec. 7.4), we allow the primary background parameters to float, as described in Sec. 7.3.4.

7.3.1 Data–Monte Carlo differences

To account for possible differences between data and MC, we perform studies on control samples with the same final state as signal (see App. E). These studies demonstrate that the MC is a reasonable representation of the data, but that the MC must be shifted and/or scaled to agree with data. The exact amount depends on the number of neutrals in the signal mode, and is given in Tab. 7.11.

Recent results [48, 49, 50] show that the values used in the standard *BABAR* Monte Carlo for the $K^*(892)$ mass and width parameters differ by several standard deviations from the most recent and precise determinations. We compute the corrections for $K^*(892)^0$ from [48]; for $K^*(892)^+$, we use a weighted average of the results in [49, 50]. The correction factors are listed in Tab. 7.11. The $K^*(892)$ mass corrections are only applied in the LMR, as the $K\pi$ mass cuts in the HMR admit only the tail from the $K^*(892)$.

Table 7.11: Shifts and scale factors applied to signal PDF parameters in order to correct for differences between data and Monte Carlo.

Parameter	$\rho^0 K^{*0}$ & $f_0 K^{*0}$	$\rho^- K^{*+}$
ΔE shift (MeV)	-2.62 ± 0.13	14 ± 3
ΔE scale factor	0.968 ± 0.006	0.89 ± 0.06
m_{ES} shift (MeV)	-0.133 ± 0.016	-0.38 ± 0.13
m_{ES} scale factor	0.970 ± 0.005	0.84 ± 0.04
$m_{K^*(892)}$ scale factor	0.947 ± 0.029	0.916 ± 0.012
$m_{K^*(892)}$ shift (MeV)	-0.7 ± 0.5	3.00 ± 0.24

7.3.2   Resonance helicity

In the case of vector–vector (VV) decays of the B, the angular distribution of the final state is *a priori* unknown. It is a combination of *S*-, *P*-, and *D*- wave contributions. For decays $B \rightarrow V_1 V_2$, with V_1 and V_2 decaying into pseudoscalar mesons, the angular distribution in the helicity frame is

$$\frac{1}{\Gamma}\frac{d^2\Gamma}{d\cos\theta_1 d\cos\theta_2} = \frac{9}{4}\left\{\frac{1}{4}(1-f_L)\sin^2\theta_1\sin^2\theta_2 + f_L\cos^2\theta_1\cos^2\theta_2\right\}, \qquad (7.6)$$

where f_L is the fraction of the longitudinal-spin component. The different angular distributions (transverse vs. longitudinally polarized) lead to different detector acceptances for these two components, so the f_L-dependence can substantially affect the measured branching fractions.

We take these detector acceptance effects into account for the final signal PDF, so the total signal PDF can be written in `RooFit` (the normalization for each component is omitted) as

$$\mathcal{P}^{\text{hel}}_{\text{sig}}(\theta_1, \theta_2, f_L) = \left[(1-F_L)\sin^2\theta_1\sin^2\theta_2 + F_L\cos^2\theta_1\cos^2\theta_2\right] \times \mathcal{G}_1(\theta_1)\mathcal{G}_2(\theta_2), \quad (7.7)$$

where $\mathcal{G}_1(\theta_1)$ and $\mathcal{G}_2(\theta_2)$ are parameterizations of the detector acceptance effects for the two helicity angles. The quantity F_L is given by

$$F_L = \frac{f_L}{(1-f_L)R_\epsilon + f_L}, \qquad (7.8)$$

with R_ϵ (typically $\sim$2) the ratio of transverse to longitudinal efficiency.

For the K^* and ρ, θ_H is defined as the angle between the direction of one of the K^*/ρ daughters and that of the K^*/ρ in the K^*/ρ parent rest frame. The daughter used is positively-charged (or the only charged) for the ρ case or the pion for the K^* case.

For continuum background, we expect $\mathcal{H} \equiv |\cos\theta_H|$ to have a nearly flat distribution, as the daughter particles are randomly combined to form resonance candidates. The $B\overline{B}$ background $\cos\theta_H$ distribution varies according to the contributing modes.

7.3.3 Input observable correlations

Note that the likelihood for one event defined by Eq. (7.2) is a sum of several components—signal, continuum background, and $B\overline{B}$ backgrounds. Each term is a product of distributions measured with MC or sideband data for each of the event observables described above. This procedure assumes that within each component there are no correlations among these observables. We measure the correlation coefficients, given in App. A, and find that few of them are as large as 10%.

Correlations among signal observables can lead to small biases in the signal yield and are accounted for by determining a fit bias in our validation studies (see Sec. 7.4).

7.3.4 Floating background parameters

We choose to float the most important background PDF parameters in the fit. These include the ΔE slope, the background Fisher mean and sigmas, the ARGUS exponent, the dominant polynomial coefficients of the resonance mass distributions and helicities, and the fraction of real ρ, f_0, and K^* resonances in the background. We do not float parameters to which our signal yields are insensitive (such as tail components of Fisher). By doing this we include uncertainties in the values of these parameters in the statistical error from the fit in most cases, and improve the determination of their values by making use of the larger statistics available in the full on-resonance sample. We have tested with toy MC that our fitter can handle the number of degrees of freedom we use in our final fits.

The detailed lists of which $q\overline{q}$ background PDF parameters float for the $K^*(892)$ signals are given in App. A. For the HMR, the details are in App. B and C.

7.4   Validation of Fits

Before unblinding the dataset, we perform extensive validation studies. Some of these studies for the $K^*(892)$ signals are documented in this chapter. Additional studies were performed in order to establish what $B\overline{B}$ backgrounds to include, to inform the decision to separately fit the LMR and HMR, to determine how many continuum background PDF parameters could be floated in the final fit, etc. As the studies presented in this chapter are performed before unblinding the datasets, the number of signal and $(K\pi)_0^*$ events does not match that which is found in the final fit. Additional toy studies are performed after unblinding; those use the same procedure as described here and are documented in Ch. 8.1. The results of embedded toy studies for the $(K\pi)_0^{*0}$ and $f_0 K_2^*(1430)^0$ channels are given in App. B. Those for $\rho^-(K\pi)_0^{*+}$ are given in App. C.

We generate toy MC samples matching the size of the on-resonance datasets in order to validate fit convergence, determine fit bias, and confirm that we are not neglecting $B\overline{B}$ backgrounds which could bias the signal. In all cases, the continuum background is generated from the PDF distributions. Typically, we embed events from the full MC simulation for signals and $B\overline{B}$ backgrounds, as this allows us to test the effect of correlations amongst the observables (the fit bias results come from such studies). Low MC statistics in the $b \to c$ backgrounds ($\sim 5\times$ the number of events expected in data) limits the number of toy MC experiments we can produce; thus our embedded toy results have only 100 experiments. In cases where we are studying the effect of another background (with high MC statistics) we generate signal and $B\overline{B}$ backgrounds from the PDFs in order not to badly oversample those datasets.

Note: the studies in this section were performed using an incorrect PDF for the $\mathcal{H}_\rho$ distribution in $\rho(K\pi)_0^*$ MC. This is shown to have little effect on embedded toy biases. The final toy studies based on run 1-6 results (Sec. 8.1) incorporate the correct PDF.

Table 7.12: Results of embedded toy studies for $\rho^0 K^*(892)^0$. We report the number of events embedded from MC ("Input"), the fit result, the bias on that yield, and the mean statistical error on the yield. In both studies, 100/100 fits converge. For the study embedding no signal (bottom), we fix $f_L = 0.5$ and signal $\mathcal{A}_{ch}$ to the $\mathcal{A}_{ch}$ of the dataset.

Mode	Input	Fit	Bias	Stat. err.
$\rho^0 K^*(892)^0$	333	367 ± 3	34 ± 3	37
$f_0 K^*(892)^0$	149	153 ± 2	4 ± 2	21
$f_L\ (\rho^0 K^*(892)^0)$	0.5	0.449 ± 0.006	-0.051 ± 0.006	0.069
$\mathcal{A}_{ch}\ (\rho^0 K^*(892)^0)$	-0.039	-0.032 ± 0.012	0.007 ± 0.012	0.05
$\mathcal{A}_{ch}\ (f_0 K^*(892)^0)$	-0.039	-0.052 ± 0.016	0.013 ± 0.016	0.07
$\mathcal{A}_{ch}$ (Bkg)	-0.03911	-0.03915 ± 0.0003	-0.00004 ± 0.00030	0.004
$\rho^0 K^*(892)^0$	0	18 ± 3	18 ± 3	25
$f_0 K^*(892)^0$	0	-1 ± 2	-1 ± 2	11
$f_L\ (\rho^0 K^*(892)^0)$	0.5	0.5	—	—
$\mathcal{A}_{ch}$ (Bkg)	-0.03911	-0.03889 ± 0.0003	0.0002 ± 0.0003	0.004

7.4.1 Validation studies in $\rho^0 K^*(892)^0$

In the $\rho^0 K^*(892)^0$ and $f_0 K^*(892)^0$ validation studies, we embed/generate the expected number of $B\overline{B}$ backgrounds and fix their yields in the fits. These backgrounds are: 204 $\rho^0 (K\pi)_0^{*0}$, 25 $f_0 (K\pi)_0^{*0}$, 15 $a_1^- K^+$, 49 $f_2(1270)K^{*0}$, 209 $D^- \pi^+$, 433 D^0 cocktail, and 76 charmless cocktail events. Each experiment includes 18792 events, where the remaining events are generated from the $q\overline{q}$ background PDFs. We float the nominal 17 $q\overline{q}$ PDF parameters, as discussed in Sec. 7.3.4 and listed in App. A.1.

The results of 100 embedded toy experiments are given in Tab. 7.12; 100/100 of the fits converged. We give the results for two scenarios. In the first, we embed the expected number of signal events based on the published run 1-4 analysis [28] and allow signal $\mathcal{A}_{ch}$ and f_L parameters to float. In the second scenario, we embed no signal and fix $\mathcal{A}_{ch}$ for both $\rho^0 K^*(892)^0$ and $f_0 K^*(892)^0$ to the value in the on-peak data sample ($\mathcal{A}_{ch} = -0.039$) and $f_L = 0.5$.

From Tab. 7.12, it seems that about half of the bias on the $\rho^0 K^*(892)^0$ signal yield comes

from imperfect modeling of the $B\overline{B}$ backgrounds, or correlations amongst the observables in those $B\overline{B}$ backgrounds. The bias on $f_0 K^*(892)^0$ from $B\overline{B}$ backgrounds is consistent with zero.

We also run 500 pure toy experiments (all events generated from PDFs), generating the same number of events as for the top section of Tab. 7.12. The pulls from all floated variables are listed in Tab. 7.13. 100% of these fits converge floating 17 continuum background PDF parameters, demonstrating the fitter's ability to handle these degrees of freedom. The toy pull means (sigmas) are all consistent with zero (one). The abbreviations for the floating background parameters are described in App. A.

7.4.2 Validation studies in $\rho^- K^*(892)^+$

In the $\rho^- K^*(892)^+$ validation studies, we embed/generate the expected number of $B\overline{B}$ backgrounds and fix their yields in the fits. These backgrounds are: 42 $\rho^-(K\pi)_0^{*+}$, 7 $a_1^- K^+$, 9 $\rho^+ \rho^-$, and 129 $D^0 \rho^-$ events. Each experiment includes 9705 events, where the remaining events are generated from the $q\overline{q}$ background PDFs. We float the nominal 13 $q\overline{q}$ PDF parameters, as discussed in Sec. 7.3.4 and listed in App. A.2.

The results of 100 embedded toy experiments are given in Tab. 7.14; 100/100 of the fits converged. We give the results for two scenarios. In the first, we embed the expected number of signal events based on the published run 1-4 analysis [28] and allow $\rho^- K^*(892)^+$ $\mathcal{A}_{ch}$ and f_L parameters to float. In the second scenario, we embed no signal and fix $\mathcal{A}_{ch}$ for $\rho^- K^*(892)^+$ to the value in the on-peak data sample ($\mathcal{A}_{ch} = -0.072$) and $f_L = 0.5$.

We also run 500 pure toy experiments (all events generated from PDFs), generating the same number of events as for the top section of Tab. 7.14. The pulls from all floated variables are listed in Tab. 7.15. 99% of these fits converge floating 13 continuum background PDF parameters, demonstrating the fitter's ability to handle these degrees of freedom. The toy pull means (sigmas) are all consistent with zero (one) except for $N_{\rho^- K^*(892)^+}$ and f_L. We discuss these below.

Table 7.13: Results of a pure toy study for $\rho^0 K^*(892)^0$. We report pull means and sigmas for all parameters floated in the fit, as well as the mean error on each parameter. 500/500 fits converge.

| Parameter | Pure Toy Pulls | | mean err |
	mean	sigma	
$N_{\rho^0 K^*(892)^0}$	-0.01 ± 0.05	1.03 ± 0.03	36.088
$f_{L,\rho^0 K^*(892)^0}$	0.02 ± 0.05	1.07 ± 0.03	0.0720
$A_{CP,\rho^0 K^*(892)^0}$	-0.05 ± 0.04	0.98 ± 0.03	0.0532
$N_{f_0 K^*(892)^0}$	-0.05 ± 0.05	1.03 ± 0.03	20.782
$A_{CP,f_0 K^*(892)^0}$	0.04 ± 0.05	1.02 ± 0.03	0.0696
$N_{q\bar{q}}$	0.02 ± 0.05	1.04 ± 0.03	137.81
$A_{CP,q\bar{q}}$	0.01 ± 0.01	0.30 ± 0.01	0.0040
de_Bkg_P01	0.00 ± 0.04	0.99 ± 0.03	0.0134
fis_BkgC_asym	-0.02 ± 0.05	1.04 ± 0.04	0.0185
fis_BkgC_mean	0.11 ± 0.04	0.93 ± 0.03	0.0066
fis_BkgC_rms	-0.07 ± 0.04	0.98 ± 0.03	0.0044
hK_Bkg_P01	0.06 ± 0.05	1.03 ± 0.03	0.0158
hK_Bkg_P02	-0.05 ± 0.04	1.00 ± 0.03	0.0117
hK_Bkg_P03	0.06 ± 0.05	1.00 ± 0.03	0.0123
hR_Bkg_P01	0.01 ± 0.04	0.99 ± 0.03	0.0131
hR_Bkg_P02	0.00 ± 0.04	0.95 ± 0.03	0.0120
mK_Bkg_Poly_P01	0.03 ± 0.04	1.00 ± 0.03	0.0167
mK_Bkg_Poly_P02	-0.05 ± 0.04	0.95 ± 0.03	0.0207
mK_Bkg_fracKst	-0.05 ± 0.04	1.00 ± 0.03	0.0117
mR_Bkg_Poly_P01	0.06 ± 0.04	1.00 ± 0.03	0.0202
mR_Bkg_Poly_P02	0.05 ± 0.05	1.02 ± 0.03	0.0247
mR_Bkg_fracRho	0.05 ± 0.05	1.03 ± 0.03	0.0162
mR_Bkg_fracf0	-0.05 ± 0.05	1.03 ± 0.03	0.0052
mes_Bkg_c	0.10 ± 0.05	1.01 ± 0.03	2.7035

Table 7.14: Results of an embedded toy study for $\rho^- K^*(892)^+$. We report the number of events embedded from MC ("Input"), the fit result, the bias on that yield, and the mean statistical error on the yield. 100/100 fits converge.

Mode	Input	Fit	Bias	Stat. err.
$\rho^- K^*(892)^+$	70	83 ± 2	13 ± 2	25
$f_L\ (\rho^- K^*(892)^+)$	0.50	0.447 ± 0.028	-0.053 ± 0.028	0.22
$\mathcal{A}_{ch}\ (\rho^- K^*(892)^+)$	-0.072	0.046 ± 0.032	-0.026 ± 0.032	0.16
$\mathcal{A}_{ch}$ (Bkg)	-0.072	-0.072 ± 0.0004	0 ± 0.0004	0.005
$\rho^- K^*(892)^+$	0	3.5 ± 2.1	3.5 ± 2.1	19
$f_L\ (\rho^- K^*(892)^+)$	0.50	—	—	—
$\mathcal{A}_{ch}\ (\rho^- K^*(892)^+)$	-0.072	—	—	—
$\mathcal{A}_{ch}$ (Bkg)	-0.072	-0.072 ± 0.0002	0 ± 0.0002	0.005

Table 7.15: Results of a pure toy study for $\rho^- K^*(892)^+$. We report pull means and sigmas for all parameters floated in the fit, as well as the mean error on each parameter. 495/500 fits converge.

	Pure Toy Pulls		
Parameter	mean	sigma	mean err
$N_{\rho^- K^*(892)^+}$	-0.12 ± 0.05	1.06 ± 0.03	24.648
$f_{L,\rho^- K^*(892)^+}$	0.23 ± 0.05	1.06 ± 0.04	0.4255
$A_{CP,\rho^- K^*(892)^+}$	-0.02 ± 0.04	1.00 ± 0.03	0.2000
$N_{q\bar{q}}$	0.02 ± 0.04	0.99 ± 0.03	100.82
$A_{CP,q\bar{q}}$	0.02 ± 0.01	0.23 ± 0.01	0.0053
de_Bkg_P01	-0.02 ± 0.04	0.96 ± 0.03	0.0177
fis_BkgC_asym	0.05 ± 0.05	1.01 ± 0.03	0.0164
fis_BkgC_mean	0.06 ± 0.05	1.03 ± 0.03	0.0044
fis_BkgC_rms	-0.03 ± 0.04	0.99 ± 0.03	0.0031
hK_Bkg_P01	0.05 ± 0.04	0.96 ± 0.03	0.0147
hK_Bkg_P02	-0.01 ± 0.05	1.03 ± 0.03	0.0128
hR_Bkg_P01	-0.02 ± 0.05	1.03 ± 0.03	0.0173
hR_Bkg_P02	-0.03 ± 0.04	0.99 ± 0.03	0.0144
mK_Bkg_Poly_P01	0.03 ± 0.05	1.02 ± 0.03	0.0207
mK_Bkg_fracKst	-0.02 ± 0.05	1.01 ± 0.03	0.0121
mR_Bkg_Poly_P01	0.02 ± 0.04	0.98 ± 0.03	0.0224
mR_Bkg_fracRho	0.01 ± 0.05	1.04 ± 0.03	0.0130
mes_Bkg_c	0.01 ± 0.05	1.09 ± 0.03	3.6462

The longitudinal fraction f_L has a non-Gaussian distribution in pure toys. This issue was observed in the previous analysis and is discussed in detail in Sec. 5 (p. 14-18) of version 11 of BAD 1430 [29]. For reference, we repeat the conclusions here.

We define the efficiency-corrected longitudinal fraction f_L in Eq. (1.4) as

$$\frac{1}{\Gamma} \frac{d^2\Gamma}{d\cos\theta_{K^{*0}} d\cos\theta_{\rho^{+,0}}} \propto \frac{1}{4}(1 - f_L)\sin^2\theta_{K^*}\sin^2\theta_\rho + f_L\cos^2\theta_{K^*}\cos^2\theta_\rho \ .$$

But f_L is not a simple ratio of longitudinal to transverse signal events because the selection efficiencies are different for these two polarization states. Thus, we define the uncorrected f_L as

$$f_{L,raw} = \frac{N_L}{N_L + N_T} \ , \tag{7.9}$$

where N_L and N_T are the number of observed longitudinal and transverse signal events, respectively. The relationship between $f_{L,raw}$ and f_L is given by

$$
\begin{aligned}
f_{L,raw} &= \frac{\epsilon_L f_L}{\epsilon_L f_L + \epsilon_T(1 - f_L)} \\
f_L &= \frac{f_{L,raw}}{R + f_{L,raw}(1 - R)} \quad \text{where} \quad R = \frac{\epsilon_L}{\epsilon_T} \ .
\end{aligned}
\tag{7.10}
$$

As shown in [29], the smaller R becomes, the less Gaussian the distribution of f_L. In $\rho^- K^*(892)^+$, $R = 0.44$. Additionally, Ref. [29] demonstrates that the asymmetry of the f_L distribution decreases for an increased numbers of signal events, as well as for larger values of f_L. For this reason, we do not observe such a prominent asymmetry in $\rho^0 K^*(892)^0$. In Fig. 7.1 we show the f_L distributions from 500 pure toy experiments for both $\rho^- K^*(892)^+$ and $\rho^0 K^*(892)^0$.

Due to the asymmetry in f_L for $\rho^- K^*(892)^+$, the reported pull mean (from a Gaussian fit) is shifted high. Fig. 7.2 shows the pull, value, and error on f_L for $\rho^- K^*(892)^+$ with Gaussian fits overlaid. The fit quality is poor for the value and error; those plots are included only for reference and the results of the Gaussian fits are not used.

The $\rho^- K^*(892)^+$ yield pull in Tab. 7.15 is skewed negative. By looking at the pull distribution (see Fig. 7.3), we can see that a few experiments with anomalously small pull values
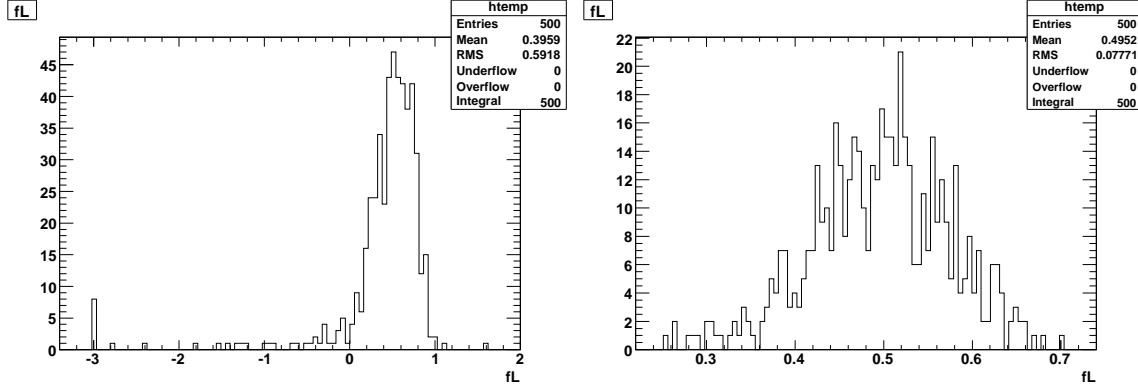
Figure 7.1: Fraction of longitudinal polarization f_L from 500 pure toy experiments for $\rho^- K^*(892)^+$ (left) and $\rho^0 K^*(892)^0$ (right). In both cases $f_L = 0.5$ was generated. The small ratio $R = \epsilon_L/\epsilon_T = 0.44$ for $\rho^- K^*(892)^+$ along with the small number of signal events (70) result in the more asymmetric distribution.
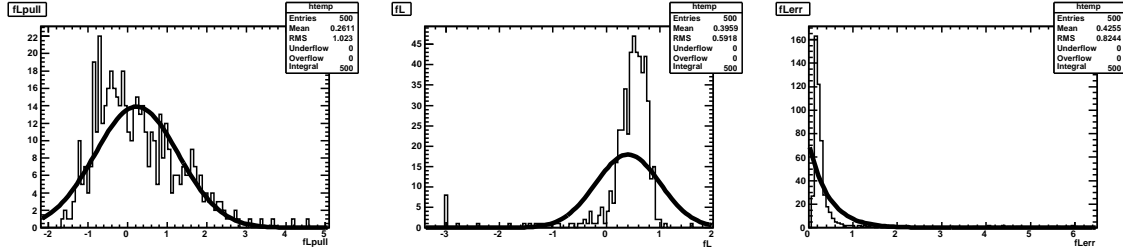
Figure 7.2: Fraction of longitudinal polarization f_L from 500 pure toy experiments for $\rho^- K^*(892)^+$. Pull (left), parameter value (center), and parameter error (right) with Gaussian fits overlaid. The pull quoted in Tab. 7.15 is from the pull fit (left).

are shifting the mean of the Gaussian fit. By eye, one expects the pull mean to be quite consistent with zero.

In both pure and embedded toys for $\rho^- K^*(892)^+$, we use the value for the m_{ES} ARGUS exponent (mes_Bkg_c) determined from floating this parameter in a blind fit to run 1-6 on-peak data. This fit finds mes_Bkg_c $= -11.0 \pm 3.7$ whereas the PDF fit using only ΔE sideband data finds mes_Bkg_c $= -6.6 \pm 6.6$. When we run toys using the ARGUS exponent from the PDF fit, about 10% of the fits report a value for the ARGUS exponent around -1, accompanied by an unreasonably small uncertainty. When we use the value deteremined by a fit to the entire dataset, the ARGUS exponent in all experiments converges to a reasonable (Gaussian-distributed) value near
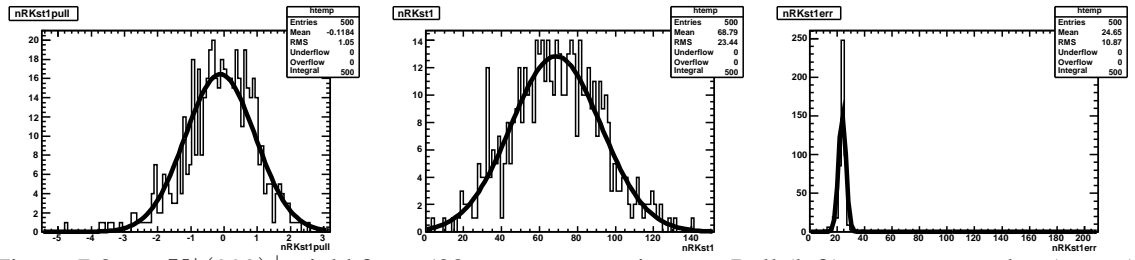
Figure 7.3: $\rho^- K^*(892)^+$ yield from 500 pure toy experiments. Pull (left), parameter value (center), and parameter error (right) with Gaussian fits overlaid. The pull quoted in Tab. 7.15 is from the pull fit (left).

$-11.$

Chapter 8

Results on the Full *BABAR* Dataset

In the following sections we present the final results based on the full *BABAR* dataset. The results for the $K^*(892)$ channels are presented in Sec. 8.1, followed by those results involving a $(K\pi)_0^*$ or $K_2^*(1430)$ in Sec. 8.2.

The branching fraction for each decay chain with a single polarization is obtained from

$$\mathcal{B} = \frac{Y - Y_0}{\epsilon \prod \mathcal{B}_i \, N_B} , \tag{8.1}$$

where Y is the yield of signal events from the fit, Y_0 is the fit bias discussed in Sec. 7.4 and given in Tab. 8.1 and 8.6, ϵ is the MC efficiency evaluated from the simulation, $\mathcal{B}_i$ is the branching fraction for the ith unstable B daughter ($\mathcal{B}_i$ having been set to unity in the MC simulation), and $N_B = (471.0 \pm 2.8) \times 10^6$ is the number of produced B^0 mesons. The values of $\mathcal{B}_i$ are taken from Particle Data Group world averages [2].

For the $B \to VV$ channels ($\rho K^*(892)$), we must also take into account the fraction of longitudinally polarized events and the different MC efficiencies for the longitudinally polarized (ϵ_L) and transversely polarized (ϵ_T) events. Thus for the $\rho K^*(892)$ channels, we calculate the branching fraction as

$$\mathcal{B}_{VV} = \frac{Y - Y_0}{(f_L \epsilon_L + (1 - f_L)\epsilon_T) \, \prod \mathcal{B}_i \, N_B} . \tag{8.2}$$

We assume the branching fraction of $\Upsilon(4S)$ to B^+B^- and $B^0\overline{B}^0$ to be the same and equal to 50%, consistent with the measurements [2]. We take

$$\mathcal{B}(f_0 \to \pi\pi) = 100\% \quad \text{and}$$

$$\mathcal{B}((K\pi)_0^* \to K\pi) = 100\%$$

as these branching fractions are poorly known. Unlike in the previous *BABAR* analysis [28], we include the ratio

$$\frac{\Gamma(\pi^+\pi^-)}{\Gamma(\pi\pi)} = \frac{2}{3}, \tag{8.3}$$

in the product of daughter branching fractions.

For the ρ^-K^{*+} channels, we apply an efficiency correction to the MC of roughly $97\%/\pi^0$. The specific value of this neutrals correction are determined by calculating a correction as a function of π^0 lab momentum for a detailed MC simulation of the signal channel. The correction is determined from a study of tau decays to modes with π^0's.

For all signals obtained from a one-step ML fit, we determine the significance of observation S by taking the difference between the value of $-2\ln\mathcal{L}$ for the zero signal hypothesis and the value at its minimum. For $\rho^0(K\pi)_0^{*0}$, $f_0(K\pi)_0^{*0}$, and $f_0K_2^*(1430)^0$, the fit method does not readily provide a $-2\ln\mathcal{L}$ curve, so we compute the significance assuming Gaussian uncertainties, which gives us a conservative lower limit on S.

For $\rho^-(K\pi)_0^{*+}$, which has a significance $< 3\sigma$ including systematics, we quote a 90% confidence level (C.L.) upper limit, given by the solution $\mathcal{B}_{90}$ to the equation

$$\frac{\int_0^{\mathcal{B}_{90}} \mathcal{L}(b)db}{\int_0^{\infty} \mathcal{L}(b)db} = 0.9, \tag{8.4}$$

where $\mathcal{L}(b)$ is the value of the likelihood for branching fraction b. Systematic uncertainties are taken into account by convolving the likelihood with a Gaussian function representing the systematic uncertainties.

8.1 $K^*(892)$ **Results**

We show the results for $\rho^0 K^*(892)^0$, $f_0 K^*(892)^0$, and $\rho^- K^*(892)^+$ in Tab. 8.1. The table gives the number of combinations per event for data (before selection of the best candidate), the number of events to fit, the signal yield, the MC efficiency and corrections that are applied to it, the product branching fractions (for final states where a specific decay chain was required in MC), the statistical significance, the central value of the branching fraction, and the measured charge asymmetry. For the $\rho K^*(892)$ channels, we give both the longitudinal and transverse MC efficiencies, as well as the longitudinal polarization fraction determined by the fit. The statistical significance is taken as the square root of the difference between the value of $-2\ln \mathcal{L}$ for zero signal and the value at its minimum.

The results of embedded toy studies designed to approximate the fit results are given in Tab. 8.2 for $\rho^0 K^*(892)^0$ and Tab. 8.3 for $\rho^- K^*(892)^+$. We extract the fit biases listed in Tab. 8.1 from these studies.

8.1.1 $B^0 \to \rho^0 K^*(892)^0$ **and** $f_0 K^*(892)^0$ **plots**

We show sPlots, projection plots, likelihood ratio plots, one sigma contours in branching fraction and f_L, and $-2\ln(\mathcal{L})$ plots including systematic errors for $\rho^0 K^*(892)^0$ and $f_0 K^*(892)^0$ in Fig. 8.1-8.5. For the projection plots, we cut on the signal/background likelihood ratio, calculated with the variable plotted removed from the fit, in order to enhance the visibility of signal.

Table 8.1: ML fit results for $B^0 \to \rho^0 K^{*0}$, $f_0 K^{*0}$, and $\rho^- K^{*+}$.

ML fit quantity	$\rho^0 K^{*0}$	$f_0 K^{*0}$	$\rho^- K^{*+}$
Fit signal yield	376 ± 37	220 ± 23	167 ± 27
Yield fit bias (evts)	44 ± 3	2.1 ± 1.6	23 ± 3
Uncorr. f_L	$0.350^{+0.074}_{-0.081}$	—	$0.367^{+0.118}_{-0.138}$
f_L Fit bias	-0.045 ± 0.008	—	-0.009 ± 0.014
#Data combs/evt		1.02	1.14
#MC combs/evt	1.06(ln) 1.02(tr)	1.03	1.17(ln) 1.13(tr)
MC SXF (%)	7.30(ln) 1.86(tr)	4.13	21.9(ln) 12.9(tr)
Evts to fit		18791	9705
MC ϵ(%)		18.30 ± 0.06	
long.	14.34 ± 0.05	—	4.94 ± 0.03
trans.	25.07 ± 0.06	—	11.18 ± 0.05
Neutrals corr. (%)	—	—	94.3(ln) 94.5(tr)
$\prod \mathcal{B}_i$ (%)	0.667	0.444	0.333
f_L	$0.40 \pm 0.08 \pm 0.05$	—	$0.38 \pm 0.13 \pm 0.03$
$\mathcal{B}(10^{-6})$	$5.1 \pm 0.6 \pm 0.5$	$5.7 \pm 0.6 \pm 0.3$	$10.3 \pm 2.3 \pm 1.3$
Stat. sign. (σ)	11.1	14.0	6.4
Signf. w/ syst (σ)	8.0	11.9	5.1
Uncorr. signal $\mathcal{A}_{ch}$	-0.065 ± 0.092	$+0.069 \pm 0.100$	$+0.197 \pm 0.151$
Corr. signal $\mathcal{A}_{ch}$	$-0.06 \pm 0.09 \pm 0.02$	$+0.07 \pm 0.10 \pm 0.02$	$+0.21 \pm 0.15 \pm 0.02$
Background $\mathcal{A}_{ch}$		-0.040 ± 0.008	-0.077 ± 0.011

Table 8.2: Results of embedded toy studies for $\rho^0 K^*(892)^0$. We report the number of events embedded from MC ("Input"), the fit result with the mean statistical error on the yield, and the bias on that yield. 99/100 fits converge.

Mode	Input	Fit	Bias
$\rho^0 K^*(892)^0$	333	377 ± 36	44 ± 3
f_L ($\rho^0 K^*(892)^0$)	0.387	0.342 ± 0.075	-0.045 ± 0.008
$\mathcal{A}_{ch}$ ($\rho^0 K^*(892)^0$)	-0.039	-0.024 ± 0.092	0.015 ± 0.008
$f_0 K^*(892)^0$	218	220.1 ± 22.8	2.1 ± 1.6
$\mathcal{A}_{ch}$ ($f_0 K^*(892)^0$)	-0.039	-0.026 ± 0.102	0.013 ± 0.010
$\mathcal{A}_{ch}$ (Bkg)	-0.0391	-0.0389 ± 0.0080	0.0002 ± 0.0004
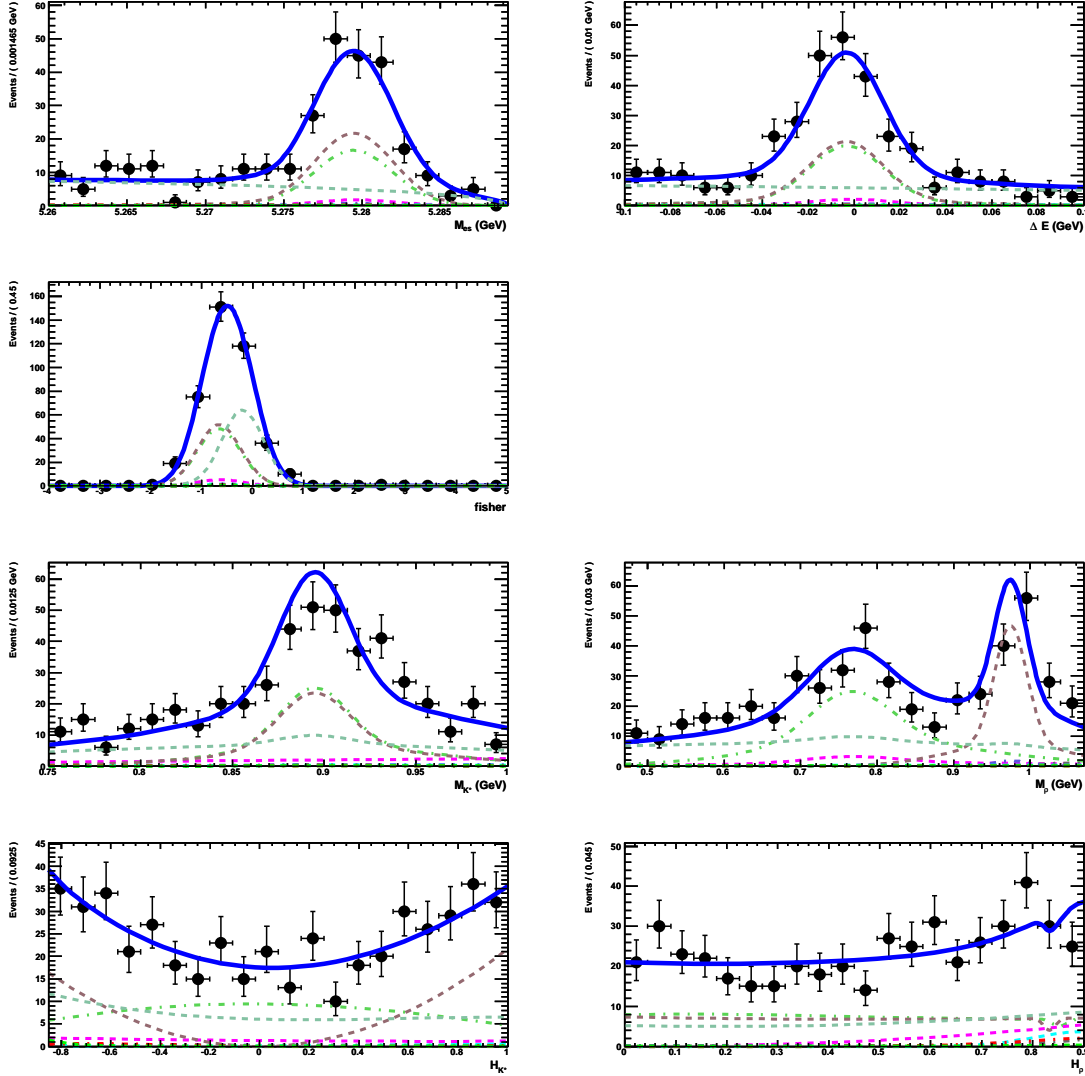
Figure 8.1: Projection plots of the $\rho^0 K^*(892)^0$ and $f_0 K^*(892)^0$ fit results on run 1-6 data. Left to right, top to bottom: m_{ES}, ΔE, $\mathcal{F}$, $m(K^+\pi^-)$, $m(\pi^+\pi^-)$, $\mathcal{H}(K^+\pi^-)$, and $\mathcal{H}(\pi^+\pi^-)$. The solid blue curve shows the total fit result, the green dash-dot curve is $\rho^0 K^*(892)^0$, brown dashed is $f_0 K^*(892)^0$, and the dashed pale aqua is continuum background.
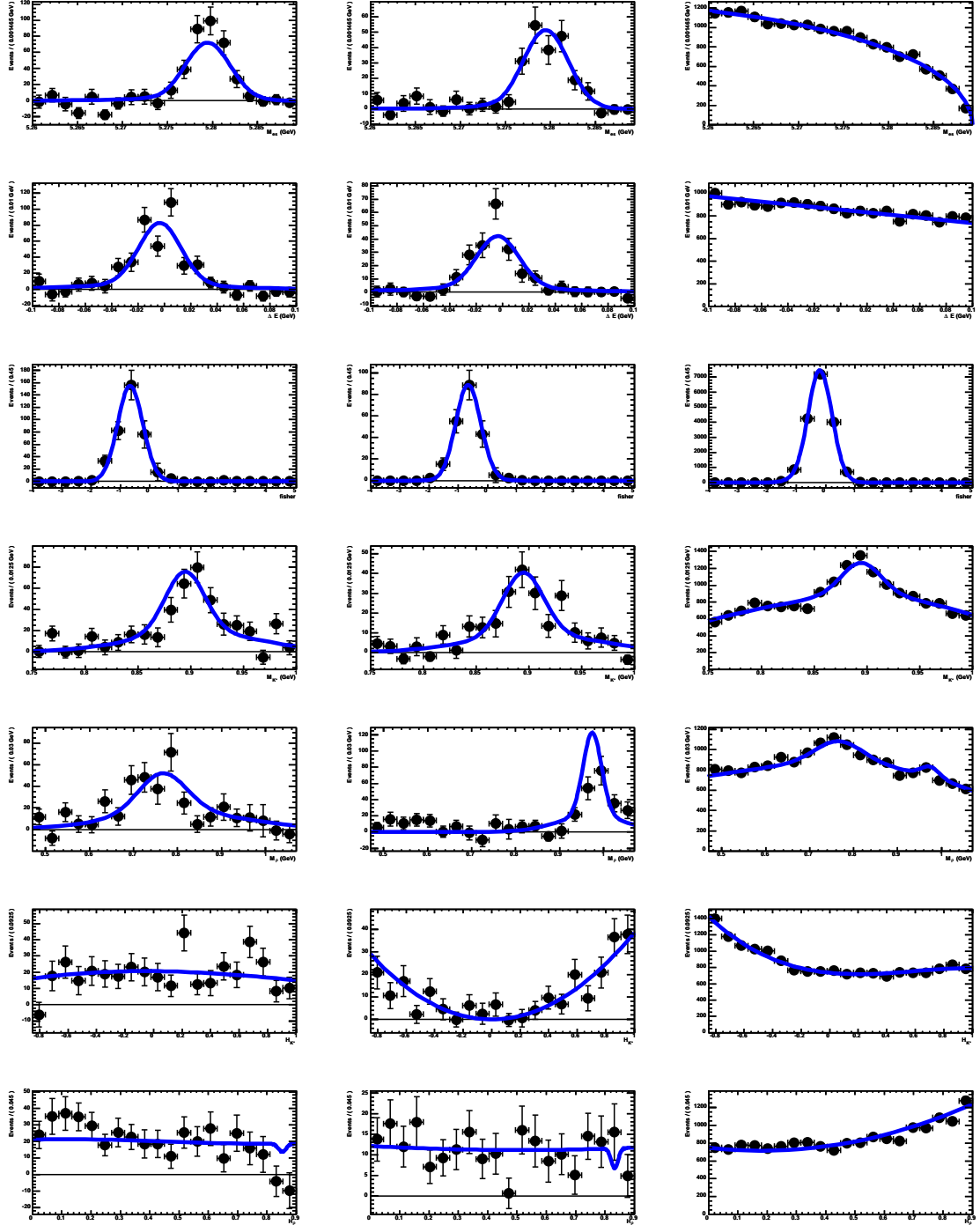
Figure 8.2: sPlots of (left to right) $\rho^0 K^*(892)^0$, $f_0 K^*(892)^0$, and continuum background. Plots are, top to bottom: m_{ES}, ΔE, $\mathcal{F}$, $m(K^+\pi^-)$, $m(\pi^+\pi^-)$, $\mathcal{H}(K^+\pi^-)$, and $\mathcal{H}(\pi^+\pi^-)$. Points show run 1-6 data, blue curves are the fit result computed without the variable plotted.
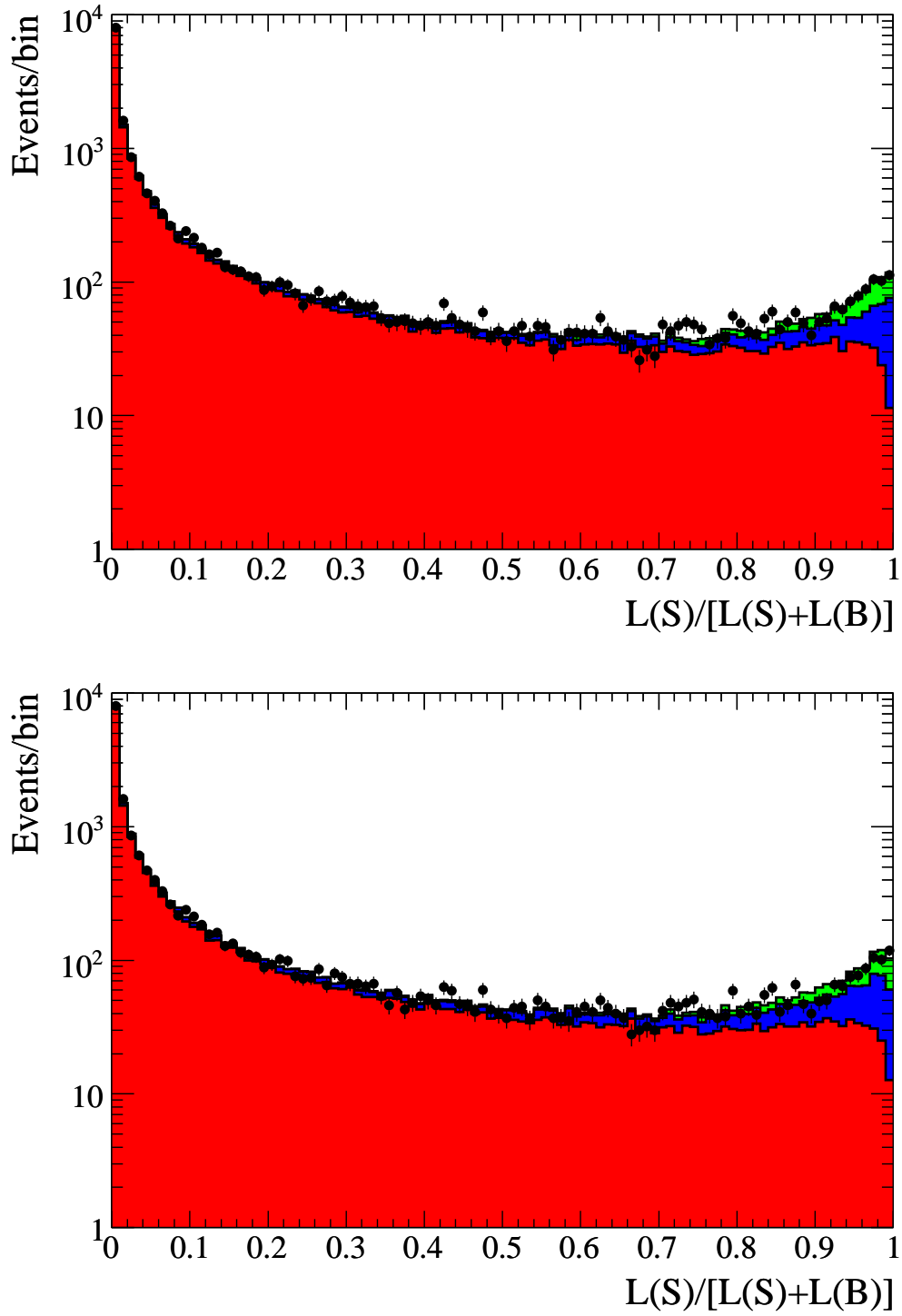
Figure 8.3: $\ln\mathcal{L}$ plots for $\rho^0 K^*(892)^0$ (top) and $f_0 K^*(892)^0$ (bottom) on run 1-6 data. Continuum background is red, the sum of all $B\overline{B}$ backgrounds (including $f_0 K^*(892)^0$ for $\rho^0 K^*(892)^0$ and vice versa) is blue, and signal is green.

Table 8.3: Results of an embedded toy study for $\rho^- K^*(892)^+$. We report the number of events embedded from MC ("Input"), the fit result with the mean statistical error on the yield, and the bias on that yield. 100/100 fits converge.

Mode	Input	Fit	Bias
$\rho^- K^*(892)^+$	150	173 ± 28	23 ± 3
$f_L\ (\rho^- K^*(892)^+)$	0.42	0.411 ± 0.127	-0.009 ± 0.014
$\mathcal{A}_{ch}\ (\rho^- K^*(892)^+)$	-0.072	-0.056 ± 0.153	0.016 ± 0.014
$\mathcal{A}_{ch}$ (Bkg)	-0.072	-0.0722 ± 0.0004	0.0000 ± 0.0004
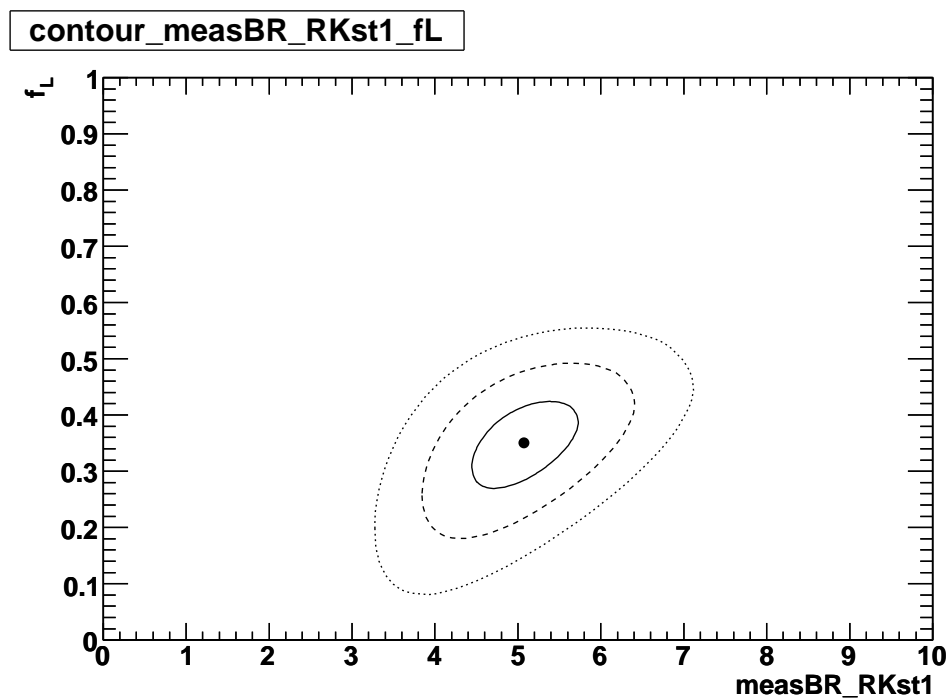
Figure 8.4: One sigma contours for $\rho^0 K^*(892)^0$ in branching fraction (10^{-6}) and f_L on run 1-6 data.
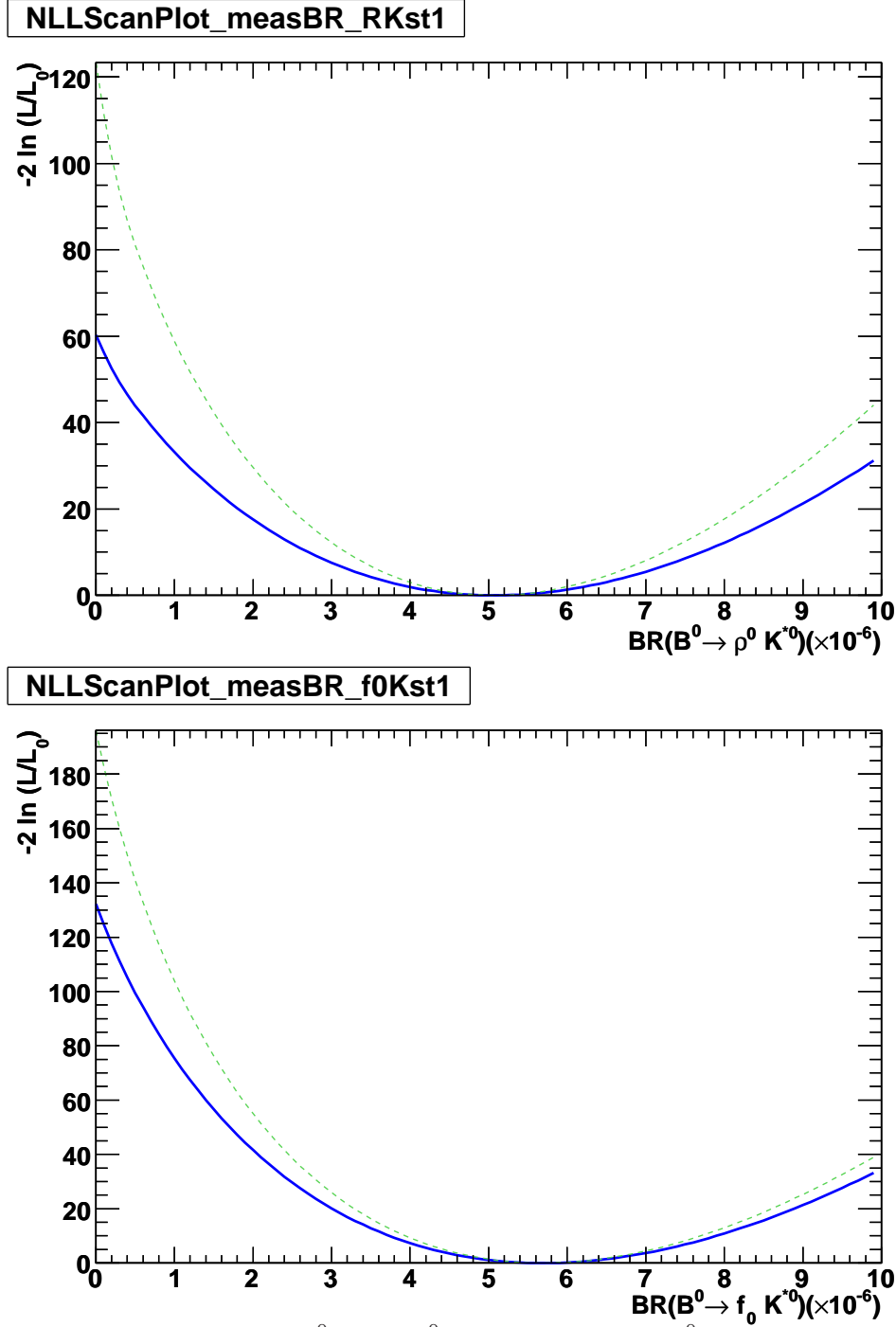
Figure 8.5: $-2\ln(\mathcal{L})$ plots for $\rho^0 K^*(892)^0$ (top) and $f_0 K^*(892)^0$ (bottom) branching fractions. The solid blue curves includes systematic uncertainties, the dashed green curves are statistical only.

8.1.2 Discussion of f_L measurement in $\rho^0 K^*(892)^0$

In run 1-4, this analysis measured $f_L = 0.48 \pm 0.09$ compared to the published *BABAR* measurement on run 1-4 of $f_L = 0.57 \pm 0.09 \pm 0.08$. On run 1-6, we measure $f_L = 0.40 \pm 0.08 \pm 0.05$, a marked decrease from the run 1-4 value. In this section we describe several studies performed after unblinding to understand this change, as well as to understand the behavior of the statistical uncertainty as a function of f_L.

In Tab. 8.4 we show the uncorrected f_L results[1] split into run 1-4 and run 5-6. It appears that the value of f_L in the run 5-6 data has fluctuated downward compared to run 1-4.

Table 8.4: $\rho^0 K^*(892)^0$ yield and f_L results split by run block.

Dataset	yield	Raw f_L
Run 1-4	201 ± 27	0.449 ± 0.090
Run 5-6	173 ± 25	0.238 ± 0.127
Run 1-6	378 ± 37	0.348 ± 0.078

Dependence of f_L error and bias on f_L value

To investigate why the uncertainty for the f_L measurement did not decrease much when doubling the dataset, we run hybrid pure/embedded toy studies for a variety of f_L values. We embed 344 $\rho^0 K^*(892)^0$ and 220 $f_0 K^*(892)^0$ signal events, but draw all backgrounds from the PDFs (as we have low MC statistics in several $B\overline{B}$ background samples). The number of background events is equal to what was used in the run 1-6 fit. We run 500 experiments for each case, with close to 100% convergence. The results are given in Tab. 8.5. We find the fitted f_L distributions mildly non-Gaussian (especially for the lower values of f_L); by eye, the fitted mean should be slightly higher. However, the pull distributions are well described by Gaussians, giving high confidence

---

[1]This study was performed with slightly different $B\overline{B}$ background values for $\rho^0 (K\pi)_0^{*0}$ and $f_0(K\pi)_0^{*0}$ as we only had preliminary results for those channels at the time.

Table 8.5: Hybrid toy study embedding 344 $\rho^0 K^*(892)^0$ and 220 $f_0 K^*(892)^0$ events from MC
and generating all $B\overline{B}$ and $q\overline{q}$ background from the PDFs.

Generated f_L	Fit f_L	Bias
0.3	0.266 ± 0.081	-0.034 ± 0.004
0.4	0.361 ± 0.075	-0.039 ± 0.003
0.5	0.462 ± 0.068	-0.038 ± 0.003
0.6	0.561 ± 0.062	-0.039 ± 0.003

in the uncertainty on f_L. From these studies, the uncertainty clearly increases as the value of f_L

decreases.

   Also included in Tab. 8.5 is the bias on f_L from the hybrid toy study. The bias appears

quite constant across various values of f_L. This value is fairly consistent with the measured bias in

Tab. 8.2, though that bias is slightly larger, as one would expect if the bias is somehow sensitive to

the correlations in the $B\overline{B}$ backgrounds.

8.1.3 $B^0 \rightarrow \rho^- K^{*+}$ **plots**

   We show sPlots, projection plots, likelihood ratio plots, one sigma contours in branching

fraction and f_L, and $-2\ln(\mathcal{L})$ plots including systematic errors for $\rho^- K^*(892)^+$ in Fig. 8.6-8.10.

For the projection plots, we cut on the signal/background likelihood ratio, calculated with the vari-

able plotted removed from the fit, in order to enhance the visibility of signal.
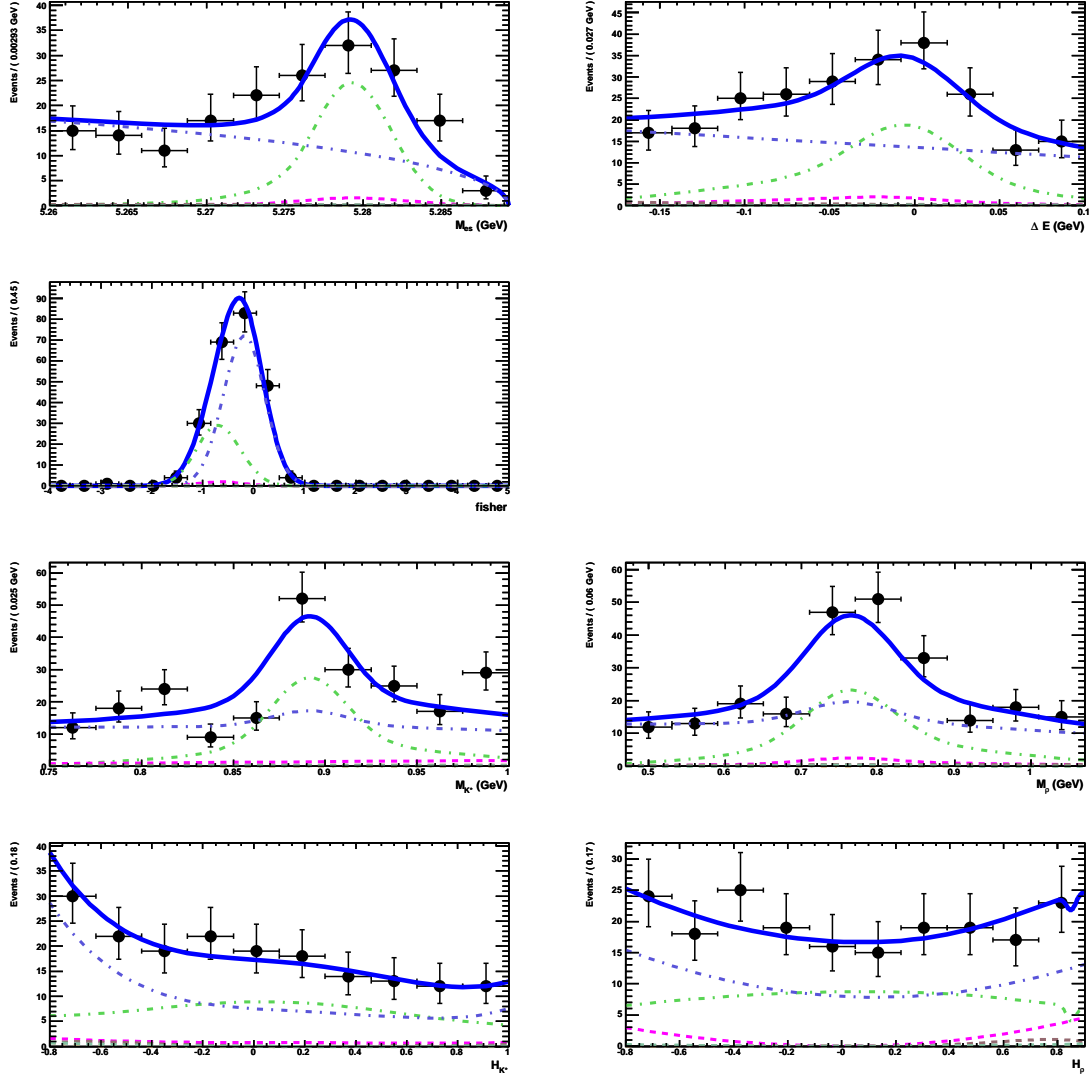
Figure 8.6: Projection plots of the $\rho^- K^*(892)^+$ fit results on run 1-6 data. Left to right, top to bottom: m_{ES}, ΔE, $\mathcal{F}$, $m(K^+\pi^0)$, $m(\pi^0\pi^-)$, $\mathcal{H}(K^+\pi^0)$, and $\mathcal{H}(\pi^0\pi^-)$. The solid blue curve shows the total fit result, the green dash-dot curve is $\rho^- K^*(892)^+$, the dashed pink is $\rho^-(K\pi)_0^{*+}$, and the dashed blue is continuum background.
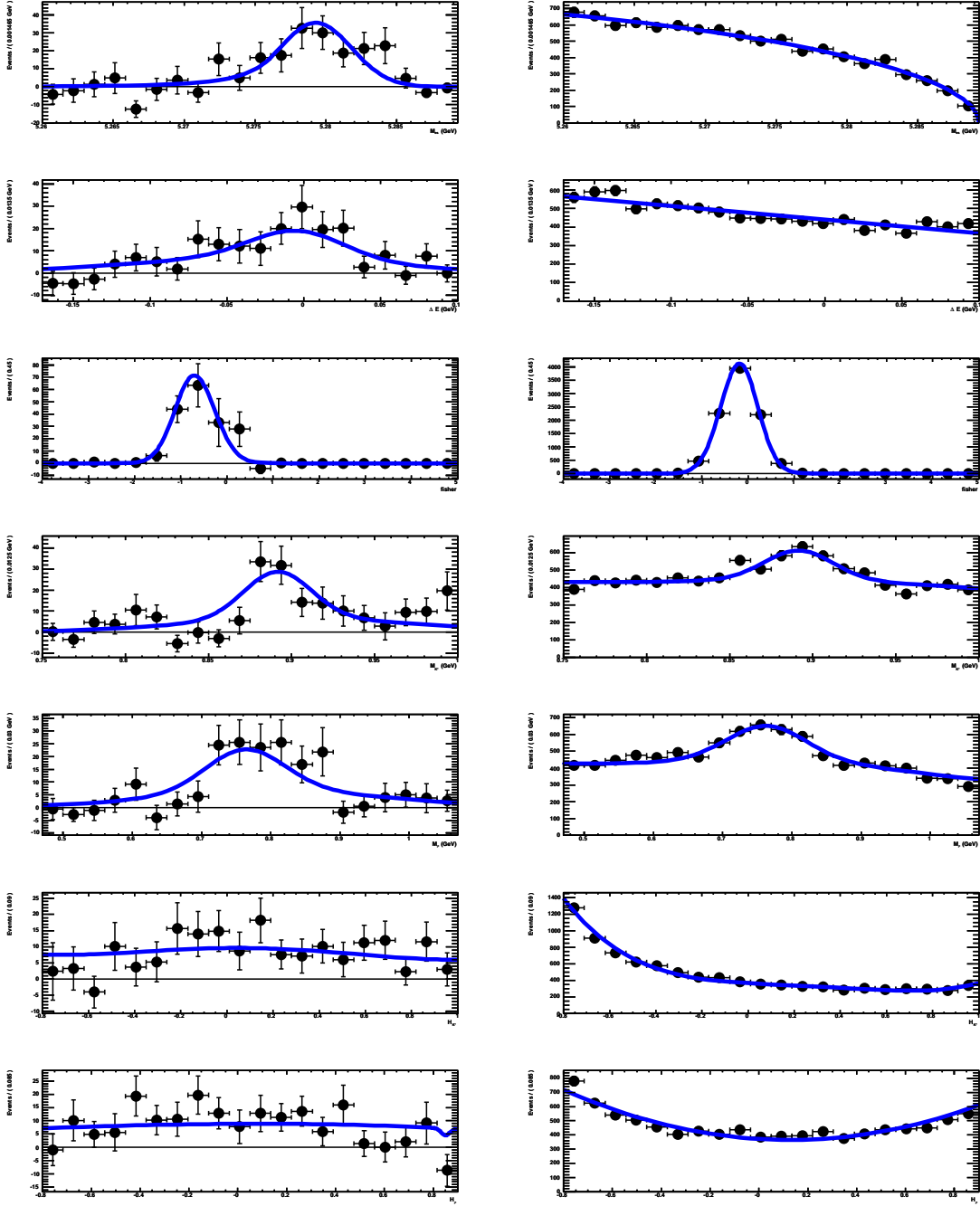
Figure 8.7: sPlots of $\rho^- K^*(892)^+$ (left) and continuum background (right). Plots are, top to bottom: m_{ES}, ΔE, $\mathcal{F}$, $m(K^+\pi^0)$, $m(\pi^0\pi^-)$, $\mathcal{H}(K^+\pi^0)$, and $\mathcal{H}(\pi^0\pi^-)$. Points show run 1-6 data, blue curves are the fit result computed without the variable plotted.
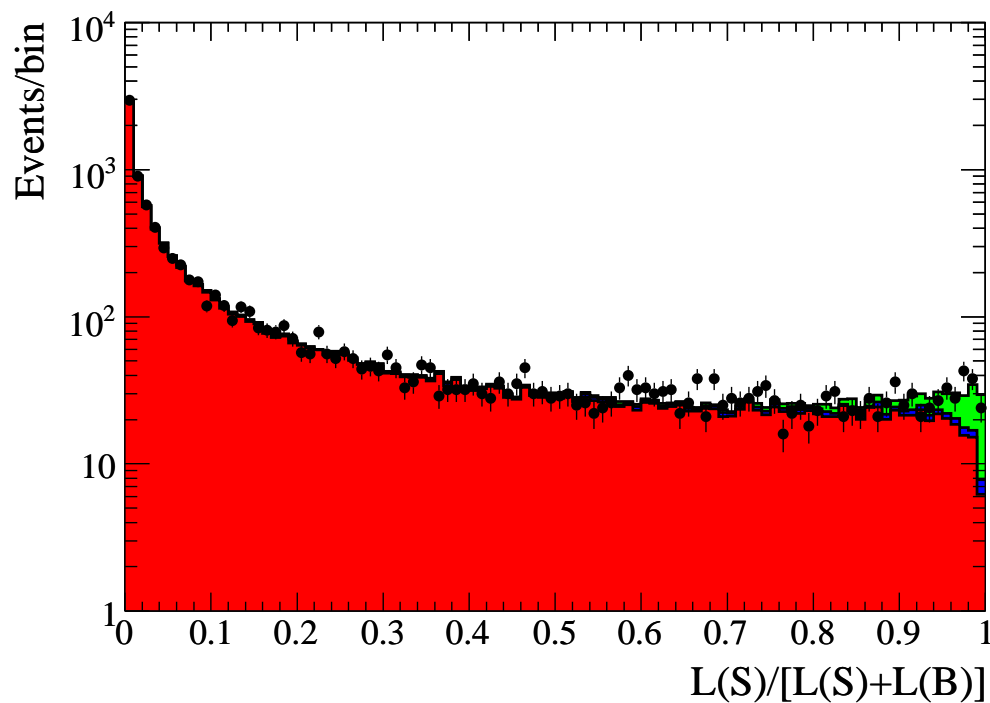
Figure 8.8: $\ln \mathcal{L}$ plots for $\rho^- K^*(892)^+$ on run 1-6 data. Continuum background is red, the sum of all $B\bar{B}$ backgrounds is blue, and signal is green.
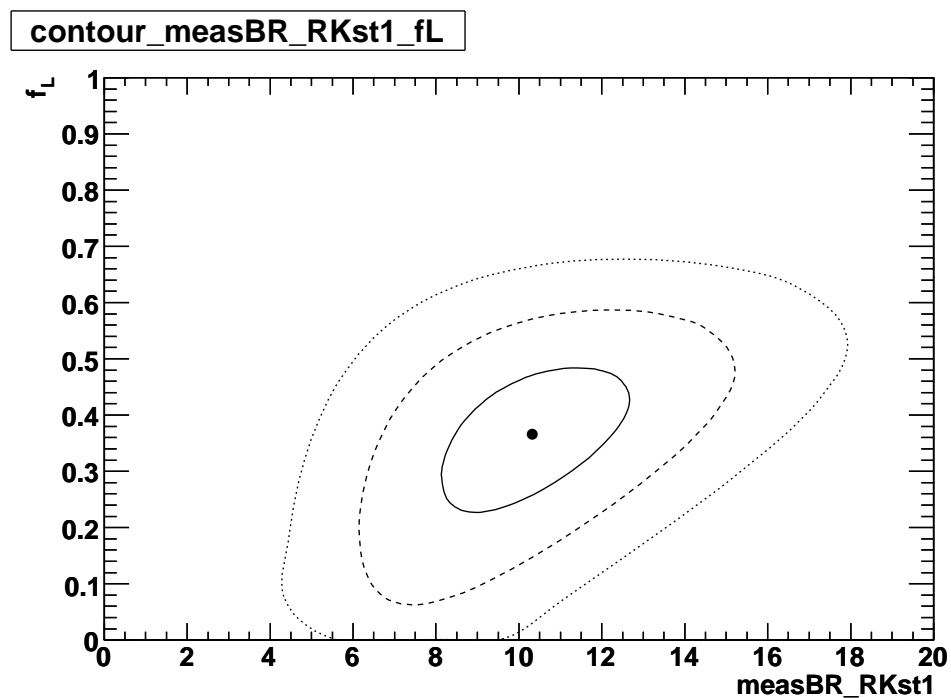
Figure 8.9: One sigma contours for $\rho^- K^*(892)^+$ in branching fraction (10^{-6}) and f_L on run 1-6 data.
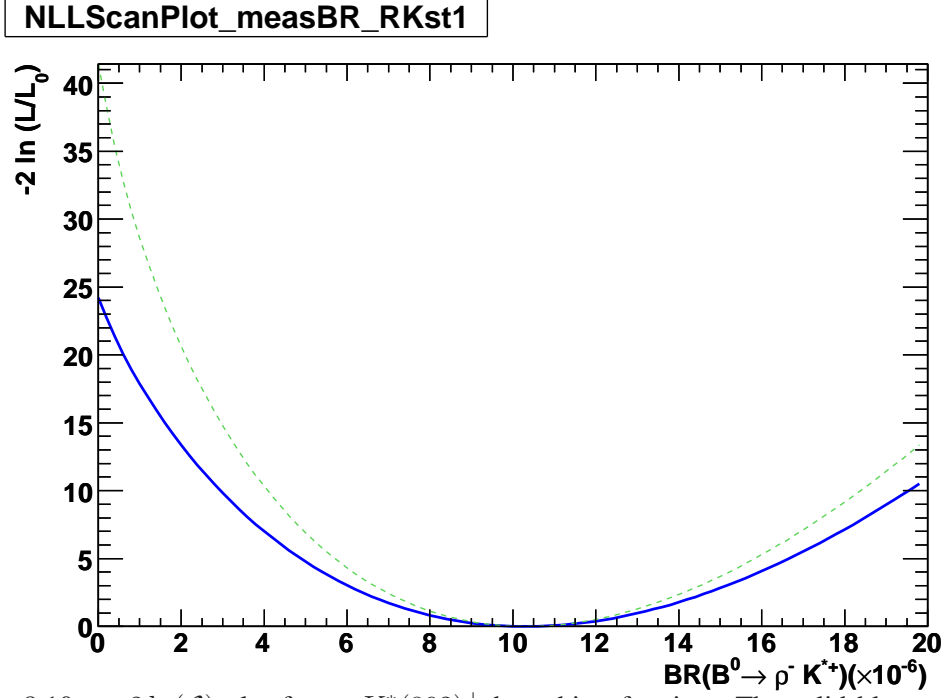
Figure 8.10: $-2\ln(\mathcal{L})$ plot for $\rho^- K^*(892)^+$ branching fraction. The solid blue curve includes systematic uncertainties, the dashed green curve is statistical only.

8.2 $(K\pi)_0^*$ and $K_2^*(1430)$ Results

We present the results for $B^0 \to \rho^0 (K\pi)_0^{*0}$, $f_0 (K\pi)_0^{*0}$, $f_0 K_2^*(1430)^0$, and $\rho^- (K\pi)_0^{*+}$. Additional analysis details, including sPlots and projection plots, are given in App. B and C.

In Fig. 8.11 we show the $-2\ln(\mathcal{L})$ curve including systematic errors for $\rho^- (K\pi)_0^{*+}$. In Fig. 8.12(a) we project the data and fit functions from the first step of the HMR $(K\pi)_0^{*0}$ and $K_2^*(1430)^0$ fits onto the $m_{K^+\pi^-}$ distribution. Fig. 8.12(b–c) shows the results of the second step HMR fit, distinguishing between ρ^0 and f_0 hypotheses; in these plots, we do not cut on $\ln\mathcal{L}$, as these *sWeighted* samples already contain only (b) $(K\pi)_0^{*0}$ or (c) $K_2^*(1430)^0$ signal events.

Ref. [5] extracts the resonant $K_0^*(1430)^0$ fraction of the LASS-parameterized $(K\pi)_0^{*0}$, finding the resonant fraction to account for 81% of the LASS shape in $B^+ \to (K\pi)_0^{*0}\pi^+$ decays. Using this resonant fraction along with the daughter branching fraction $\mathcal{B}(K_0^*(1430) \to K\pi) =$

Table 8.6: ML fit results for $B^0 \to \rho^0(K\pi)_0^{*0}$, $f_0(K\pi)_0^{*0}$, $f_0 K_2^*(1430)^0$, and $\rho^-(K\pi)_0^{*+}$. For the $(K\pi)_0^*$ modes, we assume $\mathcal{B}((K\pi)_0^* \to K\pi) = 100\%$. *The significances for $\rho^-(K\pi)_0^{*+}$ are calculated the normal way; for all other modes, we conservatively assume Gaussian uncertainties.

ML fit quantity	$\rho^0(K\pi)_0^{*0}$	$f_0(K\pi)_0^{*0}$	$f_0 K_2^*(1430)^0$	$\rho^-(K\pi)_0^{*+}$
Fit signal yield	$1045 \pm 36 \pm 118$	$88 \pm 19 \pm 10$	$134 \pm 14 \pm 23$	221 ± 74
Fit bias (events)	80 ± 11	7 ± 1	0 ± 2	-5 ± 8
Events to fit		37157		13259
MC ϵ(%)	9.60	12.48	15.32	4.80
Neutrals corr. (%)	—	—	—	94.3
$\prod \mathcal{B}_i$ (%)	66.7	44.4	21.7	33.3
Corr. $\epsilon \times \prod \mathcal{B}_i$ (%)	6.40	5.55	3.32	1.51
$\mathcal{B}(10^{-6})$	$31 \pm 4 \pm 3$	$3.1 \pm 0.8 \pm 0.7$	$8.6 \pm 1.7 \pm 0.9$	$32 \pm 10 \pm 6$
Stat. sign. (σ)	7.6	3.9	5.0	3.2*
Signf. w/ syst (σ)	6.4	3.0	4.4	2.8*

$(93 \pm 10)\%$ [2], we find the resonant branching fractions

$$\mathcal{B}(B^0 \to \rho^0 K_0^*(1430)^0) = 27 \pm 4 \pm 2 \pm 3$$

$$\mathcal{B}(B^0 \to f_0 K_0^*(1430)^0) \times \mathcal{B}(f_0 \to \pi\pi) = 2.7 \pm 0.7 \pm 0.5 \pm 0.3$$

$$\mathcal{B}(B^0 \to \rho^- K_0^*(1430)^+) = 28 \pm 10 \pm 5 \pm 3 \,,$$

where the uncertainties are statistical, systematic, and from the $K_0^*(1430) \to K\pi$ branching fraction, respectively.

NLLScanPlot_measBR_RKst0
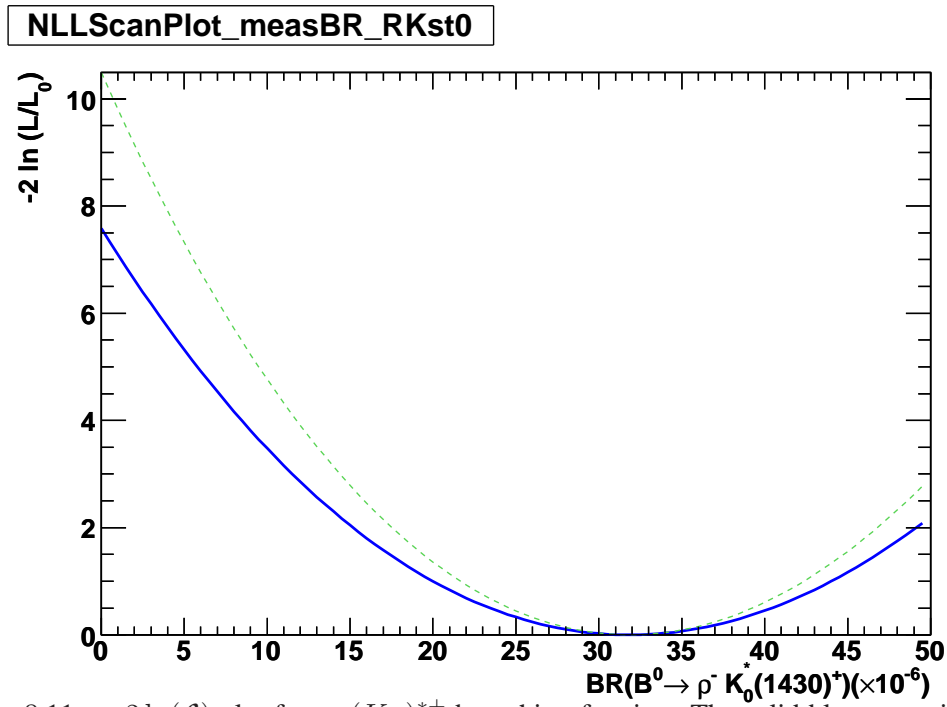
Figure 8.11: $-2\ln(\mathcal{L})$ plot for $\rho^-(K\pi)_0^{*+}$ branching fraction. The solid blue curve includes systematic uncertainties, the dashed green curve is statistical only.
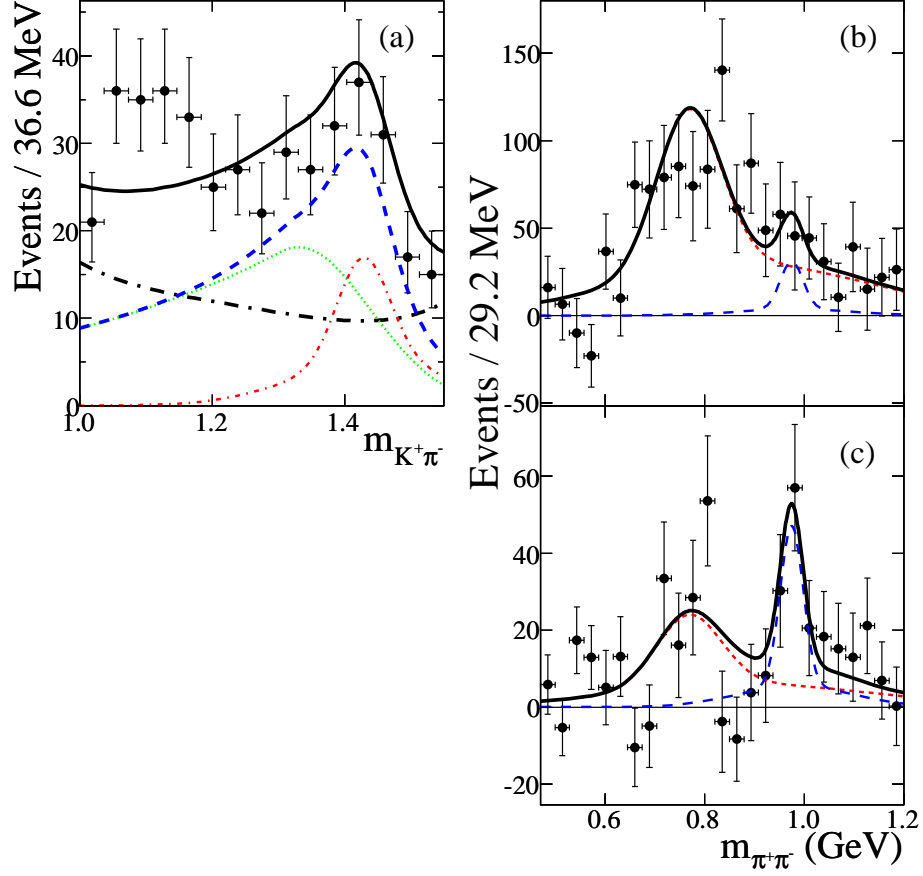
Figure 8.12: Invariant mass projections for HMR $\rho^0(K\pi)_0^{*0}$, $f_0(K\pi)_0^{*0}$, and $f_0 K_2^*(1430)^0$ signals (a) $K^+\pi^-$ mass, (b) $\pi^+\pi^-$ mass for $(K\pi)_0^{*0}$, (c) $\pi^+\pi^-$ mass for $K_2^*(1430)^0$. The solid curve is the fit function. Color online: in (a) the black long-dash-dotted is the total background, the blue dashed curve is the total signal contribution, green dotted is the $(K\pi)_0^{*0}$ component, and the $K_2^*(1430)^0$ is red dashed. In (b) and (c) ρ^0 signal is red dashed, f_0 is blue long-dashed.

Chapter 9

Systematic Errors

We itemize estimates of the various sources of systematic errors important for these measurements. Table 9.1 show the results of our evaluation of these uncertainties. We tabulate separately the additive and multiplicative uncertainties. That is, we distinguish between those errors that concern a bias on the yield and those that affect the efficiency and total number of $B\overline{B}$ events, since only the former affect the significance of the result. The additive systematic uncertainties are the dominant source of systematics for the results presented in this paper. The final row of the table provides the total systematic error in units of branching fraction for each channel.

9.1 Additive systematic errors

- ML fit yield: In order to determine the ML fit yield systematic, we would like to float PDF signal parameters in the fit. For the moderate number of signal events observed, however, this is not practical. As an alternative, we use control samples to study how well the MC models the data in ΔE, m_{ES}, $\mathcal{F}$ and the resonance masses. From these studies, we determine nominal shifts and scale factors to apply to our signal PDFs; these correction factors are tabulated in Tab. 7.11 for ΔE, m_{ES}, and m_{K^*}. For $\mathcal{F}$, we found no correction necessary for the nominal

Table 9.1: Estimates of systematic errors.

Quantity	$\rho^0 K^{*0}$	$\rho^0 K_0^{*0}$	$f_0 K^{*0}$	$f_0 K_0^0$	$f_0 K_2^{*0}$	$\rho^- K^{*+}$	$\rho^- K_0^{*+}$
Additive errors (events)							
ML fit	2.7	3.7	1.1	0.3	0.7	6.7	21.3
Fit bias	22.2	41.8	1.9	12.5	5.0	11.9	8.4
$B\overline{B}$ background	14.8	5.1	2.7	0.4	0.6	6.0	3.2
$f_0(980)$ parameters	3.5	10.0	8.8	10.0	2.5	—	—
LASS parameters	—	29.5	—	2.5	7.7	—	31.0
Interference	10.1	57.5	1.8	6.5	9.9	8.4	18.1
Total additive (events)	28.9	77.9	9.6	17.5	16.8	17.1	42.7
Multiplicative errors (%)							
Track multiplicity	1.0	1.0	1.0	1.0	1.0	1.0	1.0
Track finding	0.7	0.7	0.7	0.7	0.7	0.4	0.4
π^0 efficiency	—	—	—	—	—	3.8	3.6
Number $B\overline{B}$	0.6	0.6	0.6	0.6	0.6	0.6	0.6
Branching fractions	—	—	—	—	1.2	—	—
MC statistics	0.08	0.07	0.06	0.04	0.05	0.06	0.05
$\cos\theta_T$	1.5	1.5	1.5	1.5	1.5	1.5	1.5
PID	1.0	1.0	1.0	1.0	1.0	1.0	1.0
f_L uncertainty	2.6	—	—	—	—	2.1	—
Total multiplicative (%)	3.4	2.3	2.3	2.3	2.6	4.9	4.2
Total systematic [$\mathcal{B}(10^{-6})$]	0.5	2.7	0.3	0.7	0.9	1.3	6.1

fit, but include the statistical uncertainty from the control samples when we allowed the $\mathcal{F}$ signal parameters to float (see App. E). We vary the signal parameters around their nominal values by the uncertainties listed in Tab. 7.11 and App. E to obtain the fit yield systematic error. This uncertainty is larger for the $\rho^- K^{*+}$ channels, as the $\overline{D}^0 \pi^0$ control sample has lower statistics than the $D^- \pi^+$ sample used for the $\rho^0 K^{*0}$ channels.

- <u>ML fit bias</u>: The fit bias arises mostly from correlations among the fit variables, which are neglected in the ML fit. Studies of this bias are described in Sec. 7.4; the associated uncertainty is the sum in quadrature of half the correction and its statistical uncertainty. For the $\rho^0/f_0(K\pi)_0^{*0}$ and $f_0 K_2^*(1430)^0$ channels, we add the uncertainty on the total bias in quadrature with half the bias scaled by the ratio of ρ^0 or f_0 events to their sum. This is the dominant

Table 9.2: Systematic errors on $K^*(892)$ BFs (in events) from varying $B\overline{B}$ background yields within their uncertainties.

Quantity	$\rho^0 K^{*0}$	$f_0 K^{*0}$	$\rho^- K^{*+}$
Other $B\overline{B}$ Background	1.08	0.22	0.27
$f_2(1270)K^{*0}$ yield	0.39	0.28	—
$\rho(K\pi)_0^{*0}$ yield	14.7	0.54	5.99
$f_0(K\pi)_0^{*0}$ yield	0.89	2.58	—

systematic in the $\rho^0 K^*(892)^0$ channels and is among the top systematics in the others.

- $B\overline{B}$ background: We take into account our uncertain knowledge of the $B\overline{B}$ backgrounds by varying the $B\overline{B}$ background yields (which are fixed in the nominal fit) by the uncertainties listed in Sec. 7.2 for the $K^*(892)$ channels and App. B and C for the $(K\pi)_0^*$ and $K_2^*(1430)$ channels. These uncertainties take into account the uncertainties on the measured branching fractions and efficiencies for these background modes. The correlations between these yield parameters are taken into account for the final $B\overline{B}$ background systematic. For the $K^*(892)$ channels, the dominant effect is from our uncertainty on the $(K\pi)_0^*$ yields. In Tab. 9.2 we list the contributions of the various background channels to the $B\overline{B}$ background uncertainty for our $K^*(892)$ signals.

- $f_0(980)$ width: The width of the f_0 is not accurately measured. The PDG quotes a width between 40 to $100\,\mathrm{MeV}$ and it is simulated in *BABAR* MC with a width of $50\,\mathrm{MeV}$. In the LMR, we allow the f_0 width and mean to float in the fit and take half the difference in the shift in yield as a systematic. In the HMR, the statistics are too limited to allow these parameters to float. Instead, we use the parameters from allowing the $f_0 K^*(892)^0$ mean and width to float in the LMR, and quote half the resulting variation in yields from the nominal HMR fit. This is amongst the top systematics for $f_0(K\pi)_0^{*0}$ and $\rho^0(K\pi)_0^{*0}$.

- <u>LASS shape</u>: In the HMR fits, we reweight the nonresonant MC with LASS parameters shifted by plus and minus one standard deviation (see Tab. 6.4) and take the larger of the yield differences with respect to the nominal as the systematic error. The LASS systematic is the dominant one for $\rho^-(K\pi)_0^{*+}$ and second-leading for $\rho^0(K\pi)_0^{*0}$.

- <u>Interference</u>: In our nominal fits, we do not account for interference between the scalar and vector K^*, or between the vector and tensor. The interference between ρ^0 and f_0 integrates to zero over the symmetric $\mathcal{H}_\rho$ range. We estimate the magnitude of the K^* interference effect in a separate calculation, which takes into account the relevant mass and helicity acceptance functions, and varies the relative strong phases between components over the full range. As interference can affect the K^* lineshape, we conservatively take this systematic to be additive. This is among the dominant systematic uncertainties in the HMR fits.

We know mass and helicity dependence of the magnitude and phase of the complex amplitudes that describe the decay via each partial wave. If the constant, overall phase shift (δ_0) between amplitudes were known, we could integrate the squared sum of the amplitudes to determine how much the interference contributes to the decay rate. Since δ_0 is unknown, we average over this parameter when computing the interference-related systematic uncertainty for each mode. We integrate the decay rate for values of δ_0 from 0 to 2π in steps of 0.1. We find the maximum fraction of the interference contribution and scale it by $1/\sqrt{12}$ (because we assume that δ_0 is uniformly distributed over the range $(0, 2\pi)$) to find the rms error. We find this systematic error to be $0.8 - 5.0\%$ in $K^*(892) - (K\pi)_0^*$ interference and $5.5 - 8.2\%$ in $(K\pi)_0^* - K_2^*(1430)$ interference. One expects this systematic to be larger for $(K\pi)_0^* - K_2^*(1430)$ interference, given the overlap of the resonances. For the $(K\pi)_0^*$ channels, we calculate both $(K\pi)_0^* - K^*(892)$ and $(K\pi)_0^* - K_2^*(1430)$ interference effects and add them in quadrature.

9.2   Multiplicative systematic uncertainties

- <u>Trigger efficiency</u>: The B counting group measured the trigger efficiency for multi-hadron events to be in excess of 0.9993. We neglect the systematic error on the tiny inefficiency from this source.

- <u>Track multiplicity</u>: This is for the cut on the minimum number of tracks in the event. We require the reconstruction of at least one track from the other B decay. The signal MC inefficiency for this cut is a few percent. We assign an uncertainty of 1%.

- <u>Track finding/efficiency</u>: The Tau3-1 tracking efficiency study [51] determines that no efficiency correction is needed for R24 data and SP10 MC. The systematic uncertainty derives from the following formula: 0.172%/GoodTracksLoose track plus 0.170%/GoodTracksVeryLoose track added in quadrature with the correction factor of 0.115% (GTL tracks) or 0.111% (GTVL tracks). We use the average correction factor based on the number of each type of track in our sample, though the difference is negligible.

- <u>π^0 finding</u>: We use a script provided by the Neutrals Group to calculate the π^0 efficiency correction (about 97%/π^0) and its associated systematic (about 1.5%/π^0). We compute this correction separately for the π^0 from the ρ^- and from the K^{*+}, and multiply the corrections together to determine the final neutrals correction. As the systematic uncertainties are correlated, we add them linearly for the two π^0's in the $\rho^- K^{*+}$ events.

- <u>Luminosity, B counting</u>: We determine the error on B counting from the error given by the official luminosity/B counting script, where $N_{B\bar{B}} = (471.0 \pm 2.8) \times 10^6$. The B counting group finds a 0.6% systematic uncertainty for R24 data [52].

- <u>Branching fractions of daughters</u>: The K^* daughter branching fractions come from the Clebsh-Gordon coefficients and so are not assigned an uncertainty. We also do not assign an un-

certainty for $\rho \rightarrow \pi\pi$. As the branching fraction of $f_0 \rightarrow \pi^+\pi^-$ is unknown, we quote $\mathcal{B}(B^0 \rightarrow f_0 K^{*0}) \times \mathcal{B}(f_0 \rightarrow \pi\pi)$, where the ratio $\Gamma(f_0 \rightarrow \pi^+\pi^-)/\Gamma(f_0 \rightarrow \pi\pi) = 2/3$ is used. For the $K_2^*(1430)$, the branching fraction uncertainty is taken from the PDG [2]. For the $(K\pi)_0^*$, we assume that $\mathcal{B}((K\pi)_0^* \rightarrow K\pi) = 100\%$ and do not assign a systematic uncertainty, as this branching fraction is poorly measured.

- <u>MC statistics</u>: This is calculated for the number of MC signal events simulated for each decay (typically around 430,000), and is determined based on

$$\delta(\epsilon) = \sqrt{\frac{\epsilon(1-\epsilon)}{N_{\text{generated}}}} \,, \tag{9.1}$$

where ϵ is the MC efficiency and $N_{\text{generated}}$ is the number of MC events generated.

- <u>Event shape cuts</u>: There are two variables used for event shape cuts, $\cos\theta_{\text{T}}$ and $\mathcal{F}$. For $\cos\theta_{\text{T}}$, the systematic uncertainty estimate is from the control sample study in App. C of BAD 1772 [53]. It is given by:

$$\delta_{\cos\theta_{\text{T}}} = 0.05 \times (1 - (|\cos\theta_{\text{T}}| \text{ cut value})) \tag{9.2}$$

For $\mathcal{F}$, the systematic uncertainty is included in the ML fit yield discussed above.

- <u>Particle ID</u>: We apply PID tweaking in these analyses to make the MC efficiency more closely match that in data. In previous analyses to quasi-two-body final states, the effect of these corrections has been determined to be small. We quote a systematic uncertainty of 1%, which we believe to be conservative.

- <u>f_L uncertainty</u>: Signal yield reconstruction efficiency for the VV channels depends on f_L. As a result, any systematic uncertainty on f_L translates into a systematic uncertainty on the efficiency through the following expression:

$$\frac{\Delta\epsilon}{\epsilon} = \frac{\epsilon_L - \epsilon_T}{f_L\epsilon_L + (1-f_L)\epsilon_T}\Delta f_L \tag{9.3}$$

The systematic error on f_L (Δf_L) is given in Sec. 9.4; the longitudinal and transverse signal efficiencies are given in Tab. 8.1.

9.3   Charge asymmetry systematics

Most of the systematic uncertainties found for branching fraction measurements cancel for the charge asymmetry measurement. The primary sources of bias could be due to tracking differences between opposite charged tracks, PID differences, differences due to the interaction cross sections in the detector and the effect of $B\overline{B}$ background.

We have studied this bias in a number of ways including control samples and fits to other data samples. The bias for large samples of signal MC with a high-momentum pion is small, typically consistent with zero and the bias for modes with a high-momentum kaon is -0.007 ± 0.002 [54]. The measured asymmetry for $q\bar{q}$ data is near -0.001 ± 0.004 (Sec. 11.2 of [54]). It is not clear why we see a difference between the values in data and MC. We use a combination of control sample studies [55], various calculations of detector interaction effects and the results mentioned above from [54] to conclude that an approximate average $\mathcal{A}_{ch}$ bias is -0.010 ± 0.005 for modes with a primary kaon and 0.000 ± 0.005 for modes with a primary pion. We assign a correction and systematic, as appropriate, to the signal charge asymmetries. Because of the softer momentum spectrum of the kaons and pions here, we assign a systematic error of 0.015 rather than 0.005. This is supported by the charge asymmetry of the background; the corrected background $\mathcal{A}_{ch}$ is always smaller than 0.015.

To study the potential effect of a bias due to $\mathcal{A}_{ch}$ from $B\overline{B}$ background, we fix the charmless $B\overline{B}$ $\mathcal{A}_{ch}$ to ± 0.10 in the fit and take the change in the signal $\mathcal{A}_{ch}$ as a systematic error. This effect is negligible (the change is $\lesssim 0.005$ in all cases).

In addition, there can be a dilution effect due to the yield fit bias. This effect has been

very small for most previous studies. Since the asymmetry and fit biases are fairly small for this analysis, we take this effect to be negligible for this analysis also.

We round the total $\mathcal{A}_{ch}$ systematic error up to 0.02 for all measurements.

9.4 Systematic uncertainty on f_L

We report the systematic uncertainties of f_L for $\rho^0 K^{*0}$ and $\rho^- K^{*+}$ in Tab. 9.3.

- Bias uncertainty: We use embedded toy MC to evaluate any bias in the f_L measurements. We correct for the bias and assign an uncertainty equal to 100% of its value $\oplus$ the uncertainty on the bias.

- ML fit: We vary the signal parameters as discussed in Sec. 9.1.

- $B\overline{B}$ background: We assign a uncertainties based on varying the $B\overline{B}$ background yields within their uncertainties, as in Sec. 9.1.

- $f_0(980)$ width: We allow the f_0 width and mean to float in the $\rho^0/f_0 K^{*0}$ fit and take half the shift in $\rho^0 K^{*0}$ f_L as a systematic.

Table 9.3: Estimates of systematic errors on f_L.

Quantity	$\rho^0 K^{*0}$	$\rho^- K^{*+}$
Bias	0.046	0.016
ML fit	0.003	0.012
$B\overline{B}$ background	0.019	0.024
$f_0(980)$ width	0.004	—
Total	0.050	0.031

Chapter 10

Summary and Discussion

We observe for the first time $B^0 \to f_0 K^*(892)^0$, $\rho^- K^*(892)^+$, and $\rho^0 (K\pi)_0^{*0}$ with greater than 5σ significance, including systematics. We present first evidence for $B^0 \to f_0(K\pi)_0^{*0}$ with 3.0σ and $f_0 K_2^*(1430)^0$ with 4.4σ significance. All branching fraction measurements have greater than 3σ significance including systematics, except $\rho^-(K\pi)_0^{*+}$ for which we also quote a 90% C.L. upper limit. No significant direct CP-violation is observed. Our results are consistent with and supersede those reported in Ref. [28].

For the $K^*(892)$ modes, we find the following results

$$\mathcal{B}(B^0 \to \rho^0 K^{*0}) = (5.1 \pm 0.6 \pm 0.5) \times 10^{-6} \quad (10.1)$$

$$f_L(\rho^0 K^{*0}) = 0.40 \pm 0.08 \pm 0.05$$

$$\mathcal{A}_{ch}(\rho^0 K^{*0}) = -0.06 \pm 0.09 \pm 0.02$$

$$\mathcal{B}(B^0 \to \rho^- K^{*+}) = (10.3 \pm 2.3 \pm 1.3) \times 10^{-6} \quad (10.2)$$

$$f_L(\rho^- K^{*+}) = 0.38 \pm 0.13 \pm 0.03$$

$$\mathcal{A}_{ch}(\rho^- K^{*+}) = +0.21 \pm 0.15 \pm 0.02$$

$$\mathcal{B}(B^0 \to f_0 K^{*0}) \times \mathcal{B}(f_0 \to \pi\pi) \times \mathcal{B}(f_0 \to \pi\pi) = (5.7 \pm 0.6 \pm 0.3) \times 10^{-6} \quad (10.3)$$

$$\mathcal{A}_{ch}(f_0 K^{*0}) = +0.07 \pm 0.10 \pm 0.02 \,.$$

The $\rho^0 K^{*0}$ results agree with previous *BABAR* [28] and Belle [34, 35] results and are consistent with predictions from QCDF [9, 36, 10]. The $\rho^- K^{*+}$ results are within the previous *BABAR* upper limit and agree with QCDF predictions. Both $\rho^0 K^{*0}$ and $\rho^- K^{*+}$ BFs are, however, higher than the theory central values. The predicted f_L for $\rho^- K^{*+}$ is higher than the measured value, though the theory errors are still large. We find a branching fraction for $f_0 K^{*0}$ somewhat larger than previous 90% CL upper limits, though it is within one sigma of the QCDF prediction[37].

For $f_0(K\pi)_0^{*0}$ and $f_0 K_2^*(1430)^0$, we find,

$$\mathcal{B}(B^0 \to f_0(K\pi)_0^{*0}) \times \mathcal{B}(f_0 \to \pi\pi) \times \mathcal{B}((K\pi)_0^* \to K\pi)$$

$$= (3.1 \pm 0.8 \pm 0.7) \times 10^{-6} \quad (10.4)$$

$$\mathcal{B}(B^0 \to f_0 K_2^*(1430)^0) \times \mathcal{B}(f_0 \to \pi\pi)$$

$$= (8.6 \pm 1.7 \pm 0.9) \times 10^{-6} \,. \quad (10.5)$$

We are aware of no theoretical predictions with which to compare these results.

For $\rho(K\pi)_0^*$, we find,

$$\mathcal{B}(B^0 \to \rho^0 (K\pi)_0^{*0}) \times \mathcal{B}((K\pi)_0^* \to K\pi)$$

$$= (31 \pm 4 \pm 3) \times 10^{-6} \tag{10.6}$$

$$\mathcal{B}(B^0 \to \rho^- (K\pi)_0^{*+}) \times \mathcal{B}((K\pi)_0^* \to K\pi)$$

$$= (32 \pm 10 \pm 6) \times 10^{-6} \tag{10.7}$$

$$< 48 \times 10^{-6} . \tag{10.8}$$

Using the $K_0^*(1430)^0$ resonant fraction of the LASS $(K\pi)_0^{*0}$ from Ref. [5], we can calculate the branching fractions for the $K_0^*(1430)$ component of our $(K\pi)_0^*$ channels. We find,

$$\mathcal{B}(B^0 \to \rho^0 K_0^*(1430)^0) = 27 \pm 4 \pm 2 \pm 3 \tag{10.9}$$

$$\mathcal{B}(B^0 \to f_0 K_0^*(1430)^0) \times \mathcal{B}(f_0 \to \pi\pi) = 2.7 \pm 0.7 \pm 0.5 \pm 0.3 \tag{10.10}$$

$$\mathcal{B}(B^0 \to \rho^- K_0^*(1430)^+) = 28 \pm 10 \pm 5 \pm 3 . \tag{10.11}$$

These results are consistent with the QCDF predictions [37], though the experimental central values are lower than the predictions. The pQCD predictions, however, are 4σ low for $\rho^0 K_0^*(1430)^0$ and 1.4σ low for $\rho^- K_0^*(1430)^+$ in the second scenario presented in Ref. [38] (SII); the situation is worse in the first scenario (SI), in which the predicted central value $\mathcal{B}$'s are roughly an order of magnitude too small for $\rho^- K_0^*(1430)^+$ and a factor of 50 too small for $\rho^0 K_0^*(1430)^0$. The difference between the two pQCD scenarios involves including the $K_0^*(1430)$ resonances in the lowest lying $q\bar{q}$ scalar nonet (SII) or in the first excited state nonet (SI).

10.1   Discussion of f_L measurements

As mentioned in Ch. 1, QCD Factorization [9, 36, 10] predicts the following hierarchy pattern for the $\rho K^*(892)$ polarization fractions,

$$f_L(\rho^0 K^{*+}) > f_L(\rho^- K^{*+}) > f_L(\rho^+ K^{*0}) > f_L(\rho^0 K^{*0}) . \tag{10.12}$$

We compare the experimental values including our updated results. We use the *BABAR* result in Ref. [32] for the $\rho^0 K^{*+}$ polarization ($f_L(\rho^0 K^{*+}) = 0.78 \pm 0.12$) and averaging the previous *BABAR* [28] and Belle [35] results for $\rho^+ K^{*0}$ ($f_L(\rho^+ K^{*0}) = 0.47 \pm 0.08$). Thus we find

$$
\begin{array}{ccccccc}
f_L(\rho^0 K^{*+}) & > & f_L(\rho^+ K^{*0}) & \gtrsim & f_L(\rho^0 K^{*0}) & \gtrsim & f_L(\rho^- K^{*+}) \\
0.78 \pm 0.12 & & 0.47 \pm 0.08 & & 0.40 \pm 0.08 \pm 0.05 & & 0.38 \pm 0.13 \pm 0.03
\end{array}
\tag{10.13}
$$

which agrees with the experimental finding that f_L ($\rho^0 K^{*+}$) is largest. With the current experimental sensitivities, the three smallest f_L values are consistent with each other at 1σ. Thus a true comparison of the rest of the hierarchy requires additional experimental input.

We can compare the f_L results from $\rho K^*(892)$ to the other VV channels in which f_L has been measured. A compilation of charmless longitudinal polarization fraction results as of August 2010 is given in Fig. 10.1 [26]. The $\rho K^*(892)$ f_L values measured in this thesis are somewhat lower than, but consistent with, the ϕK^* and ωK^* results, which are also dominated by penguin diagrams.

10.2 Branching fraction comparison for $\rho K_0^*(1430)$ and $\pi K_0^*(1430)$

In Ref. [37], Cheng *et. al.* find that in QCDF the rates for $B \to \rho K_0^*(1430)$ are substantially larger than those for $\pi K_0^*(1430)$ because two penguin amplitudes contribute constructively for ρ and destructively for π. Though Cheng *et. al.* find that their predictions for $\pi K_0^*(1430)$ channels are typically low compared to experiment by a factor of $3 - 4$. The QCDF predictions in Ref. [37] do not include weak annihilation amplitudes, which the authors suspect are important for the $\pi K_0^*(1430)$ channels. In Tab. 10.1 we compare the measured $\pi K_0^*(1430)$ world average branching fractions with the $\rho K_0^*(1430)$ branching fractions measured in this thesis [26]. Only the $B^0 \to (d\overline{u})^- K_0^*(1430)^+$ channel has been measured for both ρ and π; in this channel, the branching fractions are in excellent agreement, contrary to the prediction that the ρ channels should have
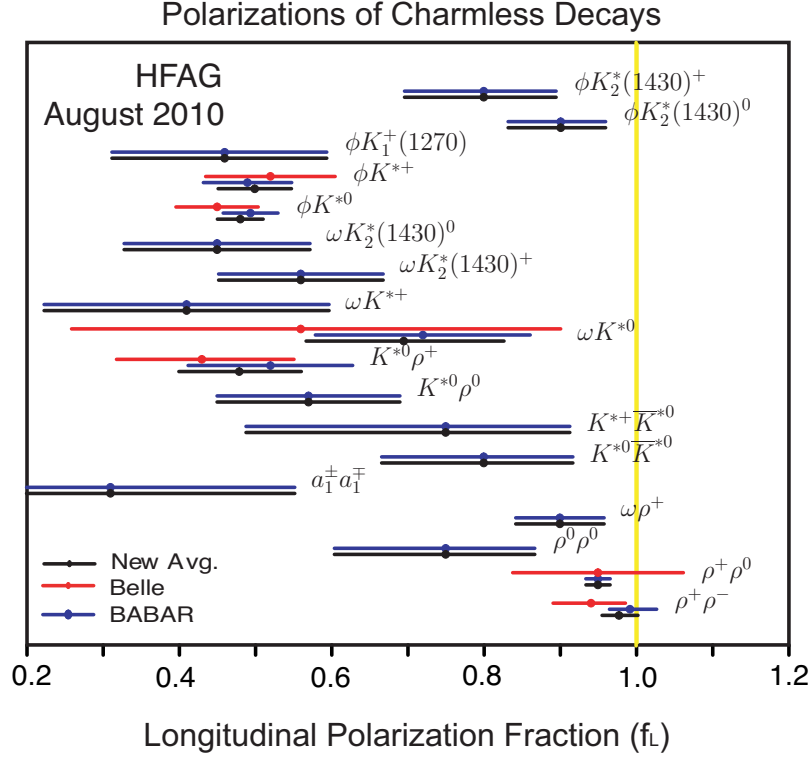
Figure 10.1: World average f_L results from charmless B decays [26].

Table 10.1: Branching fraction comparison between $B \rightarrow \pi K_0^*(1430)$ [26] and $\rho K_0^*(1430)$ channels.

$\pi K_0^*(1430)$	BF	$\rho K_0^*(1430)$	BF
$\pi^+ K_0^*(1430)^0$	45^{+9}_{-7}	$\rho^+ K_0^*(1430)^0$	—
$\pi^0 K_0^*(1430)^+$	—	$\rho^0 K_0^*(1430)^+$	—
$\pi^+ K_0^*(1430)^+$	33 ± 7	$\rho^- K_0^*(1430)^+$	$28 \pm 10 \pm 5 \pm 3$
$\pi^0 K_0^*(1430)^0$	—	$\rho^0 K_0^*(1430)^0$	$27 \pm 4 \pm 2 \pm 3$

larger rates than the π channels.

Table 10.2: Summary of the results presented in this thesis, recent Belle results, and recent theoretical predictions from QCDF. Branching fractions are in units of 10^{-6}. The upper limits are at the 90% confidence level. The predicted $f_0 K^{*0}$ BF is multiplied by a factor of $3/4$, as Ref. [37] includes a factor of $\mathcal{B}(f_0 \to \pi^+ \pi^-) = 0.5$, whereas this thesis uses only the isospin ratio $\Gamma(f_0 \to \pi^+ \pi^-)/\Gamma(f_0 \to \pi\pi) = 2/3$. †In [9, 36] it is pointed out than an error in [10] causes the f_L predictions for $\rho^0 K^{*0}$ to be under-estimated.

	BABAR (this thesis)	Belle[34]	CY[9, 36]	BRY[10]
$B^0 \to \rho^0 K^{*0}$				
$\mathcal{B}$	$5.1 \pm 0.6 \pm 0.5$	$2.1^{+0.8+0.9}_{-0.7-0.5}$	$4.6^{+3.6}_{-3.5}$	$2.4^{+3.5}_{-2.0}$
f_L	$0.40 \pm 0.08 \pm 0.05$	—	$0.39^{+0.60}_{-0.31}$	$^\dagger 0.22^{+0.53}_{-0.14}$
A_{CP}	$-0.06 \pm 0.09 \pm 0.02$	—	—	$-0.15^{+0.17}_{-0.32}$
$B^0 \to \rho^- K^{*+}$				
$\mathcal{B}$	$10.3 \pm 2.3 \pm 1.3$	—	$8.9^{+4.9}_{-5.6}$	$5.5^{+5.9}_{-3.3}$
f_L	$0.38 \pm 0.13 \pm 0.03$	—	$0.53^{+0.45}_{-0.32}$	$0.61^{+0.38}_{-0.29}$
A_{CP}	$+0.21 \pm 0.15 \pm 0.02$	—	—	$0.05^{+0.40}_{-0.17}$
	BABAR (this thesis)	Belle[34]	CCY[37]	
$B^0 \to f_0 K^{*0}$				
$\mathcal{B}$	$5.7 \pm 0.6 \pm 0.3$	< 2.2	$4.8^{+5.3}_{-2.0}$	
A_{CP}	$+0.07 \pm 0.10 \pm 0.02$	—	—	

10.3 Numerical comparisons with theory

In Tab. 10.2 we compare the $K^*(892)$ results measured in this thesis with theoretical predictions and, if available, Belle results. The predicted $f_0 K^{*0}$ BF is scaled up by a factor of 0.75, as Ref. [37] includes a factor of $\mathcal{B}(f_0 \to \pi^+ \pi^-) = 0.5$, whereas this thesis uses only the isospin ratio $\Gamma(f_0 \to \pi^+ \pi^-)/\Gamma(f_0 \to \pi\pi) = 2/3$. In Tab. 10.3 we perform the same comparison for the $(K\pi)_0^*$ channels.

Table 10.3: Results from this thesis compared with recent theoretical predictions from QCDF [37] and pQCD [38]. Branching fractions are in units of 10^{-6}. The two scenarios reported in Ref. [38] represent two interpretations of the scalar mesons (see Sec. 3.1). For simplicity, we have added the theory errors in quadrature.

Branching Fraction	*BABAR* (this thesis)	QCDF [37]	pQCD SI [38]	pQCD SII [38]
$\mathcal{B}(B^0 \rightarrow \rho^0 K_0^*(1430)^0)$	$27 \pm 4 \pm 2 \pm 3$	37^{+27}_{-14}	$0.47^{+0.24}_{-0.21}$	$4.8^{+1.5}_{-1.0}$
$\mathcal{B}(B^0 \rightarrow \rho^- K_0^*(1430)^+)$	$28 \pm 10 \pm 5 \pm 3$	51^{+71}_{-27}	$3.3^{+1.1}_{-1.0}$	$10.5^{+4.4}_{-2.6}$

Appendix A

PDF Plots, Correlations, and Final Parameter Values in $K^*(892)$ Channels

In the following sections, we include PDF plots, correlations, and the values of the parameters that float in the final fits for our $K^*(892)$ (LMR) analyses. The naming convention for the floating parameters is: ΔE polynomial coefficients (`de_Bkg_P01`); $\mathcal{F}$ mean (`fis_BkgC_mean`), $\mathcal{F}$ rms (`fis_BkgC_rms`), $\mathcal{F}$ asymmetry (`fis_BkgC_asym`); m_{ES} ARGUS exponent (`mes_Bkg_c`); real ρ or K^* fraction (e.g. `mR_Bkg_fracS`); resonance background slope terms (e.g. `mR_Bkg_Poly_P01`); and polynomial coefficients for the ρ and K^* helicities (e.g. `hK_Bkg_P01`). We include the fit yield of background (`nBkg`) and signal events (`nRKst1` and `nf0Kst1`), the longitudinal fraction of $B \to \rho K^*$ (`fL`), and the fraction of positively charged events in the signal sample (`Frac_nRKst1_chgCat_Plus` and `Frac_nf0Kst1_chgCat_Plus`).

For the plots, individual components of a two component fit such as a double Gaussian are shown as dashed and dot-dashed lines.

Resonant mass PDFs are occasionally fit on one MC sample and used to describe that resonance in a similar mode. For example, in the $\rho^- K^{*+}$ analysis, the ρ^- mass is fit on $\rho^- K^{*+}$

MC, but the same PDF is used to describe the $\pi^0\pi^-$ mass for $\rho^-\rho^+$ $B\overline{B}$ background. In such cases, the PDF (blue dashed line) is overlaid on the signal MC sample in question (histogram). The scaling between PDF and MC is approximate.

A.1 $B^0 \rightarrow \rho^0 K^*(892)^0$ **Correlations, Fit Results, and PDF Plots**

A.1.1 $\rho^0 K^*(892)^0$ **Correlation Tables**

```
 Correlation matrix for onData:
               mES      deltaE     fisher     mKstar      mRho      hKstar
  deltaE    -0.0158
  fisher    -0.0646     0.0045
  mKstar     0.0130    -0.0032    -0.0198
    mRho     0.0216    -0.0143    -0.0607     0.0082
  hKstar     0.0044    -0.0025     0.0212    -0.0096    -0.0036
    hRho     0.0174    -0.0168    -0.0727     0.0146     0.1169    -0.0006


Correlation matrix for RKst0MC:
               mES      deltaE     fisher     mKstar      mRho      hKstar
  deltaE    -0.0444
  fisher    -0.0513    -0.0128
  mKstar     0.0271    -0.0133    -0.0179
    mRho     0.0107     0.0014    -0.0230     0.0022
  hKstar     0.1143     0.0309    -0.0174     0.0087    -0.0504
    hRho    -0.0766    -0.0116     0.0444    -0.0167     0.0315    -0.0459


 Correlation matrix for RKst1LMC:
               mES      deltaE     fisher     mKstar      mRho      hKstar
  deltaE    -0.1018
  fisher    -0.0105    -0.0049
  mKstar     0.0094     0.0221    -0.0050
    mRho    -0.0329     0.0379    -0.0002    -0.0008
  hKstar     0.0177    -0.0154     0.0120     0.0120     0.0000
    hRho    -0.0509     0.0278     0.0035    -0.0097     0.0175     0.0269


 Correlation matrix for RKst1TMC:
               mES      deltaE     fisher     mKstar      mRho      hKstar
  deltaE    -0.0953
  fisher    -0.0148    -0.0108
  mKstar     0.0025     0.0307    -0.0068
    mRho    -0.0058     0.0162    -0.0083    -0.0035
```

```
  hKstar     0.0121   -0.0029   -0.0020    0.0051   -0.0026
    hRho    -0.0260   -0.0018    0.0017    0.0012    0.0008    0.0119
```

Correlation matrix for f0Kst0MC:

	mES	deltaE	fisher	mKstar	mRho	hKstar
deltaE	-0.0237					
fisher	-0.0497	-0.0157				
mKstar	0.0068	0.0055	-0.0156			
mRho	0.1062	0.0418	-0.0325	0.0043		
hKstar	0.0924	0.0361	-0.0260	-0.0039	0.1275	
hRho	-0.0466	-0.0086	0.0080	0.0009	-0.1334	0.0035

Correlation matrix for f0Kst1MC:

	mES	deltaE	fisher	mKstar	mRho	hKstar
deltaE	-0.0971					
fisher	-0.0149	-0.0066				
mKstar	-0.0042	0.0196	-0.0068			
mRho	0.0637	0.0307	-0.0186	0.0052		
hKstar	0.0159	-0.0155	0.0041	0.0125	0.0004	
hRho	-0.0466	0.0100	0.0014	0.0036	-0.0628	0.0217

Correlation matrix for a1mKpMC:

	mES	deltaE	fisher	mKstar	mRho	hKstar
deltaE	0.0164					
fisher	-0.0430	-0.0225				
mKstar	0.0226	-0.0115	-0.0132			
mRho	-0.0039	-0.0099	0.0008	-0.0051		
hKstar	0.0428	-0.0239	-0.0238	-0.0552	0.0532	
hRho	0.0531	-0.0634	-0.0117	-0.0037	0.0908	0.1227

Correlation matrix for f2KstLnMC:

	mES	deltaE	fisher	mKstar	mRho	hKstar
deltaE	-0.0407					
fisher	-0.0147	0.0085				
mKstar	0.0021	0.0080	-0.0096			
mRho	0.2073	-0.0718	-0.0479	0.0245		
hKstar	0.0082	-0.0088	-0.0160	0.0268	-0.0065	
hRho	-0.2075	0.0993	0.0353	-0.0122	-0.4113	0.0272

Correlation matrix for f2KstTrMC:

	mES	deltaE	fisher	mKstar	mRho	hKstar
deltaE	0.0181					
fisher	-0.0610	-0.0178				
mKstar	0.0105	0.0230	-0.0239			

```
    mRho     0.3500     0.0370    -0.0856    -0.0132
  hKstar     0.0022     0.0224     0.0038     0.0302    -0.0229
    hRho    -0.1970    -0.0765     0.0478    -0.0066    -0.3525     0.0164


Correlation matrix for DpiMC:
              mES     deltaE     fisher     mKstar       mRho     hKstar
  deltaE    -0.0520
  fisher    -0.0549     0.0038
  mKstar    -0.0449     0.0314     0.0045
    mRho     0.0298    -0.1218    -0.0289    -0.0033
  hKstar    -0.0640     0.0390     0.0052     0.2722    -0.0593
    hRho     0.1521    -0.1882    -0.0402    -0.0233    -0.0543     0.0495


Correlation matrix for D0BkgMC:
              mES     deltaE     fisher     mKstar       mRho     hKstar
  deltaE     0.0142
  fisher    -0.0153     0.0020
  mKstar    -0.0194     0.0514     0.0371
    mRho    -0.0075    -0.0659    -0.0039    -0.0259
  hKstar    -0.0026     0.0363    -0.0110     0.0629    -0.0049
    hRho     0.1427    -0.0895    -0.0595     0.0409    -0.0487    -0.0641


Correlation matrix for ChmlsMC:
              mES     deltaE     fisher     mKstar       mRho     hKstar
  deltaE    -0.0269
  fisher    -0.0227    -0.0102
  mKstar     0.0195    -0.0116     0.0093
    mRho    -0.0537     0.0639     0.0629     0.0017
  hKstar     0.1607    -0.1582     0.0023     0.0819     0.0235
    hRho    -0.0367     0.0374     0.0476     0.0241     0.2383     0.1904
```

A.1.2 $\rho^0 K^*(892)^0$ **Fit Results**

The Run 1-6 fit on $\rho^0 K^*(892)^0$ finds the following values for the parameters which were

allowed to float:

```
     Constant Parameter     Value
     --------------------  ------------
               biasfL      -4.5000e-02
                 effL       1.4340e-01
                 effT       2.5070e-01
            fitBiasR1       4.4000e+01
            fitBiasf1       2.1000e+00
                  nBB       4.7100e+02
                nChmls       7.6000e+01
               nD0Bkg       4.3300e+02
                 nDpi       2.0900e+02
               nRKst0       2.1500e+02
               na1mKp       1.5000e+01
              nf0Kst0       1.9000e+01
               nf2Kst       4.7000e+01
              prodBRf0      4.4400e-01
             prodBRrho      6.6670e-01


     Floating Parameter   InitialValue     FinalValue (+HiError,-LoError)       GblCorr.
     --------------------  ------------  ----------------------------------    --------
     Frac_nBkg_chgCat_Plus    5.1956e-01     5.1983e-01 (+3.99e-03,-3.99e-03)    0.149860
    Frac_nRKst1_chgCat_Plus   5.1956e-01     5.3194e-01 (+4.67e-02,-4.64e-02)    0.209085
    Frac_nf0Kst1_chgCat_Plus  5.1956e-01     4.6533e-01 (+5.10e-02,-5.06e-02)    0.138908
             de_Bkg_P01      -1.1603e-01    -1.3768e-01 (+1.34e-02,-1.35e-02)    0.018789
                    fL        5.0000e-01     3.5034e-01 (+7.37e-02,-8.08e-02)    0.534863
            fis_BkgC_asym    -2.1893e-01    -1.9203e-01 (+1.79e-02,-1.77e-02)    0.157782
            fis_BkgC_mean    -1.6937e-01    -1.4923e-01 (+6.60e-03,-6.58e-03)    0.358891
             fis_BkgC_rms     4.8618e-01     4.7366e-01 (+4.41e-03,-4.40e-03)    0.343322
              hK_Bkg_P01     -2.7581e-01    -2.8317e-01 (+1.59e-02,-1.58e-02)    0.551406
              hK_Bkg_P02      2.2191e-01     2.1028e-01 (+1.18e-02,-1.18e-02)    0.160898
              hK_Bkg_P03     -4.6645e-02    -6.0734e-02 (+1.24e-02,-1.24e-02)    0.551334
              hR_Bkg_P01      3.2441e-01     2.7618e-01 (+1.34e-02,-1.34e-02)    0.125106
```

```
          hR_Bkg_P02     1.4372e-01      1.1426e-01 (+1.24e-02,-1.24e-02)   0.070365
    mK_Bkg_Poly_P01     2.5177e-02      2.7766e-02 (+1.65e-02,-1.67e-02)   0.367206
    mK_Bkg_Poly_P02    -1.2796e-01     -1.3094e-01 (+2.11e-02,-2.08e-02)   0.625782
      mK_Bkg_fracKst     1.6692e-01      1.5963e-01 (+1.15e-02,-1.13e-02)   0.671722
    mR_Bkg_Poly_P01    -1.0238e-01     -1.1335e-01 (+2.03e-02,-2.05e-02)   0.665281
    mR_Bkg_Poly_P02    -8.2385e-02     -9.1596e-02 (+2.47e-02,-2.47e-02)   0.778904
      mR_Bkg_fracRho     1.1271e-01      1.2148e-01 (+1.61e-02,-1.63e-02)   0.805159
       mR_Bkg_fracf0     2.5791e-02      1.6976e-02 (+5.12e-03,-5.03e-03)   0.660306
         measBR_RKst1     5.0000e+00      5.0730e+00 (+6.53e-01,-6.28e-01)   0.572180
        measBR_f0Kst1     5.0000e+00      5.6939e+00 (+6.04e-01,-5.84e-01)   0.218344
            mes_Bkg_c    -2.8679e+01     -2.0140e+01 (+2.72e+00,-2.75e+00)   0.147246
                 nBkg     1.7309e+04      1.7092e+04 (+1.38e+02,-1.37e+02)   0.182568

Asym wrt Frac_nRKst1_chgCat_Plus
 1-2*(Frac_nRKst1_chgCat_Plus) = -0.0638797 +/- 0.093006 (+-0.0927479, -0.0933337)


Asym wrt Frac_nf0Kst1_chgCat_Plus
 1-2*(Frac_nf0Kst1_chgCat_Plus) = 0.0693485 +/- 0.101424 (+-0.101194, -0.101931)


Asym wrt Frac_nBkg_chgCat_Plus
 1-2*(Frac_nBkg_chgCat_Plus) = -0.0396523 +/- 0.00798304 (+-0.00797943, -0.00798752)
```

A.1.3 $\rho^0 K^*(892)^0$ **PDF Plots**
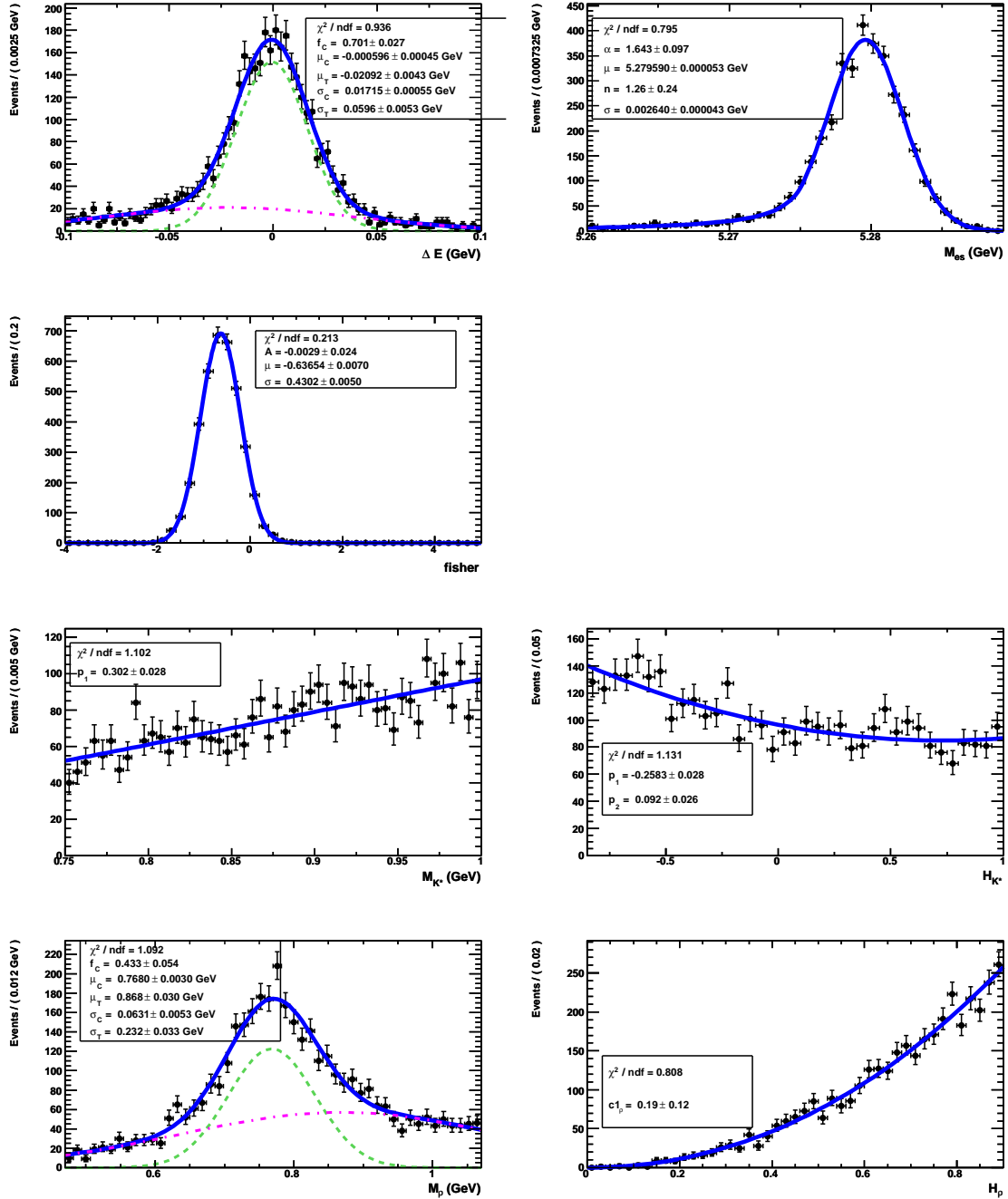
Figure A.1: PDFs for $\rho^0(K\pi)_0^{*0}$. From left to right, top to bottom: ΔE, m_{ES}, $\mathcal{F}$, $m(K^+\pi^-)$, $\mathcal{H}(K^+\pi^-)$, $m(\pi^+\pi^-)$, $\mathcal{H}(\pi^+\pi^-)$.
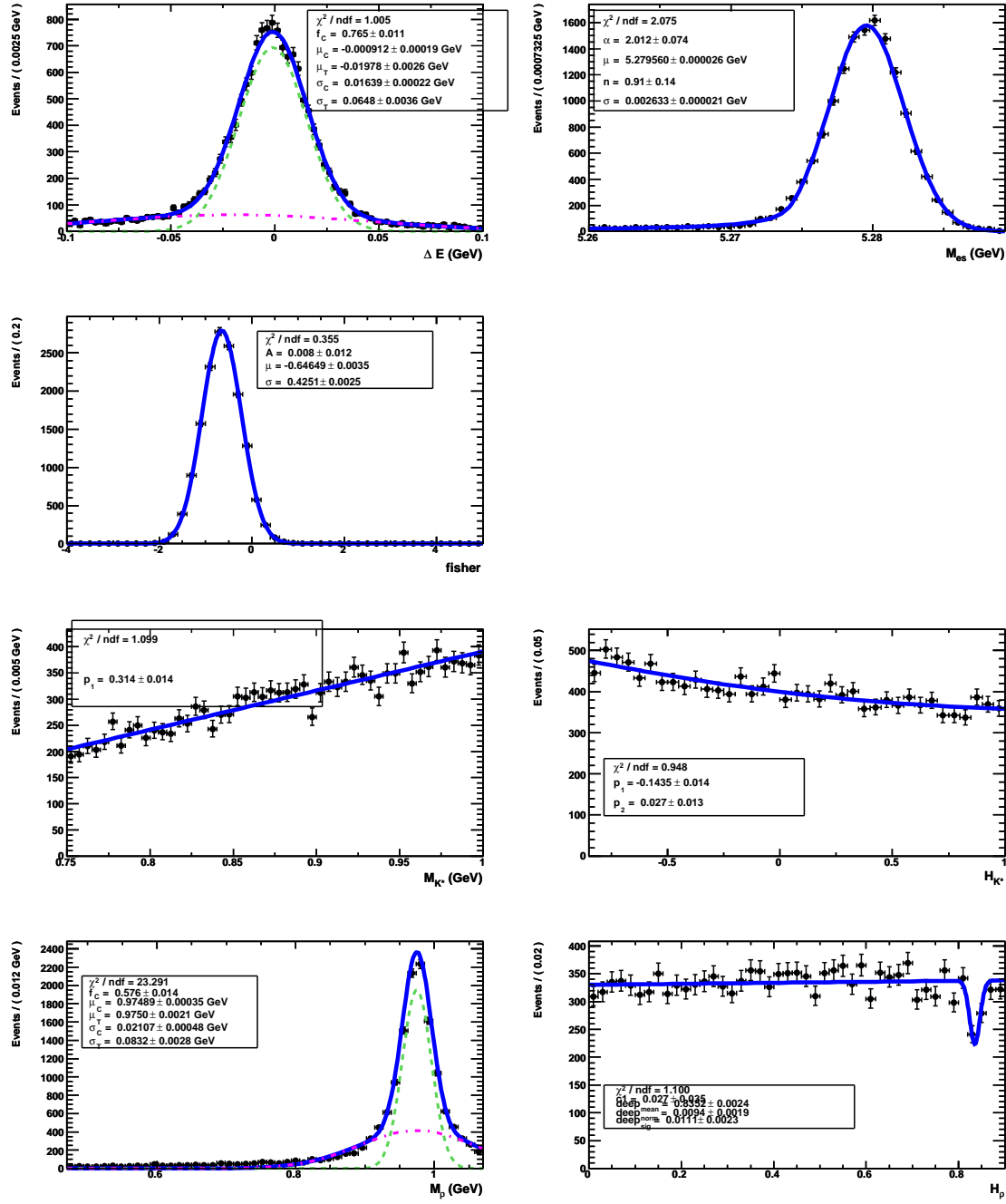
Figure A.2: PDFs for $f_0(K\pi)_0^{*0}$. From left to right, top to bottom: ΔE, m_{ES}, $\mathcal{F}$, $m(K^+\pi^-)$, $\mathcal{H}(K^+\pi^-)$, $m(\pi^+\pi^-)$, $\mathcal{H}(\pi^+\pi^-)$.
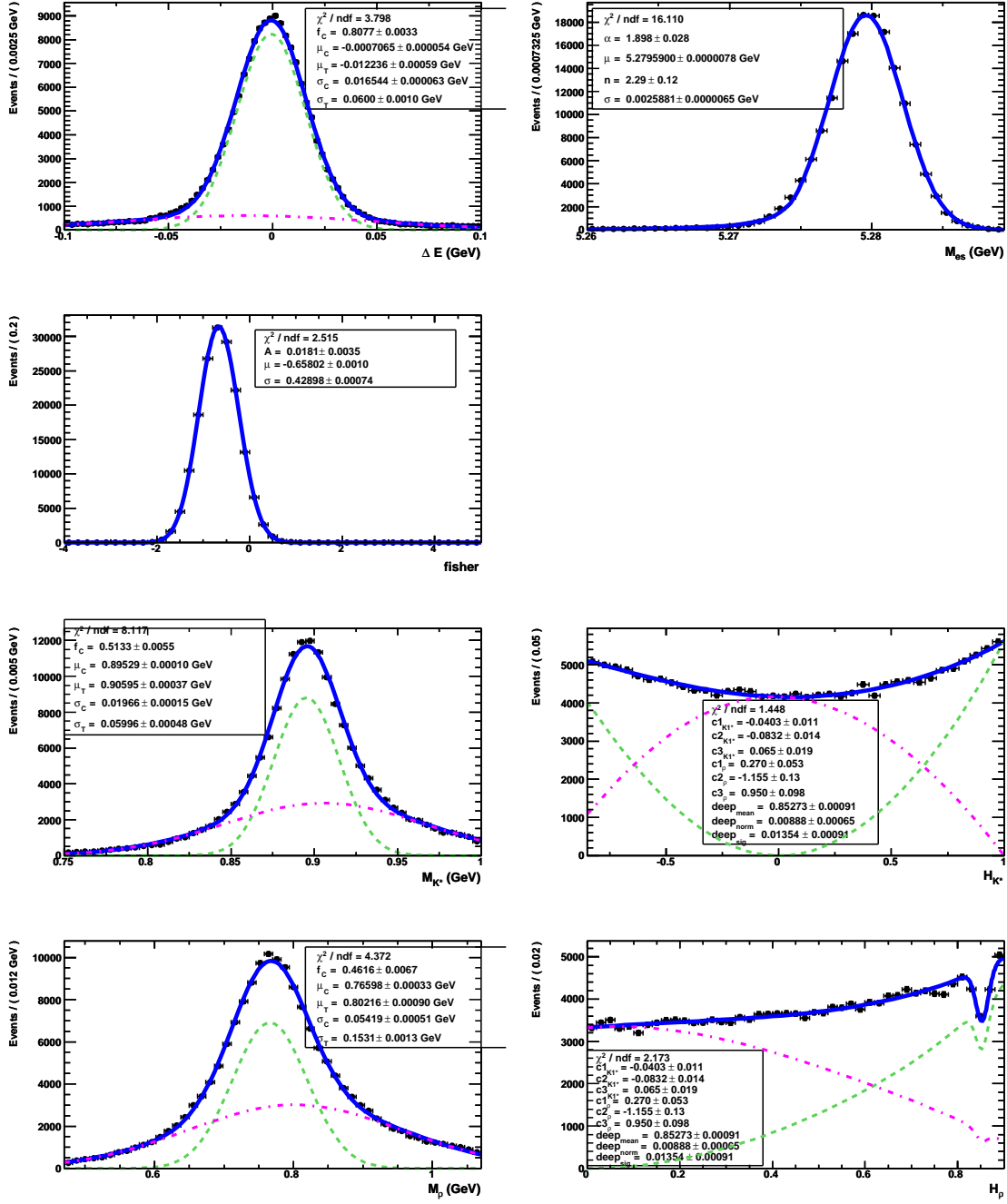
Figure A.3: PDFs for $\rho^0 K^*(892)^0$. From left to right, top to bottom: ΔE, m_{ES}, $\mathcal{F}$, $m(K^+\pi^-)$, $\mathcal{H}(K^+\pi^-)$, $m(\pi^+\pi^-)$, $\mathcal{H}(\pi^+\pi^-)$.
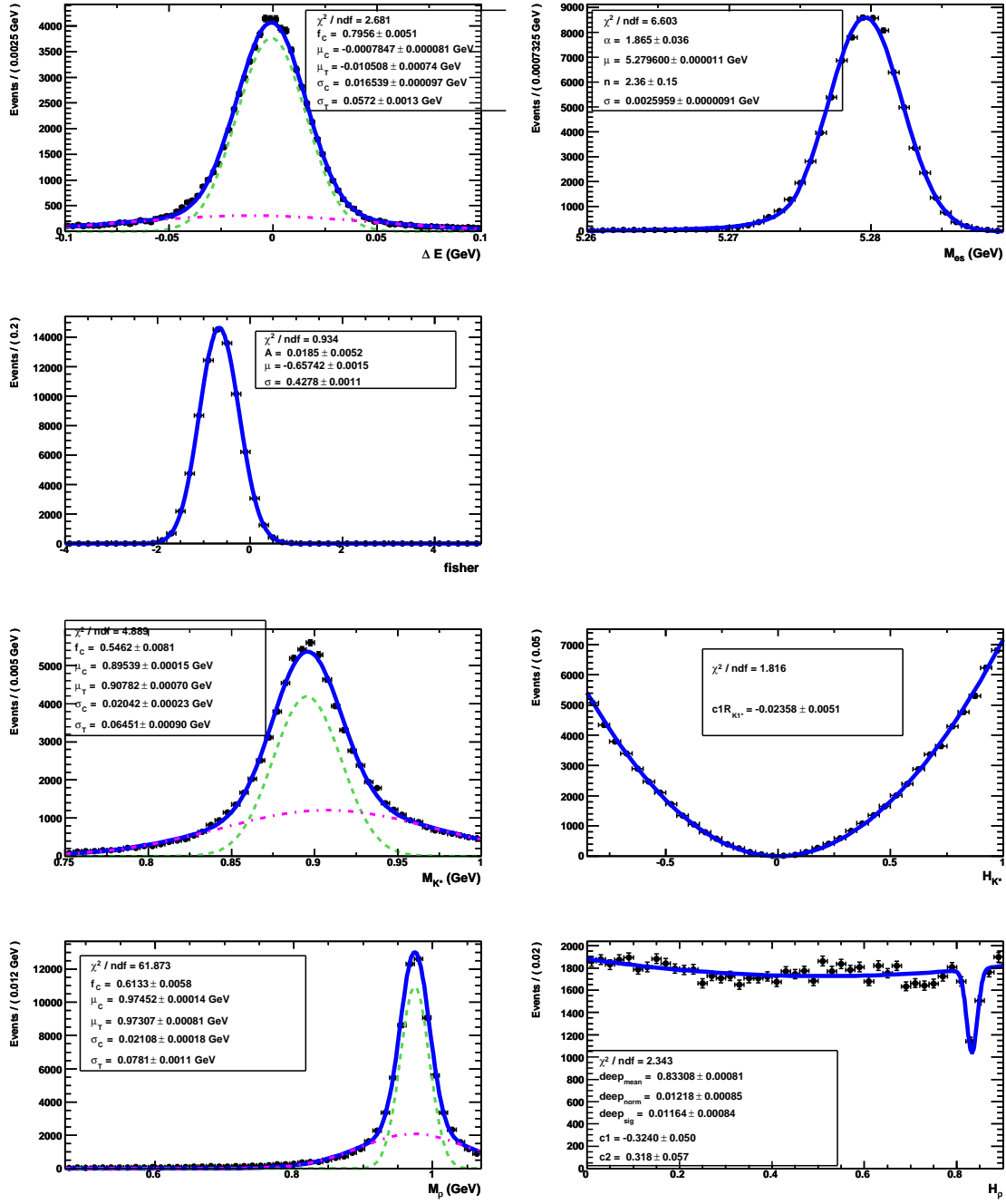
Figure A.4: PDFs for $f_0 K^*(892)^0$. From left to right, top to bottom: ΔE, m_{ES}, $\mathcal{F}$, $m(K^+\pi^-)$, $\mathcal{H}(K^+\pi^-)$, $m(\pi^+\pi^-)$, $\mathcal{H}(\pi^+\pi^-)$.
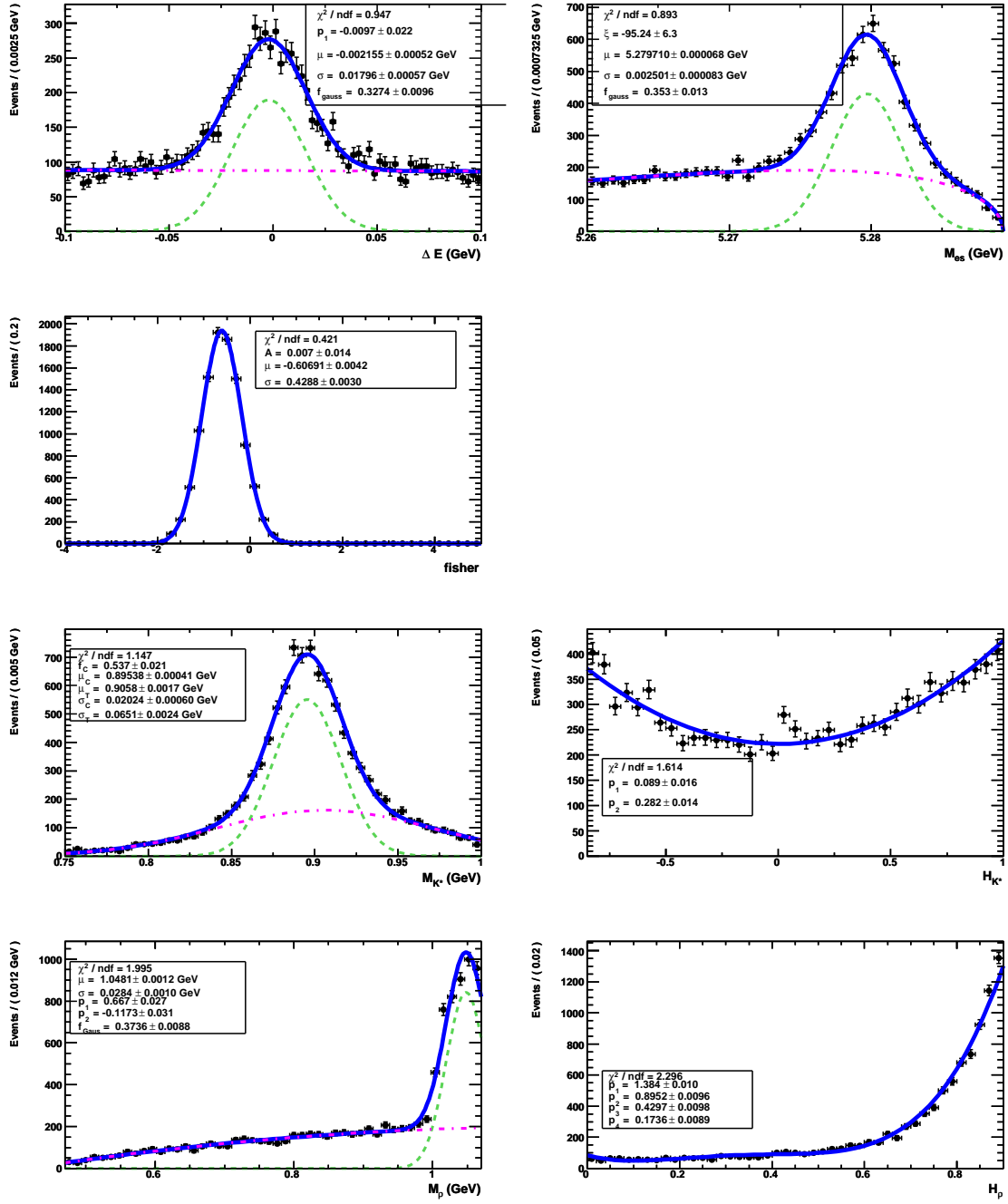
Figure A.5: PDFs for $f_2(1270)(K\pi)_0^{*0}$. From left to right, top to bottom: ΔE, m_{ES}, $\mathcal{F}$, $m(K^+\pi^-)$, $\mathcal{H}(K^+\pi^-)$, $m(\pi^+\pi^-)$, $\mathcal{H}(\pi^+\pi^-)$.
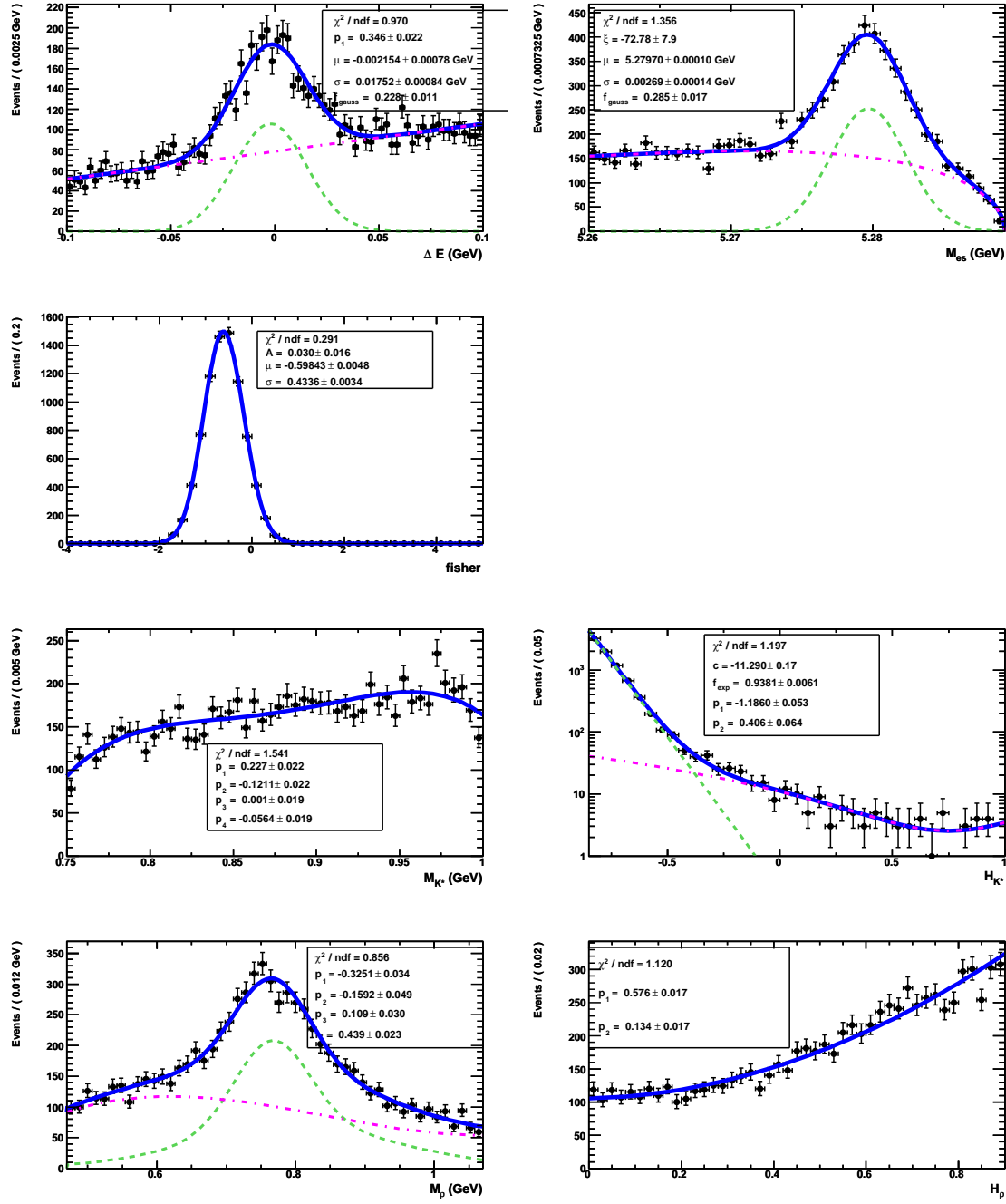
Figure A.6: PDFs for $a_1^- K^+$ (background to $B^0 \to \rho^0 K^*(892)^0$). From left to right, top to bottom: ΔE, m_{ES}, $\mathcal{F}$, $m(K^+\pi^-)$, $\mathcal{H}(K^+\pi^-)$, $m(\pi^+\pi^-)$, $\mathcal{H}(\pi^+\pi^-)$.
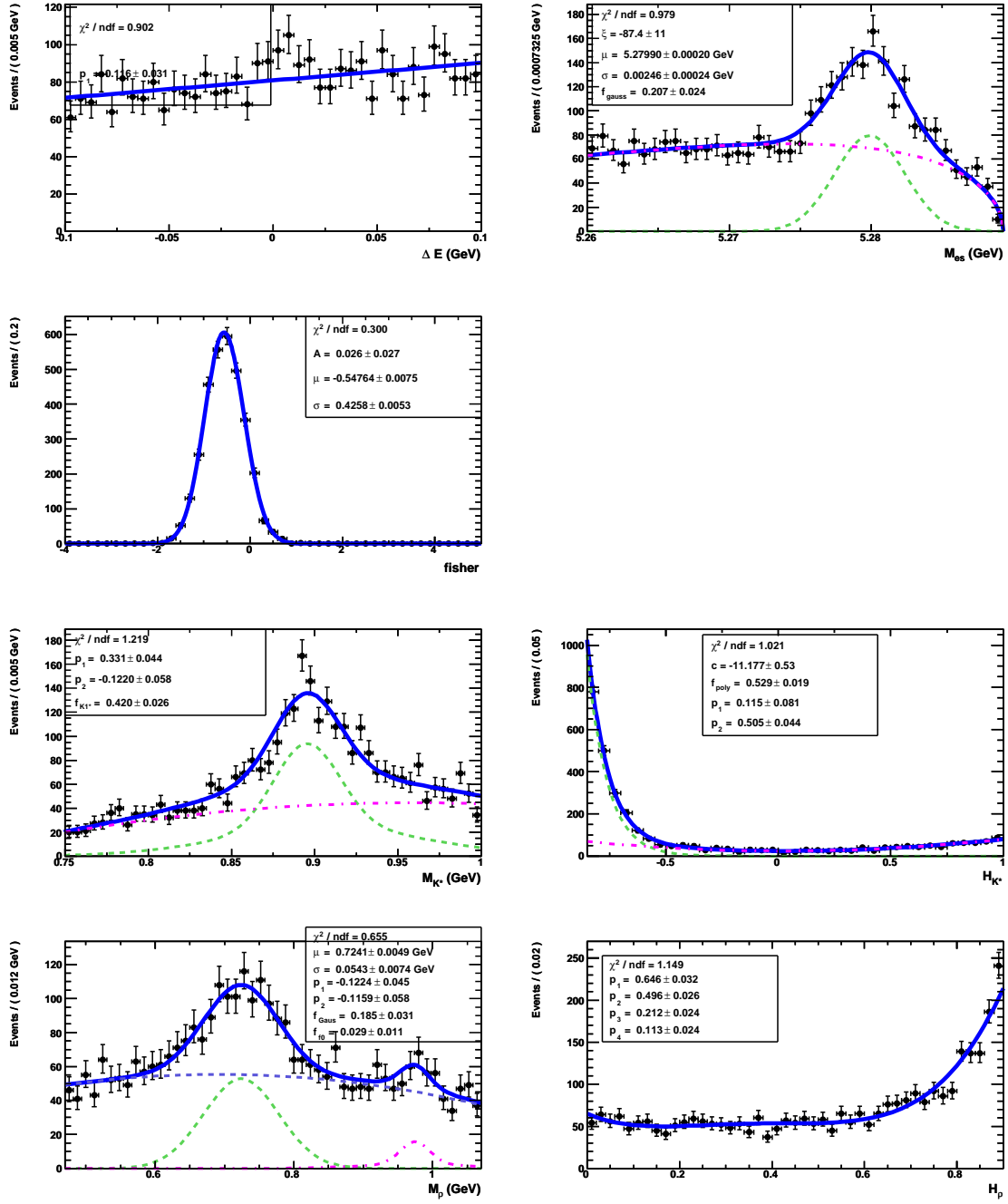
Figure A.7: PDFs for the charmless cocktail (background to $B^0 \to \rho^0 K^*(892)^0$). From left to right, top to bottom: ΔE, m_{ES}, $\mathcal{F}$, $m(K^+\pi^-)$, $\mathcal{H}(K^+\pi^-)$, $m(\pi^+\pi^-)$, $\mathcal{H}(\pi^+\pi^-)$.
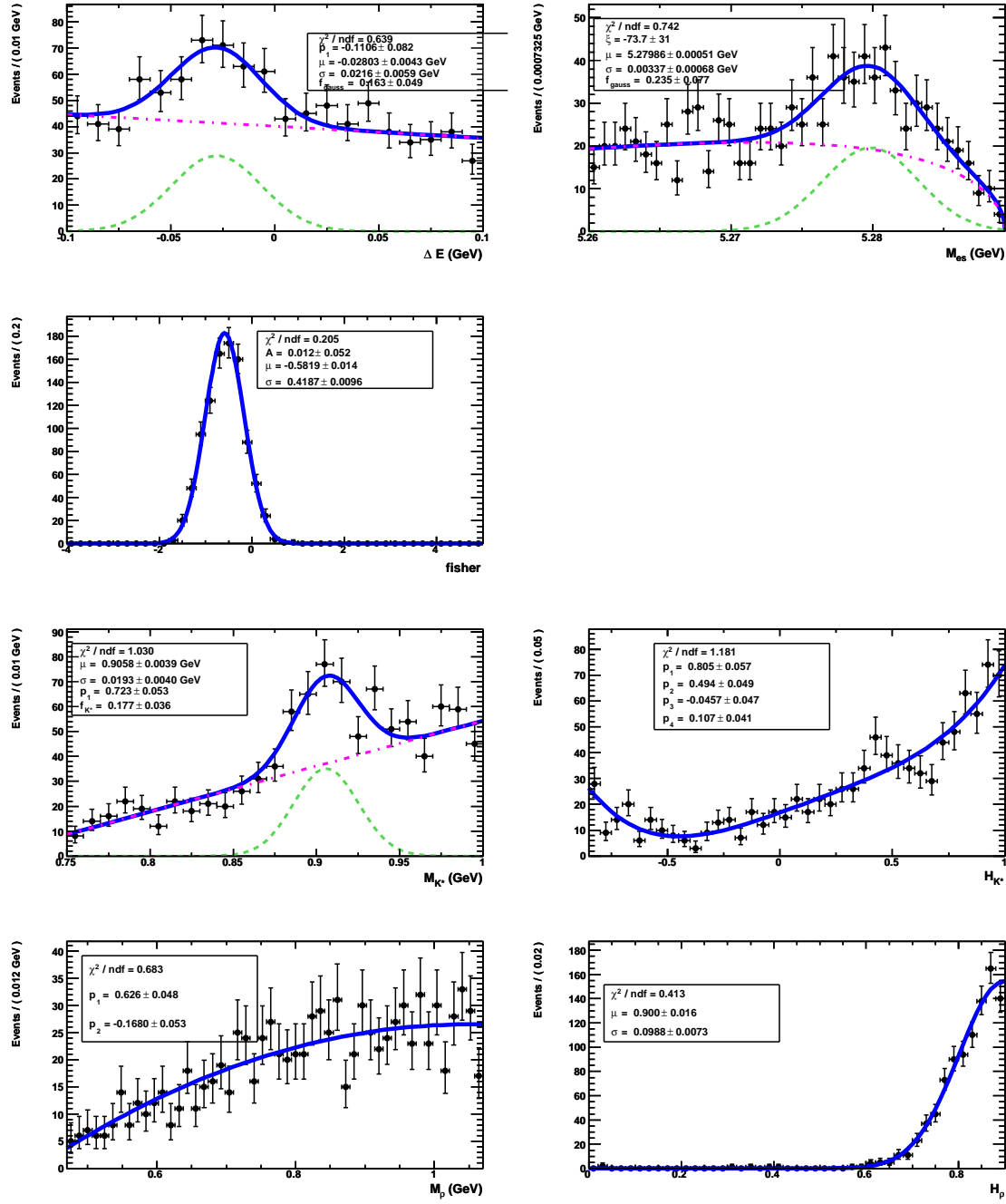
Figure A.8: PDFs for $B^0 \to D^-\pi^+$ with $D^- \to K^+\pi^-\pi^-$ (background to $B^0 \to \rho^0 K^*(892)^0$). From left to right, top to bottom: ΔE, m_{ES}, $\mathcal{F}$, $m(K^+\pi^-)$, $\mathcal{H}(K^+\pi^-)$, $m(\pi^+\pi^-)$, $\mathcal{H}(\pi^+\pi^-)$.
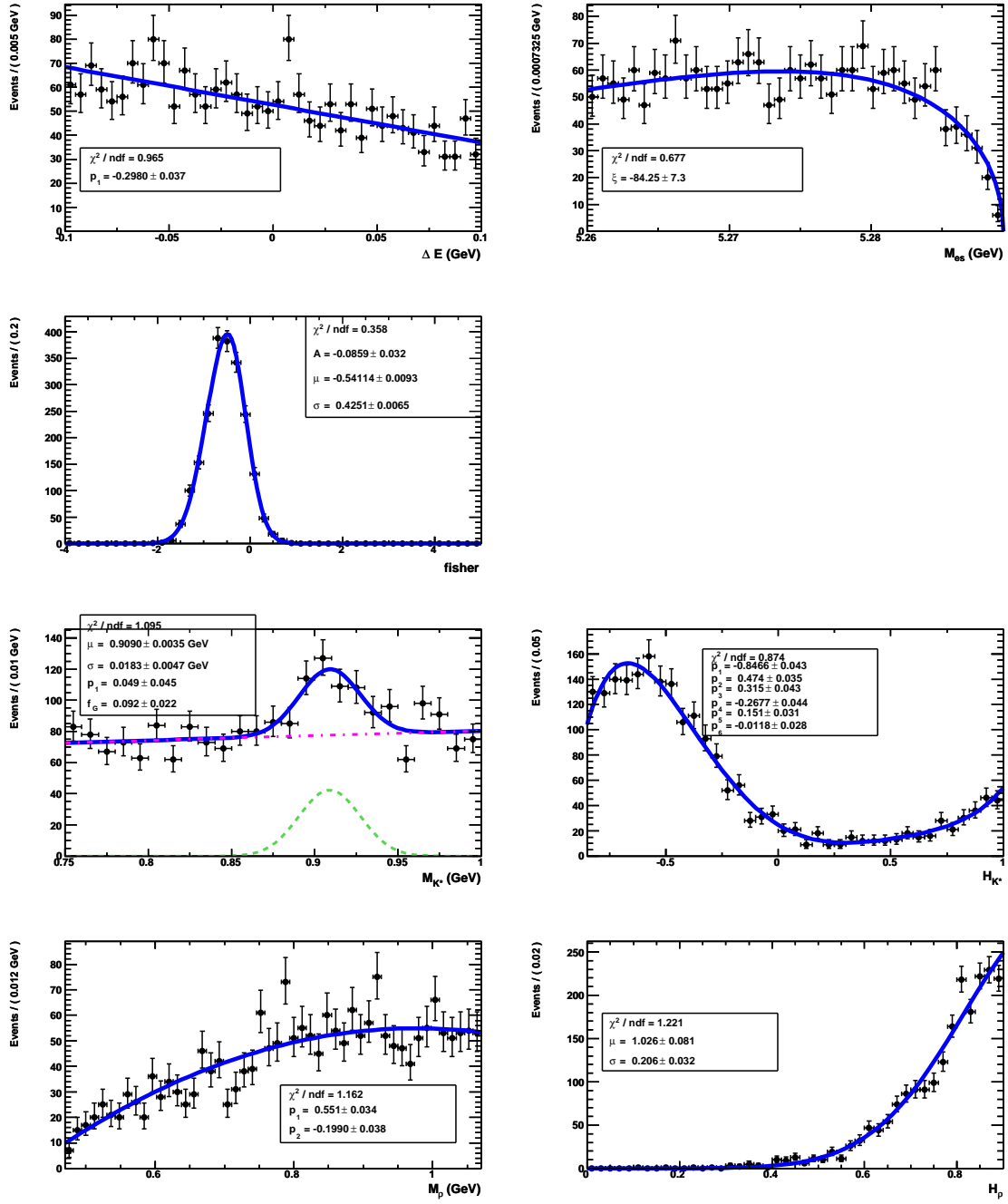
Figure A.9: PDFs for the D^0 cocktail (background to $B^0 \to \rho^0 K^*(892)^0$), which includes $\overline{D}^0 \pi^+$ and $\overline{D}^{*0} \pi^+$ with $\overline{D}^{*0} \to \overline{D}^0 \pi^0$ and $\overline{D}^0 \to K^+ \pi^- \pi^0$. From left to right, top to bottom: ΔE, m_{ES}, $\mathcal{F}$, $m(K^+\pi^-)$, $\mathcal{H}(K^+\pi^-)$, $m(\pi^+\pi^-)$, $\mathcal{H}(\pi^+\pi^-)$.
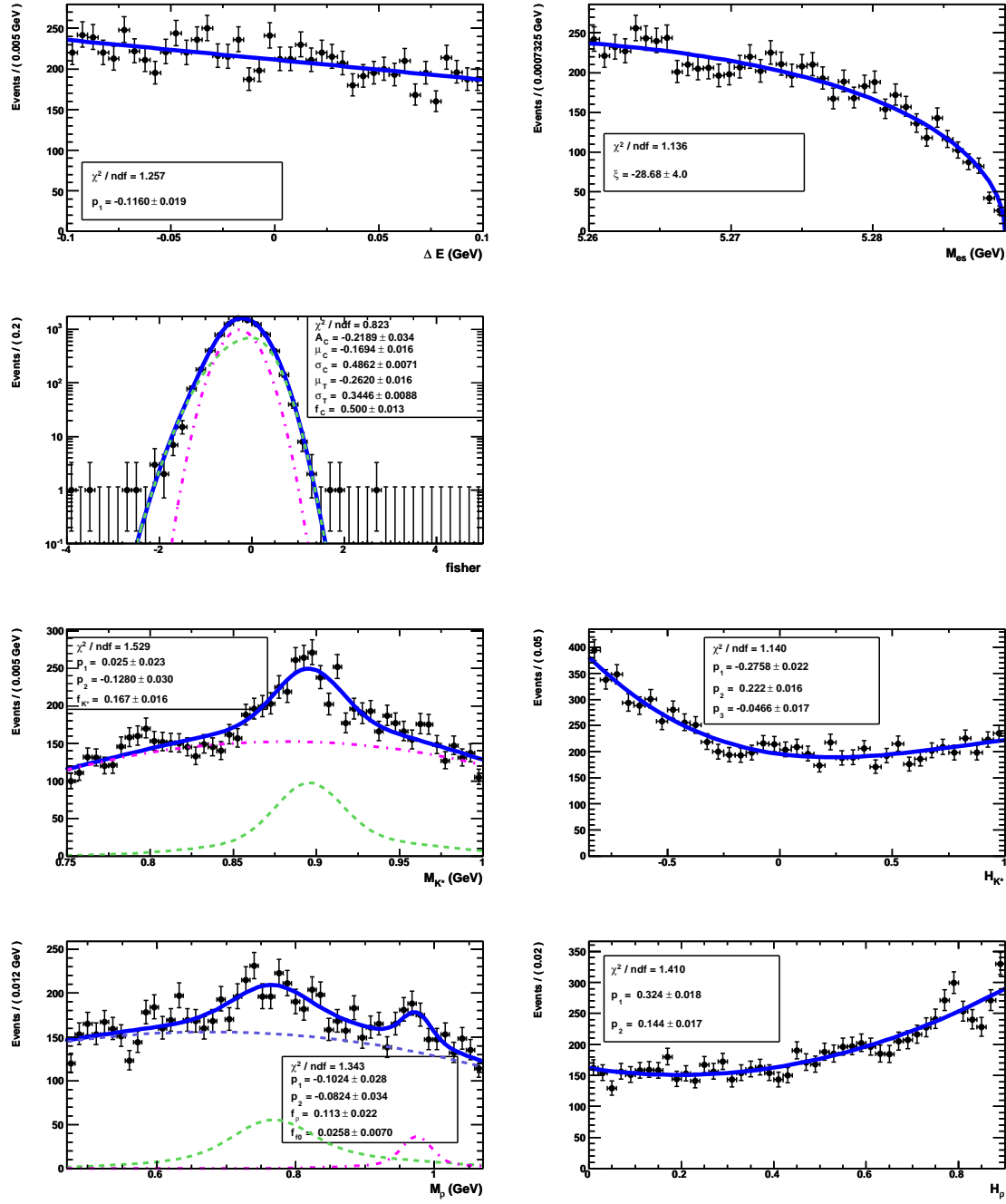
Figure A.10: PDFs for $q\bar{q}$ continuum background for $B^0 \rightarrow \rho^0 K^*(892)^0$. From left to right, top to bottom: ΔE, m_{ES}, $\mathcal{F}$, $m(K^+\pi^-)$, $\mathcal{H}(K^+\pi^-)$, $m(\pi^+\pi^-)$, $\mathcal{H}(\pi^+\pi^-)$.

A.2 $B^0 \to \rho^- K^{*+}$ **Correlations, Fit Results, and PDF Plots**

A.2.1 $\rho^- K^{*+}$ **Correlation Tables**

```
 Correlation matrix for onData:
            mES     deltaE    fisher    mKstar     mRho     hKstar
  deltaE   -0.0022
  fisher   -0.0218   -0.0195
  mKstar   -0.0038   -0.0065   -0.0486
    mRho    0.0105   -0.0002   -0.0502    0.0108
  hKstar    0.0020    0.0018    0.0275    0.0544    0.0273
    hRho    0.0304   -0.0032   -0.0370   -0.0223    0.0742   -0.0627

Correlation matrix for RKst0MC:
            mES     deltaE    fisher    mKstar     mRho     hKstar
  deltaE    0.0878
  fisher   -0.0613    0.0052
  mKstar    0.0550   -0.0102   -0.0108
    mRho    0.0133    0.0002    0.0370   -0.0071
  hKstar    0.1378    0.0106   -0.0607    0.0182   -0.0299
    hRho    0.0014   -0.0595   -0.0240    0.0147    0.0349   -0.0837

 Correlation matrix for RKst1LMC:
            mES     deltaE    fisher    mKstar     mRho     hKstar
  deltaE   -0.0049
  fisher   -0.0428    0.0009
  mKstar    0.0393    0.0621   -0.0249
    mRho   -0.0093    0.0450    0.0007   -0.0081
  hKstar    0.0538   -0.0806   -0.0253    0.0563    0.0049
    hRho    0.0011   -0.1135   -0.0194   -0.0101    0.0025   -0.0559

 Correlation matrix for RKst1TMC:
            mES     deltaE    fisher    mKstar     mRho     hKstar
  deltaE    0.0204
  fisher   -0.0241   -0.0201
  mKstar    0.0139    0.0849   -0.0073
    mRho    0.0107    0.0524   -0.0080   -0.0116
  hKstar    0.0320   -0.0220   -0.0174    0.0202    0.0003
    hRho    0.0044   -0.0572   -0.0161    0.0010    0.0084   -0.0131

 Correlation matrix for D0rhoMC:
            mES     deltaE    fisher    mKstar     mRho     hKstar
  deltaE   -0.0118
  fisher   -0.0083   -0.0262
```

```
   mKstar    -0.0276     0.0246     0.0096
     mRho     0.0195    -0.0266     0.0433    -0.0300
   hKstar    -0.0513     0.0588    -0.0888     0.1351    -0.0593
     hRho     0.0962    -0.0614    -0.0727    -0.0659     0.0243    -0.2557
```

```
Correlation matrix for a1mKpMC:
               mES      deltaE     fisher     mKstar       mRho      hKstar
   deltaE     0.0949
   fisher    -0.0731     0.0008
   mKstar    -0.0294    -0.0330    -0.0239
     mRho     0.0321    -0.0031    -0.0014     0.0055
   hKstar     0.0578    -0.0290    -0.0291    -0.0645     0.0734
     hRho     0.0929    -0.0560     0.0125     0.0218    -0.0216     0.0462
```

```
Correlation matrix for rhorhoMC:
               mES      deltaE     fisher     mKstar       mRho      hKstar
   deltaE     0.1556
   fisher    -0.0716    -0.0768
   mKstar     0.0499     0.0814    -0.0793
     mRho    -0.0029     0.0161    -0.0092     0.0089
   hKstar    -0.0388    -0.0176     0.0162     0.1680    -0.0031
     hRho    -0.0463    -0.0673    -0.0151    -0.0148     0.0277    -0.0122
```

```
Correlation matrix for ChmlsMC:
               mES      deltaE     fisher     mKstar       mRho      hKstar
   deltaE    -0.0478
   fisher    -0.0704     0.0362
   mKstar     0.0010    -0.0220    -0.0275
     mRho    -0.0229     0.0386     0.0193     0.0110
   hKstar     0.0757    -0.1899     0.0317     0.1625     0.1006
     hRho     0.0086     0.0997    -0.0625     0.0711     0.0876    -0.0081
```

A.2.2 $\rho^- K^{*+}$ **Fit Results**

The Run 1-6 fit on $\rho^- K^{*+}$ finds the following values for the parameters which were allowed to float:

```
    Constant Parameter     Value
    --------------------   ------------
                    effL    4.9400e-02
                    effT    1.1180e-01
               fitBiasR1    2.3000e+01
                     nBB    4.7100e+02
                  nD0rho    1.2900e+02
                  nRKst0    6.0000e+01
                  na1mKp    7.0000e+00
                 nrhorho    9.0000e+00
                  prodBR    3.3330e-01


    Floating Parameter    InitialValue      FinalValue (+HiError,-LoError)     GblCorr.
    --------------------  ------------    ----------------------------------   --------
  Frac_nBkg_chgCat_Plus    5.3612e-01     5.3872e-01 (+5.34e-03,-5.33e-03)    0.175735
 Frac_nRKst1_chgCat_Plus   5.3612e-01     4.0162e-01 (+7.54e-02,-7.66e-02)    0.230321
              de_Bkg_P01   -2.0120e-01    -2.1481e-01 (+1.77e-02,-1.76e-02)    0.042308
                      fL    5.0000e-01     3.6572e-01 (+1.18e-01,-1.39e-01)    0.580658
             fis_BkgC_asym  -1.9158e-02    -2.3281e-02 (+1.63e-02,-1.63e-02)    0.118485
             fis_BkgC_mean  -2.0573e-01    -1.9769e-01 (+4.47e-03,-4.49e-03)    0.224655
              fis_BkgC_rms   4.0202e-01     4.0475e-01 (+3.25e-03,-3.22e-03)    0.171696
                hK_Bkg_P01  -7.3529e-01    -7.4219e-01 (+1.49e-02,-1.47e-02)    0.133718
                hK_Bkg_P02   4.8951e-01     4.7385e-01 (+1.30e-02,-1.32e-02)    0.156015
                hR_Bkg_P01  -1.1618e-01    -1.0295e-01 (+1.78e-02,-1.78e-02)    0.056934
                hR_Bkg_P02   3.2503e-01     2.8829e-01 (+1.46e-02,-1.48e-02)    0.125330
          mK_Bkg_Poly_P01  -5.0675e-02    -6.6453e-02 (+2.12e-02,-2.12e-02)    0.289079
            mK_Bkg_fracKst   1.3826e-01     1.3858e-01 (+1.19e-02,-1.18e-02)    0.316583
          mR_Bkg_Poly_P01  -1.8389e-01    -1.4499e-01 (+2.18e-02,-2.19e-02)    0.139823
            mR_Bkg_fracRho   2.6174e-01     2.1627e-01 (+1.32e-02,-1.32e-02)    0.175536
             measBR_RKst1   1.0000e+01     1.0320e+01 (+2.35e+00,-2.19e+00)    0.634954
                 mes_Bkg_c  -6.5659e+00    -1.0509e+01 (+3.69e+00,-3.70e+00)    0.167836
                      nBkg   9.3300e+03     9.3107e+03 (+1.01e+02,-9.98e+01)    0.205765
```

```
Asym wrt Frac_nRKst1_chgCat_Plus
 1-2*(Frac_nRKst1_chgCat_Plus) = 0.196752 +/- 0.150988 (+-0.153234, -0.150786)


Asym wrt Frac_nBkg_chgCat_Plus
 1-2*(Frac_nBkg_chgCat_Plus) = -0.0774305 +/- 0.0106715 (+-0.0106663, -0.0106765)
```

A.2.3 $\rho^- K^{*+}$ **PDF Plots**
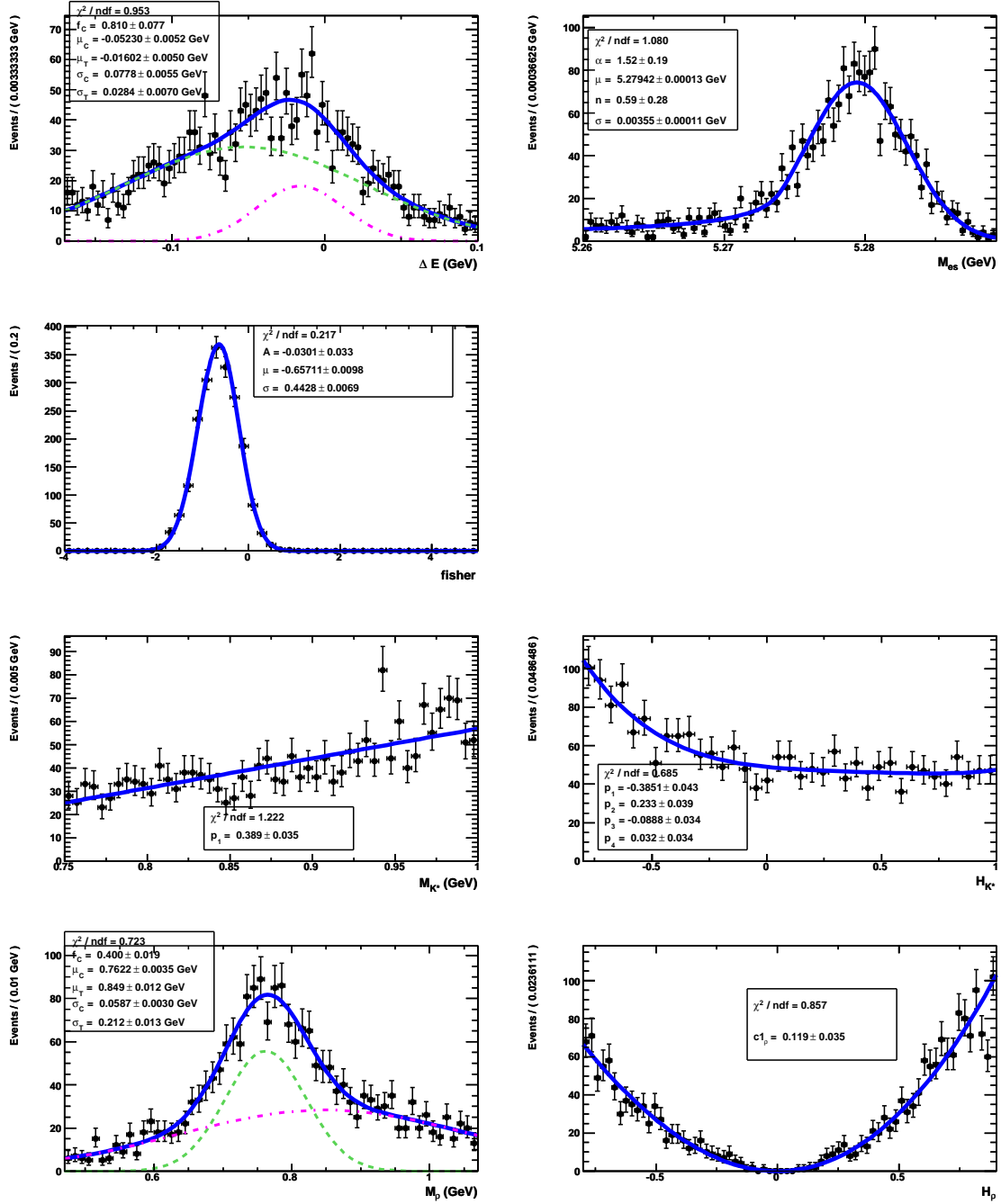
Figure A.11: PDFs for $\rho^-(K\pi)_0^{*+}$. From left to right, top to bottom: ΔE, m_{ES}, $\mathcal{F}$, $m(K^+\pi^0)$, $\mathcal{H}(K^+\pi^0)$, $m(\pi^0\pi^-)$, $\mathcal{H}(\pi^0\pi^-)$.
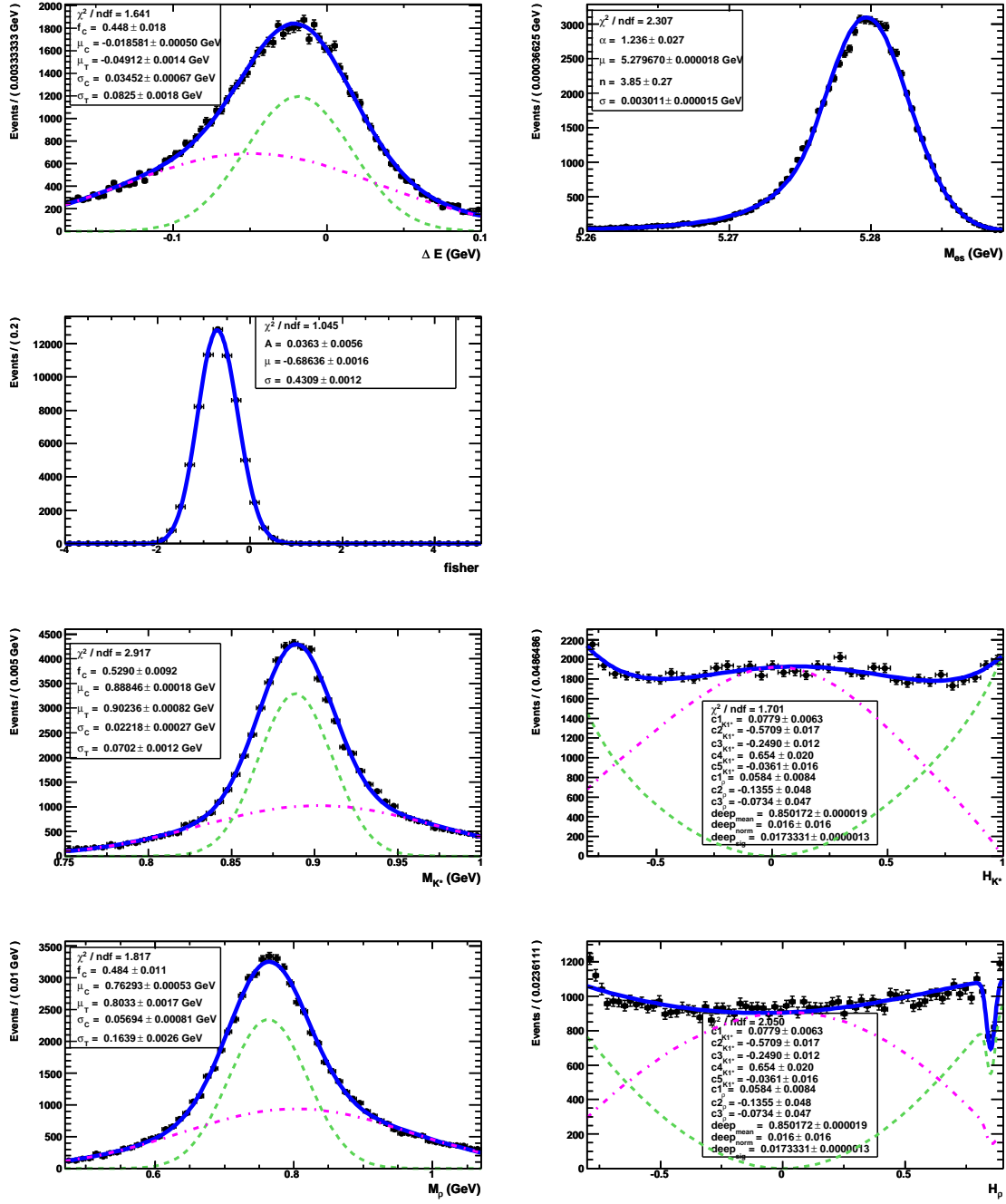
Figure A.12: PDFs for $\rho^- K^*(892)^+$. From left to right, top to bottom: ΔE, m_{ES}, $\mathcal{F}$, $m(K^+\pi^0)$, $\mathcal{H}(K^+\pi^0)$, $m(\pi^0\pi^-)$, $\mathcal{H}(\pi^0\pi^-)$.
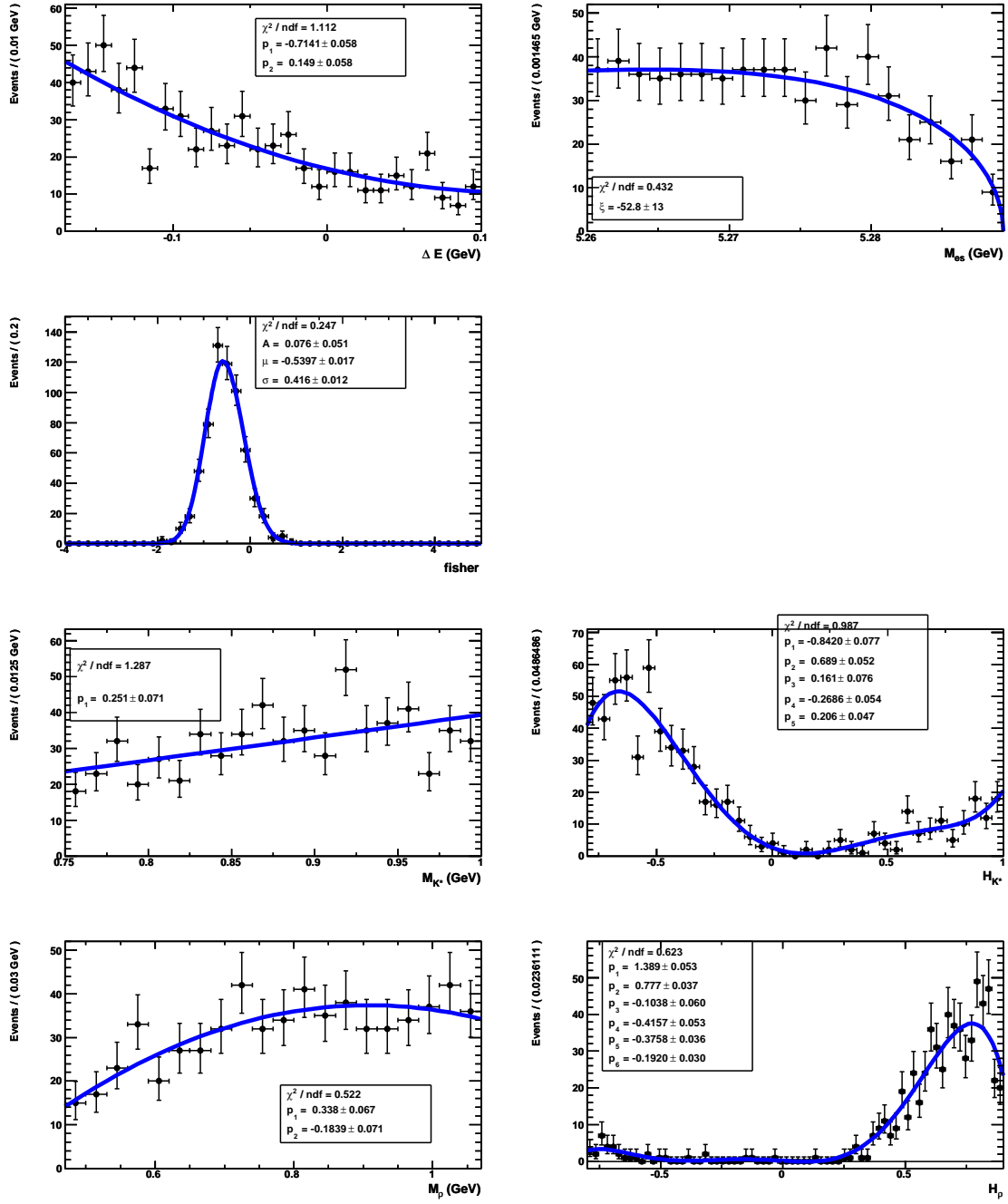
Figure A.13: PDFs for $D^0 \rho^-$ with $D^0 \to K^- \pi^+ \pi^0$ (background to $B^0 \to \rho^- K^{*+}$). From left to right, top to bottom: ΔE, m_{ES}, $\mathcal{F}$, $m(K^+ \pi^0)$, $\mathcal{H}(K^+ \pi^0)$, $m(\pi^0 \pi^-)$, $\mathcal{H}(\pi^0 \pi^-)$.

Figure A.14: PDFs for $a_1^- K^+$ (background to $B^0 \rightarrow \rho^- K^{*+}$). From left to right, top to bottom: ΔE, m_{ES}, $\mathcal{F}$, $m(K^+\pi^0)$, $\mathcal{H}(K^+\pi^0)$, $m(\pi^0\pi^-)$, $\mathcal{H}(\pi^0\pi^-)$.
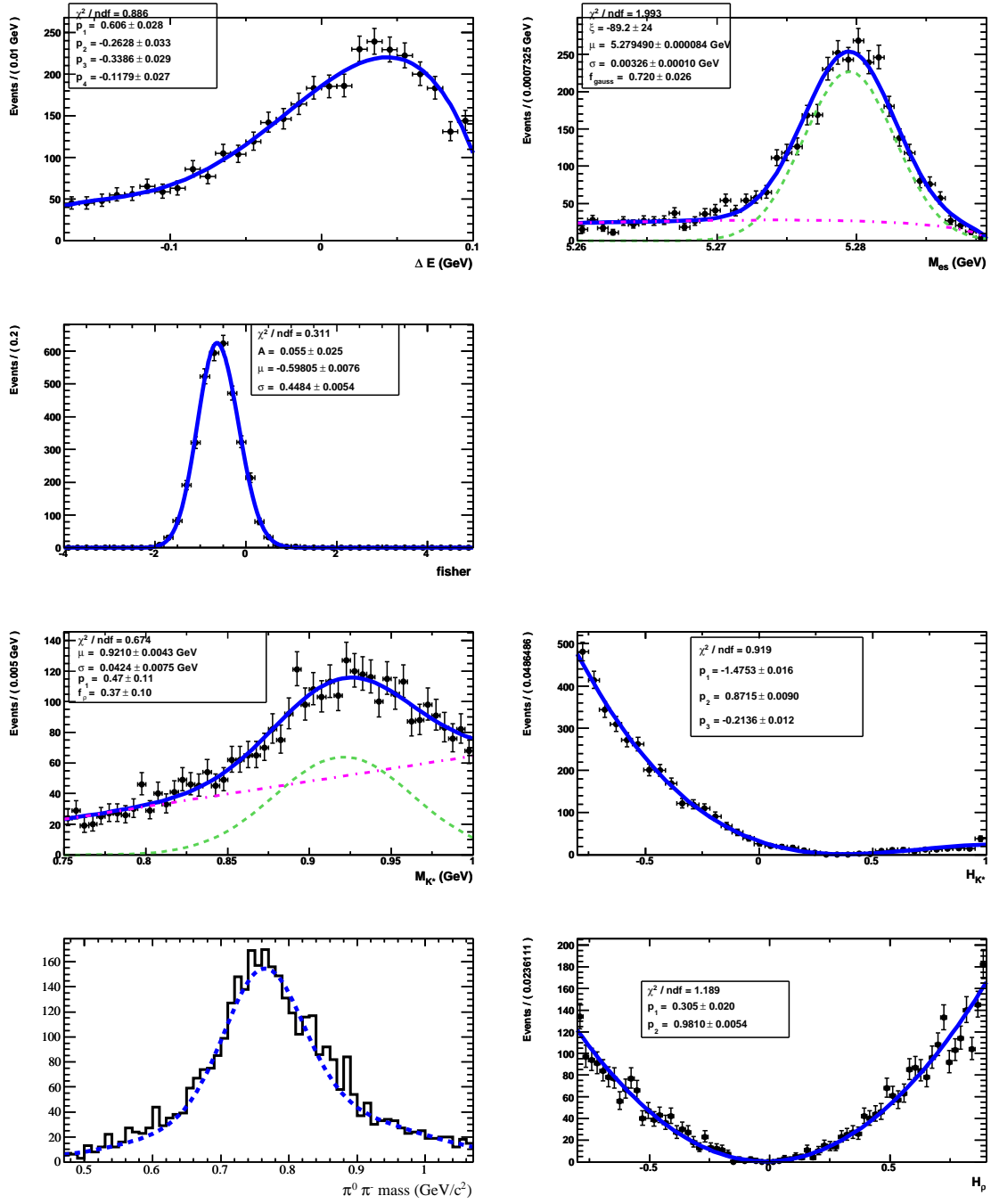
Figure A.15: PDFs for $\rho^+\rho^-$ (background to $B^0 \to \rho^- K^{*+}$). From left to right, top to bottom: ΔE, m_{ES}, $\mathcal{F}$, $m(K^+\pi^0)$, $\mathcal{H}(K^+\pi^0)$, $m(\pi^0\pi^-)$, $\mathcal{H}(\pi^0\pi^-)$.
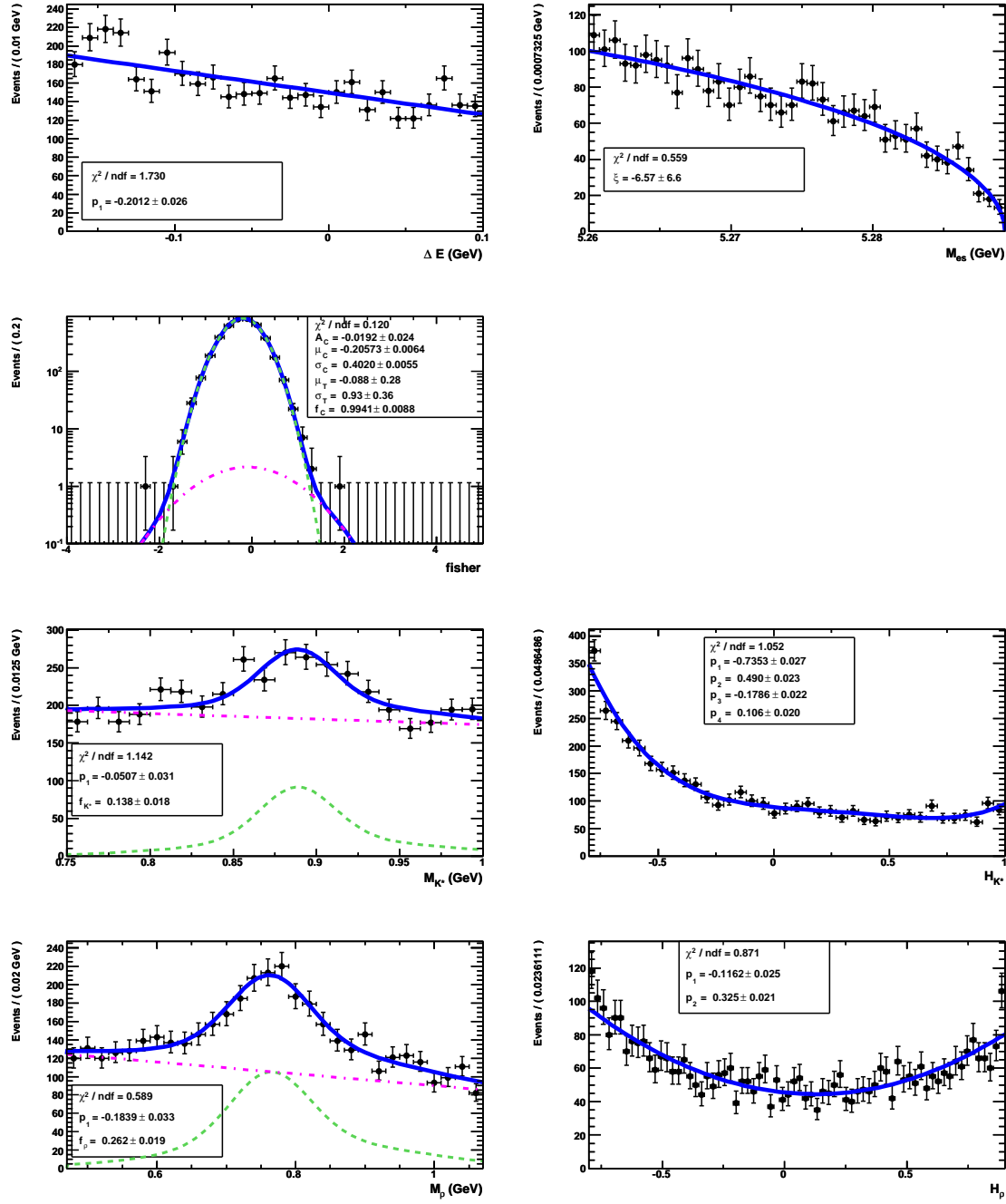
Figure A.16: PDFs for $q\bar{q}$ continuum background for $B^0 \rightarrow \rho^- K^{*+}$. From left to right, top to bottom: ΔE, m_{ES}, $\mathcal{F}$, $m(K^+\pi^0)$, $\mathcal{H}(K^+\pi^0)$, $m(\pi^0\pi^-)$, $\mathcal{H}(\pi^0\pi^-)$.
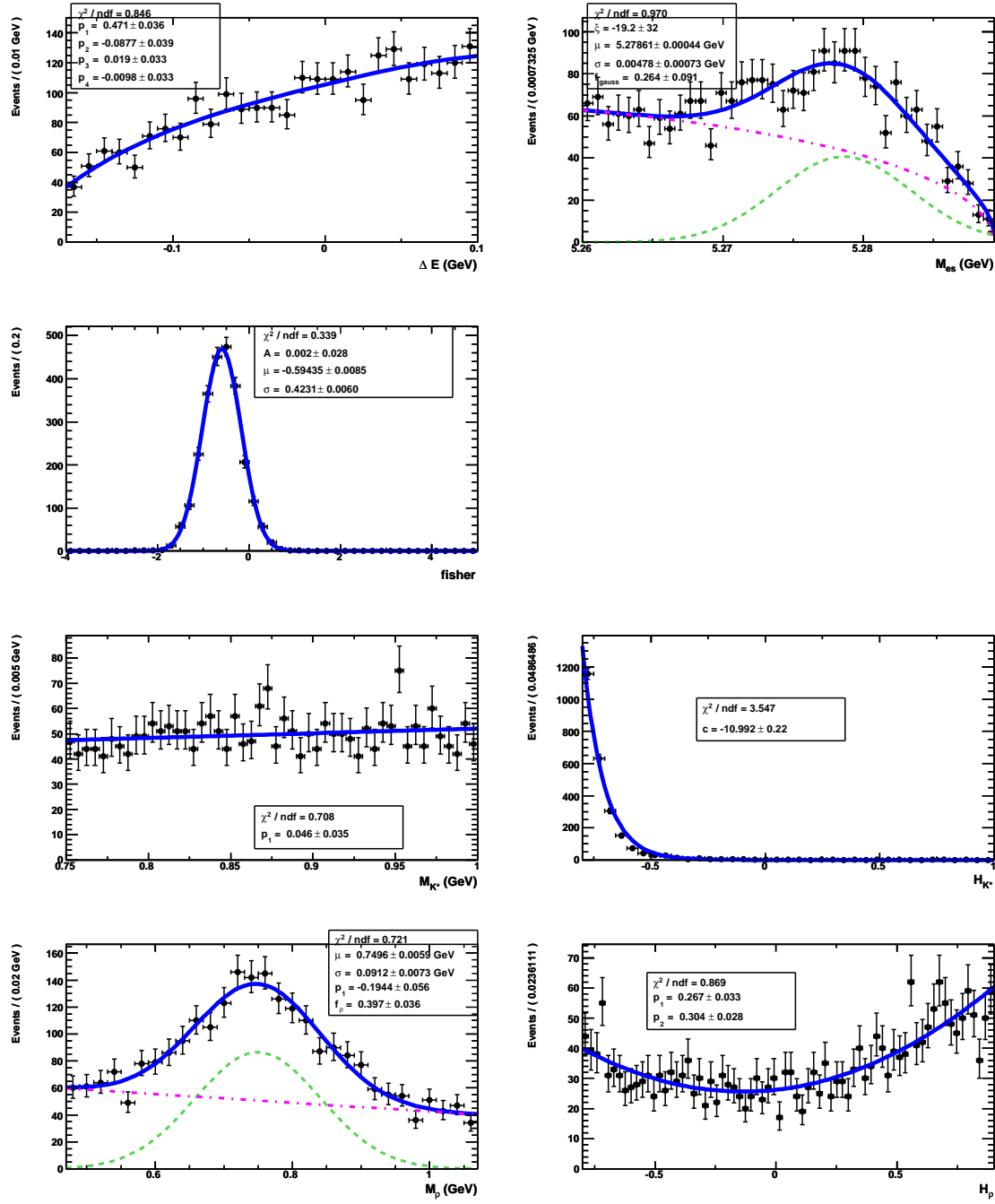
Appendix B

High $K^+\pi^-$ Mass Region Study

The $(K\pi)_0^{*0}$ has a long tail that overlaps the $K^*(892)^0$. In order to accurately extract the $\rho^0 K^{*0}$ and $f_0 K^{*0}$ branching fractions, we must first constrain the K_0^{*0} contamination in the low mass region. In doing so, we also extract branching fractions for $\rho^0(K\pi)_0^{*0}$, $f_0(K\pi)_0^{*0}$, and $f_0 K_2^*(1430)^0$ [1]. We perform this study in two steps, as described in Sec. 7.1.2. The first step is an ML fit using four observables: m_{ES}, ΔE, $\mathcal{F}$, and mass($K^+\pi^-$). This allows us to measure the "inclusive" $(K\pi)_0^{*0}$ and $K_2^*(1430)^0$ branching fractions. Second, as we see a significant K_0^{*0} signal, we use the sWeighted [47] dataset corresponding to K_0^{*0} signal and fit the $\pi^+\pi^-$ mass spectrum to determine how many signal K_0^{*0} events are paired with a ρ^0 or f_0. We perform a similar step with the sWeighted $K_2^*(1430)$ sample in order to extract the $f_0 K_2^*(1430)^0$ yield.

The ML fit has eight components: $(K\pi)_0^{*0}$ signal, $K^*(892)^0$ signal, $K_2^*(1430)^0$ signal, continuum background, and 4 $B\overline{B}$ backgrounds ($B^0 \to a_1^- K^+$, $D^- \pi^+$, D^0 cocktail, and charmless cocktail). The $B\overline{B}$ backgrounds are determined in an identical fashion as for the nominal fit region (see Sec. 7.2), with the high $K^+\pi^-$ mass cut applied. Their yields are fixed in the fit to the following

---

[1]This HMR study uses the $\pi^+\pi^-$ mass range $(0.47, 1.2)\,\mathrm{GeV}$.

163

values:

$$
\begin{aligned}
B^0 \to a_1^- K^+ &= 40 \pm 9 \\
B^0 \to D^- \pi^+ &= 922 \pm 45 \\
D^0 \text{ cocktail} &= 1798 \pm 83 \\
\text{Charmless cocktail} &= 149 \pm 34 \,.
\end{aligned}
\tag{B.1}
$$

The only difference between the LMR and the HMR $B\overline{B}$ background channels is in the composition of the charmless cocktail, which includes the channels used in the LMR as well as additional channels only relevant in the HMR. This cocktail was created with the intention of performing a joint LMR–HMR fit, and is detailed in Tab. B.1 (see Sec. 7.2 for an explanation of the table). The number of events expected in the fit region in Tab. B.1 is for the entire $K^+\pi^-$ mass range $(0.75, 1.55)\,\mathrm{GeV}$; reducing the range to the HMR results in the expected yield in Eq. (B.1).

The PDFs for the HMR fit are given in Fig. B.1-B.2.

B.1 Fit validation

To validate these fits, we perform 100 embedded toy experiments, as reported in Tab. B.2. The biases are reasonable and 100% of the fits converge. We use the appropraite type of $\rho^0 K^{*0}$ MC for the different K^{*0} signal hypotheses; for $K^*(892)^0$ and $K_2^*(1430)^0$, we assume $f_L = 0.5$.

The correlation coefficients between the three K^* yields are quite large (see below), as expected.

```
PARAMETER   CORRELATION COEFFICIENTS
            NO.    7       8       9      10
   nBkg      7   1.000 -0.146 -0.059 -0.027
   nKst0     8  -0.146  1.000 -0.674 -0.583
   nKst1     9  -0.059 -0.674  1.000  0.321
   nKst2    10  -0.027 -0.583  0.321  1.000
```

Table B.1: Charmless $B\overline{B}$ backgrounds for HMR $(K\pi)_0^{*0}$ and $K_2^*(1430)^0$ analysis. The MC efficiencies, number of expected background events in the fit (#$B\overline{B}$ Bkg), etc. are for the entire $0.75 < m_{K^+\pi^-} < 1.55\,\mathrm{GeV}$ mass region.

Signal mode: $(K\pi)_0^{*0}$ & $K_2^*(1430)^0$ Bkg. channel	Mode #	MC ϵ (%)	Est. $\mathcal{B}$ (10^{-6})	$\prod \mathcal{B}_i$	#$B\overline{B}$ Bkg	# in file
$B^+ \to a_1^0 K^+$	4874	0.63	20^*	1.000	59	2557
$B^+ \to \eta'_{\rho\gamma} K^+$	6748	0.49	$71.1^{+2.6}_{-2.6}$	0.294	47.7	2066
$B^+ \to K^+\pi^-\pi^+$ (Dalitz)	6846	0.12	$51.0^{+2.9}_{-2.9}$	1.000	28.5	1237
$B^0 \to f_2(\pi^+\pi^-)K^{*0}_{K^+\pi^-}(T, f_L = 0.5)$	10047	6.25	1.5^*	0.444	19.4	839
$B^+ \to \rho^+\rho^0(L, f_L = 0.95)$	2390	0.17	$22.8^{+1.8}_{-1.9}$	1.000	17.7	768
$B^+ \to \rho^+ K_2^{*0}(1430)_{K^+\pi^-}(L, f_L = 0.5)$	10091	0.87	5^*	0.667	13.5	584
$B^0 \to f_2(\pi^+\pi^-)K^{*0}_{K^+\pi^-}(L, f_L = 0.5)$	10046	4.07	1.5^*	0.444	12.6	546
$B^+ \to \rho^+ K^{*0}_{K^+\pi^-}(L, f_L = 0.48)$	2244	0.88	$4.4^{+1.0}_{-1.0}$	0.666	12	520
$B^0 \to K^{*0}_{K^+\pi^-}\mu^+\mu^-$	4777	3.41	$1.05^{+1.5}_{-1.3}$	0.666	11.1	480
$B^0 \to a_1^-(\rho^0\pi^-)\pi^+$	2011	0.14	$31.7^{+3.7}_{-3.7}$	0.500	10.1	437
$B^0 \to a_1^0 K^{*0}(L, f_L = 0.7)$	5329	0.44	7^*	0.667	9.5	413
$B^+ \to \rho^0 K_2^{*+}(1430)_{K^+\pi^0}(T, f_L = 0.5)$	10094	1.06	5^*	0.333	8.2	355
$B^0 \to \overline{K}^{*0}_{K\pi}K^{*0}_{K\pi}(L, fL = 0.8)$	2398	2.83	$1.28^{+0.33}_{-0.31}$	0.444	7.5	324
$B^+ \to a_1^0\pi^+$	4156	0.07	$20.4^{+5.8}_{-5.8}$	1.000	7.1	306
$B^+ \to f_0 K^{*+}_{K^+\pi^0}$	3357	1.31	$5.2^{+1.3}_{-1.3}$	0.222	7	304
$B^+ \to \rho^+\pi^- K^+$	2488	0.13	10^*	1.000	5.9	255
$B^+ \to \rho^+ K_2^{*0}(1430)_{K^+\pi^-}(T, f_L = 0.5)$	10092	0.37	5^*	0.667	5.7	247
$B^+ \to \rho^+ K^{*0}_{K^+\pi^-}(T, f_L = 0.48)$	2243	0.38	$4.8^{+1.1}_{-1.1}$	0.666	5.7	246
$B^+ \to \rho^0 K_2^{*+}(1430)_{K^+\pi^0}(L, f_L = 0.5)$	10093	0.69	5^*	0.333	5.3	230
$B^+ \to \rho^0 K^{*+}_{K^+\pi^0}(L, f_L = 0.9)$	2355	1.05	$3.2^{+1.8}_{-1.8}$	0.333	5.2	225
$B^0 \to \overline{K}^{*0}_{K\pi}K^{*0}_{K\pi}(T, fL = 0.8)$	2399	5.68	$0.26^{+0.08}_{-0.08}$	0.444	3	132
$B^0 \to \rho^0\rho^0(L, f_L = 0.75)$	2396	1	$0.55^{+0.22}_{-0.24}$	1.000	2.6	110
$B^0 \to \rho^0\rho^0(T, f_L = 0.75)$	2397	2.04	$0.18^{+0.07}_{-0.08}$	1.000	1.7	74
$B^0 \to a_1^0 K^{*0}(T, f_L = 0.7)$	5330	0.09	3^*	0.667	0.8	36
$B^+ \to a_1^+(\rho^0\pi^+)K^{*0}(L, f_L = 0.5)$	5333	0.7	$0.75^{+1.28}_{-1.28}$	0.333	0.8	35
$B^+ \to \rho^0 K^{*+}_{K^+\pi^0}(T, f_L = 0.9)$	2356	0.85	$0.36^{+0.20}_{-0.20}$	0.333	0.5	20
$B^+ \to a_1^+(\rho^0\pi^+)K^{*0}(T, f_L = 0.5)$	5334	0.2	$0.75^{+1.28}_{-1.28}$	0.333	0.2	9
$B^+ \to \rho^0 \ell^+\nu$	2814	0.02	$3.0^{+0.4}_{-0.4}$	1.000	0.2	9
Total					308.5	13364

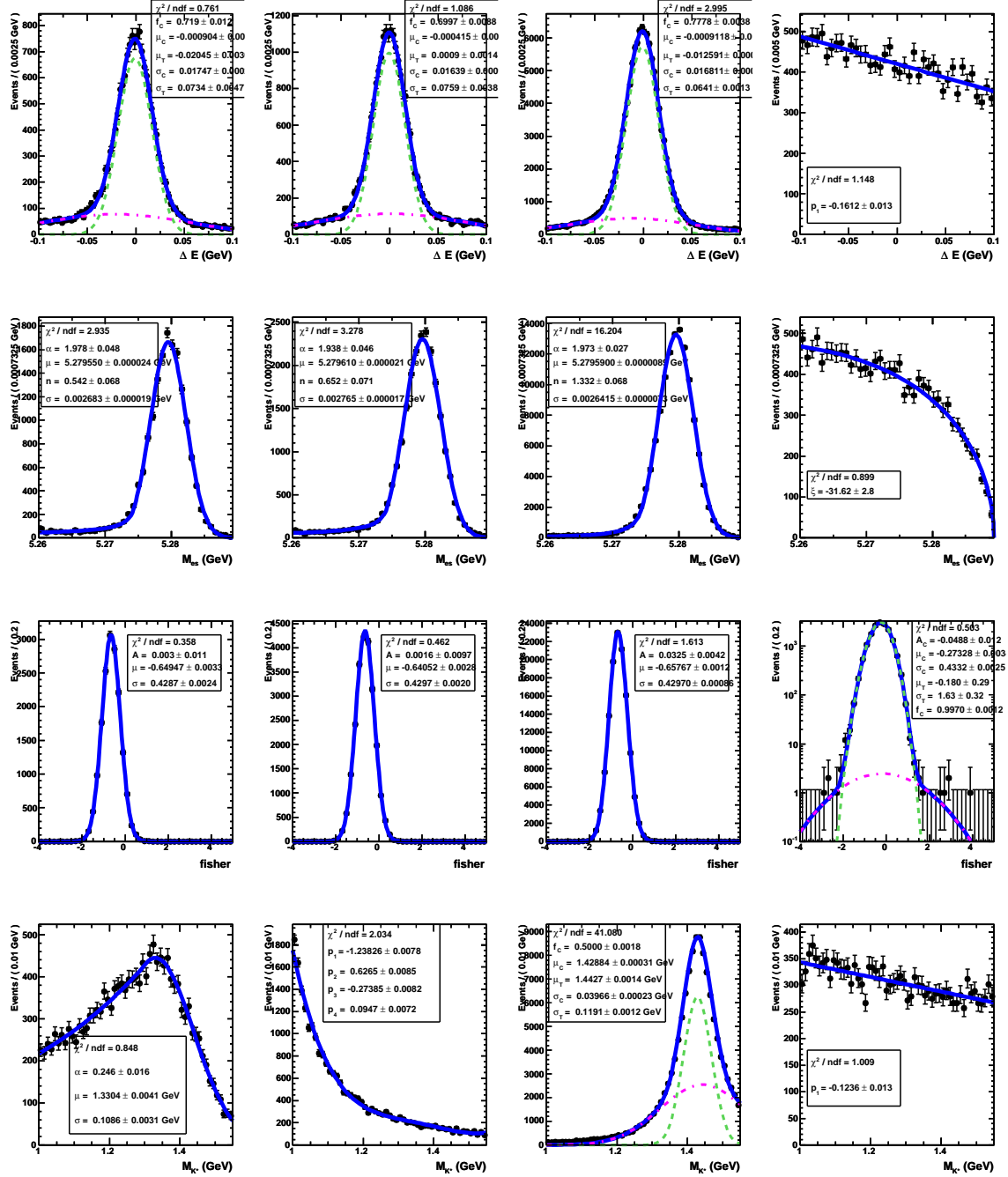Figure B.1: PDF plots for (from left to right) $(K\pi)^{*0}_0$, $K^*(892)^0$, $K^*_2(1430)^0$, continuum background. From top to bottom: ΔE, m_{ES}, $\mathcal{F}$, $K^+\pi^-$ mass.
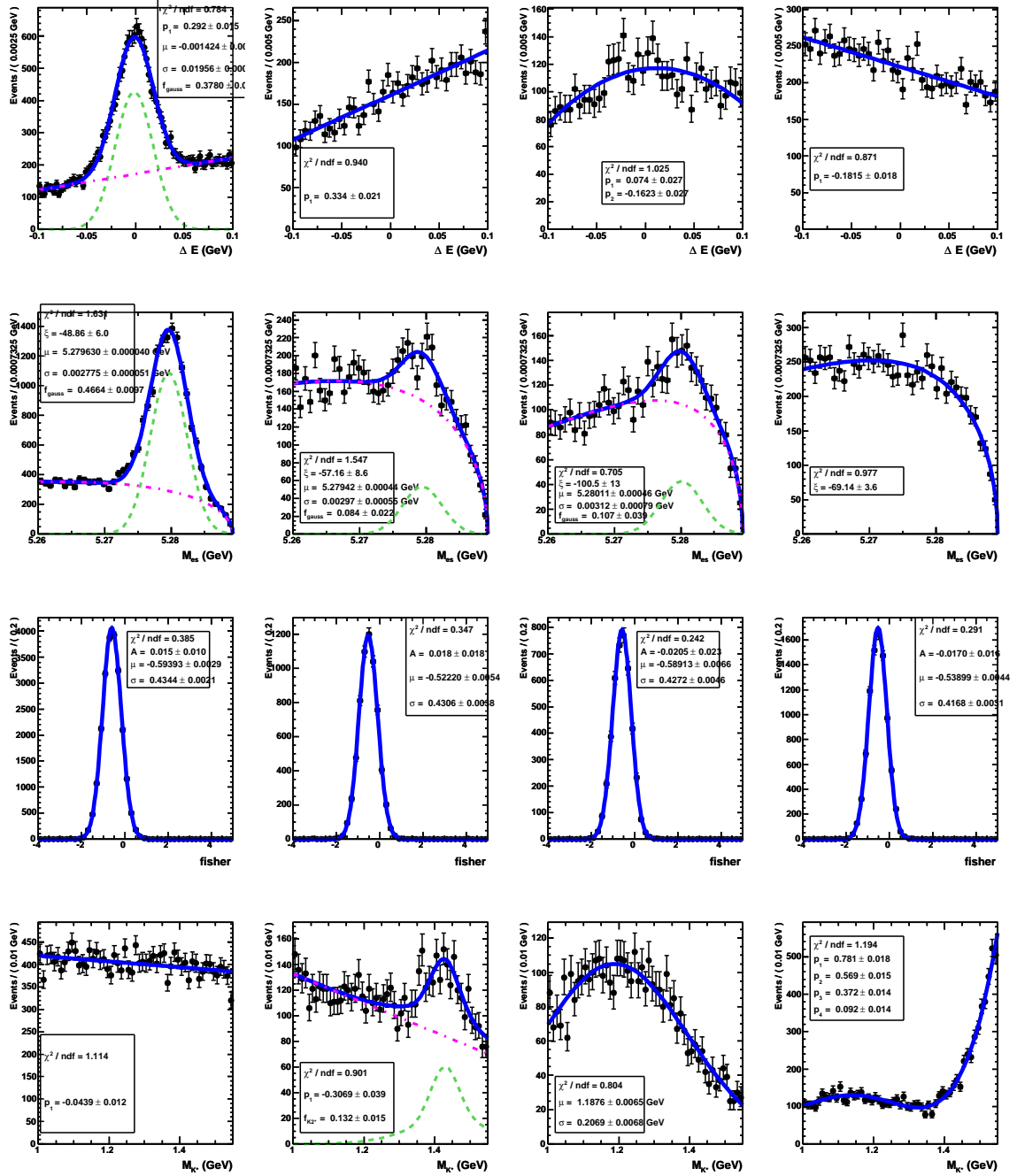
Figure B.2: PDF plots for (from left to right) $B^0 \rightarrow a_1^- K^+$, the charmless cocktail, $B^0 \rightarrow D^-\pi^+$, and the D^0 cocktail. From top to bottom: ΔE, m_{ES}, $\mathcal{F}$, $K^+\pi^-$ mass.

Table B.2: Results of an embedded toy study for the high $K^+\pi^-$ region. $B\overline{B}$ background is also embedded (with yields fixed) as described in the text. Each experiment includes 37157 events, where the difference is generated from the $q\overline{q}$ background PDFs. We report the number of events embedded from MC ("Input"), the fit result with the average statistical error, and the bias on the yield. 100/100 fits converged.

Mode	Input	Fit	Bias
$(K\pi)_0^{*0}$	1045	1132 ± 127	87 ± 12
$K^*(892)^0$	110	170 ± 81	60 ± 8
$K_2^*(1430)^0$	337	337 ± 60	0 ± 5

We test whether these large correlations cause the final fit yields to be dependent upon their initial values. We run similar toy experiments to those described above, both fitting the toy datasets with the correct (# embedded) initial values and with significantly different initial values. These fits have, on average, the same mean and statistical uncertainty, but an experiment-by-experiment difference reveals that the yields move around a fair amount. As the means and widths of both ensembles of experiments agree, however, we conclude that the correlations are acceptable.

B.2 Fit to K_0^{*0} and K_2^{*0} "inclusive" signal in run 1-6 data

For the fit to on-peak run 1-6 data, we fix the $B\overline{B}$ background yields to the values in Eq. (B.1). There are 37157 events to fit. The results are given in the "Inclusive" column of Tab. B.3.

Fig. B.3 shows the sPlots for ΔE, m_{ES}, $\mathcal{F}$, and mass($\pi^+\pi^-$). The $\pi^+\pi^-$ mass is not used to discriminate between the signal and background hypotheses, and is included here for reference. The $K^+\pi^-$ mass sPlots are not shown as the fitter has no way to distinguish between the different K^{*0} components without this observable in the fit. Fig. B.4 gives the projection plots with cuts on the K_0^{*0} signal likelihood to improve visibility of those events.

Table B.3: Results of fitting the run 1-6 data in the high $K^+\pi^-$ region. The "Inclusive" yield is the result of the first part of the fit to the full run 1-6 dataset; the "Exclusive" yields are determined by fitting the sWeighted $(K\pi)_0^{*0}$ or $K_2^*(1430)^0$ signal in the run 1-6 dataset.

Channel	Inclusive	Exclusive
$(K\pi)_0^{*0}$	1135^{+127}_{-128}	
ρ^0		$1045 \pm 36 \pm 118$
f_0		$88 \pm 19 \pm 10$
$K^*(892)^0$	123^{+83}_{-78}	
$K_2^*(1430)^0$	347^{+61}_{-59}	
ρ^0		$212 \pm 17 \pm 37$
f_0		$134 \pm 14 \pm 23$

B.3 $\pi^+\pi^-$ mass spectrum in sWeighted K_0^{*0} and K_2^{*0} signal events

After performing the ML fit to extract the inclusive K_0^{*0} signal yield, we weight the on-peak dataset with the K_0^{*0} signal sWeights. The weighted number of events in the dataset is 1134. We then fit the $\pi^+\pi^-$ invariant mass distribution over the range (0.47, 1.2) GeV to two hypotheses: ρ^0 and f_0. The PDF shapes for these hypotheses are derived from signal MC, and have the same functional forms as those used in the nominal $K^*(892)^0$ mass range fit; see Fig. B.5. We perform an equivalent fit (using the same PDFs) for the sWeighted $K_2^*(1430)^0$ signal. In the $K_2^*(1430)^0$ sample, we have 347 events to fit.

The fit results are plotted in Fig. B.6. The fit results are given in the "Exclusive" column of Tab. B.3. In Fig. B.7 we give the results for the equivalent fit (using the same PDFs) to sWeighted $K_2^*(1430)^0$ signal events.

We originally investigated including a non-resonant $\pi^+\pi^-$ component in addition to the ρ^0 and f_0 hypotheses. When allowed this extra degreed of freedom, the fitter finds a non-resonant $\pi^+\pi^-$ yield consistent with zero. Fig. B.6-B.7 visually indicate that indeed, a non-resonant $\pi^+\pi^-$ component does not appear necessary.
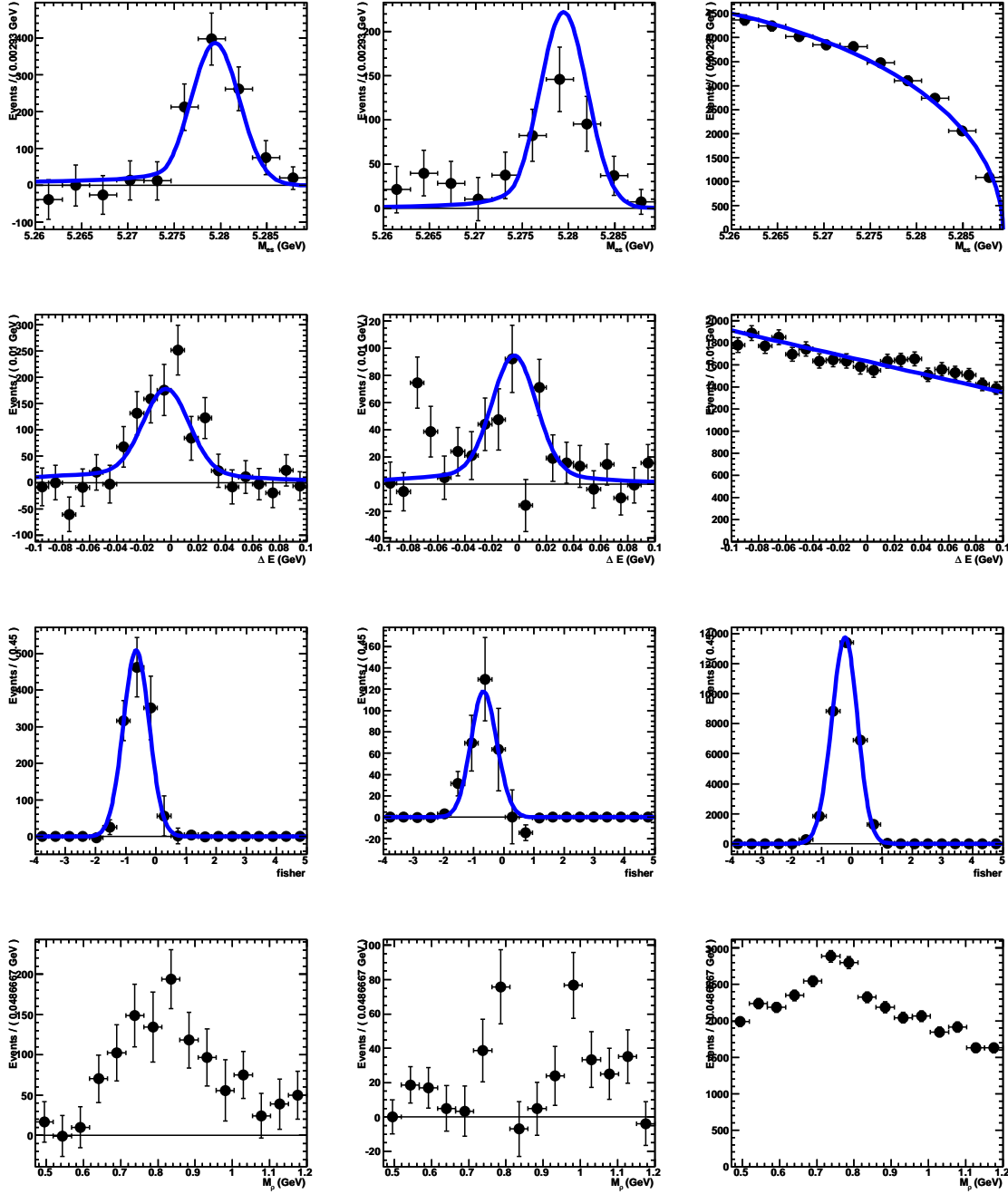
Figure B.3: sPlots of (left to right) K_0^{*0}, K_2^{*0}, and continuum background. Plots are, top to bottom: m_{ES}, ΔE, $\mathcal{F}$, and mass($\pi^+\pi^-$).
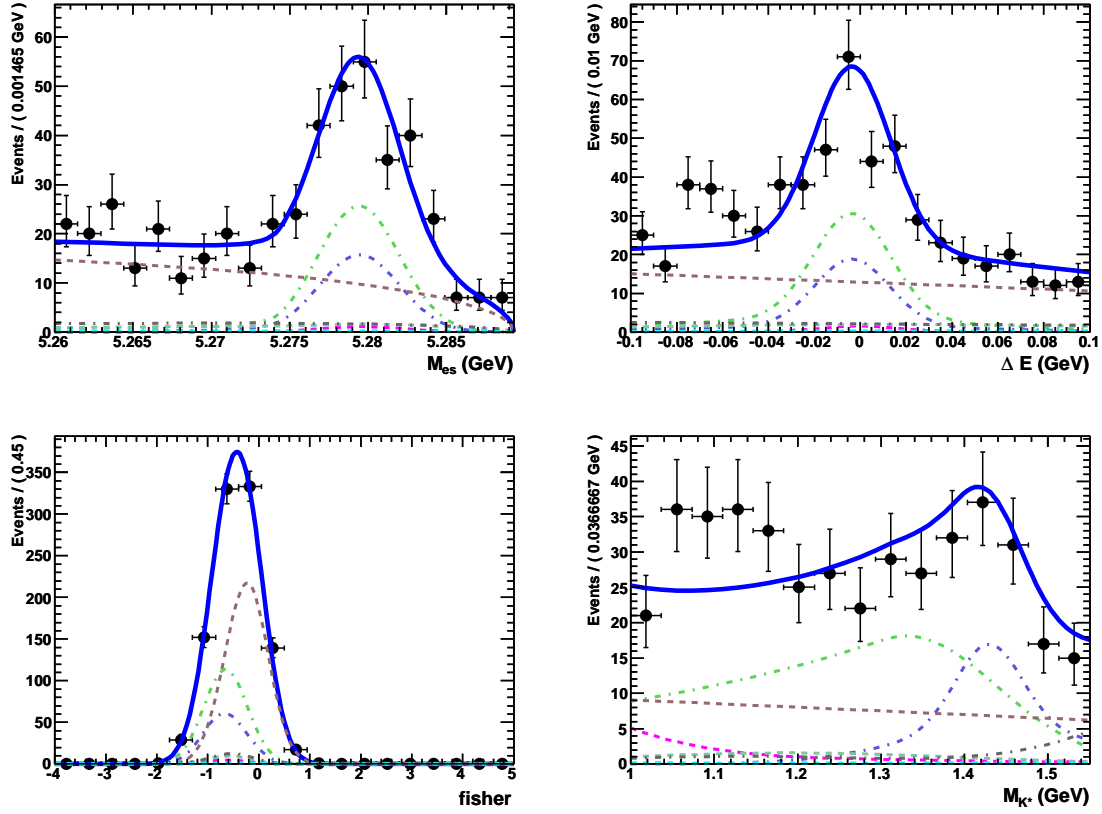
Figure B.4: Projection plots of the high mass region fit. Left to right, top to bottom: m_{ES}, ΔE, $\mathcal{F}$, and mass($K^+\pi^-$). The solid blue curve shows the total fit result, the green curve is K_0^{*0}, pink is K_1^{*0}, dashed blue is K_2^{*0}, and brown is continuum background. A cut on the K_0^{*0} signal likelihood is applied to enhance the visibility of the signal.

B.4 Statistical uncertainty on the exclusive yields

The statistical uncertainties on the exclusive yields are determined based on the $m(\pi^+\pi^-)$ fit to the sWeighted $(K\pi)_0^{*0}$ or $K_2^*(1430)$ signal datasets. These uncertainties do not take into account the error on the inclusive K_0^{*0} or K_2^{*0} signal yield measurement. This is equivalent to the difference between a regular and an extended ML fit. We therefore add by hand the appropriate fraction of the inclusive $(K\pi)_0^{*0}$ or $K_2^*(1430)^0$ yield uncertainty. This is included as the second uncertainty in Tab. B.3.
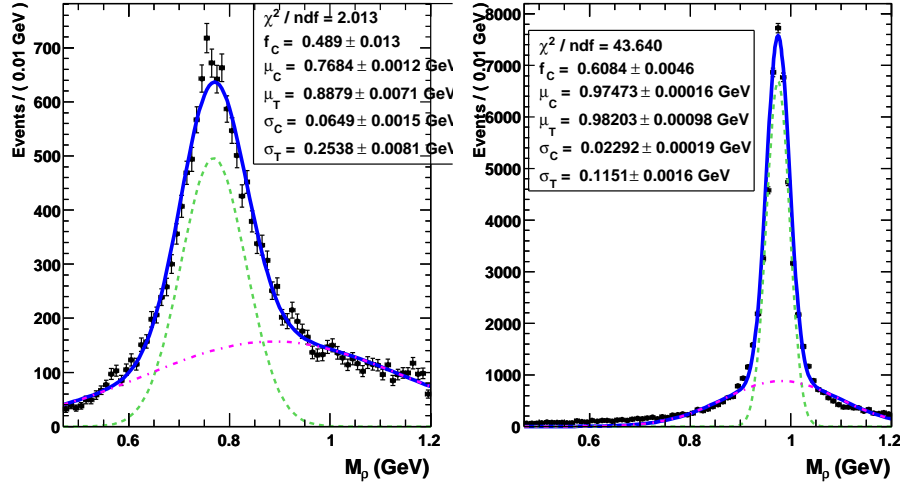
Figure B.5: PDF plots for the exclusive $m(\pi^+\pi^-)$ fit. Left: ρ^0 hypothesis, right: f_0.
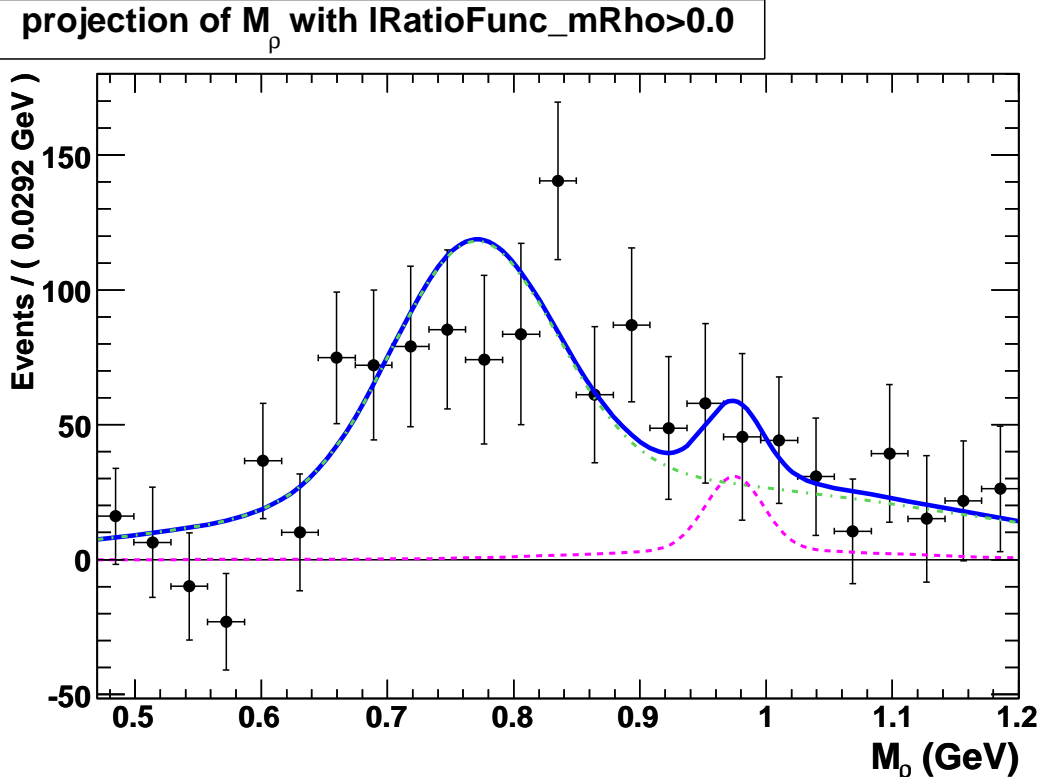
Figure B.6: Plot showing the results of the fit to the $\pi^+\pi^-$ mass spectrum for the sWeighted $(K\pi)_0^{*0}$ signal (points with error bars) in the high $K^+\pi^-$ mass region. The solid blue curve shows the total fit result, the green curve is ρ^0 and pink is f_0.
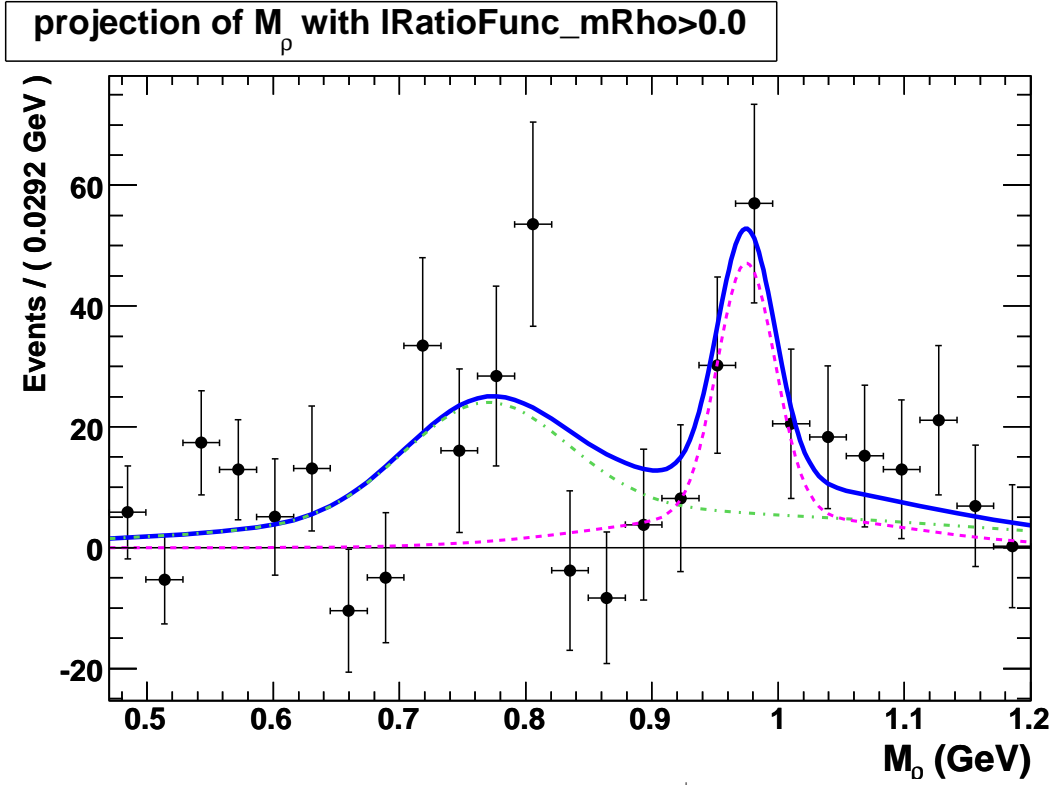
Figure B.7: Plot showing the results of the fit to the $\pi^+\pi^-$ mass spectrum for the sWeighted $K_2^*(1430)^0$ signal (points with error bars) in the high $K^+\pi^-$ mass region. The solid blue curve shows the total fit result, the green curve is ρ^0 and pink is f_0.

B.5 Extrapolating $(K\pi)_0^{*0}$ yields to the LMR

The efficiencies for the various exclusive MC samples in both the LMR and HMR are given in Tab. B.4. Using the selection efficiency in the LMR and the final BF results listed in Tab. 8.6, we calculate the number of $(K\pi)_0^{*0}$ events expected in our LMR fit.

$$N(\rho^0(K\pi)_0^{*0}) = 215 \pm 34 \tag{B.2}$$

$$N(f_0(K\pi)_0^{*0}) = 19 \pm 6 \tag{B.3}$$

The final branching fraction results are given in Tab. 8.6 for those channels we consider signal. In Tab. B.5 we compute the BF for $\rho^0 K_2^*(1430)^0$ assuming $f_L = 0.5$. This value is used to calculate the interference systematic for $\rho^0(K\pi)_0^{*0}$ (see Sec. 9).

Table B.4: Number of events selected, number of MC events generated, and selection efficiencies for the low (LMR) and high (HMR) $K^+\pi^-$ mass regions. $^\dagger N_{\mathrm{gen}}$ for $\rho^0(K\pi)^{*0}_0$ is the product of the number of 3-body phase space events generated times the efficiencies to reweight the $K^+\pi^-$ mass to a LASS distribution and that of reweighting the $\mathcal{H}_\rho$ distribution.

	LMR			HMR	
	# evts	N_{gen}	ϵ	# evts	ϵ
Run 1-6 Data	18792	—	—	37157	—
$\rho^0(K\pi)^{*0}_0$	3723	$168463^\dagger$	0.02210	16446	0.09595
$\rho^0 K^*(892)^0$ ln	61506	429000	0.14337	8750	0.02040
$\rho^0 K^*(892)^0$ tr	107552	429000	0.25070	14610	0.03406
$\rho^0 K_2^*(1430)^0$ ln	—	373000	—	44904	0.12039
$\rho^0 K_2^*(1430)^0$ tr	—	373000	—	79126	0.21213
$f_0(K\pi)^{*0}_0$	14881	506200	0.02940	63192	0.12484
$f_0 K^*(892)^0$	78501	429000	0.18299	11024	0.02570
$f_0 K_2^*(1430)^0$	—	423000	—	64820	0.15324

Table B.5: High $K^+\pi^-$ mass sideband result for $\rho^0 K_2^*(1430)^0$ from run 1-6 data. Branching fraction uncertainties are statistical only. Results for all other channels are given in Tab. 8.6.

ML fit quantity	$\rho^0 K_2^*(1430)^0$
Fit signal yield	$212 \pm 17 \pm 37$
Fit bias	0 ± 5
Corrected yield	212^{+41}_{-40}
MC ϵ (%)	12.0(ln) 21.2(tr)
$\prod \mathcal{B}_i$ (%)	32.5
f_L (assumed)	0.5
$\mathcal{B}(10^{-6})$	8.3 ± 1.6
signif (stat only)	5.3

B.6   High $K^+\pi^-$ mass fit results

The run 1-6 inclusive fit results, including all floating PDF parameters:

```
Constant Parameter     Value
--------------------   -----------
          nChmls       1.4900e+02
          nD0Bkg       1.7980e+03
            nDpi       9.2200e+02
          na1mKp       4.0000e+01


Floating Parameter   InitialValue     FinalValue (+HiError,-LoError)      GblCorr.
--------------------  -----------    ---------------------------------    --------
        deBkg_P01     -1.6117e-01    -1.7104e-01 (+9.92e-03,-9.91e-03)    0.039385
      fisBkgC_asym    -4.8845e-02    -4.0173e-02 (+9.24e-03,-9.22e-03)    0.155106
      fisBkgC_mean    -2.7328e-01    -2.5189e-01 (+2.66e-03,-2.64e-03)    0.299384
       fisBkgC_rms     4.3316e-01     4.2453e-01 (+1.90e-03,-1.90e-03)    0.238560
        mK_Bkg_P01    -1.2363e-01    -1.8705e-01 (+1.04e-02,-1.03e-02)    0.230873
         mesBkg_c     -3.1623e+01    -1.8564e+01 (+2.05e+00,-2.09e+00)    0.246398
             nBkg      3.2860e+04     3.2629e+04 (+2.01e+02,-2.02e+02)    0.319706
            nKst0      1.0000e+03     1.1345e+03 (+1.27e+02,-1.28e+02)    0.818753
            nKst1      8.8000e+01     1.2283e+02 (+8.30e+01,-7.82e+01)    0.729203
            nKst2      3.0000e+02     3.4676e+02 (+6.10e+01,-5.93e+01)    0.633606
```

Run 1-6 exclusive $(K\pi)_0^{*0}$ fit results:

```
Floating Parameter   InitialValue     FinalValue (+HiError,-LoError)      GblCorr.
--------------------  -----------    ---------------------------------    --------
            nRho0      8.0000e+02     1.0452e+03 (+3.65e+01,-3.60e+01)    0.392503
              nf0      1.0000e+02     8.7904e+01 (+1.94e+01,-1.83e+01)    0.392503
```

Run 1-6 exclusive $K_2^*(1430)^0$ fit results:

```
Floating Parameter   InitialValue     FinalValue (+HiError,-LoError)      GblCorr.
--------------------  -----------    ---------------------------------    --------
            nRho0      8.0000e+02     2.1252e+02 (+1.73e+01,-1.65e+01)    0.299779
              nf0      1.0000e+02     1.3445e+02 (+1.48e+01,-1.40e+01)    0.299779
```

Appendix C

High $K^+\pi^0$ Mass Region Study

The $(K\pi)_0^{*+}$ has a long tail that overlaps the $K^*(892)^+$. In order to accurately extract the

$\rho^- K^{*+}$ branching fraction, we must first constrain the K_0^{*+} contamination in the low mass region

(LMR). We do this with a separate ML fit in the high mass region (HMR), defined as

$$1.0 < m(K^+\pi^0) < 1.55 \, \mathrm{GeV} \, . \tag{C.1}$$

The ML fit includes five observables: m_{ES}, ΔE, $\mathcal{F}$, mass($\pi^-\pi^0$), and mass($K^+\pi^0$). Seven com-

ponents are included in the fit: $\rho^-(K\pi)_0^{*+}$, $\rho^- K^*(892)^+$, $\rho^- K_2^*(1430)^+$, continuum background,

and 3 $B\overline{B}$ backgrounds ($B^- \to D^0_{K^-\pi^+\pi^0}\rho^-$, $B^0 \to a_1^- K^+$, and $B^0 \to \rho^+\rho^-$). The $B\overline{B}$ back-

ground yields are fixed in the fit, and are discussed in more detail in Sec. C.1. The PDFs for all

components are given in Sec. C.7.

C.1 $B\overline{B}$ backgrounds to high mass $K^+\pi^0$

To determine which $B\overline{B}$ backgrounds to include in the fit, we first run on generic $B\overline{B}$

MC. For those dominant modes passing preselection, we generate exclusive MC samples and apply

the high mass preselection. Tab. C.1 and C.2 give the dominant backgrounds, as well as number of

Table C.1: Dominant charm $B\overline{B}$ backgrounds for $\rho^- K^{*+}_{K^+\pi^0}$ in the high $K^+\pi^0$ mass region.

Signal mode: $\rho^0 K^{*0}$ Bkg. channel	Mode #	MC ϵ (%)	Est. $\mathcal{B}$ (10^{-6})	$\prod \mathcal{B}_i$	#$B\overline{B}$ Bkg
$B^+ \to \overline{D}^0_{K^+\pi^-\pi^0}\rho^+$	2441	0.05	13400^{+1800}_{-1800}	0.140	433.6
$B^0 \to \overline{D}^0_{K^+\pi^-\pi^0}\pi^0$	2191	0.18	261^{+24}_{-24}	0.139	30.2
$B^0 \to D^{*-}\rho^+ \ (D^{*-} \to \overline{D}^0\pi^-,\ \overline{D}^0 \to K^+\pi^-\pi^0)$	1239	0.01	6800^{+900}_{-900}	0.094	24.4
$B^+ \to D^0\rho^- (D^0 \to K\pi)$	2436	0.03	$1340.0^{+180.0}_{-180.0}$	0.0381	6
$B^0 \to \overline{D}^{*0}\pi^0 \ (\overline{D}^{*0} \to \overline{D}^0\pi^0,\ \overline{D}^0 \to K^+\pi^-)$	9915	0.05	170^{+40}_{-40}	0.026	1.1
Total					495.3

Table C.2: Dominant charmless $B\overline{B}$ backgrounds for $\rho^- K^{*+}_{K^+\pi^0}$ in the high $K^+\pi^0$ mass region.

Signal mode: $\rho^0 K^{*0}$ Bkg. channel	Mode #	MC ϵ (%)	Est. $\mathcal{B}$ (10^{-6})	$\prod \mathcal{B}_i$	#$B\overline{B}$ Bkg
$B^0 \to \rho^+\rho^- (L, f_L = 0.978)$	2498	0.14	$23.7^{+3.1}_{-3.1}$	1.000	15.4
$B^0 \to a_1^-(\rho^-\pi^0)K^+$	4960	0.34	$16.3^{+3.7}_{-3.7}$	0.500	12.9
$B^+ \to a_1^0 K^+$	4874	0.13	20^*	1.000	11.8
$B^+ \to \pi^0\pi^0 K^{*+}(892)_{K^+\pi^0} \ (N.R.)$	10566	0.13	15^*	0.667	6.2
$B^0 \to a_1^-(\rho^-\pi^0)K^{*+}_{K^+\pi^0}(L, f_L = 1)$	5323	0.27	20^*	0.167	4.3
$B^+ \to a_1^+(\rho^+\pi^0)\pi^0$	4957	0.07	$26.4^{+6.8}_{-6.8}$	0.500	4
$B^0 \to K^{*0}_{K^+\pi^-}\pi^0\pi^0$	4148	0.18	5^*	0.667	2.8
$B^0 \to \rho^-\pi^+\pi^0$	2491	0.05	10^*	1.000	2.4
$B^+ \to \rho^+\pi^- K^+$	2488	0.05	10^*	1.000	2.3
$B^+ \to a_1^0 K^{*+}_{K^+\pi^0}(L, f_L = 1)$	5327	0.14	10^*	0.333	2.2

events expected in the run 1-6 data.

Given these expectations, we include three $B\overline{B}$ background hypotheses in the ML fit: $B^- \to D^0_{K^-\pi^+\pi^0}\rho^-$, $B^0 \to a_1^- K^+$, and $B^0 \to \rho^+\rho^-$. We fix these $B\overline{B}$ background yields to their expected values,

$$N_{D^0_{K^-\pi^+\pi^0}\rho^-} = 427 \pm 58 \,,$$

$$N_{a_1^- K^+} = 13 \pm 3 \,,$$

$$N_{\rho^+\rho^-} = 15 \pm 2 \,. \tag{C.2}$$

To ensure that the $B\overline{B}$ backgrounds not explicitly included do not bias the fit result, we perform toy MC studies embedding additional $B\overline{B}$ background. As a representative $B \to D$ background, we chose $B^0 \to \overline{D}^0_{K^+\pi^-\pi^0}\pi^0$ (as we have large MC statistics for it), and embedded 60 events. We also create a cocktail of the remaining charmless backgrounds listed in Tab. C.2, and embedded 30 events from that cocktail. As we have only $\sim 5\times$ the expected number of $D^0\rho^-$ background events, we cannot perform a great many toy experiments in which we embedded all signals and backgrounds. Instead, we simulate the fitted components with the PDFs and embed only the $\overline{D}^0_{K^+\pi^-\pi^0}\pi^0$ and Charmless Cocktail events from MC. The results of this study indicate no bias on the $\rho^-(K\pi)^{*+}_0$ yield from the neglected background channels.

C.2 $\rho^- K^*(892)^+$ in the high mass $K^+\pi^0$ fit

For the purposes of this study, the $\rho^- K^*(892)^+$ yield can be considered a $B\overline{B}$ background. Its MC selection efficiency is 0.848% (longitudinal), 1.700% (transverse). Given the run 1-4 result [28] of $BF(\rho^- K^*(892)^+_{K^+\pi^0}) = 5.4^{+4.1}_{-3.8}$, and assuming $f_L = 0.5$, we expect 11 $\rho^- K^*(892)^+$ events in the high $K^+\pi^0$ mass sample. We allow this yield to float in the fit.

C.3 Fit validation

To validate these fits, we perform 100 embedded toy experiments, as reported in Tab. C.3. The biases are reasonable and 100% of the fits converge. We use the appropraite type of $\rho^- K^{*+}$ MC for the different K^{*+} signal hypotheses; for $K^*(892)^+$ and $K^*_2(1430)^+$, we assume $f_L = 0.5$.

C.4 Run 1-6 results for the high mass $K^+\pi^0$ fit

The results from fitting run 1-6 data are given in Tab. C.4. The branching fraction results for $\rho^-(K\pi)^{*+}_0$ are given in Tab. 8.6. In order to calculate the interference systematic for $\rho^-(K\pi)^{*+}_0$,

Table C.3: Results of an embedded toy study for the high $K^+\pi^0$ mass region. $B\overline{B}$ background is also embedded (with yields fixed) as described in the text. Each experiment includes 13259 events, where the difference is generated from the $q\overline{q}$ background PDFs. We report the number of events embedded from MC ("Input"), the fit result with the average statistical error, and the bias on the yield. 100/100 fits converged.

Mode	Input	Fit	Bias
$(K\pi)_0^{*+}$	230	225 ± 77	-5 ± 8
$K^*(892)^+$	13	3 ± 63	-10 ± 7
$K_2^*(1430)^+$	88	94 ± 39	6 ± 4

we must have an estimate of the $\rho^- K_2^*(1430)^+$ branching fraction. We assume $f_L = 0.5$ and calculate the $\rho^- K_2^*(1430)^+$ BF in Tab. C.5.

Table C.4: ML fit results for the high $K^+\pi^0$ mass sideband.

Mode	Fit
$\rho^-(K\pi)_0^{*+}$	221 ± 74
$\rho^- K^*(892)^+$	9 ± 67
$\rho^- K_2^*(1430)^+$	76 ± 36

sPlots are in Fig. C.1 and projection plots are given in Fig. C.2. The $K^+\pi^-$ mass sPlots are not shown as the fitter has no way to distinguish between the K_0^{*+}, K_1^{*+}, and K_2^{*+} components without this observable in the fit.

C.5 Extrapolating $\rho^-(K\pi)_0^{*+}$ yields to the $\rho^- K^*(892)^+$ mass region

The efficiencies for the various exclusive MC samples in both the LMR and HMR are given in Tab. C.6. Using these efficiencies and the branching fraction results reported in Tab. 8.6,
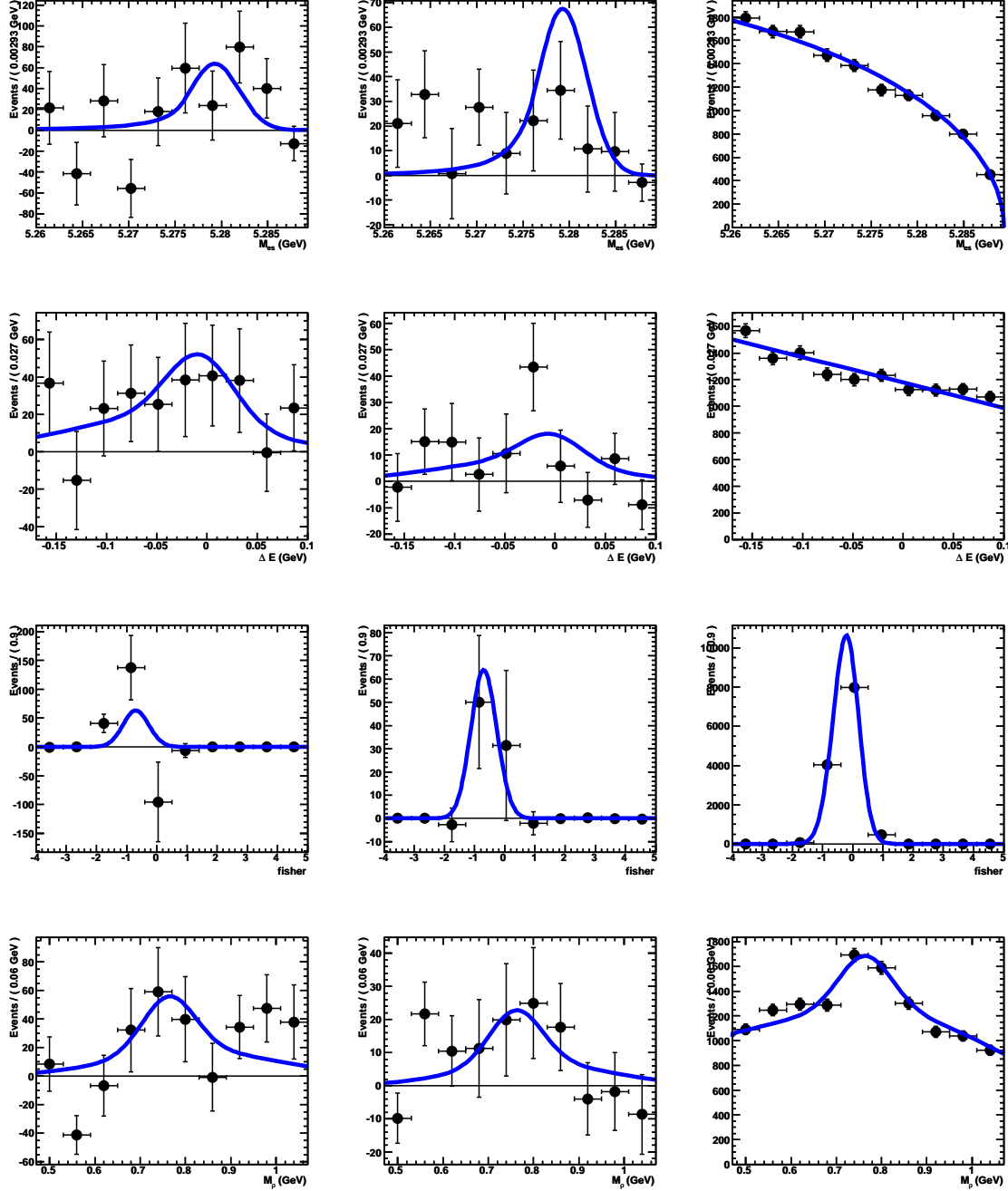
Figure C.1: sPlots of (left to right) K_0^{*+}, K_2^{*+}, and continuum background. Plots are, top to bottom: m_{ES}, ΔE, $\mathcal{F}$, and mass($\pi^-\pi^0$).

Table C.5: High $K^+\pi^0$ mass sideband results for $\rho^- K_2^*(1430)^+$ from run 1-6 data. Uncertainties are statistical only. $\rho^-(K\pi)_0^{*+}$ results are in Tab. 8.6

ML fit quantity	$\rho^- K_2^*(1430)^+$
Fit signal yield	76 ± 36
Fit bias	6 ± 4
Corrected yield	$92 \pm 39 \pm 5$
MC ϵ (%)	4.67(ln) 9.41(tr)
$\prod \mathcal{B}_i$ (%)	0.163
f_L (assumed)	0.5
$\mathcal{B}(10^{-6})$	13.0 ± 6.7

Table C.6: Number of events selected, number of MC events generated, and selection efficiencies for the $K^+\pi^0$ LMR and HMR. $^\dagger N_{\text{gen}}$ for $\rho^-(K\pi)_0^{*+}$ is the product of the number of 3-body phase space events generated times the efficiencies to reweight the $K^+\pi^0$ mass to a LASS distribution and that of reweighting the $\mathcal{H}_\rho$ distribution.

	LMR			HMR	
	# evts	N_{gen}	ϵ	# evts	ϵ
Run 1-6 Data	9705	—	—	13259	—
$\rho^-(K\pi)_0^{*+}$	2046	$171965^\dagger$	0.01190	8125	0.04802
$\rho^- K^*(892)^+$ ln	21185	429000	0.04938	3638	0.00848
$\rho^- K^*(892)^+$ tr	47963	429000	0.11180	7293	0.01700
$\rho^- K_2^*(1430)^+$ ln	—	423000	—	19746	0.04668
$\rho^- K_2^*(1430)^+$ tr	—	423000	—	39807	0.09411

we can extrapolate the fitted number of $\rho^-(K\pi)_0^{*+}$ events into the LMR. We expect

$$N_{\rho^-(K\pi)_0^{*+}} = 60 \pm 23 \tag{C.3}$$

in the $K^+\pi^0$ LMR.

C.6 High $K^+\pi^0$ mass fit results

The run 1-6 inclusive fit results, including all floating PDF parameters:

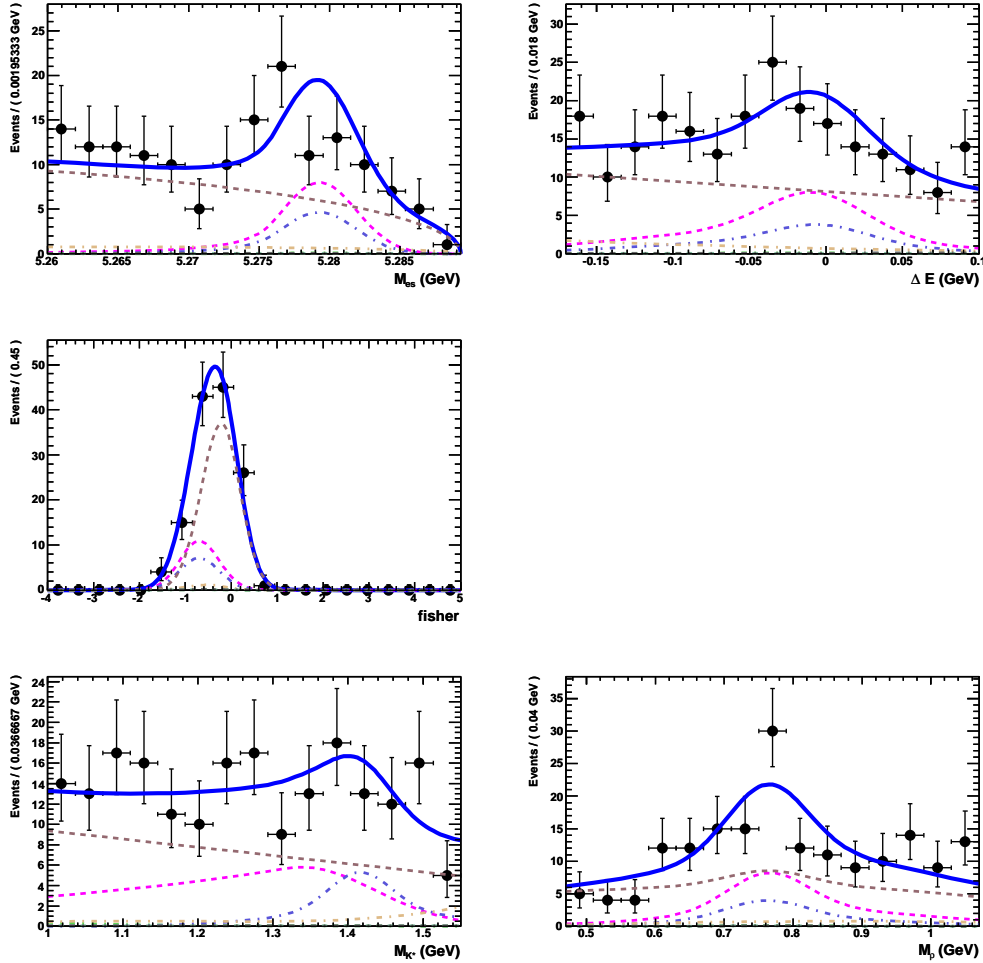Figure C.2: Projection plots of the high $K^+\pi^0$ mass region fit. Left to right, top to bottom: m_{ES}, ΔE, $\mathcal{F}$, mass($K^+\pi^0$), and mass($\pi^-\pi^0$). The solid blue curve shows the total fit result, the pink curve is K_0^{*+}, blue is K_2^{*+}, and the dashed brown is continuum background. A cut on the K_0^{*+} signal likelihood is applied to enhance the visibility of the signal.

```
   Constant Parameter     Value
---------------------  ------------
     BRModel_nD0rho      4.2700e+02
     BRModel_na1mKp      1.3000e+01
    BRModel_nrhorho      1.5000e+01
                eff      4.5300e-02
            fitBias     -5.0000e+00
                nBB      4.7100e+02
             prodBR      3.3330e-01


   Floating Parameter  InitialValue    FinalValue (+HiError,-LoError)    GblCorr.
---------------------  ------------  ----------------------------------  --------
       BRModel_nBkg     1.2593e+04     1.2476e+04 (+1.26e+02,-1.25e+02)  0.402483
      BRModel_nRKst1    1.1000e+01     8.1680e+00 (+6.89e+01,-6.58e+01)  0.795092
      BRModel_nRKst2    1.0000e+02     7.5242e+01 (+3.73e+01,-3.56e+01)  0.691048
          de_Bkg_P01   -2.1202e-01    -2.0636e-01 (+1.55e-02,-1.54e-02)  0.055809
        fis_BkgC_asym  -5.5811e-02    -5.1458e-02 (+1.49e-02,-1.49e-02)  0.147839
        fis_BkgC_mean  -2.5322e-01    -2.4544e-01 (+4.30e-03,-4.31e-03)  0.386857
         fis_BkgC_rms   4.2727e-01     4.2301e-01 (+3.03e-03,-3.00e-03)  0.278541
           mK_Bkg_P01  -2.9013e-01    -3.1046e-01 (+1.60e-02,-1.60e-02)  0.271507
      mR_Bkg_Poly_P01  -8.7227e-02    -1.0513e-01 (+1.94e-02,-1.96e-02)  0.328023
      mR_Bkg_Poly_P02  -1.0123e-01    -7.5162e-02 (+3.11e-02,-3.03e-02)  0.783538
       mR_Bkg_fracRho   1.7187e-01     1.8305e-01 (+2.11e-02,-2.10e-02)  0.798063
        measBR_RKst0    3.0000e+01     3.1935e+01 (+1.04e+01,-1.03e+01)  0.846073
            mes_Bkg_c  -2.2017e+01    -1.2467e+01 (+3.32e+00,-3.32e+00)  0.303216
```

C.7   PDF plots for the high mass $K^+\pi^0$ fit

PDF distributions for the high mass $K^+\pi^0$ fit are shown in Fig. C.3–C.9. The observables are (left to right, top to bottom): ΔE, m_{ES}, $\mathcal{F}$, mass($K^+\pi^0$), mass($\pi^-\pi^0$).

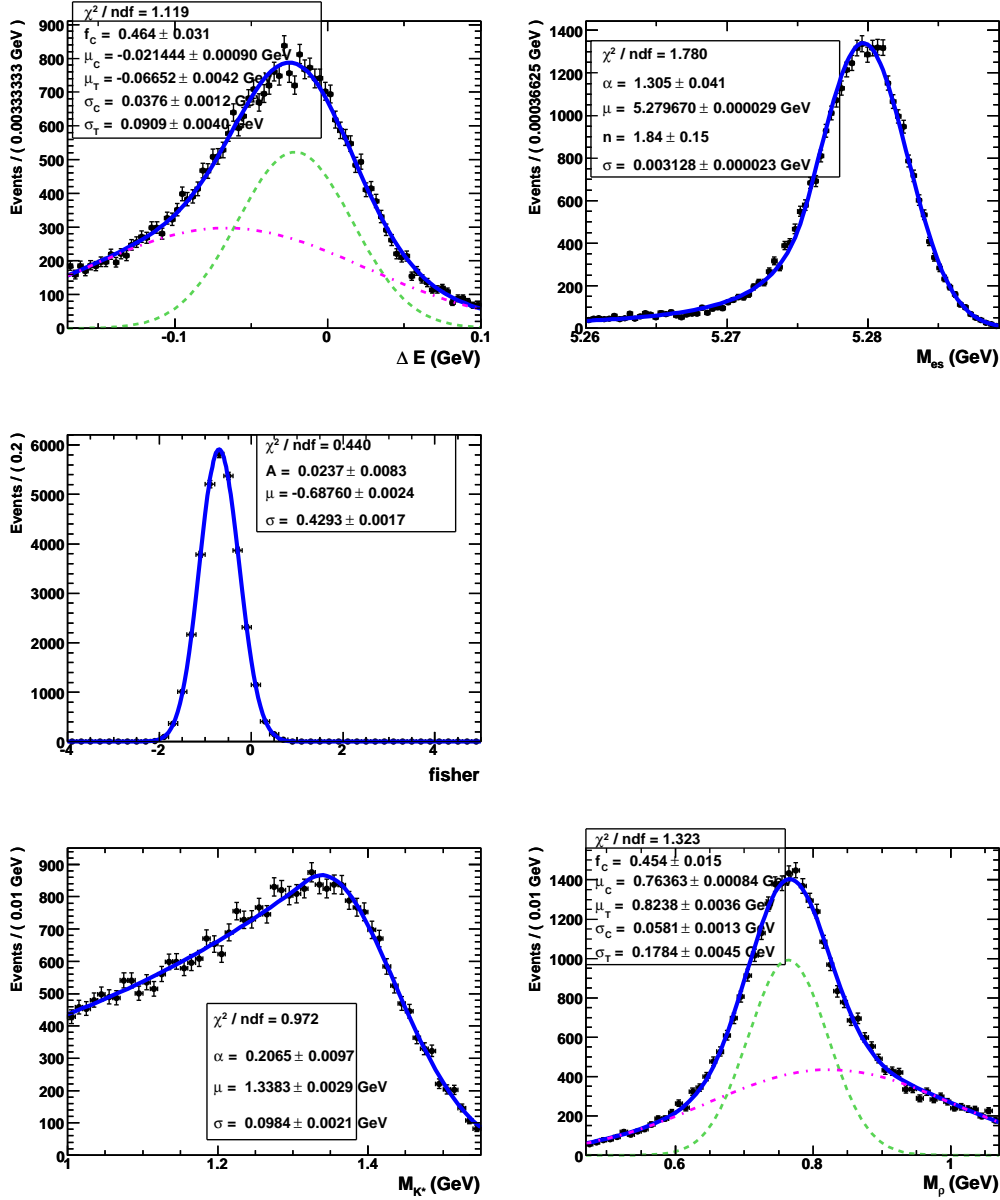Figure C.3: PDFs for $\rho^-(K\pi)_0^{*+}$ in the high mass $K^+\pi^0$ region.
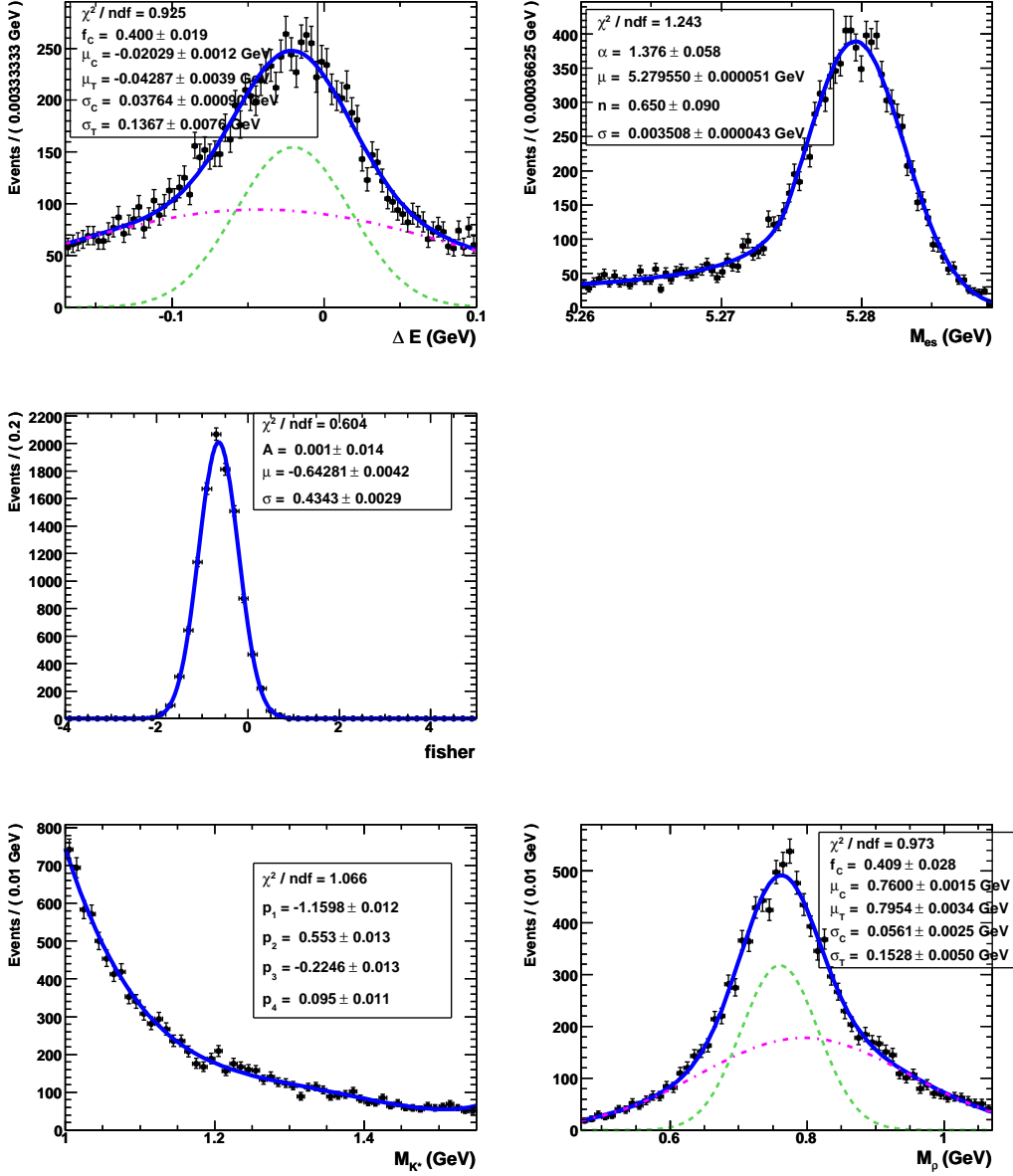
Figure C.4: PDFs for $\rho^- K^*(892)^+$ in the high mass $K^+\pi^0$ region.

Figure C.5: PDFs for $\rho^- K_2^*(1430)^+$ in the high mass $K^+\pi^0$ region.

Figure C.6: PDFs for $D^0\rho^-$ with $D^0 \to K^-\pi^+\pi^0$ in the high mass $K^+\pi^0$ region.

Figure C.7: PDFs for $a_1^- K^+$ in the high mass $K^+\pi^0$ region.

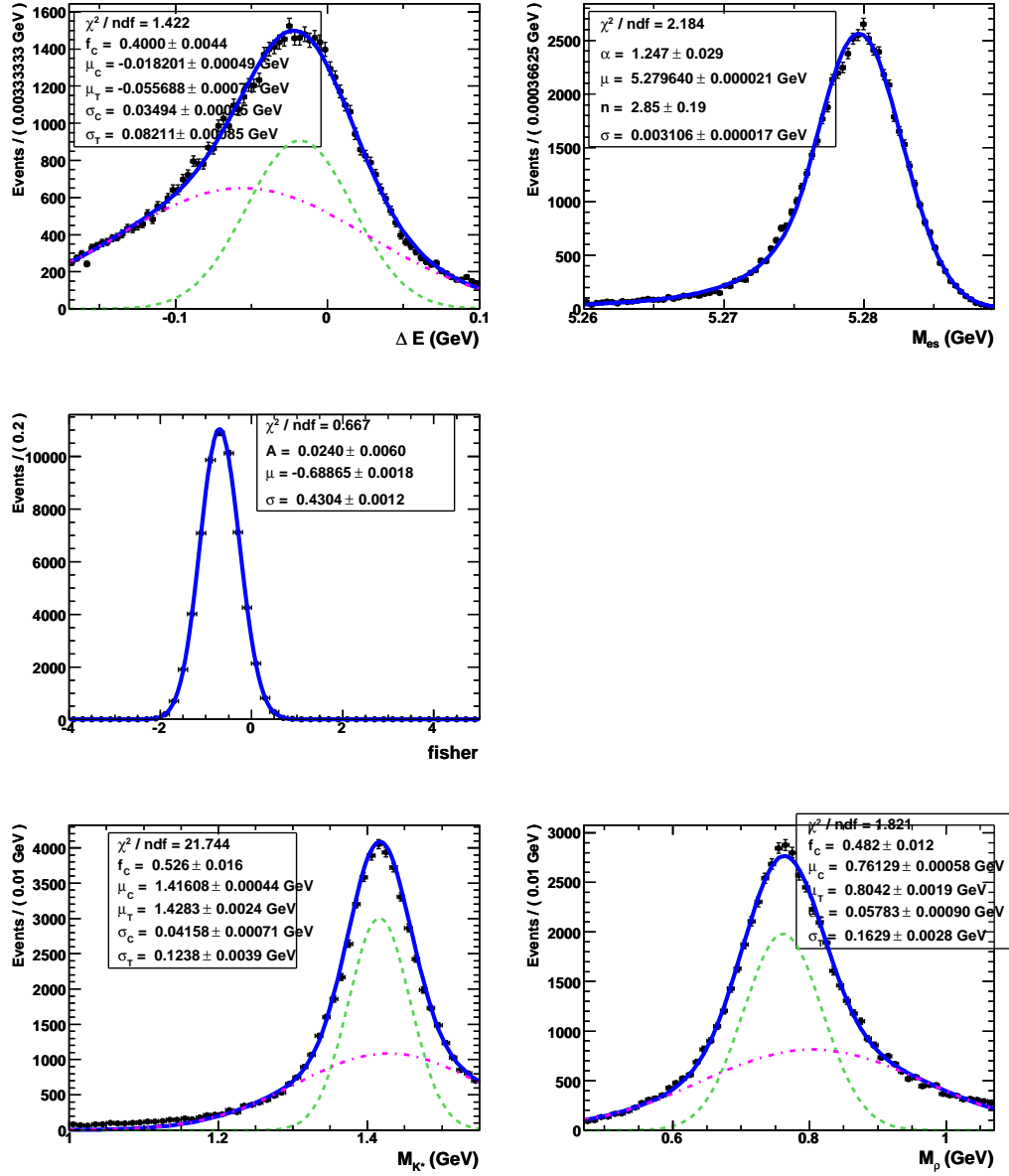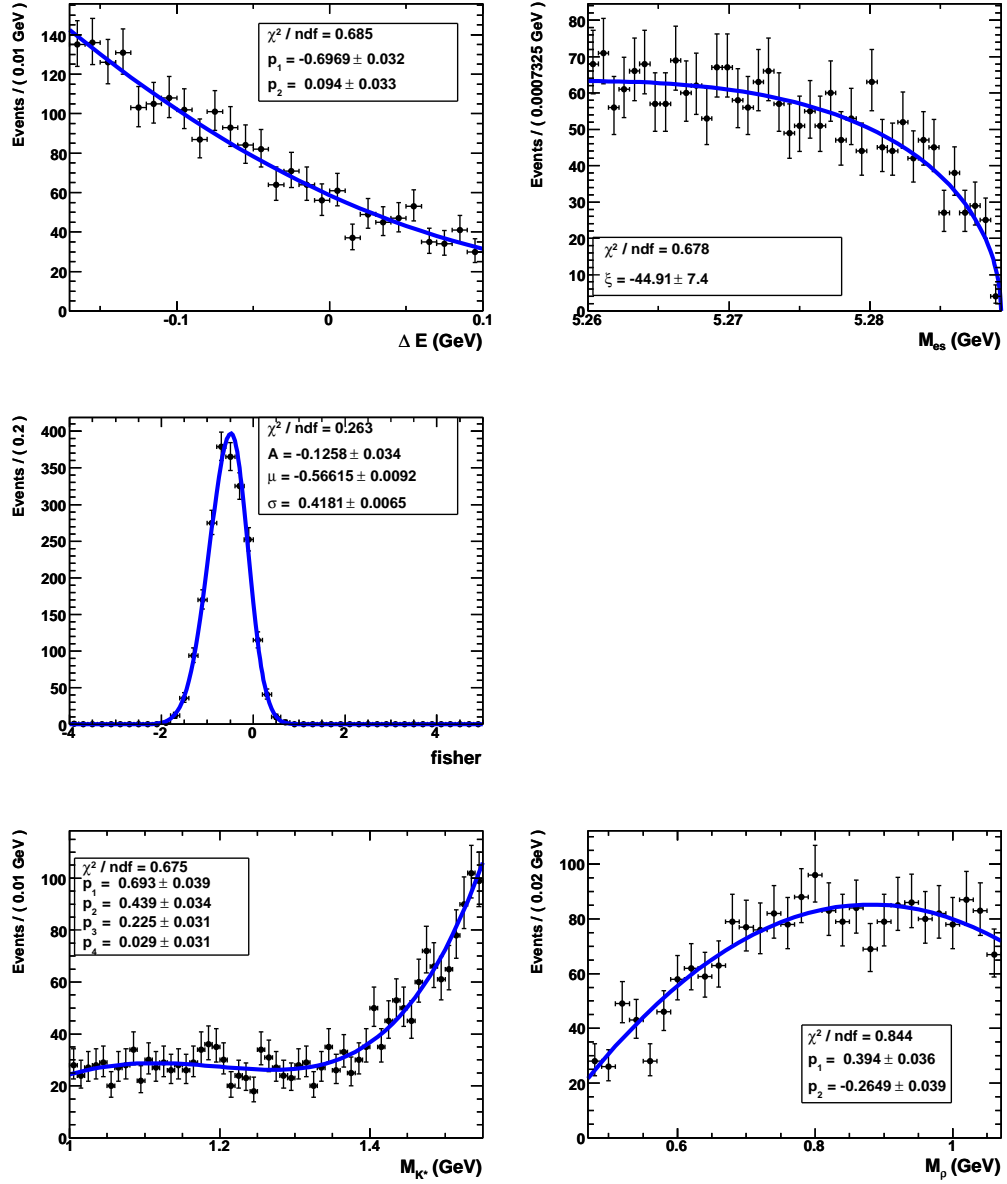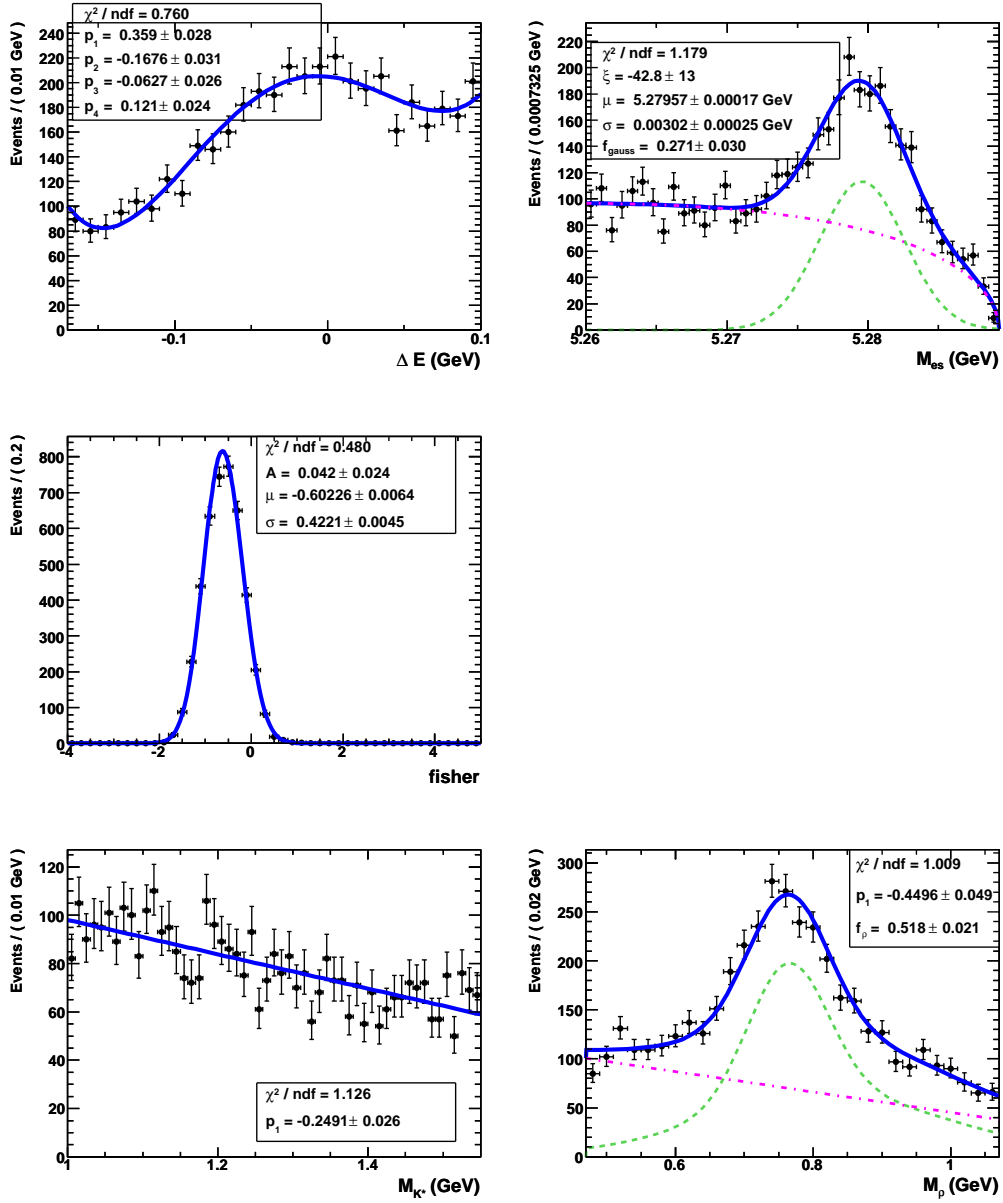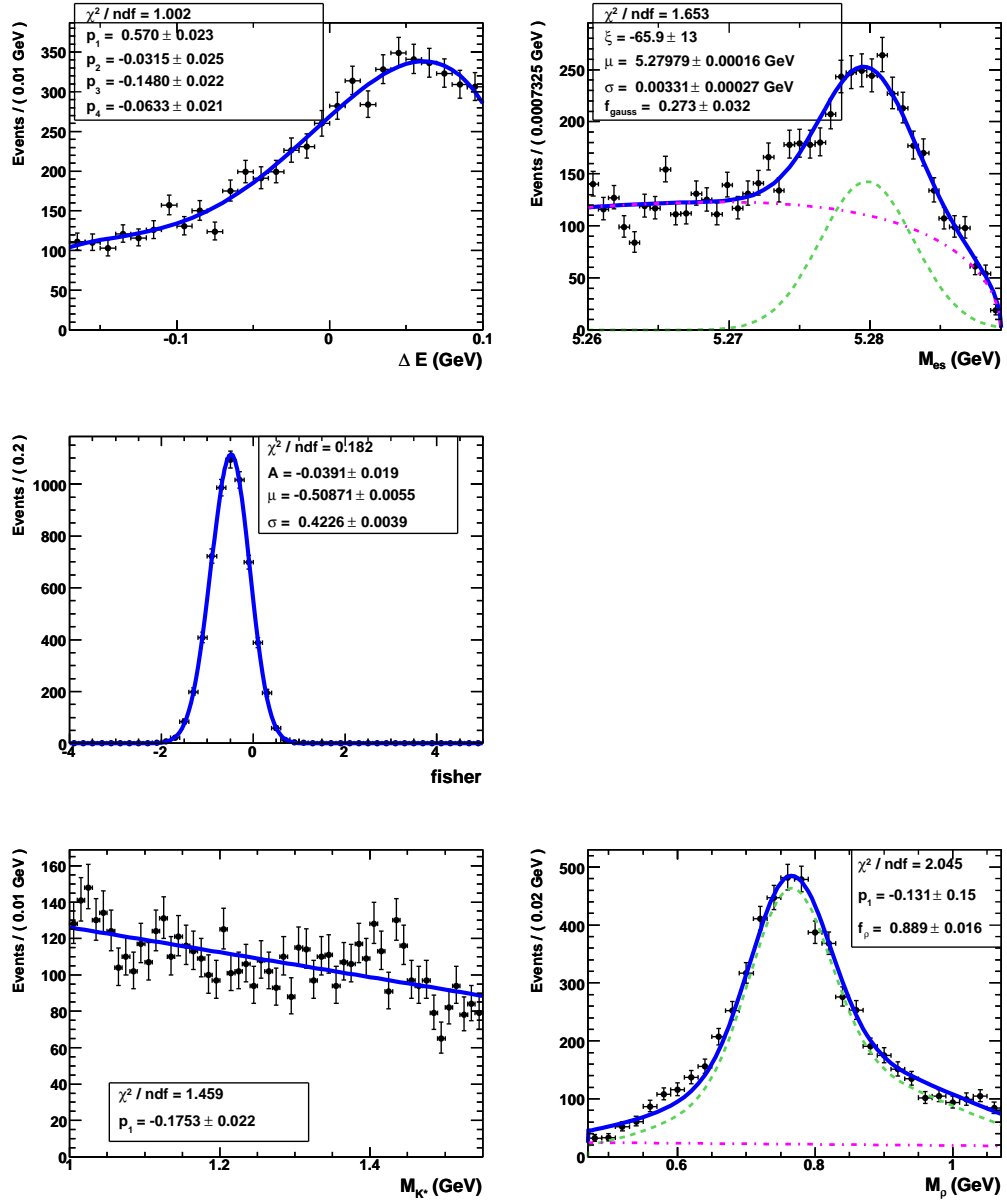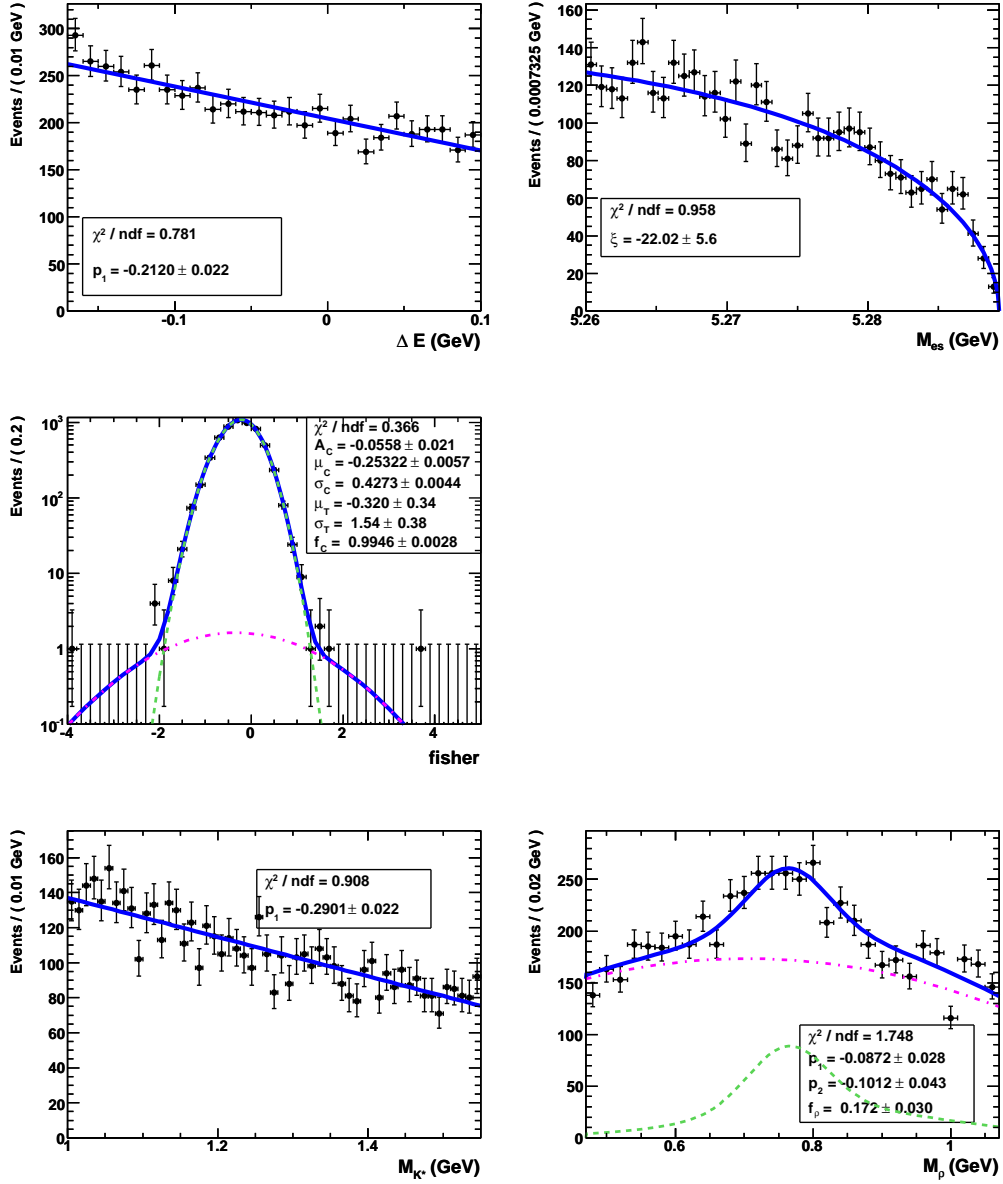Figure C.8: PDFs for $\rho^+\rho^-$ in the high mass $K^+\pi^0$ region.

Figure C.9: PDFs for $q\bar{q}$ continuum background in the high mass $K^+\pi^0$ region.

Appendix D

High $\pi^+\pi^-$ Mass Region Study

The previous analysis of $B^0 \to \rho^0 K^*(892)^0$ [28] included a high mass $\pi^+\pi^-$ resonance as a $B\overline{B}$ background. To determine the importance of such high mass states, we open up the $m(\pi^+\pi^-)$ region to $(0.47, 1.47)\,\mathrm{GeV}$, using the standard LMR $K^*(892)^0$ mass region $(0.75 < m(K^+\pi^-) < 1.0\,\mathrm{GeV})$. We consider the resonances: $\rho^0(770)$, $f_0(980)$ and $f_2(1270)$.

In the 2010 PDG [2], the $f_2(1270)$ has the properties:

$$
\begin{aligned}
m_{f_2(1270)} &= (1275.1 \pm 1.2)\,\mathrm{MeV} \\
\Gamma_{f_2(1270)} &= (185.1^{+2.9}_{-2.4})\,\mathrm{MeV} \\
\mathcal{B}(f_2(1270) \to \pi\pi) &= (84.8^{+2.4}_{-1.2})\%\,.
\end{aligned}
$$

In our MC simulation of the $f_2(1270)$, we use:

$$
\begin{aligned}
m_{f_2(1270)} &= 1275\,\mathrm{MeV} \\
\Gamma_{f_2(1270)} &= 185\,\mathrm{MeV}\,.
\end{aligned}
$$

This study is performed in two stages, as in App. B. First, we obtain an "inclusive" measurement of the $K^*(892)^0$ yield for the entire $\pi^+\pi^-$ mass range. For this, we use an ML fit with with four observables: m_{ES}, ΔE, $\mathcal{F}$, and $\mathrm{mass}(K^+\pi^-)$. Second, as we see a significant

$K^*(892)^0$ signal, we use the sWeighted [47] dataset corresponding to $K^*(892)^0$ signal and fit the $K^+\pi^-$ mass spectrum to determine how many signal $K^*(892)^0$ events are paired with a ρ^0, f_0, or $f_2(1270)$.

We include the same $B\overline{B}$ background components as in the LMR fit, determined in an equivalent fashion to that described in Sec. 7.2.1. After re-making the charmless and D^0 cocktails and re-running preselection on all samples, we expect the following backgrounds in Run 1-6 data. The $(K\pi)_0^{*0}$ component includes both the $\rho^0(K\pi)_0^{*0}$ and $f_0(K\pi)_0^{*0}$ backgrounds, extrapolated from the measured number of events in App. B.

$$
\begin{aligned}
N_{a_1^- K^+} &= 17 \\
N_{D^- \pi^+} &= 439 \\
N_{D^0} &= 931 \\
N_{\text{Chmls}} &= 105 \\
N_{(K\pi)_0^{*0}} &= 250
\end{aligned}
\tag{D.1}
$$

PDFs for all components are given in Fig. D.1-D.2.

D.1 Fit validation

To validate these fits, we perform 100 embedded toy experiments, as reported in Tab. D.1. The bias on the inclusive $K^*(892)^0$ yield is reasonable and 100% of the fits converge. For the signal events, we embed $\rho^0 K^*(892)^0$ MC and assume $f_L = 0.5$.

D.2 "Inclusive" fit to $K^*(892)^0$ signal with wide $m(\pi^+\pi^-)$

For the fit to on-peak run 1-6 data, we fix the $B\overline{B}$ background yields to the values listed in Eq. D.1. There are 29147 on-peak events in the run 1-6 data set. The results of the inclusive fit
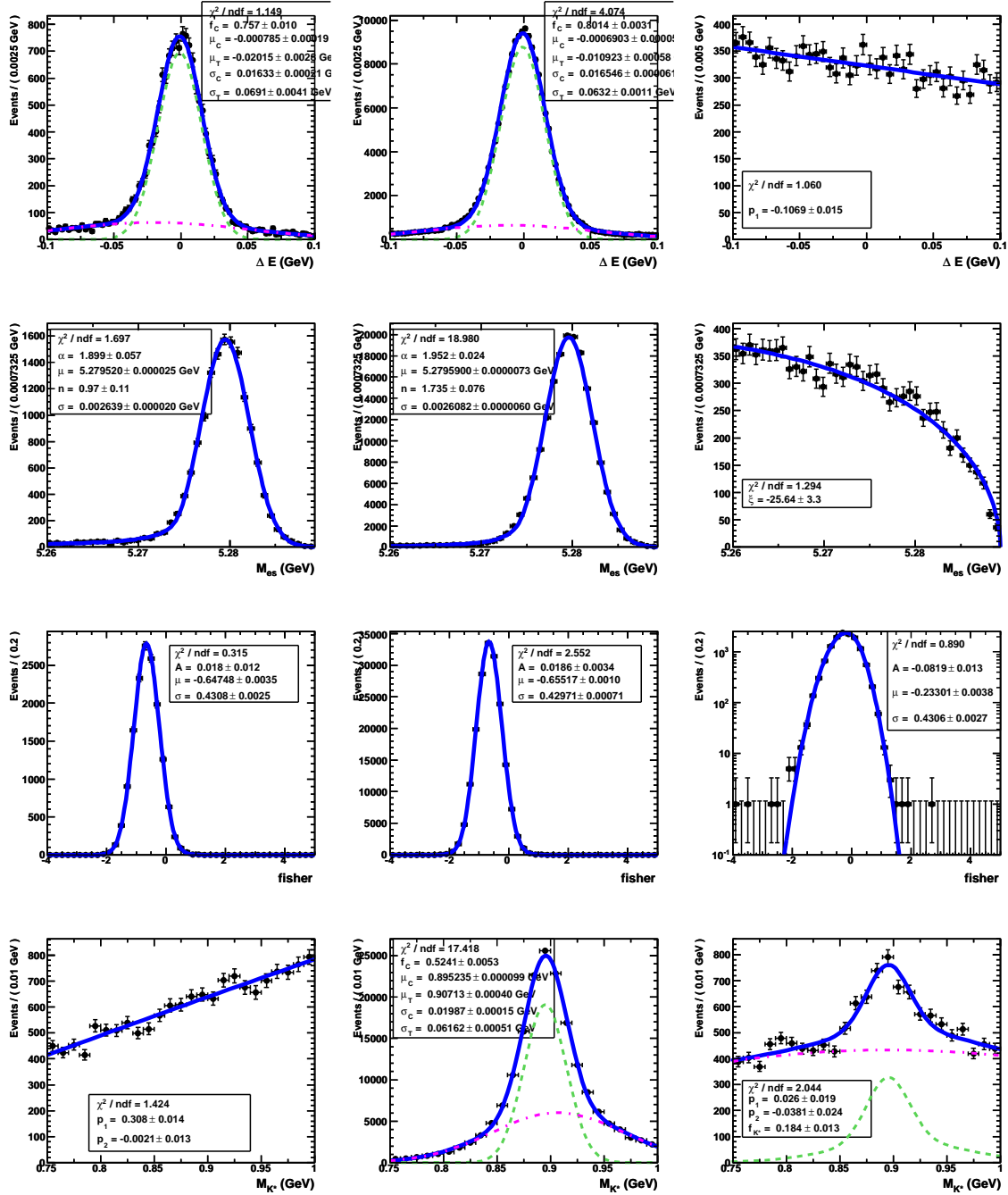
Figure D.1: PDF plots for (from left to right) $(K\pi)^{*0}_0$, $K^*(892)^0$, continuum background. From top to bottom: ΔE, m_{ES}, $\mathcal{F}$, $(K^+\pi^-)$ mass.
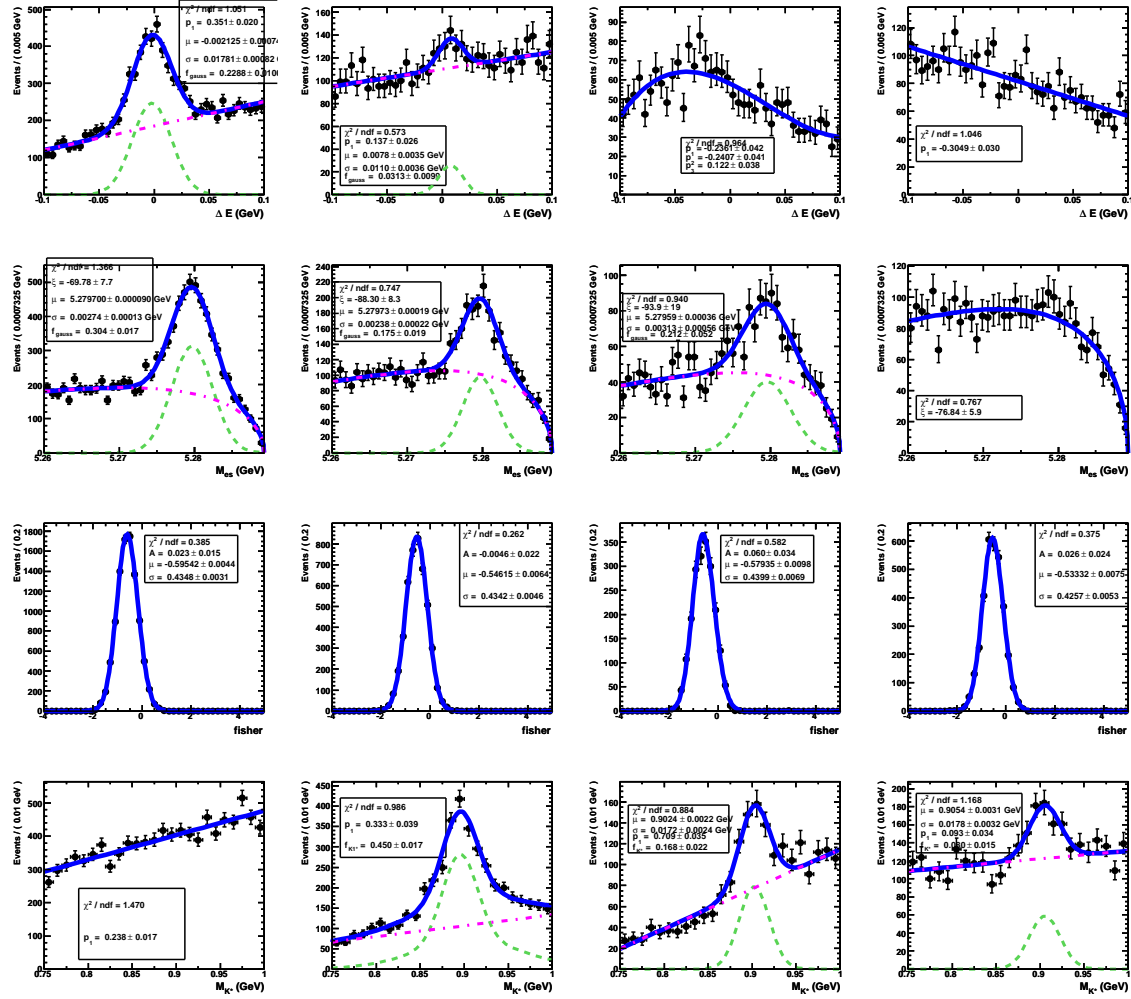
Figure D.2: PDF plots for (from left to right) $B^0 \to a_1^- K^+$, charmless cocktail, $D^-\pi^+$, and D^0 cocktail. From top to bottom: ΔE, m_{ES}, $\mathcal{F}$, $(K^+\pi^-)$ mass.

Table D.1: Results of an embedded toy study for the wide $\pi^+\pi^-$ region. $B\overline{B}$ background (see Eq. D.1) is embedded with yields fixed. Each experiment includes 29147 events, where the difference is generated from the $q\overline{q}$ background PDFs. We report the number of events embedded from MC ("Input"), the fit result with the average statistical error, and the bias on the yield. 100/100 fits converged.

Mode	Input	Fit	Bias
$K^*(892)^0$	1400	1456 ± 62	56 ± 4

Table D.2: On-peak Run 1-6 fit results for $0.47 < m(\pi^+\pi^-) < 1.47$ GeV. The fit is performed in two stages, first extracting the inclusive $K^*(892)^0$ yield, then using the sWeighted $K^*(892)^0$ signal sample to fit for three $\pi^+\pi^-$ mass hypotheses. The "Corrected" column has had the fit bias subtracted off and includes a systematic uncertainty from this procedure.

	Inclusive	Exclusive	Corrected
$K^*(892)^0$	1447 ± 63		$1391 \pm 63 \pm 28$
$\rho(770)^0 K^{*0}$		$577 \pm 27 \pm 25$	$555 \pm 27 \pm 25 \pm 12$
$f_0(980)K^{*0}$		$219 \pm 19 \pm 10$	$211 \pm 19 \pm 10 \pm 6$
$f_2(1270)K^{*0}$		$652 \pm 27 \pm 28$	$627 \pm 27 \pm 28 \pm 13$
Continuum	25929 ± 173		

are given in Tab. D.2.

We give the fit results after subtracting the fit bias in the "Corrected" column of Tab. D.2. For the exclusive yields, we subtract the appropriate fraction of the fit bias based on the fraction of ρ^0, f_0, or $f_2(1270)$ events to the total. The uncertainty from this procedure is quoted as a systematic error on the yield, which we define as half the fit bias on that exclusive yield $\oplus$ the uncertainty on the total fit bias.

Fig. D.3 gives the projection plots with cuts on the $K^*(892)^0$ signal likelihood to improve visibility of the signal events. Fig. D.4 shows the sPlots for ΔE, m_{ES}, $\mathcal{F}$, and mass($\pi^+\pi^-$) from the inclusive fit. The $\pi^+\pi^-$ mass is not used to discriminate between the signal and background hypotheses, but is included for reference.
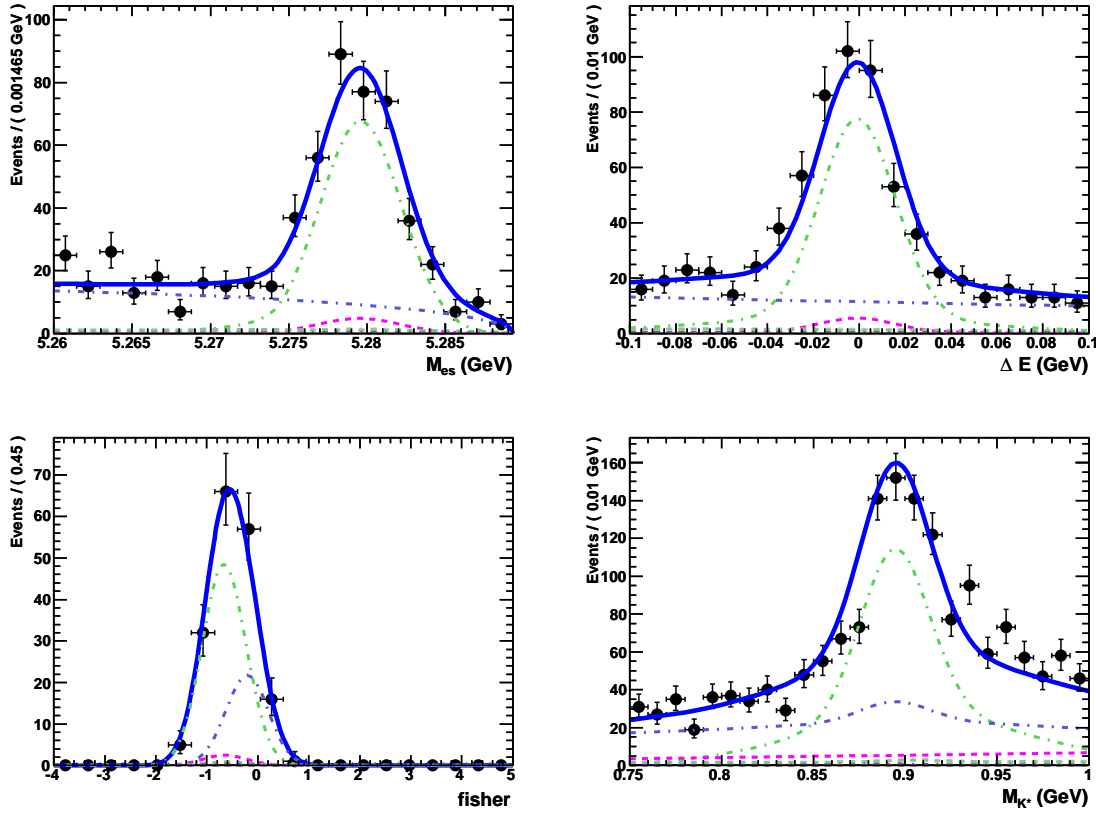
Figure D.3: Projection plots of the first stage fit to the wide $\pi^+\pi^-$ mass region. Left to right, top to bottom: m_{ES}, ΔE, $\mathcal{F}$, and mass($K^+\pi^-$). The solid blue curve shows the total fit result, the green curve is $K^*(892)^0$, pink is $(K\pi)_0^{*0}$, and the dashed blue is continuum background. A cut on the $K^*(892)^0$ signal likelihood is applied to enhance the visibility of the signal.
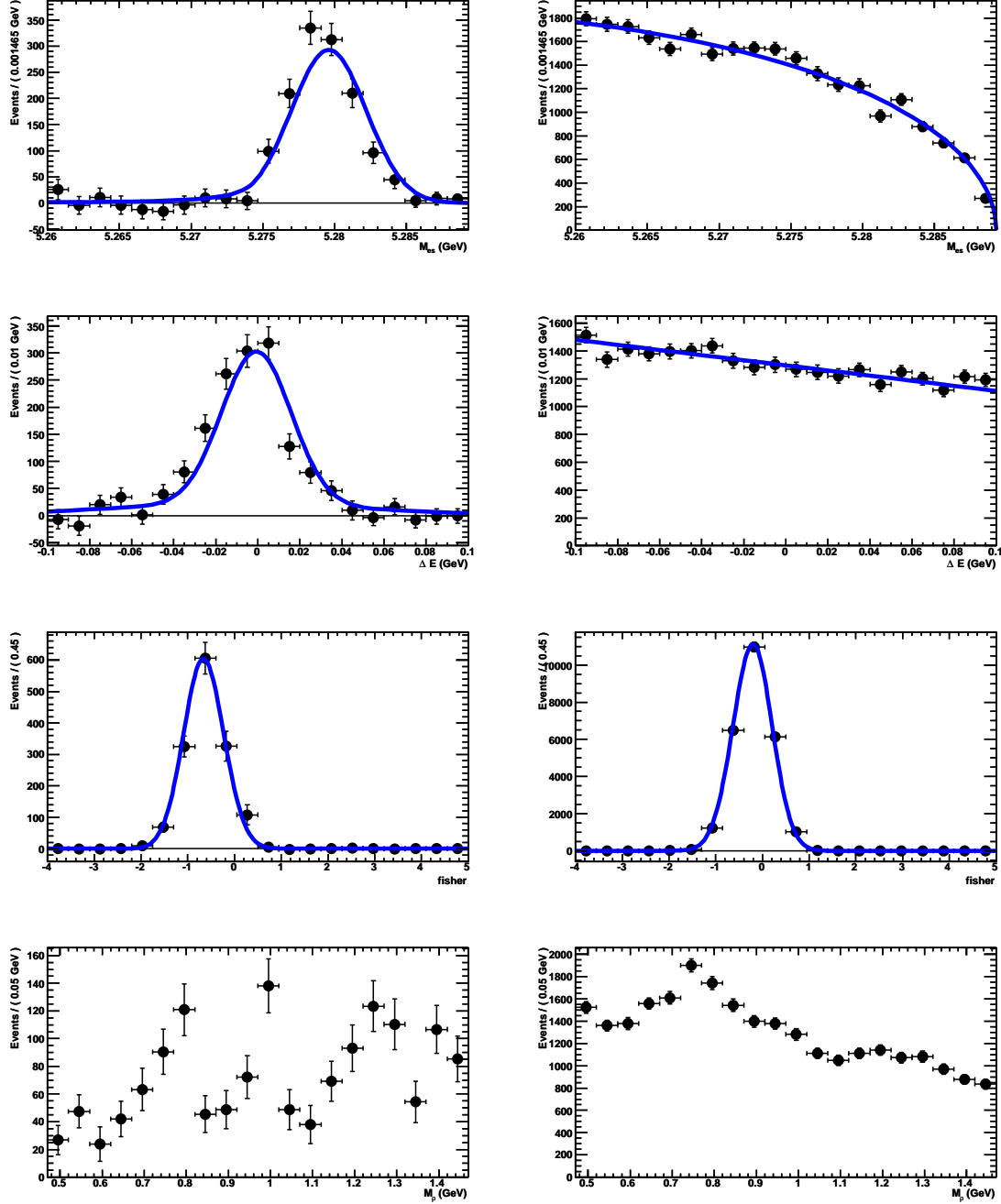
Figure D.4: sPlots of $K^*(892)^0$ (left) and continuum background (right). Plots are, top to bottom: m_{ES}, ΔE, $\mathcal{F}$, and mass($\pi^+\pi^-$).

D.3 $\pi^+\pi^-$ **mass spectrum in sWeighted** $K^*(892)^0$ **signal**

After performing the ML fit to extract the "inclusive" $K^*(892)^0$ signal yield, we weight the on-peak dataset with the $K^*(892)^0$ signal sWeights. The weighted number of events in the dataset is 1448 events for run 1-6. We then fit the $\pi^+\pi^-$ invariant mass distribution over the range $(0.47, 1.47)\,\mathrm{GeV}$ to three hypotheses: ρ^0, f_0, and $f_2(1270)$. The PDF shapes for these hypotheses are double Gaussians derived from signal MC. The fit results are plotted in Fig. D.5. The fit yields are given in Tab. D.2.
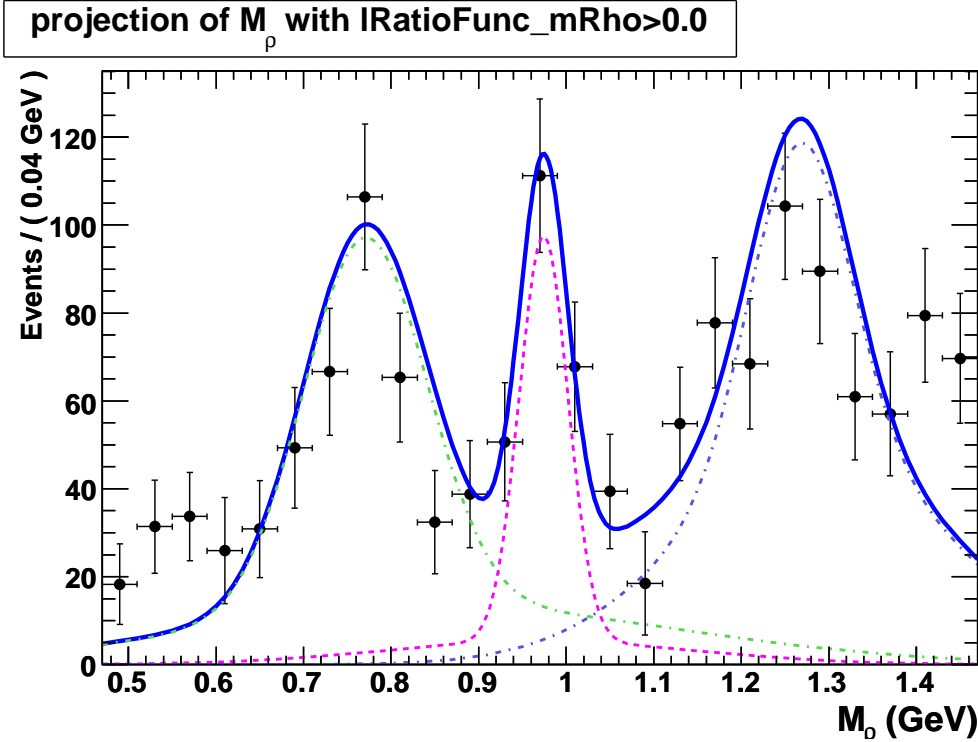
Figure D.5: Results of the fit to the $\pi^+\pi^-$ mass spectrum for the sWeighted $K^*(892)^0$ signal (points with error bars) in the $K^+\pi^-$ mass region $(0.75, 1.0)\,\mathrm{GeV}$. The solid blue curve shows the total fit result, the green curve is ρ^0, pink is f_0, and the dashed blue is $f_2(1270)$.

Although we observe a large number of $f_2(1270)$ events, we choose not to consider $f_2(1270)K^*(892)^0$ as a signal in our analysis. There are several reasons for this. Although the data seem to match the MC simulated $f_2(1270)$ shape, we cannot be certain that we are observ-

ing $f_2(1270)$ events rather than $f_0(1370)$ events (a resonance for which the 2010 PDG [2] lists $m = (1200 - 1500)\,\mathrm{MeV}$ and $\Gamma = (200 - 500)\,\mathrm{MeV}$; the decay $f_0(1370) \to \pi\pi$ is listed as "seen"). Additionally, because $f_2(1270)K^*(892)^0$ is a tensor–vector mode, it can be in an S–, P–, or D–wave state. Assuming we knew all the events were actually $f_2(1270)K^*(892)^0$, we could measure f_L, but given the unknown fraction of $f_0(1370)K^*(892)^0$ events, the problem becomes quite complex.

Therefore we consider the $f_2(1270)K^*(892)^0$ events as a background to the $\rho^0 K^{*0}$ and $f_0 K^{*0}$ analysis. The problem of whether we are seeing $f_2(1270)$ or $f_0(1370)$ events becomes considerably less important in this case, as we are only dealing with a small tail of these events beneath our signal. For the LMR fit, we assume that all of these events are $f_2(1270)K^*(892)^0$.

D.4 Extrapolating the $f_2(1270)K^*(892)^0$ yield into the LMR

The efficiencies for $f_2(1270)K^*(892)^0$ in both the LMR and wide $\pi^+\pi^-$ mass regions are given in Tab. D.3. Using these efficiencies, we extrapolate the number of $f_2(1270)K^*(892)^0$ events expected in the LMR fit region $(0.47 < m(\pi^+\pi^-) < 1.07)\,\mathrm{GeV}$:

$$N_{f_2(1270)K^{*0}} = 47 \pm 3 \,. \tag{D.2}$$

Table D.3: Number of events selected, MC efficiencies (ϵ), and measured (extrapolated) $f_2(1270)K^*(892)^0$ yields for the wide (LMR) $\pi^+\pi^-$ mass region. For both the longitudinally and transversely polarized $f_2(1270)K^*(892)^0$, 427000 MC events were generated. A longitudinal fraction $f_L = 0.5$ is assumed.

	Wide $m(\pi^+\pi^-) = (0.47, 1.47)\,\mathrm{GeV}$			LMR $m(\pi^+\pi^-) = (0.47, 1.07)\,\mathrm{GeV}$		
	# evts	ϵ	measured yield	# evts	ϵ	extrapolated yield
Run 1-6 Data	29145	—	627 ± 41	18792	—	47 ± 3
$f_2(1270)K^{*0}$ ln	50540	0.1184	—	4686	0.0110	—
$f_2(1270)K^{*0}$ tr	87095	0.2040	—	5725	0.0134	—

Appendix E

Control Sample Studies

The decays $B^0 \to D^- \pi^+$ ($D^- \to K^+ \pi^- \pi^-$) and $B^0 \to \overline{D}^0 \pi^0$ ($\overline{D}^0 \to K^+ \pi^- \pi^0$) have similar topologies to the signal decays and large branching fractions. They are used as calibration channels. We apply the same selection criteria as described in Ch. 6.2 except that the $m_{\pi\pi}$ and $m_{K\pi}$ mass criteria are replaced with a mass range $1.85 < m_{D^-} < 1.89$ GeV or $1.83 < m_{\overline{D}^0} < 1.89$ GeV and no D meson veto is applied. We use the selected data to verify that the ML fit is performing correctly and that the MC is properly simulating the $\mathcal{F}$, ΔE, and m_{ES} distributions. From these studies, we extract small corrections to the MC distributions of ΔE and m_{ES}, which we apply to the signal PDFs in our LMR and HMR likelihood fits (see Tab. 7.11). We find no correction necessary for $\mathcal{F}$.

E.1 $B^0 \to D^- \pi^+$ with $D^- \to K^+ \pi^- \pi^-$ Control Sample

To study the agreement between data and MC for $B^0 \to \rho^0 K^{*0}$, we perform a ML fit analysis of $B^0 \to D^- \pi^+$ with $D^- \to K^+ \pi^- \pi^-$. The branching fractions are [2]:

$$\mathcal{B}(B^0 \to D^- \pi^+) = (2.68 \pm 0.13) \times 10^{-3}$$

$$\mathcal{B}(D^- \to K^+ \pi^- \pi^-) = (9.29 \pm 0.25) \times 10^{-2} \ .$$

The ML fit includes two components: signal and background. The signal comes from 539000 generated signal MC events (mode # 2437). The selection efficiency is: $(25.47 \pm 0.06)\%$. Given the on-peak data sample of $N_{B\bar{B}} = (471.0 \pm 2.8) \times 10^6$, we expect $29900 \pm 1700 \; D^-\pi^+$ events. A fit to on-peak run 1-6 data finds a signal yield of 27640 ± 180 (statistical error only), in reasonable agreement with expectation.

The PDFs are shown in Fig. E.1-E.2. The PDF variables are m_{ES}, ΔE, $\mathcal{F}$, and D mass. They are fit with the functions listed in Tab. E.1.

Table E.1: PDF shapes used to fit the $D^-\pi^+$ sample.

Variable	Signal PDF	Bkg PDF
m_{ES}	Crystal Ball	ARGUS + Gaus.
ΔE	Double Gaus.	1st order poly
$\mathcal{F}$	Asym. Gaus.	Asym. Gaus.
D mass	Double Gaus.	2nd order poly

In order to evaluate the agreement between data and MC simulation, we allow the "shift" and "scale" signal PDF parameters to float in the fit to data. For the double Gaussian describing ΔE, this applies the same shift to the means of both the core and tail Gaussians; the scale factor multiplies only the core width. For the Crystal Ball describing m_{ES}, the shift moves the mean and the scale multiplies the width. For the Crystal Ball shape describing m_{ES}, we test allowing the α parameter to float; its value in data is consistent with MC. The Crystal Ball parameter n is fixed to the signal MC value, $n = 8.1 \pm 0.8$.

We find consistent shift and scale factor values across all runs of on-peak data, so use the values determined from floating those parameters in run 1-6 data. The results are given in Tab. E.2. We show projection plots for runs 1-6 in Fig. E.3; sPlots of signal and background are shown in Fig. E.4.
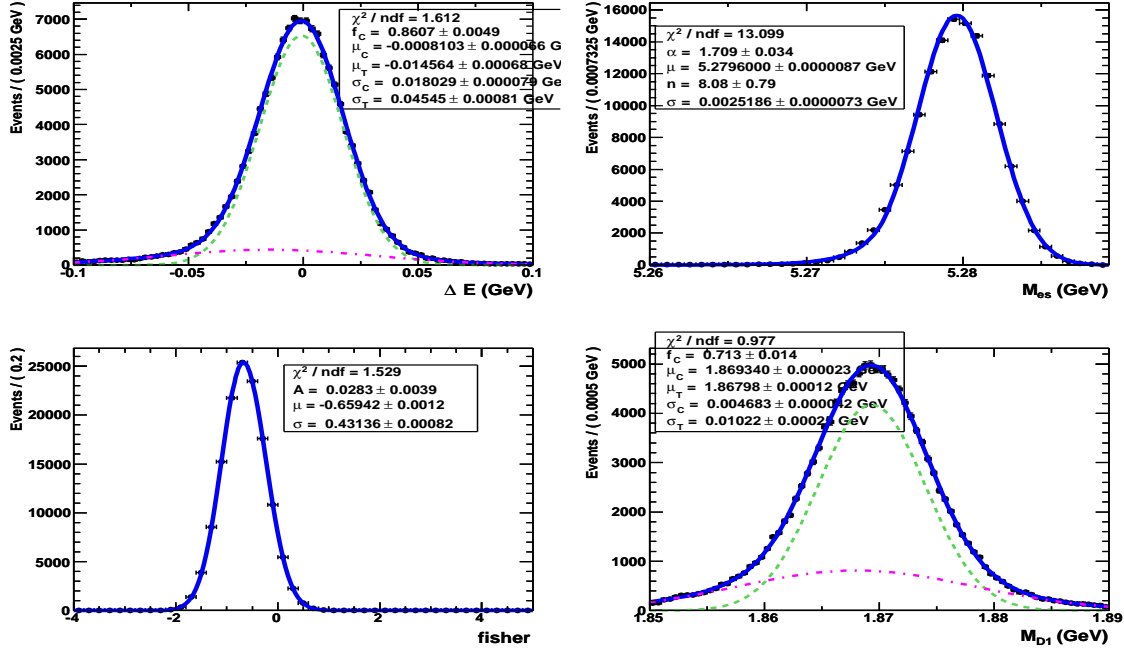
Figure E.1: $D^-\pi^+$ signal PDFs.
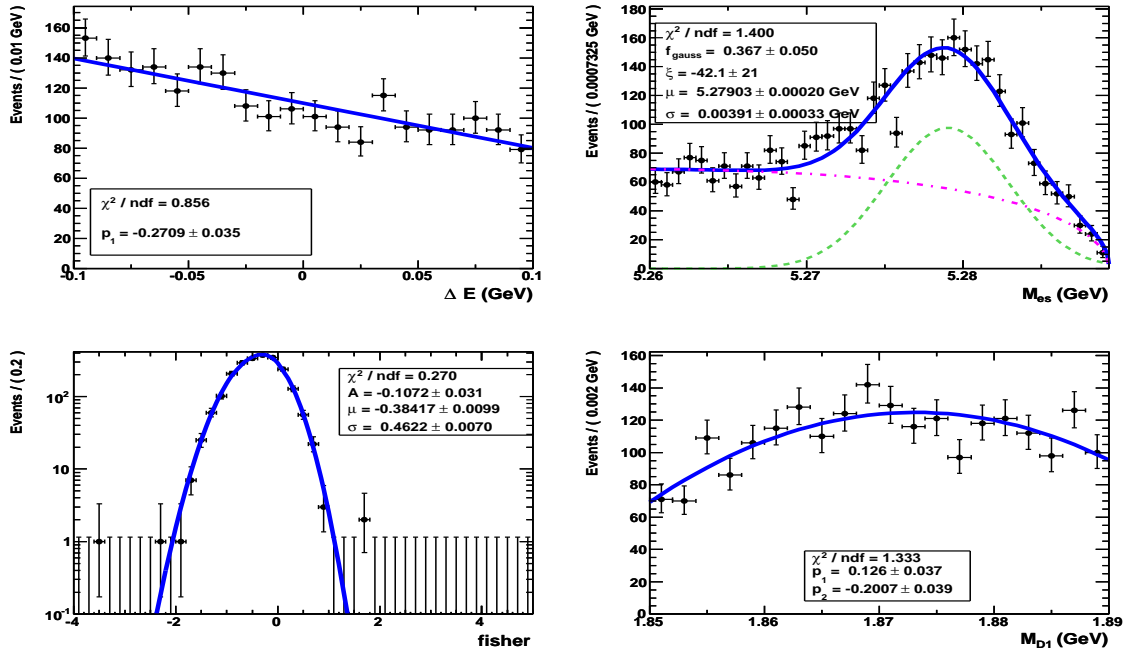
Figure E.2: $D^-\pi^+$ continuum PDFs based on on-peak sideband data from runs 1-6.

Table E.2: Shifts and scale factors obtained from floating signal PDF parameters in the control sample $B^0 \to D^-\pi^+$ with $D^- \to K^+\pi^-\pi^-$.

Parameter	$D^-\pi^+$
ΔE shift (MeV)	-2.62 ± 0.13
ΔE scale factor	0.968 ± 0.006
m_{ES} shift (MeV)	-0.133 ± 0.016
m_{ES} scale factor	0.970 ± 0.005
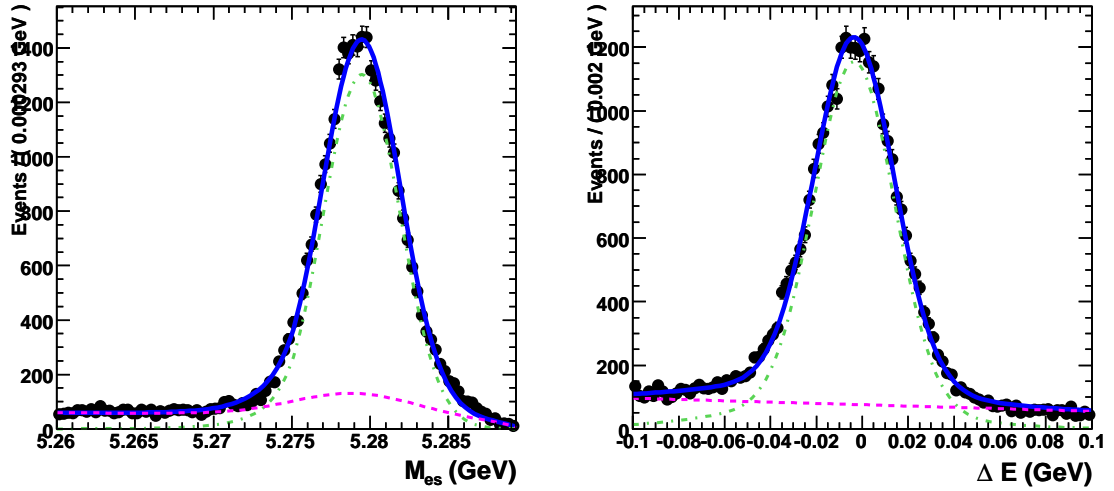
Figure E.3: Projection plots for $D^-\pi^+$ on Run 1-6 on-peak data: m_{ES} left, ΔE right. Points with error bars represent data and the solid blue curves represent the full fit function. The individual fit components are continuum background (pink dashed) and $D^-\ \pi^+$ signal (green dash-dot). The plots are made with no cut on the signal likelihood, and contain all events in the sample.

E.1.1 Fisher in $B^0 \to D^-\pi^+$

We study the data–MC agreement for the Fisher signal PDF. We fix the ΔE and m_{ES} shifts and scale factors to those given in Tab. E.2. We then allow the Fisher signal PDF parameters to float along with the signal and background yields. The results of this fit are compared with the values obtained from MC in Tab. E.3.

Given that the data and MC values are consistent, we do not shift the signal PDF parame-

Figure E.4: sPlots of the $D^-\pi^+$ fit results to Run 1-6 on-peak data. Signal is on the left, background on the right. From top to bottom: m_{ES}, ΔE, $\mathcal{F}$, D mass. The dip in the continuum ΔE sPlot is visible in sPlots of each individual run, as well as the combined Run 1-6 sample.

Table E.3: Fisher signal parameters for Data and MC from the $D^-\pi^+$ ML fit, as well as the Data-MC difference.

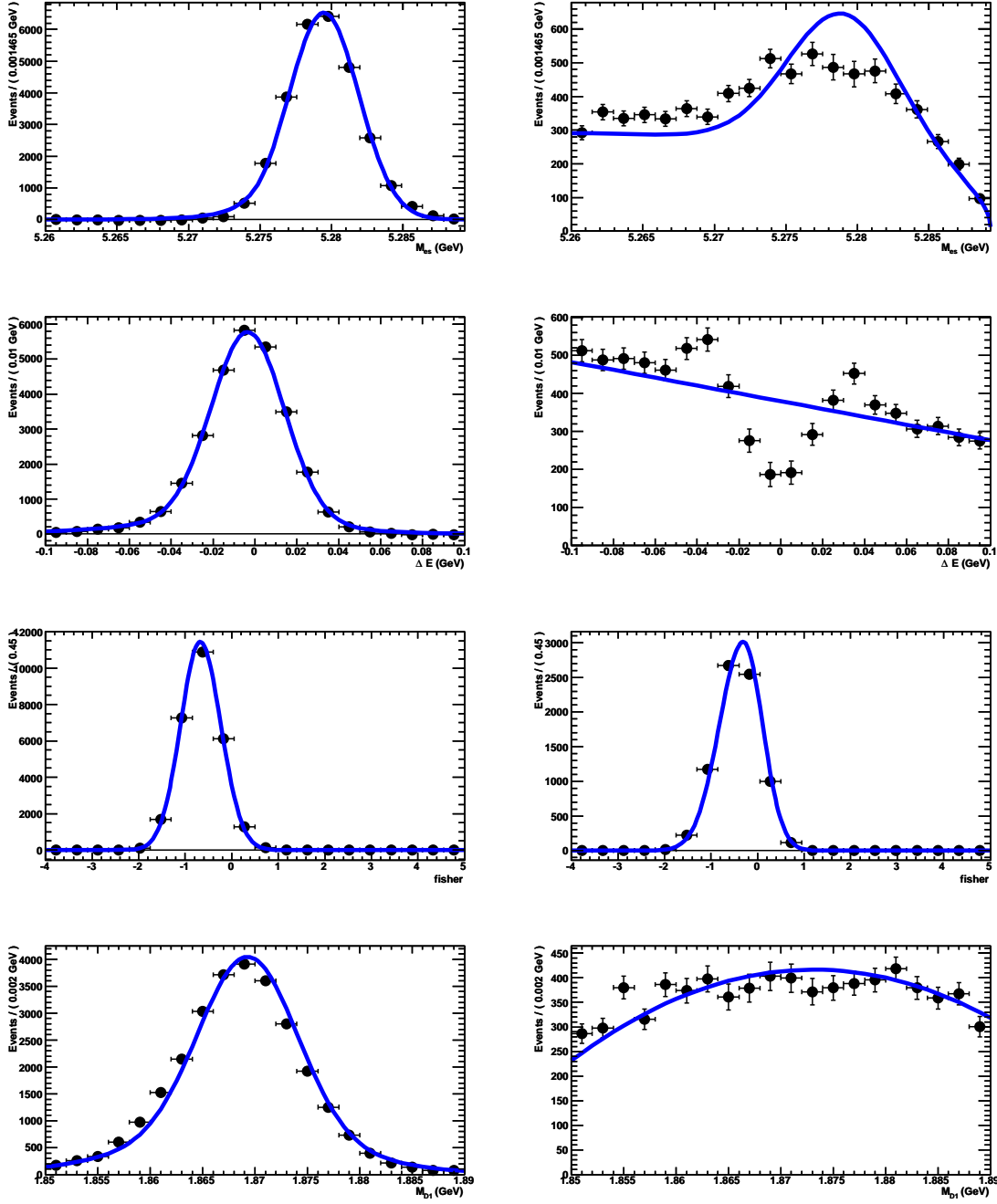| Parameter	Data	MC	Difference
Mean	-0.658 ± 0.003	-0.6594 ± 0.0012	0.001 ± 0.003
RMS	0.429 ± 0.002	0.4314 ± 0.0008	-0.002 ± 0.002
Asym.	0.036 ± 0.010	0.028 ± 0.004	0.008 ± 0.010

ters for $\rho^0 K^{*0}$, but do use these results to determine the systematic error associated with fixing the Fisher signal parameters in the $\rho^0 K^{*0}$ fits. In determining the "ML fit yield" systematic for $\rho^0 K^{*0}$ (see Sec. 9), we allow the PDF parameters to vary as

$$\mathcal{F} \text{ mean shift} = 0 \pm 0.003$$

$$\mathcal{F} \text{ RMS shift} = 0 \pm 0.002$$

$$\mathcal{F} \text{ asym shift} = 0 \pm 0.010 . \tag{E.1}$$

E.2 $B^0 \to \overline{D}^0 \pi^0$ with $\overline{D}^0 \to K^+ \pi^- \pi^0$ Control Sample

To study the agreement between data and MC for $B^0 \to \rho^- K^{*+}$, we perform a ML fit analysis of $B^0 \to \overline{D}^0 \pi^0$ with $\overline{D}^0 \to K^+ \pi^- \pi^0$. The branching fractions are [2]:

$$\mathcal{B}(B^0 \to \overline{D}^0 \pi^0) = (2.61 \pm 0.24) \times 10^{-4}$$

$$\mathcal{B}(\overline{D}^0 \to K^+ \pi^- \pi^0) = (13.9 \pm 0.5) \times 10^{-2} .$$

The ML fit includes three components: signal, $B^+ \to \overline{D}^0 \rho^+$, and continuum background. The signal comes from 1707000 generated signal MC events (mode # 2191). The selection efficiency is: $(10.11 \pm 0.02)\%$. Given the on-peak data sample of $N_{B\overline{B}} = (471.0 \pm 2.8) \times 10^6$, we expect 1727 ± 171 $\overline{D}^0 \pi^0$ events.

A study of $B\overline{B}$ generic MC showed the dominant B background to be $B^+ \to \overline{D}^0\rho^+$ with $\overline{D}^0 \to K^+\pi^-\pi^0$. We reconstruct exclusive MC (mode # 2441) and find an efficiency of $(0.294 \pm 0.003)\%$. Given the branching fraction of $\mathcal{B}(B^+ \to \overline{D}^0\rho^+) = (134 \pm 18) \times 10^{-4}$, we expect 2577 ± 354 events in the on-peak run 1-6 sample. We allow this yield to float in the fit.

The PDFs are shown in Fig. E.5-E.7. The PDF variables are m_{ES}, ΔE, $\mathcal{F}$, and D mass. They are fit with the functions listed in Tab. E.4.

Table E.4: PDF shapes used to fit the $\overline{D}^0\pi^0$ sample.

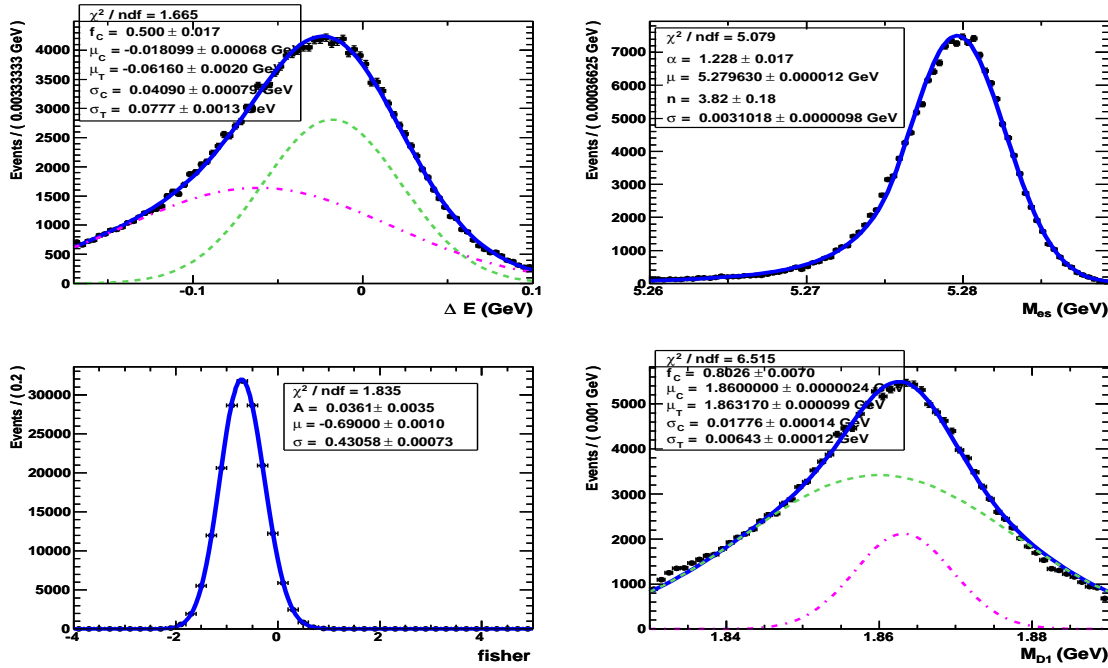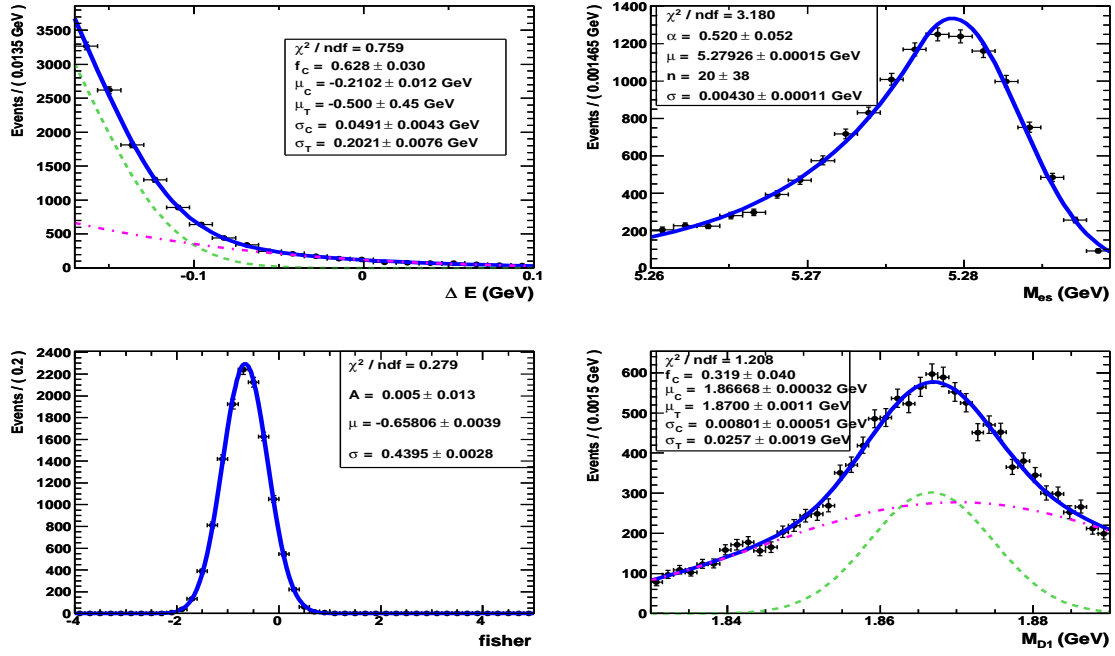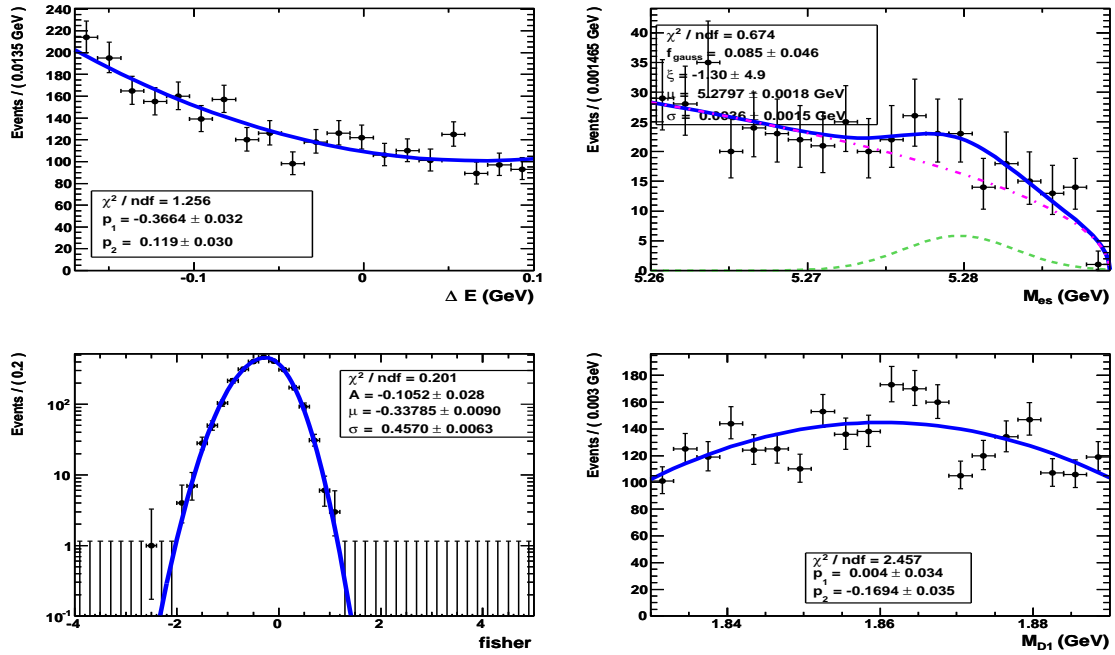| Variable	Signal PDF	$\overline{D}^0\rho^+$ PDF	Bkg PDF
m_{ES}	Crystal Ball	Crystal Ball	ARGUS + Gaus.
ΔE	Double Gaus.	Double Gaus.	2nd order poly
$\mathcal{F}$	Asym. Gaus.	Asym. Gaus.	Asym. Gaus.
D mass	Double Gaus.	Double Gaus.	2nd order poly

Figure E.5: $\overline{D}^0\pi^0$ signal PDFs.

Figure E.6: $B^+ \rightarrow \overline{D}^0 \rho^+$ background PDFs.

Figure E.7: $\overline{D}^0 \pi^0$ continuum PDFs based on on-peak sideband data from runs 1-6.

In order to evaluate the agreement between data and MC simulation, we allow the "shift" and "scale" signal PDF parameters to float in the fit to data. For the double Gaussian describing ΔE, this applies the same shift to the means of both the core and tail Gaussians; the scale factor multiplies only the core width. For the Crystal Ball describing m_{ES}, the shift moves the mean and the scale multiplies the width.

Due to the moderate statistics of this sample, we can reliably float these signal scale and shift parameters only on the full dataset, not on individual runs. In the fit to run 1-6 data, we also float four continuum background parameters: the m_{ES} Gaussian fraction, the ARGUS exponent, and the first and second degree polynomials describing ΔE. The signal and $D^0\rho^-$ yields are consistent with expectation. The results of this study are tabulated in Tab. E.5. We show projection plots for runs 1-6 in Fig. E.8; sPlots are shown in Fig. E.9.

Table E.5: Fit yields for signal and background, as well as shifts and scale factors obtained from floating signal PDF parameters in the control sample $B^0 \to \overline{D}^0\pi^0$ with $\overline{D}^0 \to K^+\pi^-\pi^0$.

Parameter	Fit Result
$D^0\pi^0$ yield	1601 ± 87
$D^0\rho^-$ yield	2973 ± 98
Continuum yield	6574 ± 125
ΔE shift (MeV)	14 ± 3
ΔE scale factor	0.89 ± 0.06
m_{ES} shift (MeV)	-0.38 ± 0.13
m_{ES} scale factor	0.84 ± 0.04

E.2.1 Fisher in $B^0 \to \overline{D}^0\pi^0$

We study the data–MC agreement for the Fisher signal PDF. We fix the ΔE and m_{ES} shifts and scale factors to those given in Tab. E.5 and fix the background ΔE and m_{ES} parameters to those determined in the above fit. We then allow the Fisher signal PDF parameters to float along
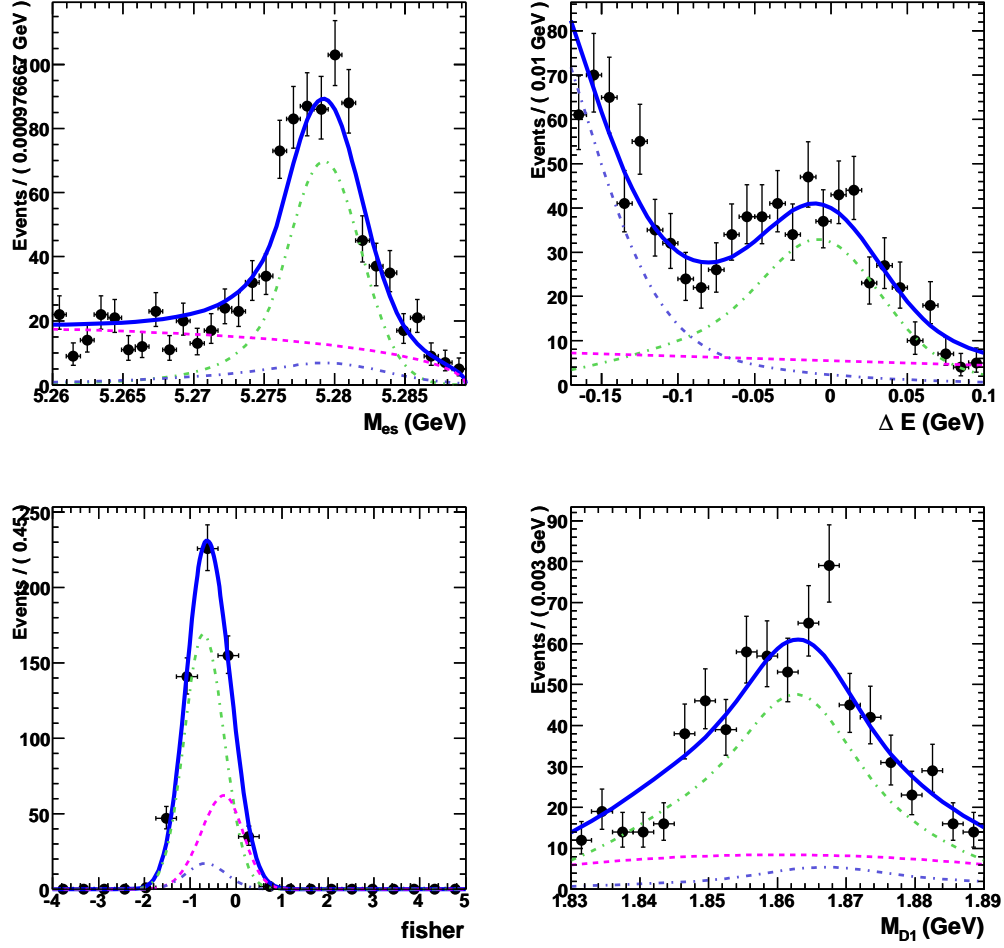
Figure E.8: Projection plots for $\overline{D}^0\pi^0$ on Run 1-6 on-peak data. From top to bottom, left to right: m_{ES}, ΔE, $\mathcal{F}$, D mass. Points with error bars represent data and the solid blue curves represent the full fit function. The individual fit components are continuum background (pink dashed), $\overline{D}^0\pi^0$ signal (green dash-dot), and $D^0\rho^-$ (blue dash-dot). The plots are made with cuts on the signal likelihood to enhance the visibility of signal.

with the signal and background yields. The results of this fit are compared with the values obtained from MC in Tab. E.6.

Given that the data and MC values are consistent, we do not shift the signal PDF parameters for ρ^-K^{*+}, but do use these results to determine the systematic error associated with fixing the Fisher signal parameters in the ρ^-K^{*+} fit. In determining the "ML fit yield" systematic for ρ^-K^{*+}
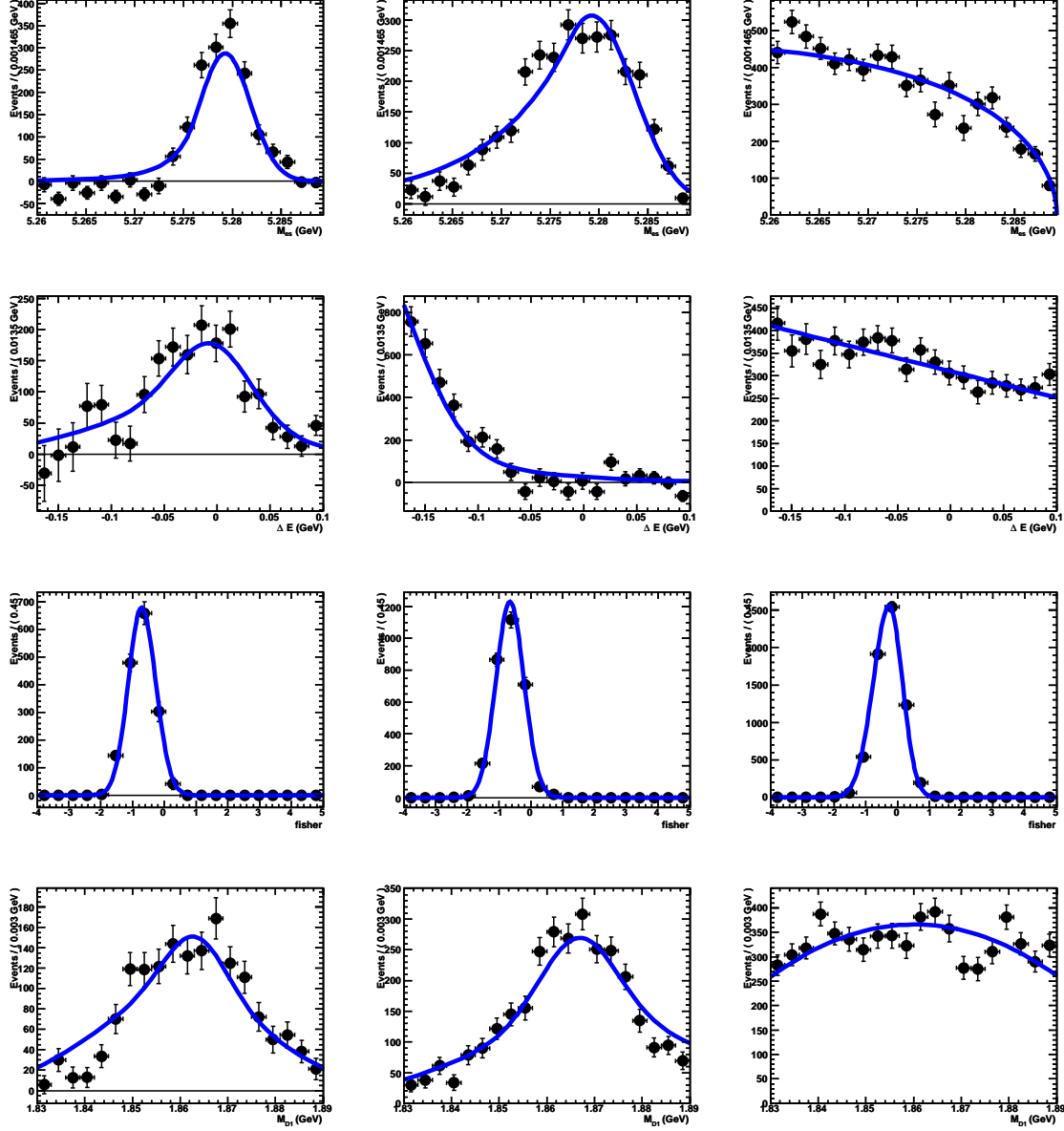
Figure E.9: sPlots for the $\overline{D}^0\pi^0$ fit results to Run 1-6 on-peak data for signal (left), $D^0\rho^-$ (center), and continuum background (right). From top to bottom: m_{ES}, ΔE, $\mathcal{F}$, D mass.

Table E.6: Fisher signal parameters for Data and MC from the $D^0\pi^0$ ML fit, as well as the Data-MC difference.

Parameter	Data	MC	Difference
Mean	-0.690 ± 0.019	-0.690 ± 0.001	0.000 ± 0.019
RMS	0.417 ± 0.014	0.4306 ± 0.0007	-0.014 ± 0.014
Asym.	0.056 ± 0.068	0.036 ± 0.004	0.020 ± 0.068

(see Ch. 9), we allow the PDF parameters to vary as

$$\mathcal{F} \text{ mean shift} = 0 \pm 0.02$$

$$\mathcal{F} \text{ RMS shift} = 0 \pm 0.015$$

$$\mathcal{F} \text{ asym shift} = 0 \pm 0.07 \ . \tag{E.2}$$

Appendix F

Tag 08 Fisher Discriminant

For event-shape discrimination, this analysis uses a Fisher discriminant based on four variables sensitive to the production dynamics and event shape: the polar angles (with respect to the beam axis in the e^+e^- CM frame) of the B candidate momentum and of the B thrust axis; and the zeroth and second angular moments $L_{0,2}$ of the energy flow, excluding the B candidate. The moments are defined by

$$L_j = \sum_i p_i \times |\cos \theta_i|^j \ , \tag{F.1}$$

where i labels a track or neutral cluster, θ_i is its angle with respect to the B thrust axis, and p_i is its momentum. We call this discriminant $\mathcal{F}_{LGD}$, and it is correlated with tagging category. We find that $\mathcal{F}_{LGD}$ is mildly correlated with tagging category [56], which identifies the flavor of the other B in the event, and places it into one of six categories based upon how it is identified. Previous analyses found somewhat improved separation between signal and continuum background when this correlation was removed [57, 58].

To reduce this correlation, we first fit $\mathcal{F}_{LGD}$ to a bifurcated Gaussian in each tagging category; see Tab. F.1 and Fig. F.1. As the data sample is dominated by continuum background, we use a sample of on-resonance data passing the $\rho^0 K^{*0}$ preselection cuts with $m_{ES} < 5.27\text{GeV}$.

Table F.1: Fit parameters from a fit with a Gaussian with different widths above and below the mean to the Legendre Fisher for each Tag 08 Category. The fits are performed on on-resonance data with $m_{ES} < 5.27$GeV and are shown in Fig. F.1. "Shift" is the value by which $\mathcal{F}_{LGD}$ was shifted to remove the correlation between $\mathcal{F}_{LGD}$ mean and tagging category.

Tag Name	Tag Cat	RarBifurGaus Params Mean	Sigma	Asym	Shift
Leptons	63	–0.608	0.458	+0.184	+0.352
Kaon I	64	–0.226	0.487	–0.235	–0.030
Kaon II	65	–0.248	0.453	–0.061	–0.009
Kaon-Pion	66	–0.264	0.446	–0.028	+0.008
Pion	67	–0.249	0.435	–0.072	–0.007
Other	68	–0.252	0.436	–0.015	–0.005
No Tag	69	–0.259	0.414	–0.024	+0.002

The resultant means are plotted as a function of Tag 08 category in Fig. F.2 and fit with a 0th order polynomial.

For this sample, fitting a linear polynomial gave a slope consistent with zero, so the best-fit line is given by the constant shift:

$$\mathcal{F}_{LGD} = -0.256 \pm 0.002 \tag{F.2}$$

We shift the value of $\mathcal{F}_{LGD}$ for each event such that the mean in each tagging category is -0.256. These shifts are listed in the last column of Tab. F.1.

F.1 Effect of including tagging categories in $\mathcal{F}$ on charge asymmetry

One might be concerned that shifting the $\mathcal{F}$ mean for each tagging category could bias the measurement of charge asymmetries. To test this, we perform the $\rho^0 K^*(892)^0$ analysis with both the Tag08 fisher described above and the standard Legendre fisher. The results are tabulated in Tab. F.2. Within uncertainties, the charge asymmetries are consistent between parameterizations. We therefore do not apply a systematic uncertainty to our $\mathcal{A}_{ch}$ measurements due to shifting $\mathcal{F}$
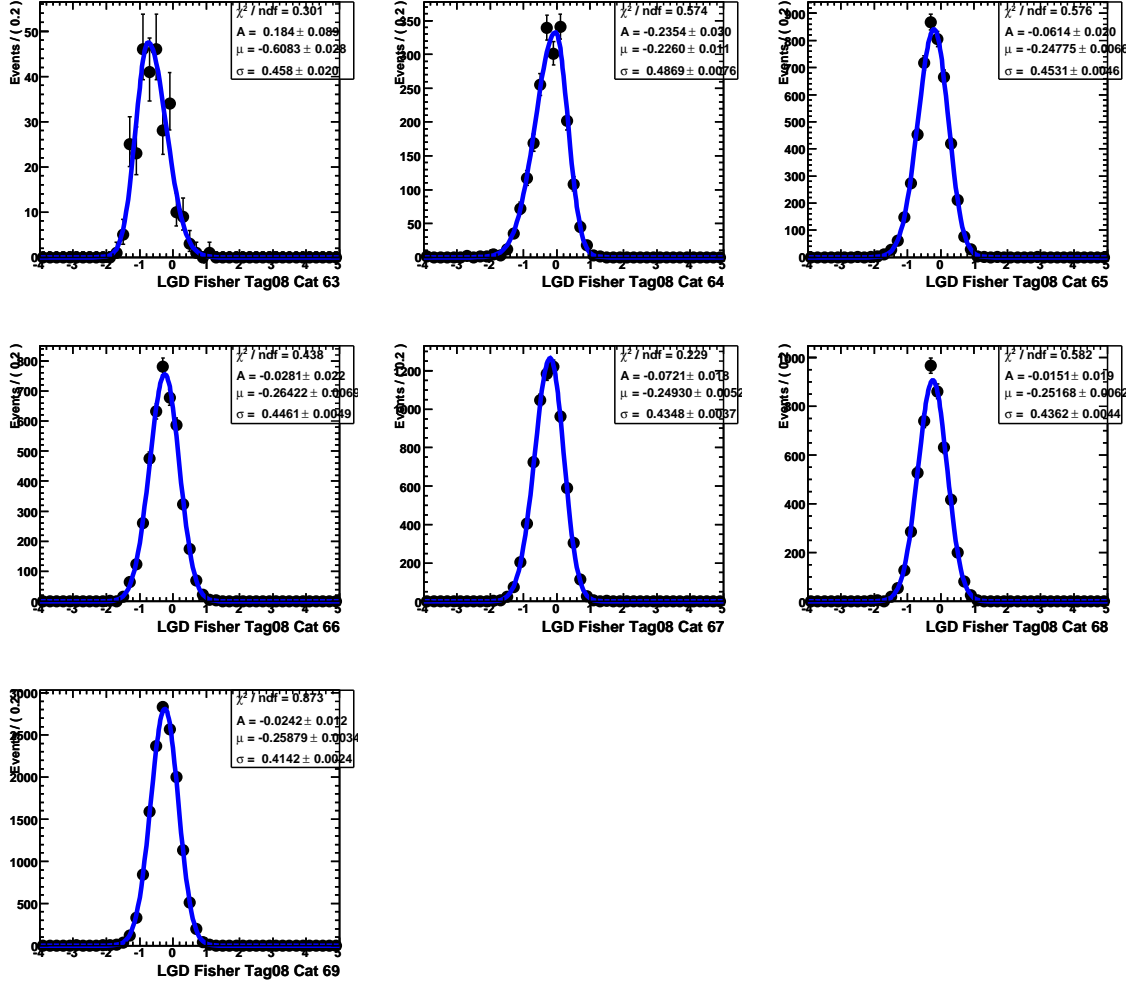
Figure F.1: Results of a bifurcated Gaussian fit to $\mathcal{F}_{LGD}$ on on-resonance data passing the $\rho^0 K^{*0}$ preselection cuts with $m_{ES} < 5.27\,\text{GeV}$. The plots go from left to right, top to bottom in order of Tagging category (63-69).

means by Tag08 tagging categories.
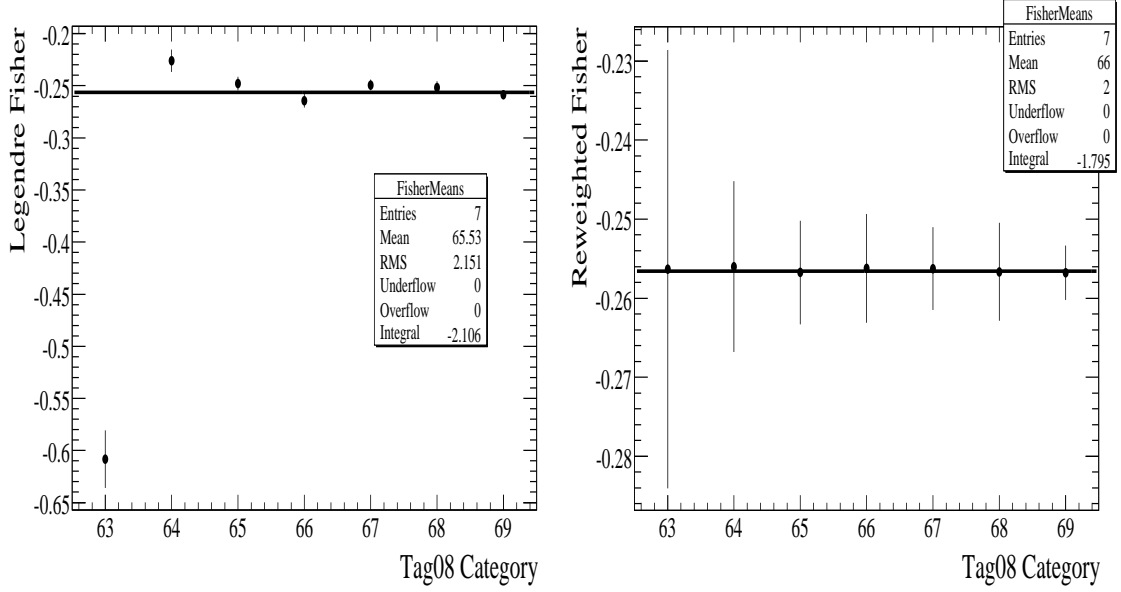
Figure F.2: Means of $\mathcal{F}_{LGD}$ fits to bifurcated Gaussians for each tagging category before shifting the means (left). On Right: means of the $\mathcal{F}$ reweighted by tagging category. The best fit 0th order polynomial (left), used for reweighting, is given by: $\mathcal{F}_{LGD} = -0.256 \pm 0.002$

Table F.2: Fitted value of charge asymmetries $\mathcal{A}_{ch}$ for the $\rho^0 K^*(892)^0$ analysis using the Legendre or Tag08 fisher discriminant. The difference between the Legendre and Tag08 $\mathcal{F}$ results is given in "diff."

	Legendre $\mathcal{F}$	Tag08 $\mathcal{F}$	diff
$\mathcal{A}_{ch}$ ($\rho^0 K^{*0}$)	-0.030 ± 0.129	-0.044 ± 0.130	$+0.014$
$\mathcal{A}_{ch}$ ($f_0 K^{*0}$)	0.069 ± 0.126	0.079 ± 0.126	-0.010
$\mathcal{A}_{ch}$ (Bkg)	-0.032 ± 0.011	-0.031 ± 0.011	-0.001

Appendix G

Comparison to *B*A*B*AR Run 1-4 Results

In this chapter, we compare our results, restricted to the run 1-4 dataset (about half the full run 1-6 dataset), to the previous *BABAR* measurements published in Ref. [28]. The $B^0 \to \rho^0 K^{*0}$ and $f_0 K^*(892)^0$ results are compared to BAD 1211 [30]. The $B^0 \to \rho^- K^{*+}$ results are compared to BAD 1430 [29].

G.1   A note on sPlots and projection plots

We use both sPlots [47] and projection plots to demonstrate visual agreement between the fit functions and the data here, in Ch. 8, and in the appendices. Projection plots include a cut on the signal likelihood to enhance the visibility of signal events. To create sPlots, a separate fit is performed in which the variable of interest (say, m_{ES}) is removed from the ML fit, and the signal yield and any floating background yields are calculated based on the remaining PDFs.

Depending upon the strength of the discriminating variable being plotted in the sPlot, the uncertainties on the fitted yields will increase. Additionally, the yields themselves often change somewhat, especially in the case where one removes a mass variable from the fit, say $m(\pi^+\pi^-)$, but then displays the separate ρ^0 and f_0 hypotheses (in this case, only the helicity distributions can

discriminate between these hypotheses). For instance, the nominal fit yield for $B^0 \to f_0 K^*(892)^0$ on run 1-4 is 136 ± 17 events, but in the sPlot shown in Fig. G.1 (center, 5th row down), the fitter finds 164 ± 35 events, and this yield is reflected in the height of the fit (blue) curve. This occasionally results (as in the case of the $f_0 K^*(892)^0$ $m(\pi^+\pi^-)$ sPlot) in apparent discrepancies between the fit function (as determined by all other variables) and the data onto which it is overlaid.

We have checked that all sPlot yields are sensible, given their uncertainties.

G.2 Comparison of $\rho^0 K^*(892)^0$ and $f_0 K^*(892)^0$ run 1-4 results

Tab. G.1 compares the run 1-4 fit results, MC efficiencies, and SXF rates from BAD 1211 and this analysis. The analysis in BAD 1211 uses SP5 and SP6 MC; this analysis uses SP10. We compare the main differences in preselection cuts in Tab. G.2. Note: the results presented in this section are from studies conducted with the $q\overline{q}$ background $\mathcal{A}_{ch}$ fixed; we now allow it to float. The signal yields are not affected.

In our analysis, we float the $\rho^0 K^*(892)^0$, $f_0 K^*(892)^0$, and $q\overline{q}$ background yields and charge asymmetries, as well as f_L for $\rho^0 K^*(892)^0$. We also float 17 $q\overline{q}$ background PDF parameters. We fix the yields of the $B\overline{B}$ backgrounds to: 99 $\rho^0(K\pi)_0^{*0}$, 12 $f_0(K\pi)_0^{*0}$, 7 $a_1^- K^+$, 25 $f_2(1270)K^{*0}$, 106 $D^-\pi^+$, 219 D^0 cocktail, and 38 charmless cocktail events. The run 1-4 data sample contains 9538 events. Fit biases are determined from an embedded toy study, and are detailed in Tab G.3. In Fig. G.1 we present sPlots of our fit to run 1-4 data.

The agreement between the $\rho^0 K^*(892)^0$ branching fractions is excellent. If one considers only the statistical uncertainties on the $f_0 K^*(892)^0$ branching fractions, assuming the two samples to be independent (a poor assumption), then the two analyses are 2.4σ apart. We discuss this further in Sec. G.2.1. In Sec. G.2.2, we compare our run 1-4 $f_0 K^*(892)^0$ results to the measurement of S-wave events by the ϕK^* analysis presented in [59, 60]. Assuming that these events are all

Table G.1: Comparison of run 1-4 on-resonance data results for this analysis and the one reported in BAD 1211 [30]. The branching fraction results for this analysis include the fit bias (see Tab. G.3). Branching fractions are given in units of 10^{-6}. For this analysis, only statistical uncertainties are tabulated; final $\mathcal{B}$ and f_L results from Ref. [30] include systematic uncertainties.

| Parameter	BAD 1211	This Analysis
A_{CP} $(\rho^0 K^*(892)^0)$	0.09 ± 0.19	-0.07 ± 0.12
f_L $(\rho^0 K^*(892)^0)$ raw	0.57 ± 0.09	0.45 ± 0.09
fit bias f_L	-0.019 ± 0.008	-0.032 ± 0.010
$N_{\rho^0 K^*(892)^0}$ raw	185 ± 30	201 ± 27
fit bias $N_{\rho^0 K^*(892)^0}$	2.4 ± 3.0	21 ± 2
ϵ Ln (%)	19.8 ± 0.08	14.34 ± 0.05
ϵ Tr (%)	27.09 ± 0.10	25.07 ± 0.06
SXF Ln (%)	19.2 ± 0.21	7.30
SXF Tr (%)	5.5 ± 0.05	1.86
$\prod \mathcal{B}_i$ (%)	0.667	0.667
$\mathcal{B}(B^0 \to \rho^0 K^{*0})$	$5.6 \pm 0.9 \pm 1.3$	5.8 ± 0.9
f_L $(\rho^0 K^*(892)^0)$	$0.57 \pm 0.09 \pm 0.08$	0.48 ± 0.09
A_{CP} $(\rho^0 K^*(892)^0)$	-0.17 ± 0.28	0.08 ± 0.12
$N_{f_0 K^*(892)^0}$	83 ± 19	137 ± 17
fit bias $f_0 K^*(892)^0$	6.8 ± 2.1	1.5 ± 1.4
ϵ (%)	21.7 ± 0.17	18.30 ± 0.06
SXF (%)	11.2 ± 0.3	4.13
$\prod \mathcal{B}_i$ (%)	0.667	0.667
$\mathcal{B}(B^0 \to f_0 K^{*0})$	$2.6 \pm 0.6 \pm 0.9$	4.6 ± 0.6
$N_{q\bar{q}}$	40880 ± 220	8635 ± 98
$\mathcal{A}_{ch}$ $(q\bar{q})$	-0.02 ± 0.01	-0.031 ± 0.011
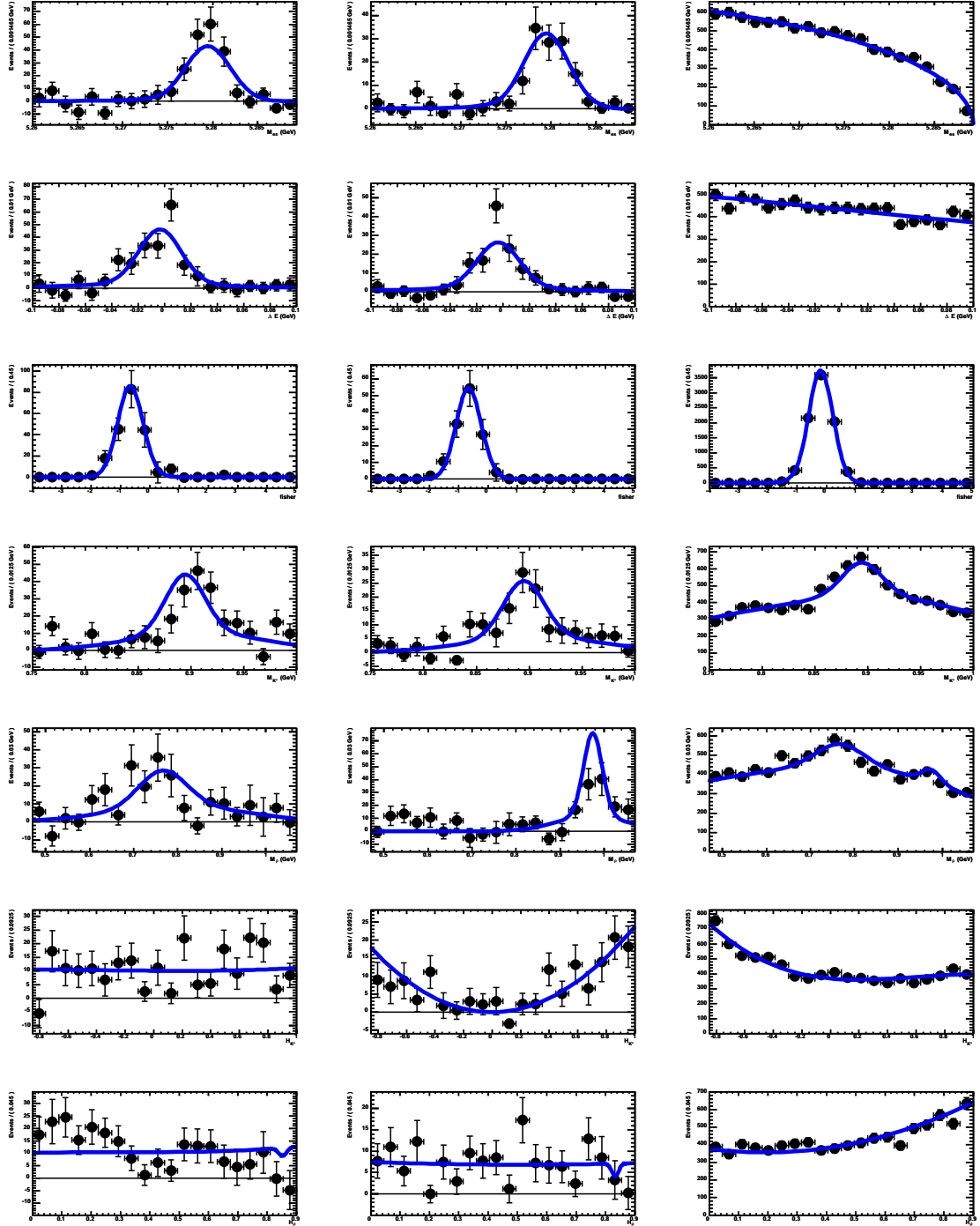
Figure G.1: sPlots of (left to right) $\rho^0 K^*(892)^0$, $f_0 K^*(892)^0$, and continuum background. Plots are, top to bottom: m_{ES}, ΔE, $\mathcal{F}$, $m(K^+\pi^-)$, $m(\pi^+\pi^-)$, $\mathcal{H}(K^+\pi^-)$, and $\mathcal{H}(\pi^+\pi^-)$. Points show run 1-4 data, blue curves are the fit result computed without the variable plotted.

Table G.2: Comparison of salient cuts between this $\rho^0 K^*(892)^0$ and $f_0 K^*(892)^0$ analysis and the one reported in BAD 1211. Masses are given in GeV.

Parameter	BAD 1211	This Analysis
m_{ES}	$(5.22, 5.29)$	$(5.26, 5.2893)$
ΔE	$(-0.15, 0.15)$	$(-0.1, 0.1)$
$|\cos\theta_T|$	< 0.8	< 0.7
$\cos\theta_{K\pi}$	$(-0.95, 1.0)$	$(-0.85, 1.0)$
$\cos\theta_{\pi\pi}$	$(-0.95, 0.95)$	$(-0.9, 0.9)$
$m(K^+\pi^-)$	$(0.767, 1.017)$	$(0.75, 1.0)$
$m(\pi^+\pi^-)$	$(0.520, 1.146)$	$(0.47, 1.07)$

Table G.3: Results of an embedded toy study for $\rho^0 K^*(892)^0$ based on the run 1-4 dataset (9538 events, total). We also embed: 99 $\rho^0(K\pi)_0^{*0}$, 12 $f_0(K\pi)_0^{*0}$, 7 $a_1^- K^+$, 25 $f_2(1270)K^{*0}$, 38 charmless cocktail, 106 $D^-\pi^+$, and 219 D^0 cocktail events. We report the number of events embedded from MC ("Input"), the fit result, the bias on that yield, and the mean statistical error on the yield. 100/100 fits converge.

Mode	Input	Fit	Bias	Stat. err.
$\rho^0 K^*(892)^0$	185	206 ± 2	21 ± 2	27
$f_L\,(\rho^0 K^*(892)^0)$	0.48	0.446 ± 0.010	-0.034 ± 0.010	0.092
$\mathcal{A}_{ch}\,(\rho^0 K^*(892)^0)$	-0.039	-0.034 ± 0.012	0.005 ± 0.012	0.063
$f_0 K^*(892)^0$	134	135.5 ± 1.4	1.5 ± 1.4	18
$\mathcal{A}_{ch}\,(f_0 K^*(892)^0)$	-0.039	-0.022 ± 0.014	0.017 ± 0.014	0.064

$f_0 \to K^+ K^-$, we can compare $f_0 K^*(892)^0$ branching fractions.

G.2.1 Discussion of $f_0 K^*(892)^0$ comparison

As shown in Tab. G.1, the agreement between the $f_0 K^*(892)^0$ yields/BFs for the nominal

analysis and that reported in BAD 1211 is, on the surface, questionable. We find 136 ± 17 events[1];

BAD 1211 reports 83 ± 19. By looking at sPlots, we can see that most of the difference is a result

---

[1]The results discussed in this section use the old $\rho^0(K\pi)_0^{*0}$ PDF for $\mathcal{H}_\rho$.

of the different signal and $B\overline{B}$ background models used in the two analyses. In Fig. G.2 (top) we

show the sPlots from Fig. 34, p. 59 of version 10 of BAD 1211 [30]. These are "Standard fit sPlots

for the $K^{*0}\rho^0$ analysis weighted by ΔE, m_{ES} and the neural network s-weights for the signal."

The bottom plots in Fig. G.2 are from p. 57, Fig. 33 of BAD 1211, and show the equivalent plots

for the "wide" fit. We can reasonably compare the BAD 1211 $m(\pi^+\pi^-)$ plots in Fig. G.2 with the

$m(\pi^+\pi^-)$ distribution for inclusive $K^*(892)^0$ signal from App. D, shown here in Fig. G.3.
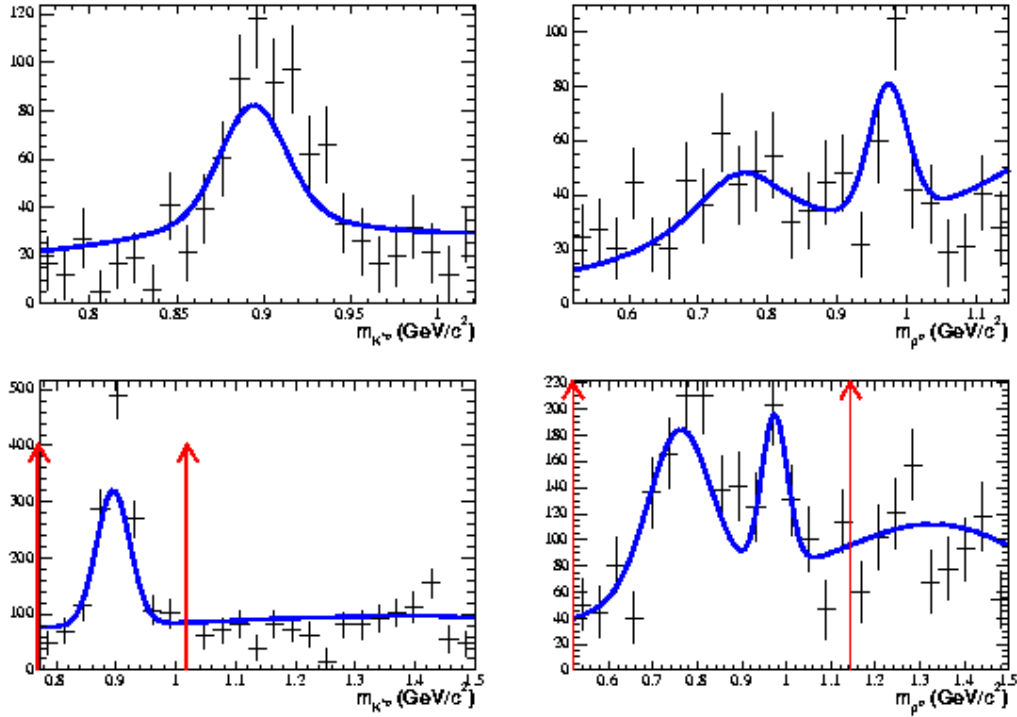
Figure G.2: Signal sPlots from BAD 1211 [30] of the K^{*0} mass (left) and $\pi^+\pi^-$ mass (right), weighted by ΔE, m_{ES}, and the neural network. Top plots are from the strict fit, which finds $N_{f_0 K^*(892)^0} = 83 \pm 19$ events; bottom plots are from the wide fit with $N_{f_0 K^*(892)^0} = 107 \pm 25$ events.

The comparison between these plots is not exact; Fig. G.2 was generated using only

ΔE, m_{ES}, and the neural network as discriminating variables, whereas Fig. G.3 includes also the

$K^*(892)^0$ mass. Thus one expects somewhat more $B\overline{B}$ background in the $\pi^+\pi^-$ mass distribu-

tions from BAD 1211. Still, by eye, the fit function in Fig. G.2 (top) underestimates the amount

Figure G.3: Results of the fit to the $\pi^+\pi^-$ mass spectrum for the sWeighted $K^*(892)^0$ signal (points with error bars) in the $K^+\pi^-$ mass region $(0.75,\ 1.0)\,\text{GeV}$. The solid blue curve shows the total fit result, the green curve is $\rh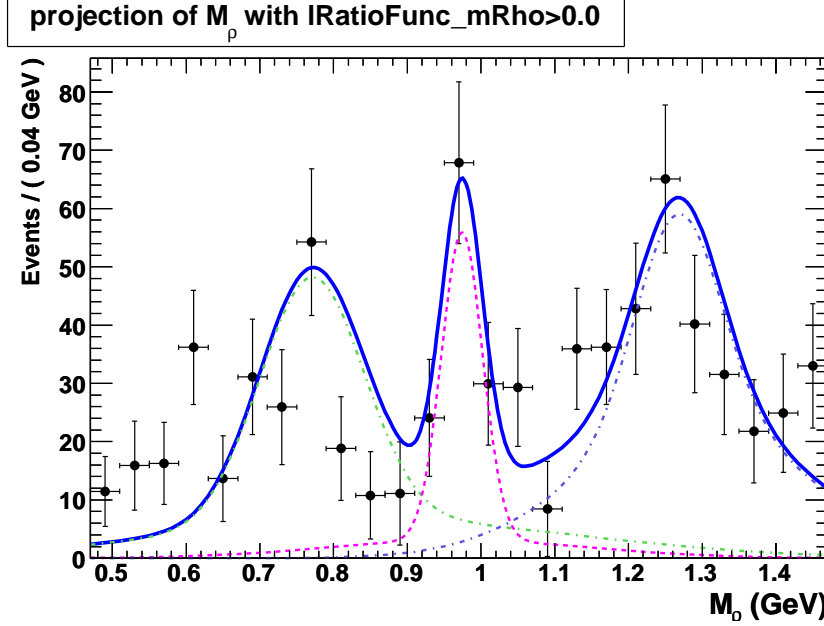o^0$, pink is f_0, and the dashed blue is $f_2(1270)$. This fit finds 126 ± 16 $f_0K^*(892)^0$ events, corresponding to a BF of $(4.0 \pm 0.5) \times 10^{-6}$. See App. D for details.

of f_0 present in the data, as it undershoots the high bin. In Fig. G.2, the non-resonant/$f_0(1370)$ background also represents a considerably larger number of events beneath the f_0 peak than the $f_2(1270)$ does in Fig. G.3.

Additionally, we note that the "wide fit" from BAD 1211 (Fig. G.2 (bottom)) found $N_{f_0K^*(892)^0} = 107 \pm 25$ events, 24 events more than were seen in the "strict" fit though the efficiency (not documented) is presumably similar between the two fits. The PDF in the wide fit sPlot better describes the f_0 peak, so one could argue that the f_0 results from the wide fit may be more reliable than those from the standard fit. The calculated BFs (Tab. 23 and 24 in BAD 1211) are $\mathcal{B}(B^0 \to f_0 K^{*0}) = 2.94 \pm 0.68$ for the wide fit and 2.60 ± 0.60 for the strict, in units of 10^{-6}; this is less of an increase than I would naively expect, given the yield difference.

In another study from BAD 1211, in which the PDF for the $B^0 \to \rho^0 K^+\pi^-$ background is altered to better match the data as observed in sPlots, the $f_0K^*(892)^0$ yield increases to 112 ± 26

Table G.4: Comparison of $B\overline{B}$ background categories from BAD 1211 and this analysis. Background conditions are quite different between the two analyses; the total number of events to fit is: $N(\text{BAD 1211}) = 49500$ vs. $N(\text{this analysis}) = 9538$.

BAD 1211	This Analysis
$B^0 \to D^- \pi^+$	$B^0 \to D^- \pi^+$
$B^0 \to c$ peaking (no $D^- \pi^+$)	—
$B^0 \to c$ non-peaking	—
$B^+ \to c$	—
—	D^0 cocktail with $D^0 \to K^- \pi^+ \pi^0$
$B^0 \to K^+ \pi^- f_0(980)$	S-wave $K^+ \pi^- f_0(980)$ & $(K\pi)_0^{*0} f_0(980)$
$B^0 \to K^{*0} f_0(1370)$	$B^0 \to K^{*0} f_2(1270)$
$B^0 \to K^+ \pi^- f_0(1370)$	—
$B^0 \to K^{*0} \pi^+ \pi^-$	—
$B^0 \to K^{**+} \pi^-$	—
$B^0 \to K^+ \pi^- \rho^0$	S-wave $K^+ \pi^- \rho^0$ & $(K\pi)_0^{*0} \rho^0$
$B^0 \to K^+ \pi^- \pi^+ \pi^-$	—
$B^0 \to$ charmless peaking	—
$B^0 \to$ charmless non-peaking	—
—	$B^0 \to a_1^- K^+$ with $a_1^- \to \rho^0 \pi^-$
—	$B^{0/+} \to$ charmless cocktail

events on the wide fit, corresponding to a BF of 3.08 ± 0.71 (Tab. 25, p. 61).

The $B\overline{B}$ background components included in this analysis and the one presented in BAD 1211 are quite different. The background categories for both fits are listed in Tab. G.4.

In BAD 1211, the analysts used $m(f_0(1370)) = 1.35\,\text{GeV}$ and $\Gamma(f_0(1370)) = 0.2\,\text{GeV}$, compared with the $f_2(1270)$ parameters used here of: $m(f_2(1270)) = 1.275\,\text{GeV}$ and $\Gamma(f_2(1270)) = 0.185\,\text{GeV}$. Given the clear peak in Fig. G.3, the data indicate that we are justified in considering a structure with mass and width corresponding to those of the $f_2(1270)$.

The study of the high $K^+ \pi^-$ mass sideband (App. B) indicates that the amount of $B^0 \to K^+ \pi^- \pi^+ \pi^-$ in the sample, where we assume the $K^+ \pi^-$ state is S-wave, can be fixed to zero. The study in App. D also provides good evidence that we do not need to consider a non-resonant

$B^0 \rightarrow K^{*0}\pi^+\pi^-$ component, as the fit in Fig. G.3 is excellent without a phase-space-distributed non-resonant $\pi^+\pi^-$ mass.

Given these studies of high mass sidebands, as well as the investigation of dominant B backgrounds from the $B\overline{B}$ generic MC (see Sec. 7.2.1), we have high confidence that we are accurately accounting for the $B\overline{B}$ backgrounds in this analysis. Comparing the $\pi^+\pi^-$ mass sPlots in Fig. G.2 to the $\pi^+\pi^-$ mass distribution of $K^*(892)^0$ events in Fig. G.3 suggests that much of the observed discrepancy in the $f_0 K^*(892)^0$ yield may be a result of the different background models employed by the two analyses.

G.2.2   Comparison of $f_0 \rightarrow \pi^+\pi^-$ and $f_0 \rightarrow K^+K^-$ for $B^0 \rightarrow f_0 K^*(892)^0$

We can also compare our measured run 1-4 $f_0 K^*(892)^0$ branching fraction[2] with that obtained by the $B^0 \rightarrow \phi K^{*0}$ analysis [59, 60], as the f_0 decays both to $\pi^+\pi^-$ and K^+K^- final states. When comparing with the ϕK^{*0} analysis, we must make several assumptions. First, the analysis measured only an S-wave K^+K^- state (using $f_0 K^*(892)^0$ MC to generate the PDFs), but did not attempt to distinguish between f_0 and a_0 resonances. For this comparison, we will assume that all the measured S-wave K^+K^- is f_0. The relevant experimental values from BAD 1428 [60] are given in Tab. G.5.

To compute the $B^0 \rightarrow f_0 K^*(892)^0$ branching fraction, one must take into account the $\pi\pi$ and $K\overline{K}$ branching fractions of the f_0. We follow the PDG [2] and define

$$R \equiv \frac{\Gamma(\pi\pi)}{\Gamma(\pi\pi) + \Gamma(K\overline{K})} \; . \tag{G.1}$$

A *BABAR* measurement [61] based on the $K^+K^-K^+$ DP finds $R = 0.52 \pm 0.12$ [2], but most prior measurements of this ratio find $R \sim 0.75$. Additionally, isospin gives us the ratios,

$$\frac{\Gamma(\pi^+\pi^-)}{\Gamma(\pi\pi)} = \frac{2}{3} \quad \text{and} \quad \frac{\Gamma(K^+K^-)}{\Gamma(K\overline{K})} = \frac{1}{2} \; . \tag{G.2}$$

---

[2]The results discussed in this section use the old $\rho^0(K\pi)_0^{*0}$ PDF for $\mathcal{H}_\rho$.

Table G.5: Experimental values related to $B^0 \to f_0 K^*(892)^0$ measurement with $f_0 \to K^+ K^-$ from Ref. [59, 60]. The S-wave $K^+ K^- K^*(892)^0$ yield is assumed to be $f_0 K^*(892)^0$.

Parameter	Value
Generated $f_0 K^*(892)^0$ MC	103000 events
Selected $f_0 K^*(892)^0$ MC	21030 events
MC ϵ	0.2042
$N_{f_0 K^*(892)^0}$	88 ± 18
$N_{B\bar{B}}$	384×10^6

Table G.6: Calculations of the total branching fraction $\mathcal{B}(B^0 \to f_0 K^*(892)^0)$ for two experimental values of the $\pi\pi$ to $K\bar{K}$ f_0 decay branching fraction.

	$\mathcal{B}(B^0 \to f_0 K^*(892)^0)$ (10^{-6})	
Analysis	$R = 0.5$	$R = 0.75$
This analysis	9.4	6.2
ϕK^* analysis	4.5	9.0

Using these, we calculate $\mathcal{B}(B^0 \to f_0 K^{*0})$ for both $R = 0.5$ and 0.75 for our run 1-4 result and the

run 1-5 result reported in BAD 1428 (see Tab. G.6). A value of R of around 0.65 would give good

agreement between our run 1-4 $f_0 K^*(892)^0$ measurement and the scalar $(K\bar{K})_0 K^{*0}$ measurement

from [59, 60], suggesting that our $f_0 K^*(892)^0$ yield compares favorably between $f_0 \to \pi^+ \pi^-$ and

$K^+ K^-$.

G.3   Comparison of $\rho^- K^*(892)^+$ run 1-4 results

We fit run 1-4 on-peak data and compare the results to the previous $\rho^- K^*(892)^+$ analysis

described in BAD 1430 [29]. The results are given in the "Nominal" column of Tab. G.7. We float

the $\rho^- K^*(892)^+$ and $q\bar{q}$ background yields and charge asymmetries, as well as f_L for $\rho^- K^*(892)^+$.

Table G.7: Comparison of run 1-4 on-resonance data results for this analysis of $B^0 \rightarrow \rho^- K^{*+}$ and the one reported in BAD 1430 [29]. Branching fractions are in units of 10^{-6} and are calculated including the fit bias. Only statistical uncertainties are tabulated.

| | | This Analysis | |
Parameter	BAD 1430	Nominal	Comparison
$N_{\rho^- K^*(892)^+}$	60^{+25}_{-22}	120 ± 20	121 ± 23
fit bias $N_{\rho^- K^*(892)^+}$	5.7	13 ± 2	15 ± 2
$f_L \, (\rho^- K^*(892)^+)$	$-0.18^{+0.52}_{-1.74}$	0.27 ± 0.15	0.43 ± 0.14
A_{CP}	0.006 ± 0.332	0.21 ± 0.16	0.07 ± 0.18
ϵ Ln (%)	6.90 ± 0.06	4.94	5.96
ϵ Tr (%)	13.76 ± 0.09	11.18	12.08
SXF Ln (%)	38.4 ± 0.5	21.9	29.5
SXF Tr (%)	23.0 ± 0.3	12.9	13.3
$\prod \mathcal{B}_i$ (%)	0.333	0.333	0.333
$\mathcal{B}(B^0 \rightarrow \rho^- K^{*+})$	$5.5^{+3.9}_{-3.5}$	14.1 ± 3.1	14.2 ± 3.5
$N_{q\bar{q}}$	15649 ± 172	4605 ± 71	19245 ± 141
$\mathcal{A}_{ch} \, (q\bar{q})$	0.005 ± 0.008	-0.063 ± 0.015	—

Table G.8: Results of an embedded toy study for $\rho^- K^*(892)^+$ based on the run 1-4 dataset (4832 events total). We also embed: 21 $\rho^-(K\pi)^{*+}_0$, 65 $D^0\rho^-$, 4 $a_1^- K^+$, and 5 $\rho^+\rho^-$ events. We report the number of events embedded from MC ("Input"), the fit result, the bias on that yield, and the mean statistical error on the yield. 100/100 fits converge.

Mode	Input	Fit	Bias	Stat. err.
$N_{\rho^- K^*(892)^+}$	108	121 ± 2	13 ± 2	21
f_L	0.26	0.273 ± 0.022	0.013 ± 0.022	0.17
$\mathcal{A}_{ch}$	-0.072	0.012 ± 0.018	0.084 ± 0.018	0.083

We also float 13 $q\bar{q}$ background PDF parameters. We fix the yields of the $B\bar{B}$ backgrounds to: 21 $\rho^-(K\pi)^{*+}_0$, 65 $D^0\rho^-$, 4 $a_1^- K^+$, and 5 $\rho^+\rho^-$ events. The run 1-4 data sample contains 4832 events. Fit biases are determined from an embedded toy study, and are detailed in Tab G.8. In Fig. G.4 we show sPlots from the nominal $\rho^- K^*(892)^+$ fit.

The agreement between the measured BF in this analysis and the previous analysis is poor. Many preselection requirements differ between the two analyses; the most important of these cuts
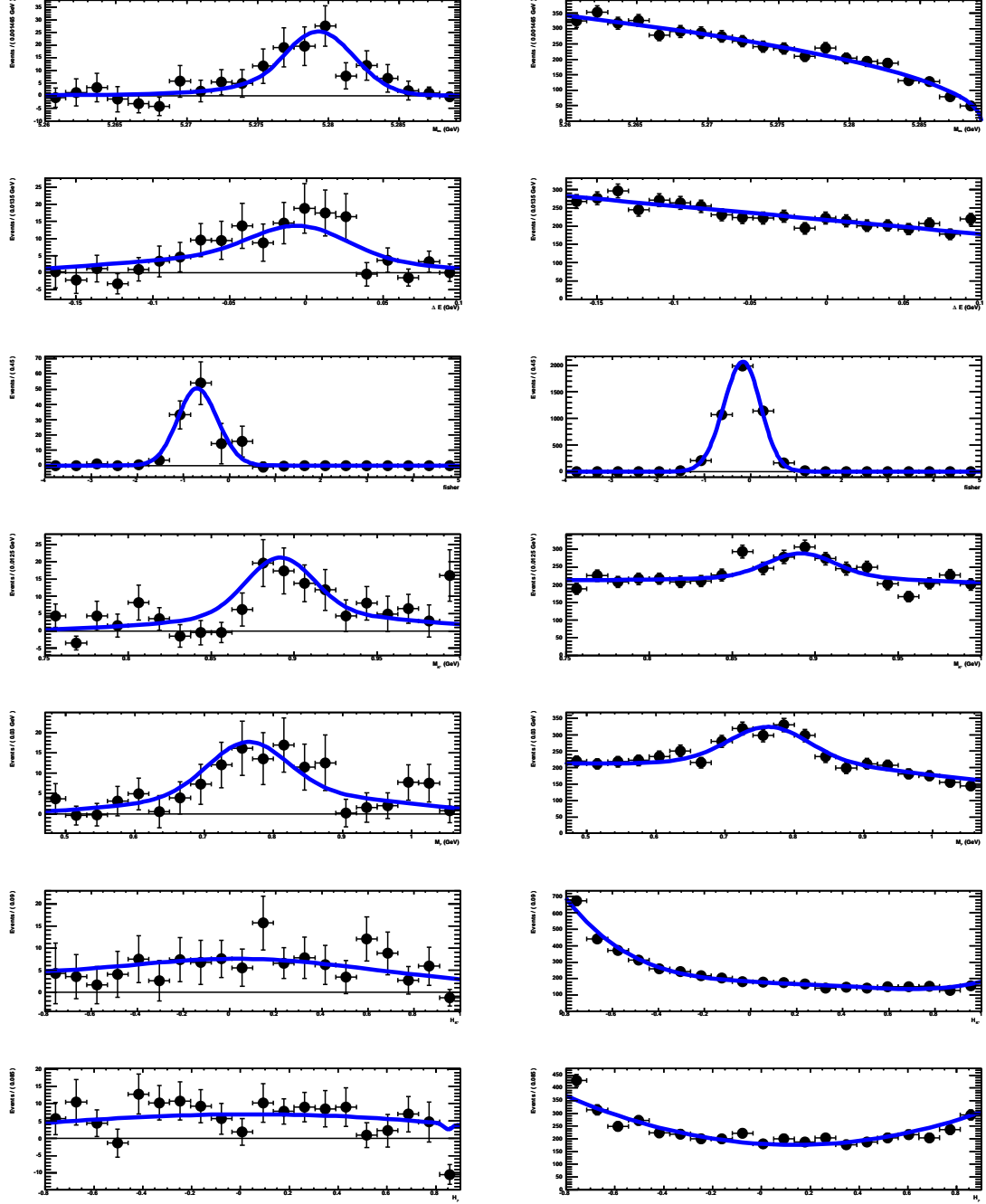
Figure G.4: sPlots of $\rho^- K^*(892)^+$ (left) and continuum background (right). Plots are, top to bottom: m_{ES}, ΔE, $\mathcal{F}$, $m(K^+\pi^0)$, $m(\pi^0\pi^-)$, $\mathcal{H}(K^+\pi^0)$, and $\mathcal{H}(\pi^0\pi^-)$. Points show run 1-4 data, blue curves are the fit result computed without the variable plotted.

Table G.9: Comparison of salient cuts between this $\rho^- K^*(892)^+$ analysis and the one reported in BAD 1430. Masses are given in GeV. The "Comparison" analysis reproduces the BAD 1430 cuts as closely as possible in order to compare results on run 1-4 data.

| | | This Analysis | |
Parameter	BAD 1430	Nominal	Comparison
m_{ES}	$(5.23, 5.29)$	$(5.26, 5.2893)$	$(5.23, 5.29)$
ΔE	$(-0.12, 0.15)$	$(-0.17, 0.1)$	$(-0.12, 0.15)$
$\|\cos\theta_T\|$	< 0.87	< 0.7	< 0.8
$\cos\theta_{K\pi}$	$(-0.8, 0.98)$	$(-0.8, 1.0)$	$(-0.8, 0.98)$
$\cos\theta_{\pi\pi}$	$(-0.8, 0.98)$	$(-0.8, 0.9)$	$(-0.8, 0.98)$
$m(\pi^+\pi^0)$	$(0.396, 1.146)$	$(0.47, 1.07)$	$(0.396, 1.146)$
$m(K^+\pi^0)$	$(0.767, 1.017)$	$(0.75, 1.0)$	$(0.767, 1.017)$
$m(\pi^0)$	$(0.10, 0.16)$	$(0.12, 0.15)$	$(0.10, 0.16)$
π^0 LAT	$(0.01, 0.6)$	—	$(0.01, 0.6)$
π^0 Energy	—	< 0.25	—
K^+ PID	KaonLHT	KaonBDTT	KaonLHT
	!ElectronMicroT		!ElectronMicroT
	!ProtonLHT		!ProtonLHT
π^- PID	!KaonLHT	PionKML	!KaonLHT
	!ElectronMicroT		!ElectronMicroT
	!ProtonLHT		!ProtonLHT

are shown in Tab. G.9. To investigate whether the difference in measured branching fractions is a result of cut differences (rather than an effect of reprocessing or model differences), we attempt to reproduce the cuts from BAD 1430. Tab. G.9 lists the cuts used for this "comparison" study. We are only able to loosen the $\cos\theta_T$ cut to $|\cos\theta_T| < 0.8$ without re-reconstructing all of our samples. After performing the "comparison" preselection, we re-make our standard background samples and all PDFs[3]. We again validate the fits with toy studies, and use an embedded toy study to calculate the fit bias.

The results of this "comparison" fit are given in Tab. G.7, where—despite the rather different background conditions—the agreement with the current analysis remains good. This indicates

---

[3]The results discussed in this section use the old $\rho^0(K\pi)_0^{*0}$ PDF for $\mathcal{H}_\rho$.

Table G.10: $B\overline{B}$ background categories and run 1-4 yields for the BAD 1430 analysis and the "comparison" analysis of $B^0 \rightarrow \rho^- K^{*+}$.

BAD 1430		"Comparison" Analysis	
Bkg type	yield	Bkg type	yield
Charm	2030 ± 126	$D^0\rho^-$	138
Charmless	58.2	$a_1^- K^+$	9
$\rho^- K^+ \pi^0$	87.2	$\rho^+ \rho^-$	8
$K^{*+}\pi^-\pi^0$	37.6	$\rho^-(K\pi)_0^{*+}$	26

that the yield difference observed between the current analysis and that described in BAD 1430 is likely due to reprocessing, model differences, and statistical fluctuations. We discuss some specific differences between BAD 1430 and the comparison analysis below.

Due to the increased background conditions in the "comparison" analysis, one could argue for an additional charmless cocktail $B\overline{B}$ background component. An embedded toy study investigating the bias resulting from not including this component gave a bias 2.7 ± 3.6 events larger (on a study of the full run 1-6 sample with an expected signal BF of 5.4×10^{-6}) than in the case where this charmless cocktail background was not embedded. As this bias increase is not statistically significant, we choose not to include a charmless cocktail background component in the "comparison" fit, thereby keeping the same background categories as in the nominal fit (see Sec. 7.2.2).

We compare the $B\overline{B}$ background models in this "comparison" analysis and BAD 1430, and show them to be quite different. The total $B\overline{B}$ background fit in BAD 1430 is 2213 ± 126 events, whereas in my comparison analysis it is 181 events. The $B\overline{B}$ background categories are tabulated in Tab. G.10; all yields are fixed in the fit except for BAD 1430's charm component.

BAD 1430 does not specify the makeup of the "charm" component of the $B\overline{B}$ background. The "charmless" component is a cocktail of 12 exclusive $B \rightarrow$charmless modes, including $B^0 \rightarrow a_1^- K^+$ (7.6 events) and $\rho^+\rho^-$ (11.9 events). The non-resonant $B\overline{B}$ background yields in BAD 1430 come from allowing the NR yields to float in fits with wider $K^+\pi^0$ or $\pi^+\pi^0$ mass ranges

(for $\rho^- K^+ \pi^0$ and $K^{*+}\pi^-\pi^0$, respectively). The $\rho^- K^+ \pi^0$ fit allows for a $\rho^- K_2^*(1430)^+$ component, but no discussion is made of describing the non-resonant $K^+\pi^0$ with a LASS parameterization, so we conclude that the analysts used a phase space model.

A more thorough comparison between the two analyses would be difficult given that another analyst performed the run 1-4 measurement in 2006.

Bibliography

[1] H.-Y. Cheng and J. G. Smith, Charmless Hadronic B-Meson Decays, Ann. Rev. Nucl. Part. Sci. **59**, 215–243 (2009).

[2] K. Nakamura et al., Review of particle physics, J. Phys. **G37**, 075021 (2010).

[3] E. M. Aitala et al., Study of the $D_s^+ \to \pi^-\pi^+\pi^+$ decay and measurement of f_0 masses and widths, Phys. Rev. Lett. **86**, 765–769 (2001), The mass and width of the $f_0(980)$ are from the Breit-Wigner parameters obtained here.

[4] D. Aston et al., A Study of $K^-\pi^+$ Scattering in the Reaction $K^-p \to K^-\pi^+n$ at 11-GeV/c, Nucl. Phys. **B296**, 493 (1988).

[5] B. Aubert et al., Dalitz-plot analysis of the decays $B^\pm \to K^\pm\pi^\mp\pi^\pm$, Phys. Rev. **D72**, 072003 (2005).

[6] M. Kobayashi and T. Maskawa, CP Violation in the Renormalizable Theory of Weak Interaction, Prog. Theor. Phys. **49**, 652–657 (1973).

[7] N. Cabibbo, Unitary Symmetry and Leptonic Decays, Phys. Rev. Lett. **10**, 531–533 (1963).

[8] D. Atwood and A. Soni, Determining the phases alpha and gamma from direct CP violation in B(u), B(d) and B(s) decays to two vectors, Phys. Rev. **D65**, 073018 (2002).

[9] H.-Y. Cheng and K.-C. Yang, Branching Ratios and Polarization in $B \rightarrow VV$, VA, AA Decays, Phys. Rev. **D78**, 094001 (2008).

[10] M. Beneke, J. Rohrer, and D. Yang, Branching fractions, polarisation and asymmetries of $B \rightarrow VV$ decays, Nucl. Phys. **B774**, 64–101 (2007).

[11] M. Beneke, M. Gronau, J. Rohrer, and M. Spranger, A precise determination of alpha using $B^0 \rightarrow \rho^+\rho^-$ and $B^+ \rightarrow K^{*0}\rho^+$, Phys. Lett. **B638**, 68–73 (2006).

[12] G. G. Ross, *Grand Unified Theories*, Benjamin/Cummings Publishing Company, Inc., Menlo Park, CA, 1985.

[13] J. Boehm, *A Measurement of Electron Neutrino Appearance with the Minos Experiment*, PhD thesis, Harvard University, 2009.

[14] J. H. Christenson, J. W. Cronin, V. L. Fitch, and R. Turlay, Evidence for the 2π Decay of the K-20 Meson, Phys. Rev. Lett. **13**, 138–140 (1964).

[15] A. Abashian et al., Search for CP nonconservation in K-20 decays, Phys. Rev. Lett. **13**, 243–246 (1964).

[16] C. S. Wu, E. Ambler, R. W. Hayward, D. D. Hoppes, and R. P. Hudson, Experimantal Test of Parity Conservation in Beta Decay, Phys. Rev. **105**, 1413–1414 (1957).

[17] P. Harrison and H. Quinn, editors, *The BABAR Physics Book: Physics at an Asymmetric B Factory*, Report of the *BABAR* Physics Workshop, SLAC Report 504, 1998.

[18] H. Quinn, B Physics and CP Violation, SLAC-PUB-8965, 2001.

[19] G. Branco, L. Lavoura, , and J. Silva, *CP Violation*, Oxford University Press, Oxford, 1 edition, 1999.

[20] B. Cahn, Some Useful Formulae for CP Violation at BaBar, 2001.

[21] B. Aubert et al., Measurement of the CP violating asymmetry amplitude $\sin(2\beta)$, Phys. Rev. Lett. **89**, 201802 (2002).

[22] L. Wolfenstein, Parametrization of the Kobayashi-Maskawa Matrix, Phys. Rev. Lett. **51**, 1945 (1983).

[23] J. Charles et al., CP violation and the CKM matrix: Assessing the impact of the asymmetric B factories, Eur. Phys. J. **C41**, 1–131 (2005), updated results and plots available at: http://ckmfitter.in2p3.fr.

[24] T. Inami and C. S. Lim, Effects of Superheavy Quarks and Leptons in Low-Energy Weak Processes $K_L \to \mu^+ \, \mu$m, $K^+ \to \pi^+ \nu\overline{\nu}$ and $K^0 \longleftrightarrow \overline{K}^0$, Prog. Theor. Phys. **65**, 297 (1981).

[25] K. Abe et al., An improved measurement of mixing-induced CP violation in the neutral B meson system, Phys. Rev. **D66**, 071102 (2002).

[26] D. Asner et al., Averages of b-hadron, c-hadron, and tau-lepton Properties, (2010), Online update at http://www.slac.stanford.edu/xorg/hfag.

[27] M. Gronau and D. London, Isospin analysis of CP asymmetries in B decays, Phys. Rev. Lett. **65**, 3381–3384 (1990).

[28] B. Aubert et al., Measurements of branching fractions, polarizations, and direct CP-violation asymmetries in $B \to \rho K^*$ and $B \to f_0 K^*$ decays, Phys. Rev. Lett. **97**, 201801 (2006).

[29] W. Park, Measurements of Branching Fraction, Polarizations, and Direct CP Asymmetry in $B^0 \to \rho^- K^{*+}$ decay, *BABAR* Analysis Document 1430, 2006.

[30] S. Emery et al., Measurements of Branching Fractions and Polarizations in $B^+ \to K^{*0}\rho^+$ and $B^0 \to K^{*0}\rho^0$ decays, *BABAR* Analysis Document 1211, 2006.

[31] L.-M. Mir, Measurement of the $B^+ \to \rho^0 K^{*+}$ branching fraction, polarization and direct-CP asymmetry, *BABAR* Analysis Document 1216, 2006.

[32] P. del Amo Sanchez et al., Measurements of branching fractions, polarizations, and direct CP-violation asymmetries in $B^+ \to \rho^0 K^{*+}$ and $B^+ \to f_0(980)K^{*+}$ decays, Phys. Rev. **D83**, 051101 (2011).

[33] S. Emery and G. Vasseur, Full angular analysis of the $B^+ \to K^{*0}\rho^+$ decay mode, *BABAR* Analysis Document 1951, 2009.

[34] S. H. Kyeong et al., Measurements of Charmless Hadronic $b \to s$ Penguin Decays in the $\pi\pi K\pi$ Final State and Observation of $B^0 \to \rho^0 K^+ \pi^-$, Phys. Rev. **D80**, 051103 (2009).

[35] K. Abe et al., Measurements of branching fractions and polarization in $B \to K^*\rho$ decays, Phys. Rev. Lett. **95**, 141801 (2005).

[36] H.-Y. Cheng and K.-C. Yang, Erratum to Branching Ratios and Polarization in $B \to VV$, VA, AA Decays, Phys. Rev. **D79**, 039903 (2008).

[37] H.-Y. Cheng, C.-K. Chua, and K.-C. Yang, Charmless B decays to a scalar meson and a vector meson, Phys. Rev. **D77**, 014034 (2008).

[38] Z.-Q. Zhang, Study of scalar meson $f_0(980)$ and $K_0^*(1430)$ from $B \to f_0(980)\rho(\omega, \phi)$ and $B \to K_0^*(1430)\rho(\omega)$ Decays, Phys. Rev. **D82**, 034036 (2010).

[39] B. Aubert et al., The *BABAR* detector, Nucl. Instrum. Meth. **A479**, 1–116 (2002).

[40] W. Menges, The *BABAR* muon system upgrade, IEEE Nucl. Sci. Symp. Conf. Rec. **5**, 1470–1474 (2006).

[41] P. Ongmongkolkul1 et al., Particle Identification Using Error Correction Output Code Multi-class Classifier, *BABAR* Analysis Document 2199, 2009.

[42] T. Dietterich and G. Bakiri, Solving Multiclass Learning Problems via Error-Correcting Output Codes, Journal of Artificial Intelligence Research **2**, 263286 (1995).

[43] S. Agostinelli et al., Nucl. Instrum. Meth. **506**, 250 (2003), The *BABAR* detector Monte Carlo simulation is based on GEANT4.

[44] D. Lange, Nucl. Instrum. Meth. **462**, 152 (2001), The *BABAR* detector Monte Carlo simulation is also based on EvtGen.

[45] W. Dunwoodie, Fits to K pi I=1/2 S-wave Amplitude and Phase Data, 2009.

[46] RooRarFit is a fitting package developed by Lei Zhang.

[47] M. Pivk and F. Le Diberder, sPlot: a statistical tool to unfold data distributions, Nucl. Instrum. Meth. **A555**, 356–369 (2005).

[48] J. M. Link et al., Hadronic mass spectrum analysis of $D^+ \rightarrow K^- \pi^+ \mu^+ \nu$ decay and measurement of the $K^*(892)^0$ mass and width, Phys. Lett. **B621**, 72–80 (2005).

[49] D. Epifanov et al., Study of $\tau^- \rightarrow K^0_S \pi^- \nu_\tau$ decay at Belle, Phys. Lett. **B654**, 65–73 (2007).

[50] S. Paramesvaran et al., Analysis of the $\tau \rightarrow K^0_S \pi \nu_\tau$ mass spectrum, and measurement of $\tau \rightarrow K^0_S \pi \nu_\tau$ and $\tau \rightarrow K^0_S \pi \pi^0 \nu_\tau$ branching fractions, *BABAR* Analysis Document 2222, 2009.

[51] *BABAR* tracking efficiency task force Tau3-1 study for R24 data and SP10 MC.

[52] G. D. McGregor, B Counting at *BABAR*, (2008).

[53] J. Becker et al., B^0 Decays to $\eta'\eta$, $\eta'\pi^0$, $\eta\pi^0$, and $\omega\pi^0$, *BABAR* Analysis Document 1772, 2008.

[54] F. Blanc et al., Branching fraction and charge asymmetry measurements in B meson Decays to $\eta'K$ and $\omega K/\pi$ decays with run1-5 data, *BABAR* Analysis Document 1678, 2006.

[55] P. Clark et al., Branching Fraction Analysis of $B \to \eta' K^*$ and $\eta' \rho$, *BABAR* Analysis Document 960, 2004.

[56] B. Aubert et al., Measurement of Time-Dependent CP Asymmetry in $B^0 \to c\bar{c}K^{(*)0}$ Decays, Phys. Rev. **D79**, 072009 (2009).

[57] F. Blanc et al., Measurements of branching fractions and charge and time-dependent asymmetries for $B \to \eta' K$, *BABAR* Analysis Document 490, 2004.

[58] F. Blanc et al., Time-Dependent CP-violating Asymmetries in B meson Decays to $\eta' K$, *BABAR* Analysis Document 906, 2004.

[59] B. Aubert et al., Time-dependent and time-integrated angular analysis of $B \to \varphi K_S^0 \pi^0$ and $\varphi K^{\pm} \pi^{\mp}$, Phys. Rev. **D78**, 092008 (2008).

[60] Y. Gao et al., Vector-Tensor and Vector-Vector Decay Amplitude Measurements with $B^0 \to \phi K^{*0}$, *BABAR* Analysis Document 1428, 2007.

[61] B. Aubert et al., Dalitz plot analysis of the decay $B^{\pm} \to K^{\pm} K^{\pm} K^{\mp}$, Phys. Rev. **D74**, 032003 (2006).